

PACIFIC EARTHQUAKE ENGINEERING RESEARCH CENTER

Seismic Behavior of Special Concentric Braced Frames under Short- and Long-Duration Ground Motions

Ali Hammad

Mohamed A. Moustafa

Department of Civil and Environmental Engineering
University of Nevada, Reno

PEER Report No. 2019/09
Pacific Earthquake Engineering Research Center
Headquarters at the University of California, Berkeley

December 2019

Disclaimer

The opinions, findings, and conclusions or recommendations expressed in this publication are those of the author(s) and do not necessarily reflect the views of the study sponsor(s), the Pacific Earthquake Engineering Research Center, or the Regents of the University of California.

Seismic Behavior of Special Concentric Braced Frames under Short- and Long-Duration Ground Motions

Ali Hammad

Mohamed A. Moustafa

Department of Civil and Environmental Engineering
University of Nevada, Reno

PEER Report 2019/09
Pacific Earthquake Engineering Research Center
Headquarters at the University of California, Berkeley

December 2019

ABSTRACT

Over the past decade, several long-duration subduction earthquakes took place in different locations around the world, e.g., Chile in 2010, Japan in 2011, China in 2008, and Indonesia in 2004. Recent research has revealed that long-duration, large-magnitude earthquakes may occur along the Cascadia subduction zone of the Pacific Northwest Coast of the U.S. The duration of an earthquake often affects the response of structures. Current seismic design specifications mostly use response spectra to identify the hazard and do not consider duration effects. Thus, a comprehensive understanding of the effect of the duration of the ground motion on structural performance and its design implications is an important issue.

The goal of this study was to investigate how the duration of an earthquake affects the structural response of special concentric braced frames (SCBFs). A comprehensive experimental program and detailed analytical investigations were conducted to understand and quantify the effect of duration on collapse capacity of SCBFs, with the goal of improving seismic design provisions by incorporating these effects. The experimental program included large-scale shake table tests, and the analytical program consisted of pre-test and post-test phases. The pre-test analysis phase performed a sensitivity analysis that used OpenSees models preliminarily calibrated against previous experimental results for different configuration of SCBFs. A tornado-diagram framework was used to rank the influence of the different modeling parameters, e.g., low-cycle fatigue, on the seismic response of SCBFs under short- and long-duration ground motions. Based on the results obtained from the experimental program, these models were revisited for further calibration and validation in the post-test analysis.

The experimental program included three large-scale shake-table tests of identical single-story single-bay SCBF with a chevron-brace configuration tested under different ground motions. Two specimens were tested under a set of spectrally-matched short and long-duration ground motions. The third specimen was tested under another long-duration ground motion. All tests started with a 100% scale of the selected ground motions; testing continued with an ever-increasing ground-motion scale until failure occurred, e.g., until both braces ruptured. The shake table tests showed that the duration of the earthquake may lead to premature seismic failure or lower capacities, supporting the initiative to consider duration effects as part of the seismic design provisions. Identical frames failed at different displacements demands because of the damage accumulation associated with the earthquake duration, with about 40% reduction in the displacement capacity of the two specimens tested under long-duration earthquakes versus the short-duration one.

Post-test analysis focused first on calibrating an OpenSees model to capture the experimental behavior of the test specimens. The calibration started by matching the initial stiffness and overall global response. Next, the low-cycle fatigue parameters were fine-tuned to properly capture the experimental local behavior, i.e., brace buckling and rupture. The post-test analysis showed that the input for the low-cycle fatigue models currently available in the literature does not reflect the observed experimental results. New values for the fatigue parameters are suggested herein based on the results of the three shake-table tests.

The calibrated model was then used to conduct incremental dynamic analysis (IDA) using 44 pairs of spectrally-matched short- and long-duration ground motions. To compare the

effect of the duration of ground motion, this analysis aimed at incorporating ground-motion variability for more generalized observations and developing collapse fragility curves using different intensity measures (IMs). The difference in the median fragility was found to be 45% in the drift capacity at failure and about 10% in the spectral acceleration (S_a). Using regression analysis, the obtained drift capacity from analysis was found to be reduced by about 8% on average for every additional 10 sec in the duration of the ground motion.

The last stage of this study extended the calibrated model to SCBF archetype buildings to study the effect of the duration of ground motion on full-sized structures. Two buildings were studied: a three-story and nine-story build that resembled the original SAC buildings but were modified with SCBFs as lateral support system instead of moment resisting frames. Two planer frames were adopted from the two buildings and used for the analysis. The same 44 spectrally-matched pairs previously used in post-test analysis were used to conduct nonlinear time history analysis and study the effect of duration. All the ground motions were scaled to two hazard levels for the deterministic time history analysis: 10% exceedance in 50 years and 2% exceedance in 50 years. All analysis results were interpreted in a comparative way to isolate the effect of duration, which was the main variable in the ground-motion pairs. In general, the results showed that the analyzed SCBFs experienced higher drift values under the long-duration suite of ground motions, and, in turn, a larger percentage of fractured braces under long-duration cases. The archetype SCBFs analysis provided similar conclusions on duration effects as the experimental and numerical results on the single-story single-bay frame.

ACKNOWLEDGMENTS

Any opinions, findings, and conclusions or recommendations expressed in this material are those of the authors and do not necessarily reflect those of the Pacific Earthquake Engineering Research Center (PEER) or the Regents of the University of California.

CONTENTS

ABSTRACT	iii
ACKNOWLEDGMENTS	v
TABLE OF CONTENTS	vii
LIST OF TABLES	xi
LIST OF FIGURES	xiii
1 INTRODUCTION.....	1
1.1 Overview	1
1.2 Research Problem	3
1.3 Methodology	4
1.4 Research Objectives.....	4
1.5 Report Outline.....	5
2 BACKGROUND AND LITERATURE REVIEW	7
2.1 Previous Research of SCBFs.....	7
2.1.1 Previous Research Studying Long-Duration Effects	9
3 MODELING AND SENSITIVITY ANALYSIS	13
3.1 Low-Cycle Fatigue Modeling.....	13
3.2 Analytical Model	15
3.2.1 Model Description	15
3.2.1.1 Gusset-Plate Connection	16
3.2.1.2 Beam-Column Connections	17
3.2.2 Calibrated Model Results.....	19
3.3 Ground-Motion Selection.....	20
3.4 Model Sensitivity Analysis	22
3.5 Nonlinear Time History Analysis Results.....	25
3.5.1 Selected Response History.....	25
3.5.2 Summary of Mean Peak Response	27
3.6 Sensitivity Analysis	29
3.6.1 Tornado Diagram Analysis.....	29

3.6.2	Variation in Drift (Displacement) Capacity.....	30
3.6.3	Variation in Base-Shear Capacity.....	31
3.7	Effect of Earthquake Duration	31
3.7.1	Collapse Assessment.....	31
3.7.2	Fragility Curves	33
4	EXPERIMENTAL PROGRAM DEVELOPMENT	35
4.1	Prototype and Specimen.....	35
4.2	Design Philosophy	38
4.3	Design Calculations.....	38
4.3.1	General.....	38
4.3.2	Brace Selection	39
4.3.3	Beam Design.....	39
4.3.3.1	<i>Beam Strength</i>	<i>39</i>
4.3.4	Column Design	40
4.3.4.1	<i>Column Strength.....</i>	<i>40</i>
4.3.4.2	<i>Column-Base Plate Connection.....</i>	<i>40</i>
4.3.5	Brace-to-Gusset Plate Connection	40
4.3.6	Gusset-Plate Design.....	41
4.3.7	Gusset Plate-to-Frame Joint Design.....	42
4.3.7.1	<i>Interface Forces</i>	<i>42</i>
4.3.7.2	<i>Gusset-to-Frame Weld Design</i>	<i>43</i>
4.3.8	Beam-to-Column (Simple Shear)	44
4.3.8.1	<i>Initial Design.....</i>	<i>44</i>
4.3.8.2	<i>Bolt Strength.....</i>	<i>44</i>
4.3.8.3	<i>Bearing Strength.....</i>	<i>44</i>
4.3.8.4	<i>Shear Strength of the Plate.....</i>	<i>44</i>
4.3.8.5	<i>Plate Bending</i>	<i>45</i>
4.3.8.6	<i>Shear Plate Welds</i>	<i>45</i>
4.4	Construction of Specimens.....	45
4.5	Material Properties.....	47
4.6	Test Setup	47
4.7	Instrumentation.....	51
4.7.1	Load, Displacement, and Acceleration Measurement	51
4.7.2	Strain Measurement	52

	4.7.3	Cameras.....	52
4.8		Ground-Motion Selection.....	53
5		EXPERIMENTAL RESULTS AND DISCUSSION.....	57
5.1		Global Response	57
	5.1.1	Test Progression and Mode of Failure	57
	5.1.2	Force-Displacement Response.....	58
	5.1.3	Acceleration Response.....	63
	5.1.4	Stiffness Degradation/Period Elongation.....	66
	5.1.5	Summary of Key Test Results	68
5.2		Local Response	70
	5.2.1	Brace Buckling.....	70
	5.2.2	Low-Cycle Fatigue and Brace Rupture.....	75
	5.2.3	Gusset Plates Strain Data	95
5.3		General Notes	102
6		POST-TEST ANALYSIS	103
6.1		Overview	103
6.2		Numerical Model Calibration.....	103
	6.2.1	Specimen S1.....	104
	6.2.2	Specimen S2.....	107
	6.2.3	Specimen S3.....	109
6.3		Fatigue Parameters Analysis	111
6.4		Incremental Dynamic Analysis.....	116
	6.4.1	Ground-Motion Selection	117
	6.4.2	Development of Collapse Fragility Curve	118
	6.4.3	Collapse Assessment.....	120
7		EFFECT OF DURATION ON ARCHETYPE SCBF BUILDINGS.....	123
7.1		Archetype Buildings	123
7.2		System Modeling	127
7.3		Ground-Motion Selection.....	128
7.4		Results and Discussions	129
	7.4.1	Three-Story Building Results	129
		7.4.1.1 10%/50 years ground-motion set.....	129

7.4.1.2	2%/50 years ground-motion set.....	132
7.4.2	Nine-Story Building Results.....	134
7.4.2.1	10%/50 years ground-motion set.....	135
7.4.2.2	2%/50 years ground-motion set.....	137
7.5	Limit States.....	140
8	SUMMARY AND CONCLUSIONS.....	143
8.1	Summary.....	143
8.2	Observations and Conclusions.....	144
8.3	Future Work.....	147
	REFERENCES.....	149

LIST OF TABLES

Table 3.1	Different recommended values for OpenSees fatigue modeling (m and ε_0).....	14
Table 3.2	Recommended <i>Steel02</i> parameters based on Karamanci and Lignos [2014]......	15
Table 3.3	Dimensions and material properties for selected UW test specimens.	16
Table 3.4	Summary of ground motions used in the sensitivity analysis.....	21
Table 3.5	Summary of varied <i>Steel02</i> input parameters used for sensitivity analysis.....	23
Table 3.6	Sensitivity analysis models parameters for diagonal (D) and (X-) brace SCBFs	24
Table 3.7	Summary of mean peak response values for all models from two motions sets.....	28
Table 4.1	Similitude scale factors used for the conducted shake table tests (after Lu et al. [2008]).....	38
Table 4.2	Steel grades.	47
Table 4.3	Characteristics of the selected ground motions for all three test specimens.....	54
Table 5.1	Summary of key test results for all runs and specimens.	69
Table 6.1	Summary of analysis results for varying low-cycle fatigue model parameters (m and ε_0) as compared to experimental results.	115
Table 6.2	Summary and average value for variation (%) in force values from experimental results associated with varying low-cycle fatigue model parameters.	116
Table 6.3	Summary and average value for variation (%) in drift values from experimental results associated with varying low-cycle fatigue model parameters.	116
Table 7.1	Member sizes of the three- and nine-story archetype buildings with representative frames used for the analysis.	126
Table 8.1	Summary of the variation in the seismic demand in SCBFs as obtained from the various analytical and experimental parts of this study.	147

LIST OF FIGURES

Figure 2.1	Typical test specimens and loading setups for UW research program on concentric braced frames (after Hsiao [2012]).	8
Figure 3.1	Typical test specimen for single-story single-bay SCBF: diagonal-braced HSS1 (left) and X-braced HSS31 (right).	15
Figure 3.2	Illustration of the proposed connection model [Hsiao et al. 2012].	17
Figure 3.3	Illustration of (a) the shear-tab connection and (b) the <i>Pinching4</i> material model in OpenSees (adopted from Hsiao et al. [2012]).	18
Figure 3.4	Illustration of the numerical model details used for the sensitivity analysis.	19
Figure 3.5	Simulated and measured responses of specimen HSS1: displacement history (top) and force history (bottom).	20
Figure 3.6	Simulated and measured force-drift responses of specimens: (a) HSS1 with diagonal single brace; and (b) HSS31 with double X-bracing.	20
Figure 3.7	Mean response spectra for short-duration (left) and long-duration (right) ground motions compared to the target MCE response spectrum of San Francisco.	22
Figure 3.8	Diagonal-bracing frame, Model #D-23 under selected short-duration ground motion: (a) hysteresis, (b) displacement, and (c) force histories.	25
Figure 3.9	Diagonal-bracing frame, Model #D-7 under selected long-duration ground motion: (a) hysteresis, (b) displacement, and (c) force histories.	26
Figure 3.10	X-bracing frame, Model #X-11 under selected short-duration ground motion: (a) hysteresis, (b) displacement, and (c) force histories.	26
Figure 3.11	X-bracing frame, Model #X-14 under selected long-duration ground motion: (a) hysteresis, (b) displacement, and (c) force histories.	27
Figure 3.12	Tornado diagrams for drift ratio (%) for single- and x-braced frames under cyclic loading and mean responses from sets of short- and long-duration ground motions. Dashed lines represent results from calibrated model presented earlier.	30
Figure 3.13	Tornado diagrams for base shear capacity for single- and x-braced frames under cyclic loading and mean responses from sets of short- and long-duration ground motions. Dashed lines represent results from the calibrated model.	32
Figure 3.14	Fitted relationship between the significant duration and the single-braced frame drift ratio at failure (drift capacity) for all cases with varied modeling parameters.	32
Figure 3.15	(a) Typical procedure for developing fragility curve: and (b) comparison of developed collapse fragility curves for single-braced frame under short- and long-duration ground motions.	34
Figure 3.16	Developed fragility curves using spectral accelerations (S_a) for single- and double-braced frames under short and long-duration ground motions.	34

Figure 4.1	A three-dimensional view of the prototype building used to determine the test specimens design forces.	36
Figure 4.2	Plan view of the prototype building.....	36
Figure 4.3	Prototype typical X-bracing geometry and illustration of the chevron braced frame consideration for determining reduced-scale specimens design forces.	37
Figure 4.4	Details and designed sections for final test specimens [dimensions in both US units (in., ft) and metric (mm) are provided].	37
Figure 4.5	Brace-to-gusset-plate connection.....	41
Figure 4.6	(a) Illustration of block shear, and (b) Whitmore width for gusset plates.	41
Figure 4.7	Recharacterized forces: (a) UFM method and (b) KISS method.....	43
Figure 4.8	Shear tab plate shear distribution.....	45
Figure 4.9	Brace slot details.	46
Figure 4.10	The three fully fabricated test specimens before shipping to UNR.	46
Figure 4.11	Schematic diagram showing the details of the shake table test setup.	48
Figure 4.12	General layout and components of shake table test setup.....	48
Figure 4.13	Elevation of actual test setup.	49
Figure 4.14	Schematic diagram showing the details of out-of-plane restraint system.....	50
Figure 4.15	String Pots, LVDTs layout, and locaton of accelerometers.....	51
Figure 4.16	Strain gages locations and distribution for each test specimen.....	52
Figure 4.17	DIC targets attached to one of the tested SCBFs and the corresponding 2D coordinates (mm) for the spatial target locations.....	53
Figure 4.18	Acceleration time histories of the long- and modified short-duration records.....	55
Figure 4.19	Acceleration response spectra of the original and matched short-duration record versus the long-duration record.	55
Figure 4.20	Time histories of the third specimen ground motion (velocity and displacement pulses shifted from peak acceleration).....	56
Figure 5.1	Typical test progression: (a) inelastic buckling, and (b) complete brace rupture	58
Figure 5.2	Specimen 1 force history.	59
Figure 5.3	Specimen 1 displacement histories at top and mid-height of frame.	59
Figure 5.4	Specimen 2 force history.	60
Figure 5.5	Specimen 2 displacement histories at top and mid-height of frame.	60
Figure 5.6	Force versus drift ratio for S1 and S2 (left), and top displacement history for both tests (right).	61
Figure 5.7	The backbone curves for S1 and S2 with both braces buckling and rupture identified.	62
Figure 5.8	Specimen 3 force history.	62

Figure 5.9	Specimen 3 displacement histories at top and mid-height of frame.	63
Figure 5.10	(a) Force versus drift ratio (hysteretic behavior) for S3; and (b) top displacement history.	63
Figure 5.11	Specimen 1 acceleration histories at different locations and heights.	64
Figure 5.12	Specimen 2 acceleration histories at different locations and heights.	64
Figure 5.13	Specimen 3 acceleration histories at different locations and heights.	65
Figure 5.14	Measured force versus estimated (expected) force as deduced from the measured top acceleration for Specimen S2.	65
Figure 5.15	The frequency response function and identified fundamental frequency for the three specimens from white noise tests.	67
Figure 5.16	Stiffness degradation with respect to fundamental period for all tested specimens, S1, S2, and S3.	67
Figure 5.17	(a) Out-of-plane brace buckling; (b) upper gusset deformation; (c) lower gusset deformation; and (d) upper brace white wash flakes.	70
Figure 5.18	Specimen 1 braces out-of-plane displacement.	71
Figure 5.19	Specimen 2 braces out-of-plane displacement.	71
Figure 5.20	Specimen 3 braces out-of-plane displacement.	72
Figure 5.21	Specimens 1, 2, and 3 braces out-of-plane deformed shape, respectively.	72
Figure 5.22	Stages of brace failure: (a) local buckling, (b) crack initiation, (c) crack propagation, and (d) fracture.	73
Figure 5.23	Specimen 1 ruptured braces locations.	73
Figure 5.24	Specimen 1 elevation with both braces ruptured.	74
Figure 5.25	Specimen 2 ruptured braces locations.	74
Figure 5.26	Specimen 3 ruptured braces locations.	74
Figure 5.27	Strain gages locations along the brace length (A, B, and C) and around the HSS brace four faces (1, 2, 3, and 4).	75
Figure 5.28	Specimen 1 north brace strains at section A.	76
Figure 5.29	Specimen 1 north brace strains at section B.	77
Figure 5.30	Specimen 1 north brace strains at section C.	78
Figure 5.31	Specimen 1 south brace strains at section A.	79
Figure 5.32	Specimen 1 south brace strains at section B.	80
Figure 5.33	Specimen 1 south brace strains at section C.	81
Figure 5.34	Specimen 2 north brace strains at section A.	82
Figure 5.35	Specimen 2 north brace strains at section B.	83
Figure 5.36	Specimen 2 north brace strains at section C.	84
Figure 5.37	Specimen 2 south brace strains at section A.	85
Figure 5.38	Specimen 2 south brace strains at section B.	86
Figure 5.39	Specimen 2 south brace strains at section C.	87
Figure 5.40	Specimen 3 north brace strains at section A.	88
Figure 5.41	Specimen 3 north brace strains at section B.	89

Figure 5.42	Specimen 3 north brace strains at section C.	90
Figure 5.43	Specimen 3 south brace strains at section A.	91
Figure 5.44	Specimen 3 south brace strains at section B.	92
Figure 5.45	Specimen 3 south brace strains at section C.	93
Figure 5.46	Number of cycles for different strain ranges as accumulated from all S1 and S2 runs until failure.	95
Figure 5.47	Representation of how outermost brace fiber accumulated damage from different strain ranges for all S1 and S2 runs until failure.	95
Figure 5.48	Strains in Specimen S1 middle top gusset plate at four identified locations.	96
Figure 5.49	Strains in Specimen S1 lower gusset plates at the several identified locations.	97
Figure 5.50	Strains in Specimen S2 middle top gusset plate at four identified locations.	98
Figure 5.51	Strains in Specimen S2 lower gusset plates at the several identified locations.	99
Figure 5.52	Strains in Specimen S3 middle top gusset plate at four identified locations.	100
Figure 5.53	Strains in Specimen S3 lower gusset plates at the several identified locations.	101
Figure 5.54	(a) Column deformation at base; (b) bottom gusset-to-column edge weld crack; and (c) yielding evidence at the link-to-column connection location.	102
Figure 6.1	Schematic representation of the OpenSees numerical model.	104
Figure 6.2	Comparison of base shear history for Specimen S1 obtained experimentally and from the OpenSees model.	105
Figure 6.3	Comparison of the relative displacement history at the top of the frame as obtained for Specimen S1 obtained experimentally and from the OpenSees model.	105
Figure 6.4	Comparison of Specimen S1 stiffness degradation obtained experimentally and from the OpenSees model.	106
Figure 6.5	Comparison of Specimen S1 force-drift relationship (hysteresis) and backbone curves obtained experimentally and from the OpenSees model.	107
Figure 6.6	Comparison of base shear history for Specimen S2 obtained experimentally and from the OpenSees model.	108
Figure 6.7	Comparison of the relative displacement history at the top of the frame as obtained for Specimen S2 obtained experimentally and from the OpenSees model.	108
Figure 6.8	Comparison of Specimen S2 stiffness degradation obtained experimentally and from the OpenSees model.	109
Figure 6.9	Comparison of Specimen S2 force-drift relationship (hysteresis) and backbone curves as obtained experimentally and from the OpenSees model.	109

Figure 6.10	Comparison of base shear history for Specimen S3 experimentally and from the OpenSees model.	110
Figure 6.11	Comparison of the relative displacement history at the top of the frame obtained for Specimen S3 experimentally and from the OpenSees model.	110
Figure 6.12	Comparison of Specimen S3 stiffness degradation obtained experimentally and from the OpenSees model.	111
Figure 6.13	Comparison of Specimen S3 force-drift relationship (hysteresis) and backbone curves obtained experimentally and from the OpenSees model.	111
Figure 6.14	Force-drift backbone for Specimen S1 modeled using different low-cycle fatigue parameters.	113
Figure 6.15	Force-drift backbone for Specimen S2 modeled using different low-cycle fatigue parameters.	113
Figure 6.16	Force-drift backbone for Specimen S3 modeled using different low-cycle fatigue parameters.	114
Figure 6.17	Short- and long-duration ground-motion response spectrum and their mean.	118
Figure 6.18	Mean response spectrum for short- and long-duration ground-motion suites.	118
Figure 6.19	IDA results for story drift as relates to PGA as the intensity measure.	119
Figure 6.20	IDA results for story drift as relates to S_a as the intensity measure.	120
Figure 6.21	Developed fragility curves for one-story one-bay SCBF with chevron braces (test specimens) using two intensity measures: (a) drift %, and (b) spectral acceleration.	120
Figure 6.22	Fitted relationship between the significant duration and frame drift capacity.	121
Figure 6.23	Fitted relationship between the significant duration and frame spectral acceleration.	121
Figure 7.1	Floor plan of the considered three-story archetype building.	124
Figure 7.2	Elevation and brace configuration of the three-story archetype building.	124
Figure 7.3	Floor plan of the considered nine-story archetype building.	125
Figure 7.4	Elevation and brace configuration of the nine-story archetype building.	126
Figure 7.5	Leaning column modeling.	127
Figure 7.6	Short- and long-duration ground-motion sets and their mean.	128
Figure 7.7	Comparison of short- and long-duration ground-motion mean for the 10%/50-years and 2%/50-years hazard level.	129
Figure 7.8	Comparison of the distribution of maximum story drift along three-story SCBF height at the 10%/50 years hazard level for short- and long-duration earthquakes.	130
Figure 7.9	Comparison of the distribution of interstory drift along three-story SCBF at the 10%/50 years hazard level for short- and long-duration earthquakes.	131

Figure 7.10	Comparison of the distribution of residual displacement along three-story SCBF at the 10%/50 years hazard level for short- and long-duration earthquakes.	131
Figure 7.11	Comparison of the distribution of floor acceleration along three-story SCBF height at the 10%/50 years hazard level for short and long-duration earthquakes.	132
Figure 7.12	Comparison of the distribution of maximum story drift along three-story SCBF at the 2%/50-years hazard level for short- and long-duration earthquakes.	133
Figure 7.13	Comparison of the distribution of interstory drift along three-story SCBF at the 2%/50-years hazard level for short- and long-duration earthquakes.	133
Figure 7.14	Comparison of the distribution of residual displacement along three-story SCBF height at the 2%/50-years hazard level for short- and long-duration earthquakes.	134
Figure 7.15	Comparison of the distribution of floor acceleration along three-story SCBF at the 2%/50-years hazard level for short- and long-duration earthquakes.	134
Figure 7.16	Comparison of the distribution of maximum story drift along nine-story SCBF at the 10%/50-years hazard level for short- and long-duration earthquakes.	135
Figure 7.17	Comparison of the distribution of maximum story displacement along nine-story SCBF height at the 10%/50-years hazard level for short- and long-duration earthquakes.	136
Figure 7.18	Comparison of the distribution of interstory drift along nine-story SCBF height at the 10%/50-years hazard level for short- and long-duration earthquakes.	136
Figure 7.19	Comparison of the distribution of residual displacement along nine-story SCBF at the 10%/50-years hazard level for short- and long-duration earthquakes.	137
Figure 7.20	Comparison of the distribution of floor acceleration along nine-story SCBF at the 10%/50-years hazard level for short- and long-duration earthquakes.	137
Figure 7.21	Distribution of maximum story drift along nine-story SCBF height at the 2%/50-years hazard level as compared for short- and long-duration earthquakes.	138
Figure 7.22	Distribution of maximum story displacement along nine-story SCBF height at the 2%/50-years hazard level as compared for short- and long-duration earthquakes.	138
Figure 7.23	Distribution of interstory drift along nine-story SCBF height at the 2%/50-years hazard level as compared for short- and long-duration earthquakes.	139
Figure 7.24	Distribution of residual displacement along nine-story SCBF at the 2%/50-years hazard level as compared for short- and long-duration earthquakes.	139

Figure 7.25	Distribution of floor acceleration along nine-story SCBF at the 2%/50-years hazard level as compared for short- and long-duration earthquakes.	140
Figure 7.26	Percentage of braces meeting a given limit state as related to total number of braces in the three-story SCBF as obtained from analysis results under the short- and long-duration ground motions scaled at 10%/50-years and 2%/50-years hazard levels.	142
Figure 7.27	Percentage of braces meeting a given limit state as related to total number of braces in the nine-story SCBF as obtained from analysis results under the short- and long-duration ground motions scaled at 10%/50-years and 2%/50-years hazard levels	142

1 Introduction

1.1 OVERVIEW

Steel structures are commonly used in regions of high seismicity because they are able to resist lateral loading because of their high ductility. Lateral systems fall under two categories: braced frames or moment frames. Braced frames, such as special concentrically braced frames (SCBFs), are a popular design choice. They are cost effective, easy to assemble, and perform satisfactorily in terms of limited drift. When considering performance-based seismic design (PBSD), SCBFs must meet life safety and collapse prevention requirements under large infrequent earthquakes. To ensure that steel designs meet such objectives, proper simulation of the nonlinear behavior is mandatory. Because existing SCBFs analytical models are heavily dependent on several assumptions, e.g., low-cycle fatigue and fatigue-induced rupture, their response needs to be carefully validated. Modeling approaches currently used in practice might not accurately predict the post-yield mechanisms and failure modes, especially under special lateral loading cases tied to low-cycle fatigue, as might occur in earthquakes long in duration. Studying such long-duration effects is realized using mostly numerical rather experimental simulation; a brief literature review is discussed below. Thus, proper modeling and numerical simulation of seismic response of SCBFs is crucial. Simplified modeling in popular platforms such as OpenSees [McKenna et al. 2006] rely on beam-column elements rather than accounting for three-dimension (3D) local behavior. This begs the question: how reliable are these models are when used to assess the behavior of SCBFs under long-duration earthquakes or in the development of fragility curves for PBSD?

Nonlinear behavior of SCBFs is controlled by the braces buckling in compression, yielding in tension, and post-buckling response through rupture. The gusset plates used to connect braces to the beams and columns must accommodate the large expected inelastic deformations and end rotations when the braces buckle, while still sustaining the full axial capacity of the brace. The actual design of gusset plates for SCBFs connections can significantly affect their deformation capacity; therefore, they need to be properly modeled to simulate large deformations associated with local and global brace buckling. Different methods are used to capture the onset of cracking or fracture of braces using strains values or components of strains, or the computed stress-strain history from the analyses. Ikeda and Mahin [1986] proposed a model based on a simplified geometric representation consisting of simply supported elastic brace member with an idealized plastic hinge located at mid-span. The analytical equations developed for this formulation were supplemented with empirically derived formulas related to the variation of tangent modulus of elasticity during cycling and the axial force-rotation relationship considered for the plastic hinge.

More complex modeling of SCBFs without relying on simplified approaches might require detailed 3D finite-element models (FEM) that uses solid elements. A recent study by Hassan and Mahmoud [2017], investigated the effect of modeling resolution on the seismic performance of a steel hospital building. Their models varied from a simplified two-dimensional (2D) model without soil–structure interaction to a complex 3D model that included soil–structure interaction. The study showed that the incorporating realistic material behavior and accurate connection modeling enhanced the system global behavior obtained from analysis. Unfortunately, a major shortcoming for such detailed or complex models is the substantial computational cost associated with such analyses, especially for structures with large numbers of degrees-of-freedom simulated through failure [Hsiao 2012].

Thus, even with recent advances in computing power, a complex 3D FEM is not typical practice in design offices. Simpler FEMs that consider a combination of one-dimensional (1D) force- or displacement-based beam–column elements and various translational and rotational springs are computationally appealing and more commonly used. Although modeling simplifications might compromise the accuracy of nonlinear analyses used to predict SCBFs seismic performance when compared to detailed 3D FEM, well-calibrated and informed FEMs that utilizes only 1D elements can still be very beneficial, providing insight for use in PBSB [Salawdeh and Goggins 2013]. For instance, such models use fundamental concepts of engineering mechanics to estimate the input parameters of its key components, which are then fine-tuned or calibrated using experimentally available research data to reasonably verify the overall geometric and component modeling assumptions. This design strategy will be used herein.

The effect of earthquake duration on system response is not fully understood, even as long-duration ground motions have occurred and been recorded recently, including: Iquique, Chile (Mw 8.2, 2014), Tohoku, Japan (Mw 9.0, 2011) and Maule, Chile (Mw 8.8, 2010), etc.. Current seismic design codes do not consider duration effects and rely mainly on spectral accelerations. The influence of earthquake duration on structural performance does not only depend on the duration definition, but it is also highly dependent on the structural model and the engineering demand parameter (EDP) or damage metric used in judging the performance.

In one of the earliest studies to tackle duration effects, Marsh and Gianotti [1995] used artificial acceleration records representing the Cascadia subduction zone earthquakes as an input for inelastic response history analyses of single-degree-of-freedom (SDOF) systems. They found that structures subjected to long-duration motions accumulate damage as a result of repeated cycles. Bommer and Martinez-Pereira [2000] reported more than 30 definitions of strong ground-motion duration in the literature. The most common duration definitions are the bracketed duration and the significant duration. The bracketed duration is defined as the measure of the time interval between the first and last exceedance of an absolute acceleration threshold, for example, 0.05g or 0.1g. The significant duration is defined as the interval over which a specific amount of Arias Intensity (AI) is achieved; this amount is usually taken as 5–95% or 5–75% of AI. The significant duration for the different ground motions is the definition adopted in this study. Recently, records of long-duration ground motions became available after events such as the Tohoku earthquake and encouraged research into the effect of earthquake duration on structural performance, which will be discussed next.

Only a few studies have considered the problem of buckling and low-cycle fatigue in SCBFs in response to long-duration earthquakes. Foschaar et al. [2012] investigated the effect of ground-motion duration on the collapse capacity of a three-story steel-braced frame. They used two record sets, one with long-duration records and the other with spectrally equivalent short-duration records. This approach isolated the effect of ground-motion duration from other ground-motion characteristics. They found that duration affects significantly the collapse capacity. The seismic response of SCBFs is dictated by brace buckling and fatigue-induced failure, which, in turn, is expected to relate to duration effects and damage accumulation from longer earthquakes.

While many studies did not necessarily look at the direct effects of short- versus longer-duration earthquakes on SCBFs, the literature contains significant research on the fatigue life of braces among other steel components. For example, Kanvinde and Deierlein [2004] reported that the ultra-low-cycle fatigue, or sometimes referred to as extremely-low-cycle fatigue, caused failure in very few cycles (of the order of ten) and is strongly influenced by microstructure. Wen and Mahmoud [2015] developed a new fracture model for ductile fracture of metal alloys that is dependent on both stress tri-axiality and the Lode parameter. The model covered both monotonic and reverse loading. Pereira et al. [2014] reported fatigue behavior of piping-grade steel under monotonic, low-cycle, and ultra-low-cycle fatigue. They reported that ultra-low cycle fatigue is characterized by high-amplitude and short-duration motion where the number of cycles is less than 100. Therefore, understanding how the seismic performance of SCBFs is dependent on the fatigue life of braces in relation to duration of an earthquake is an important research problem, which is addressed in this study.

1.2 RESEARCH PROBLEM

This study investigated the effect of earthquake duration on seismic performance of steel SCBFs with special focus on low-cycle fatigue modeling effects. The ultimate seismic behavior of SCBFs is dominated by the low-cycle fatigue-induced braces collapse. At the onset of the braces failure, most of the lateral capacity is lost, causing noticeable drift ratios, and, depending on what drift ratios correspond to the failure versus what is intended from the design, a premature failure might take place. One of the questions this study addressed was whether a longer duration ground motion would lead to a complete failure or collapse at force or displacement values lower than design values because of damage accumulation or low-cycle fatigue effects. Obviously, damage accumulation increases with the increase of the ground-motion duration, or more precisely its “significant duration,” as discussed throughout this study. The next question was whether the existing computational models (e.g., steel constitutive models or low-cycle fatigue models) accurately capture the correlation between earthquake duration and damage accumulation. Force-based and displacement-based design philosophies incorporated in current design codes and standards depend mainly on the design response spectrum corresponding to a specific location, and do not account for ground-motion duration or the accumulation of damage cycles. Thus, the third question addressed in this study was whether the current code-compliant SCBFs designs sensitive to longer duration earthquakes or are valid for such scenarios and meet life-safety code requirements. To address these outstanding issues, a comprehensive experimental and analytical study was undertaken.

1.3 METHODOLOGY

This study used an analytical and experimental framework to investigate the seismic behavior of SCBFs under long-duration earthquakes. The analytical part of the study was composed of a preliminary modeling and sensitivity analysis and post-test analysis, The experimental part included shake table tests. The first phase of the analysis focused on a preliminary investigation of duration effects on SCBFs using a detailed sensitivity analysis to understand the influence of modeling parameters. The sensitivity analysis was also used to determine whether or not current analytical methods and models capture accurately to duration effects and whether dedicated testing was needed for further validation. Preliminary analysis was used to finalize the experimental program in terms of selecting the shake table input ground motions, designing the test setup, instrumentation plan, etc. Following the sensitivity and pre-test analysis, a self-contained experimental program was conducted, i.e., the effects of short- and long-duration earthquakes were compared. Three identical one-half-scale frames were tested under different ground motions scenarios to show the effect of the duration on the overall global behavior of one-story one-bay SCBFs with chevron brace configuration and not only individual components such as the braces.

The subsequent post-test analysis used numerical models of the tested specimen and full-system analysis on selected archetype SCBFs. The experimental results were used to calibrate and validate a reliable OpenSees model that captured the behavior of the tested steel frames under both short- and long-duration ground motions. The calibrated model for the test specimens was used to assess and evaluate the current different fatigue modeling parameters available in the literature based on the tested three specimens. In order to generalize the results of the tests beyond only three tests, the calibrated model was used to conduct additional analyses under 88 ground motions with different durations. Forty-four pairs of spectrally-matched short- and long-duration records were used to conduct incremental dynamic analysis (IDA) and develop fragility curves to better quantify the duration effect on the structural safety and collapse capacity of the tested specimens.

The last part of the analysis considered full-scale SCBFs systems adopted from archetype buildings and compared these results with the results obtained from the analysis and testing of the one-half-scale single-bay single-story frames. In order to address the duration effect on realistic structures, three- and nine-story archetype buildings were selected as representative SCBFs to conduct extensive nonlinear time history analysis using the two different suites of 44 ground motions as before to represent short-crustal and long-subduction earthquake events. Only deterministic analysis was conducted in this case. The 44 pairs of ground motions were scaled to two hazard levels that corresponded to 10% and 2% exceedance in 50 years. The behavior of the full SCBFs was assessed with respect to various EDPs at the two specific hazard levels to further study the effect of earthquake duration.

1.4 RESEARCH OBJECTIVES

The overall objective of the study was to study the seismic response of SCBFs under long duration earthquakes as it relates to low-cycle fatigue. More specifically, the objectives of the analytical and experimental tasks mentioned above were as follows:

- Investigate and rank the effect of structural and low-cycle fatigue modeling parameters on the seismic response of SCBFs through detailed sensitivity analysis;
- Conduct three large-scale SCBF shake table tests under different crustal and subduction ground motions;
- Use the test data to verify and calibrate computational models for low-cycle fatigue and the tested specimens in OpenSees, and utilize the calibrated model to assess validity of existing low-cycle fatigue input parameters;
- Use the calibrated OpenSees model for the test specimens to conduct IDA and develop fragility curves under short- and long-duration suites of ground motions;
- Develop detailed numerical models for representative SCBFs from archetype buildings to use for nonlinear time history analysis under a large number of short- and long-duration ground motions; and
- Assess the seismic response of code-compliant SCBFs under short- and long-duration earthquakes to provide insight for future design guidelines development to improve seismic design and performance-based assessment of SCBFs.

1.5 REPORT OUTLINE

This report is comprised of seven chapters and four appendices. Chapter 1 introduces the research problem and the study's objectives. Chapter 2 provides a brief literature review. Chapter 3 presents the development of finite-element models for SCBFs and calibrates the model using previous relevant experimental data in addition to the details and results of the conducted sensitivity analysis. Chapter 4 describes the design and development of the experimental program, including the following: specimens design, test setup, test program, instrumentation plan, and ground motions selection for the shake table tests. The tests results and discussion of global and local behavior of the tested frames are presented in Chapter 5. Next, Chapter 6 compares the results obtain from the numerical model with the experimental test results to determine if such models are appropriate for conducting IDA and assessing existing low-cycle fatigue modeling parameters. The last part of the study is presented in Chapter 7, which extends the analysis to archetype buildings to better study the ground-motion duration effects. Overall summary and main findings and conclusions from the full study are presented in Chapter 8. The report also includes four appendices that provide detailed drawings and photographs of the specimens' fabrication and testing along with the details of the ground motions used in this study.

2 Background and Literature Review

This section presents a brief background and literature review summary focused on previous research on SCBFs and long-duration effects on structural performance.

2.1 PREVIOUS RESEARCH OF SCBFS

For life safety and collapse prevention, SCBFs are designed to develop brace buckling during large, infrequent earthquakes. After brace buckling, SCBFs exhibit highly nonlinear and inelastic behavior. Nonlinear behavior of bracing members mainly governs the system performance in SCBFs. During the 1970s and 1980s, experimental investigations were performed to better understand and improve the nonlinear behavior of SCBFs. The focus of those experimental investigations can be categorized into three groups: tests of brace components, gusset-plate connections, and full-scale braced-frame systems. Researchers who studied the post-buckling and tensile yield behavior of the brace include: Workman [1969], Wakabayashi et al. [1973], Popov et al. [1976], Kahn and Hanson [1976], Black et al. [1980], Astaneh-Asl [1983], Foutch et al. [1987], Lee and Goel [1987], and Aslani and Goel [1989].

Gusset connections were also investigated by applying tensile loads to the connections (e.g., Whitmore [1952] and Hardash and Bjorhovde [1985]). Those studies verified that the Whitmore method estimated with a sufficient degree of accuracy the maximum tensile stress in the gusset plates, and the block shear model was proposed to estimate the tensile fracture capacity. Thornton [1984] investigated the compressive capacity of the gusset plates and proposed a method to estimate the buckling strength based on the Whitmore width and the effective length of the gusset. Using the Thornton and Whitmore procedure, many experimental studies were been conducted to improve the performance of the gusset-plate connections using monotonic (e.g., Hu and Cheng [1987], Gross and Cheok [1988], Brown [1989], Cheng et al. [1994], and Sheng et al. [2002]) and cyclic loading (e.g., Rabinovitch and Cheng [1993], Walbridge et al. [1998], and Grondin et al. [2000]). The previous studies led to several key results that were comprehensively summarized and reported by Hsiao [2012].

More recent research tested full-scale SCBF systems consisting of bracing members with gusset-plate connections at the ends of the brace, which represented the interaction of the bracing member and gusset connections (e.g., Astaneh-Asl [1983], Goel and El-Tayem [1986], Aslani and Goel [1989], and Xu and Goel [1990]). These investigations mainly studied systems with single, double-angle, and double-channel bracing members. Past studies verified yield mechanisms and failure modes, e.g., brace yielding and buckling, gusset-plate yielding, brace

fracture, and gusset-plate weld tearing. Although these results improved the understanding of behavior of braces and gusset plates, this work failed to validate the performance of the full-scale concentric braced frames (CBF) systems, including bracing members, gusset connections, and framing systems, and the interaction between these individual elements. A more recent experimental study by Uriz and Mahin [2004] tested a full-scale two-story braced frame with hollow structural sections (HSS) braces and tapered gusset plates. They found that the brace placed large demands on the gusset plate connections, and, in turn, the framing members.

With the goal of improving the overall performance of SCBFs systems, a comprehensive research program was begun in 2005 at the University of Washington (UW). The research program included both experimental and analytical modeling investigations. The experiments included several configurations and systems. Thirty-two single-story single-bay CBFs were first tested at UW, which has been reported in four dissertations: Johnson [2005], Herman [2006], Kotulka [2007], and Powell [2009]. The experimental program involved also six multistory frames—three two-story and three three-story frames—but were tested at the National Center for Research Engineering (NCREE) in Taipei, Taiwan (Clark [2009] and Lumpkin [2009]). All of the specimens tested were full-scale and complete systems. Figure 2.1 shows the tested specimen geometry and test setup per Hsiao [2012].

The UW test program provided important insight into the seismic behavior of SCBFs. The seismic performance of SCBFs is strongly dependent upon the gusset-plate connection and the brace cross section. Instead of the $2t_p$ linear clearance that often leads to larger, thicker gusset plates, they proposed a model with $8t_p$ elliptical clearance, which permits smaller, more compact gusset plates. For mid-span connections, a $6t_p$ horizontal clearance zone is preferred. The tapered gusset plates behave differently compared to rectangular gussets as they may provide good end rotational capacity for the brace; the drawback is that they result in thicker gusset plates. Clearly, all components and their interaction influence the inelastic response of the SCBF system. Research at UW to improve the seismic performance of CBFs and SCBFs continues. The most recent comprehensive work on SCBFs has been performed by Hsiao [2012], which provided the basis for many aspects considered in this report, especially in the modeling of SCBFs.

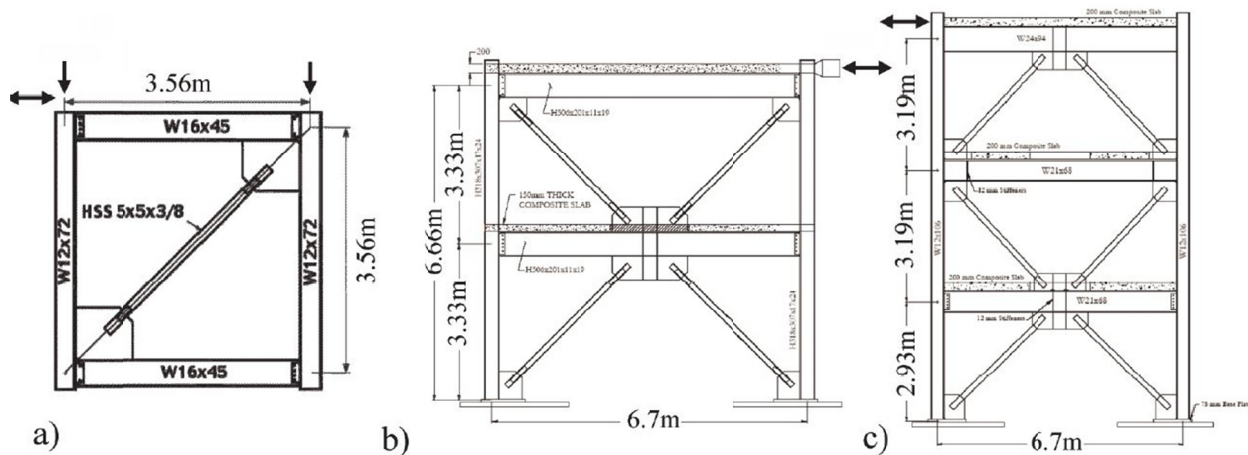


Figure 2.1 Typical test specimens and loading setups for UW research program on concentric braced frames (after Hsiao [2012]).

2.1.1 Previous Research Studying Long-Duration Effects

The duration of an earthquake is expected to affect structural response; however, current seismic design specifications commonly use response spectra to identify the hazard and do not consider duration effects. Partly this is because, historically, ground-motion records of earthquakes with long duration are less common, and most ground-motion databases include mainly short-duration records. Recently, more seismic events, longer in duration, have occurred and recorded, e.g., the 2011 Tohoku earthquake. Older studies considered synthetic ground motions and other methods to study earthquake duration effects because of the paucity of appropriate records.

This section presents a number of previous studies that considered ground-motion durations that focused on duration effects on structural response. Note: most of the research in this area was analytical or numerical, with most of the applications focused on concrete structures. The review provided next includes research results on concrete buildings or bridge columns, and some recent studies on the duration effect on steel structures, including CBFs (or SCBFs), and moment resistant frames (MRFs).

Kunnath et al. [1997] tested twelve identical reinforced concrete bridge columns. Some specimens were tested using standard cyclic loads, while others were tested using numerically predicted displacement values that represent the column's response to different ground motions. They determined that the damage sustained was due to low-cycle fatigue of the longitudinal reinforcing bars and rupture of the spirals. Other studies addressed the effect of poor confinement of reinforced-concrete bridge columns under long-duration ground motions, either experimentally [Stapleton 2004; Ranf et al. 2006] or numerically [Thompson 2004]. These studies showed that poorly confined columns will experience minor damage when subjected to a large subduction zone earthquake, and that neither the short- nor the long-duration motions caused damage to bridge columns.

Ou et al. [2014] performed both experimental and analytical studies of the seismic behavior of reinforced-concrete bridge columns under long-duration ground motions. They quantified the duration by the number of times the 5% PGA was crossed based on the acceleration history. An approximate threshold of 600 crossings was chosen to differentiate between the short- and long-duration motions. More recently, Mohammed et al. [2016] performed both experimental and numerical investigations on the effect of earthquake duration on the collapse capacity of reinforced-concrete bridge columns. They performed shake table tests on five identical large-scale columns subjected to ground motions from the 2011 Tohoku (long duration), 1989 Loma Prieta (short duration), and 2010 Maule (long duration) earthquakes. Mohammed [2016] used the results from these tests results to calibrate and validate an OpenSees model for testing bridge columns. Incremental dynamic analysis was employed, using different sets of spectrally equivalent long- and short-duration motions. Three ground-motion sets were used, one long duration and two short-duration sets. Each set consisted of 112 ground-motion records. Mohammed [2016] determined that ground-motion duration has a significant effect on displacement collapse capacity of reinforced-concrete bridge columns. Columns subjected to long-duration motions showed 25% lower displacement capacities compared to columns subjected to short-duration motions.

Other researchers have focused on the structural safety and collapse capacity of concrete structures as related to ground-motion duration. Hancock and Bommer [2007] analyzed an eight-

story reinforced concrete wall-frame building using 30 ground-motion records. The main objective was to study the correlation between ground-motion duration and different damage measures. They concluded that there was a correlation between the duration of the motion and cumulative damage measures, such as absorbed hysteretic energy and fatigue damage. Raghunandan and Leil [2013] investigated the influence of ground-motion duration on the collapse capacity of 17 reinforced-concrete building models using IDA subjected to a set of 76 ground-motion records. The study concluded that the long-duration records significantly affect the collapse capacity of a structure as it imposes higher energy demands compared to short-duration motions. Finally, Raghunandan et al. [2015] carried out nonlinear dynamic analyses on 24 buildings designed according to outdated and modern building codes for the cities of Seattle, Washington, and Portland, Oregon. They found that the median collapse capacity of the ductile (post-1970) buildings is approximately 40% less when subjected to ground motions from subduction-zone earthquakes compared to crustal earthquakes.

Unfortunately, there are only a few studies that have analyzed duration effects on steel structures. Lignos et al. [2011] studied the seismic capacity of high-rise steel buildings subjected to long-period long-duration ground motions. It was shown that connection fractures due to cumulative damage amplify maximum story-drift ratios at lower stories of high-rise buildings. Other researchers have studied steel moment-resisting frames behavior under long duration records. Li et al. [2014] investigated the collapse probability of mainshock-damaged steel buildings under aftershocks. Analytical studies were conducted utilizing structural degradation models derived from existing publicly-available NEEShub data. Although aftershocks are normally somewhat smaller in magnitude, their ground-motion intensity is not always smaller. Moreover, aftershocks may have a higher PGA compared to the mainshock, even longer in duration, and significantly different energy content as a result of the change in their location relative to the site. Li et al. [2014] found that collapse capacity of a structure may be compromised significantly when the building is subjected to a high-intensity mainshock and may collapse in response to a small aftershock following the mainshock.

Chandramohan et al. [2016] investigated the effect of ground-motion duration on the collapse capacity of different structures. Two sets of long- and short-duration ground motions were used to conduct IDA to study the effect of the ground-motion duration on a five-story steel moment frame and a reinforced-concrete bridge. The duration of the ground motion was found to have a significant influence on structural collapse capacity. The median collapse capacity estimated by the long-duration set was less by 29% and 17% than that estimated by the short-duration set for the steel frame and the bridge column, respectively. A comparison between different duration metrics was performed, and the significant duration was chosen as the preferred duration metric. Another recent study Barbosa et al. [2016] investigated the performance of steel moment-resisting frames under sets of 22 short-duration and 22 long-duration motions compared in terms of the expected level of damage caused by the earthquakes and spectral acceleration. The obtained results indicated that for large spectral accelerations, longer duration motions tend to induce larger peak interstory drifts and damage indices. In addition, the relationship between the peak interstory drift ratio and damage indices was found to be nonlinear; this level of nonlinearity increases with ground-motion duration.

Most recently, Marafi et al. [2019] simulated ground motions for a magnitude 9 Cascadia subduction zone earthquake that will affect the Puget Lowland region, including cities underlain

by the Seattle, Everett, and Tacoma sedimentary basins. This study is among several recent studies conducted at UW as part of a large research initiative named the M9 project.

Marafi et al. [2019] reported that the current national seismic maps do not account for the effects of these basins on the risk-targeted maximum considered earthquake (MCER). The simulated motions for Seattle had large spectral accelerations (at a period of 2 sec, 43% of simulated M9 motions exceeded the MCER), damaging spectral shapes (particularly at periods near 1 sec), and long durations (5–95% significant durations near 110 sec). For periods of 1 sec or larger, the resulting deformation demands and collapse likelihood for four sets of single-degree-of-freedom systems exceeded the corresponding values for motions consistent with the conditional mean spectra (CMS) at the MCER intensity. The regional variation of damage was estimated by combining probabilistic characterizations of the seismic resistance of structures and the effective spectral acceleration, $S_{a,eff}$, which accounts for the effects of spectral acceleration, spectral shape, and ground-motion duration. For high-strength, low-ductility systems located above deep basins ($Z_{2.5} > 6$ km), the likelihood of collapse during an M9 earthquake averaged 13% and 18% at 1.0 sec and 2.0 sec periods, respectively. For low-strength, high-ductility systems, the corresponding likelihoods of collapse averaged 18% and 7%.

Studies that specifically consider earthquake duration and steel CBFs or SCBFs (core of this report) are limited. Foschaar et al. [2012] investigated the effect of ground-motion duration on the collapse capacity of a three-story steel braced frame. They used two record sets, one with long-duration records and the other with spectrally equivalent short-duration records. This approach isolated the effect of the ground-motion duration from other ground-motion characteristics. They found that the duration affected the collapse capacity significantly. Using OpenSees, Tirca et al. [2015] studied the effect of mega-thrust subduction records versus crustal records by analyzing the nonlinear response of four-story, eight-story and 12-story moderately ductile (MD)-CBF office buildings located in Canada. They found that in the case of the eight-story and 12-story MD-CBF buildings, the largest demand under both crustal and subduction record sets occurred on the bottom two floors. In the case of the four-story MD-CBF building, the largest demand occurred at the top floor under the subduction-record set and at the bottom two floors under the crustal-record set. They concluded that subduction records, characterized by a longer Trifunac duration, did not affect the peak interstory drift or the peak residual interstory drift; damage was concentrated at floors characterized by lower brace over strength. To avoid the occurrence of brace fracture when subjected to ground motions scaled to match the design spectrum, it is recommended to provide a sufficient safety margin when selecting the size of bottom floor braces.

Recent M9 project work touched on SCBFs under potential subduction scenarios. Li et al. [2019] studied the effect of deep sedimentary basins and how they might increase the intensity of ground motions and their effect on SCBFs; such effects are not considered in U.S. building codes. Numerically, three-, nine-, and 20-story SCBF archetypes were subjected to large-magnitude interface earthquakes recorded in basins in Japan with similar depths as the Seattle basin. The results demonstrate that deep basins in combination with the long ground-motion duration resulted in brace fracture at lower spectral accelerations. The results suggested that the strength of the archetypes inside deep basins and subjected to interface earthquakes would need to be increased by a factor of over 2.0 to ensure similar collapse probabilities as those located outside basins and/or subjected to crustal earthquake hazards.

In summary, most of the previous studies have concluded that longer duration earthquakes can have significant effects on structural performance and there is an urgent need for long-duration effects to be considered in the seismic design of structures. Given the potential seismic hazard in the Pacific Northwest, studies on the effect of long-duration earthquakes on SCBFs is long overdue. Testing is necessary to verify that current modeling techniques, especially those models that consider low-cycle fatigue, capture duration effects. This study focused on the results of shake table test and numerical methods as the first major step in determining the effect of long-duration ground motion on the structural performance of SCBFs, with an emphasis on brace rupture and low-cycle fatigue damage associated with longer duration earthquakes.

3 Modeling and Sensitivity Analysis

The objective of this chapter is to investigate the influence of modeling parameters on the seismic response of SCBFs as it relates to ground-motion duration. This analysis was also considered as a part of the pre-test analysis used to develop the experimental part of this study and assist in the selection of potential ground-motion records.

3.1 LOW-CYCLE FATIGUE MODELING

Low-cycle fatigue modeling is a critical feature in any analysis of the response of SCBFs to seismic excitation. The *Fatigue* material parameter implemented in OpenSees is wrapped around the parent *Steel02* parameter assigned to braces that tracks the accumulated damage. One of the earliest brace-fracture models implemented in OpenSees was developed by Uriz [2005] and is based on low-cycle fatigue of constant plastic strain amplitude that predicts cumulative damage according to Miner's rule. Note: under seismic loading, the strain may not have constant amplitude [Uriz and Mahin 2008].

Based on independent research by Coffin [1953] and Manson [1965], the relationship between the plastic strain amplitude, ε_i , experienced by each cycle i , and the number of cycles to failure, N_f , is linear in the log–log domain; the slope is equal to m [Equation (3.1)], and ε_0 is the strain for a single reversal. The m and ε_0 parameters are also known as the fatigue ductility exponent and fatigue ductility coefficient, respectively. The *Fatigue* wrapper counts cycles through a modified rainflow counting scheme, which uses only recent strain history and tracks the cumulated damage, D , at each fiber. Several studies suggest using different values for m and ε_0 based on regression analysis of results from experimental data in the literature.

Table 3.1 shows a summary of the different studies and recommended models or values for estimating the m and ε_0 , and are mainly valid for structural steel braces. Note that two of the listed studies in Table 3.1 provide equations [Equations (3.2) and (3.3)] for estimating ε_0 rather than the specific values as shown here. Equation (3.2) has been proposed by Lignos and Karamanci [2013] for predicting the value of ε_0 for slenderness ratio of up to 85, which was slightly modified by Tirca and Chen [2014]—as shown in Equation (3.3)—to account for HSS braces with slenderness ratio (kL/r) between 50 and 150 using data from fourteen experimental tests.

$$\varepsilon_i = \varepsilon_0 \cdot (Nf)^m \quad (3.1)$$

$$\varepsilon_0 = 0.291 \left(\frac{kL}{r} \right) - 0.484 \left(\frac{w}{t} \right) - 0.613 \left(\frac{E}{F_y} \right) 0.3 \quad (3.2)$$

$$\varepsilon_{0\text{pred}} = 0.006 \left(\frac{kL}{r} \right) \cdot 0.859 \left(\frac{b_0}{t} \right) - 0.6 \left(\frac{E}{F_y} \right) 0.1 \quad (3.3)$$

The Giuffre–Menegotto–Pinto model [Menegotto and Pinto 1973] designated as *Steel02* material was the nonlinear constitutive law used for all members modeled in this study. The hysteresis loop simulated by the Giuffre–Menegotto–Pinto model follows the previous loading path for a new reloading curve, while deformations are accumulated. Karamanci and Lignos [2014] proposed some parameters for *Steel02*; see Table 3.2. Other researchers have used different modeling parameters to determine response, e.g., Chen and Tirca [2013] used a different set of input parameters for *Steel02* simulation in OpenSees. Aguero et al. [2006] used different set of parameters to define the transition from the elastic to plastic response and considered isotropic hardening. The *Steel02* input parameters or arguments, i.e., the OpenSees TCL command line, is illustrated in Equation [2.4] below for reader’s convenience.

$$\text{uniaxialMaterial Steel02 } \$matTag \$Fy \$E \$b \$R0 \$cR1 \$cR2 <\$a1 \$a2 \$a3 \$a4 \$sigInit> \quad (2.4)$$

A sample set of *Steel02* input [Aguero et al. 2006] uses the following values: $R_0 = 25$; $cR_1 = 0.925$; $cR_2 = 0.15$; $a_1 = a_3 = 0.00001$; $a_2 = a_4 = 0.00002$; the kinematic hardening parameter, b , set to 0.01. Note how these parameters vary from what is shown in Table 3.2 per Karamanci and Lignos [2014]. Accordingly, different sets of input parameters for *Steel02* are used in this sensitivity analysis as will be explained later.

Table 3.1 Different recommended values for OpenSees fatigue modeling (m and ε_0).

Study	m	ε_0
Lignos and Karamanci [2013]	-0.30	Equation (2.2)
Uriz and Mahin [2004]	-0.50	0.095
Tirca and Chen [2014]	-0.50	Equation (2.3)
Chen and Mahin [2012]	-0.60	0.090
Santagati et. al [2012]	-0.46	0.070
Salawdeh and Goggins [2013]	-0.50	0.190
Lai and Mahin [2012]	-0.46	0.099

Table 3.2 Recommended *Steel02* parameters based on Karamanci and Lignos [2014].

Section	b	R_0	cR_1	cR_2	a_1	a_2	a_3	a_4
HSS (rectangular)	0.001	22.	0.925	0.25	0.03	1.0	0.02	1.0
HSS (round)	0.005	24.	0.925	0.25	0.02	1.0	0.02	1.0
Wide Flange	0.001	20.	0.925	0.25	0.01	1.0	0.02	1.0

3.2 ANALYTICAL MODEL

3.2.1 Model Description

Two selected braced frames (Figure 3.1) from previous experimental studies at the UW were used in this study to verify and calibrate the analytical developed herein. The two specimens, designated as HSS1 [Johnson 2005] and HSS31 [Palmer et al. 2012], used single diagonal and X-bracing, respectively. More details for the two frames are described in Table 3.3.

Many modeling aspects used in this study followed Hsiao et al.'s [2012] methodology. Force-based nonlinear beam-column elements with five integration points were used to model the braces, beams, and columns. Fiber cross sections were employed to simulate various steel cross sections, assuming plane-strain compatibility. Concentrated spring elements were used to model the connections. The Giuffre–Menegotto–Pinto model, designated as *Steel02* material, was the nonlinear constitutive law used for all members. The OpenSees model also was used to evaluate nonlinear models with pinned or rigid joints at the brace-beam-column connections.

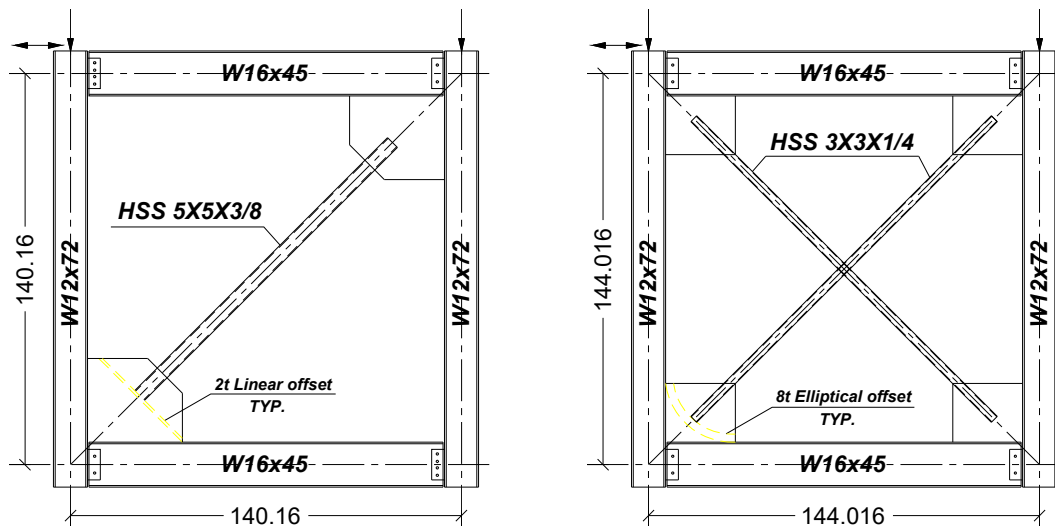


Figure 3.1 Typical test specimen for single-story single-bay SCBF: diagonal-braced HSS1 (left) and X-braced HSS31 (right).

Table 3.3 Dimensions and material properties for selected UW test specimens.

Specimen	Beam W16*45	Column W12*72	Brace HSS		Gusset plate				Clearance	
	F_y (ksi)	F_y (ksi)	Size	F_y (ksi)	a (in.)	b (in.)	t_p (in.)	F_y (ksi)	Type	$N(t)$
HSS1	59.0	59.5	5×5×3/8	69.5	34.0	30.0	0.5	118.0	Linear	2
HSS31	50.0	50.0	3×3×1/4	46.0	11.7	9.25	0.25	87.0	Elliptical	8

The accurate modeling of a SCBF must include the full cyclic inelastic behavior of the brace, including buckling in compression, yielding in tension, and post-buckling behavior. Gunnarsson [2004] demonstrated that accurate simulation of brace buckling behavior is achieved with ten or more nonlinear beam–column elements along the length of the brace. Accurate predictions of the buckling curves [AISC 2005a] were achieved using an initial displaced shape using a sine function with the apex equal 1/500 of the length of the brace. Measured material properties are provided in Table 3.3. For the constitutive model, the strain-hardening ratio of 0.01 was used. The brace was stiffer and stronger at the ends as result of the block shear length of the gusset and net section reinforcement. This increased local strength and stiffness was modeled, which reduced deformation and little local yielding occurred in this portion of the brace. To represent the complex cross section at these locations, an increased strength element was used at each end of the brace.

The models captured tensile yielding, buckling, and post-buckling behavior of the brace, which are highly nonlinear behaviors and key elements in the seismic response of the SCBF system. Significant deformation and yielding of the gusset-plate connections were also considered along with local yielding of the beams and columns adjacent to the gusset plate. The OpenSees model used mainly simplified discrete component models including beam–column elements and concentrated springs. The modeling technique is similar to models used by Hsiao et al. [2012]. Force-based nonlinear beam–column elements with five integration points were used to model the braces, beams, and columns. Fiber cross sections were employed to simulate various steel cross sections, assuming plane-strain compatibility. Concentrated spring elements were used to model the connections. The following subsections provide additional detail of the modeling approaches and quantification of the important variables used for each component of the SCBFs.

3.2.1.1 Gusset-Plate Connection

Gusset-plate connections in actual structures are neither pinned nor fixed joints, and these connections have a significant effect on the stiffness, resistance, and inelastic deformation capacity of the SCBF system. Hence, accurate simulation of these connections is required. To simulate the nonlinear out-of-plane rotational behavior of the gusset-plate connections, single and multiple springs along the brace axial direction at and beyond the end of the brace were considered and investigated. Based on research of Hsiao et al. [2012], the correct estimate of the gusset-plate stiffness is required to accurately predict the buckling capacity of the brace. The

initial stiffness of this rotational spring was based on the geometry and properties of the gusset plate. A rational estimate of gusset stiffness is provided based on Equation (3.5).

$$K^{\text{rot.cal}} = \frac{E}{L_{\text{ave}}} + \left(\frac{W_w t^3}{12} \right) \quad (3.5)$$

In design, the maximum stress in the gusset plates is approximated using the Whitmore model [1952] with a 45° projection angle; see Figure 3.2. Here, the Whitmore width is used to approximate a geometry that provides an equivalent uniform stress distribution, and represents the portion of the gusset that is most effective in resisting the loads and deformations of the brace. This width and the gusset-plate thickness are used to compute the rotational stiffness in Equation (3.5), i.e., EI/L . The flexural strength of the nonlinear rotational spring mode is also based on the Whitmore width, which is effective in computing the capacity of Whitmore cross section of the gusset plates, $W_w t_p^2/6$. The post-yield stiffness is 1% of the initial rotational stiffness. Because the gusset plate sustains minimal in-plane deformation relative to other deformations modes of the frame, it is modeled using rigid links.

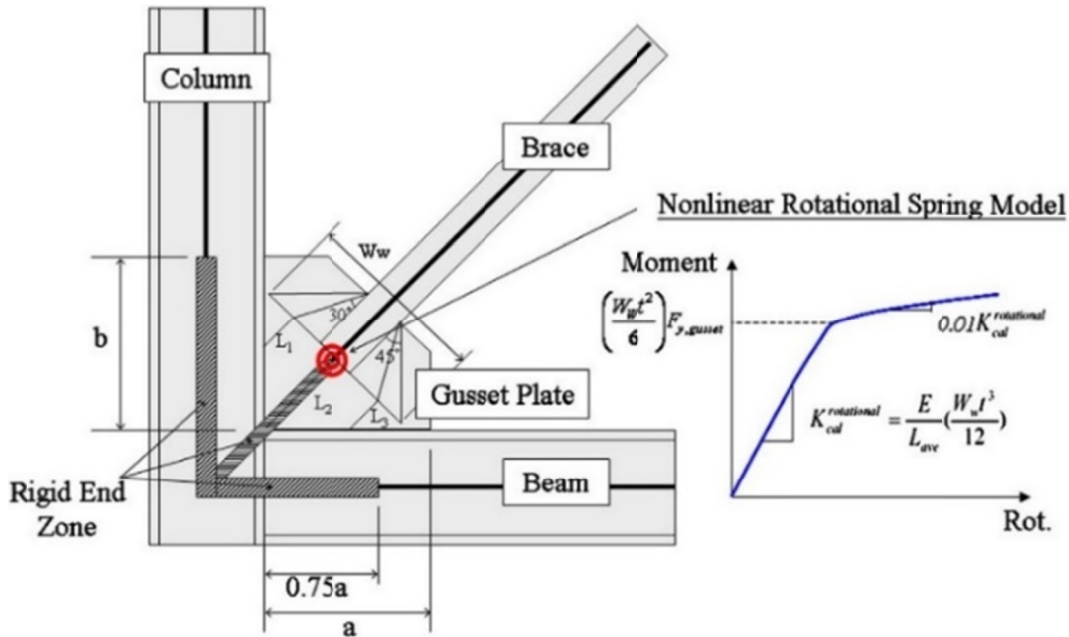


Figure 3.2 Illustration of the proposed connection model [Hsiao et al. 2012].

3.2.1.2 Beam–Column Connections

The beam-to-column connections at locations without a gusset plate were shear-plate (or shear-tab) connections. Beam–column connections at beam–column-brace connections were welded flange welded-web connections. As a result, they were treated as fully restrained connections with the simplified pinned or fixed connection models. The connections were simulated as illustrated in Figure 3.3(a). The model is a combination of the *zero-length nonlinear spring* element and the *Pinching4 material model* (both available in OpenSees), which allows to simulate degradation of strength and stiffness as shown in Figure 3.3(b). The moment-rotation model developed by Liu and Astaneh-Asl [2004] was used to estimate the initial rotational

stiffness and the maximum positive and negative moment capacities for the shear tab connections with and without slabs. The composite shear-tab connection model includes composite action for shear tabs with composite slabs bearing against the face of the column. All of the parameters of the bending moment and rotation capacity in the figures were based on Liu and Astaneh-Asl's study.

Force beam elements were used for columns, beams, and braces. Twelve force beam-column elements were used for the braces with five integration points. Co-rotational geometric transformation was used for the braces as large out-of-plane displacements were expected. All model details are illustrated in Figure 3.4.

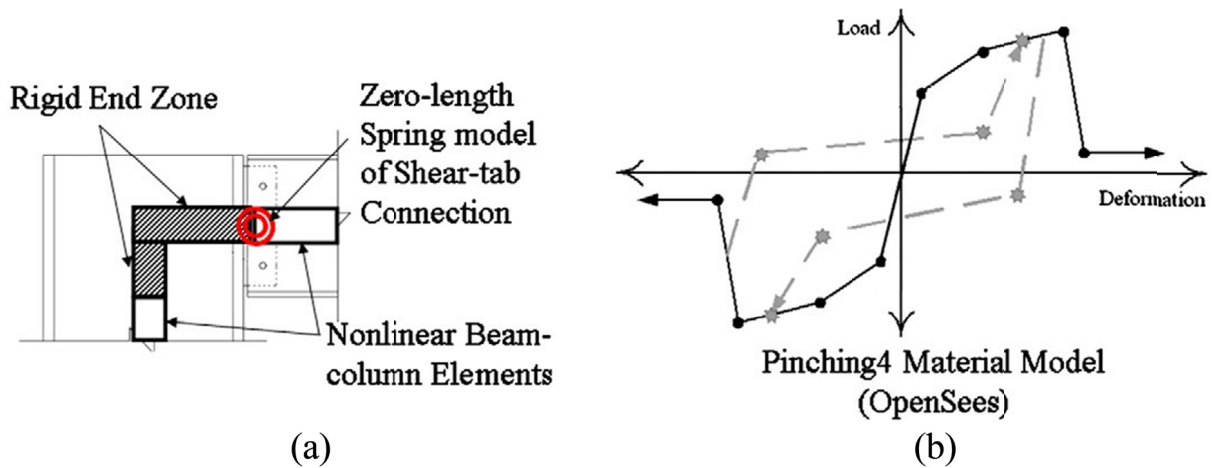


Figure 3.3 Illustration of (a) the shear-tab connection and (b) the *Pinching4* material model in OpenSees (adopted from Hsiao et al. [2012]).

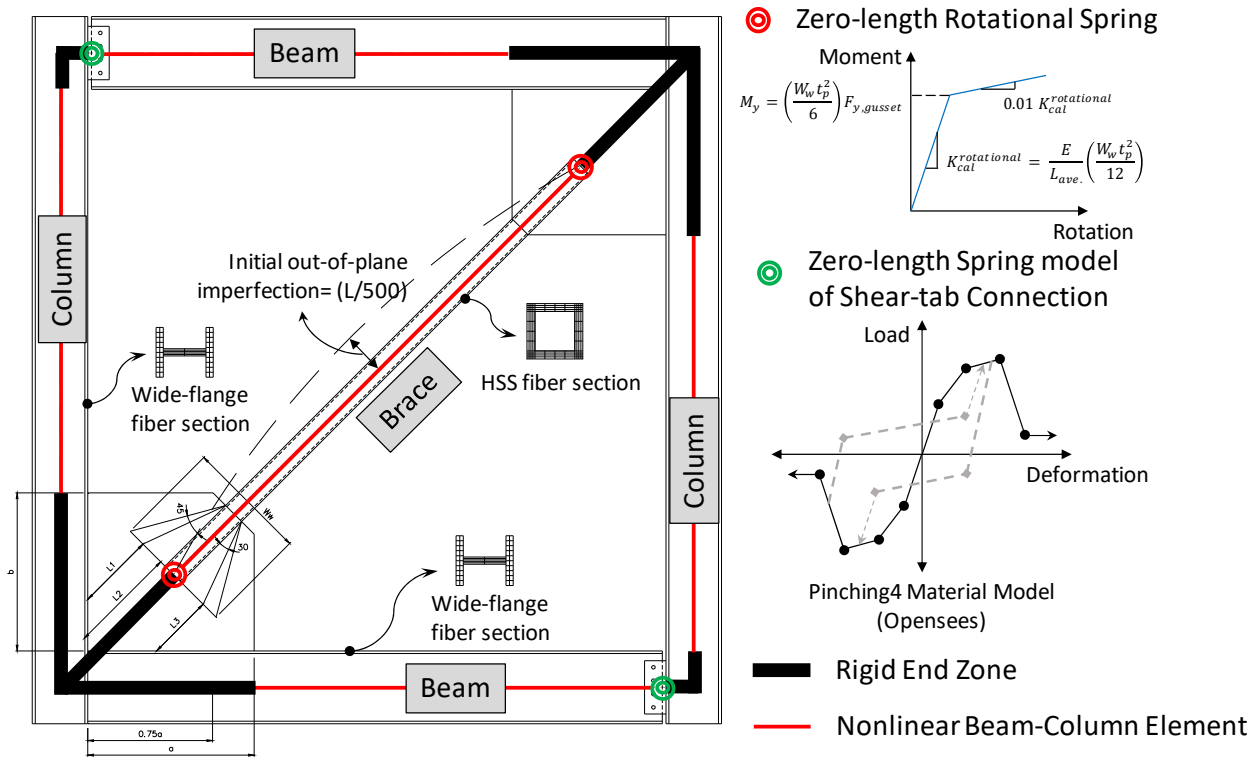


Figure 3.4 Illustration of the numerical model details used for the sensitivity analysis.

3.2.2 Calibrated Model Results

To verify and calibrate the numerical models, several iterations for calibrating the full model against experimental results were conducted for the HSS1 and HSS31 frames described above. Two criteria had to be met: (1) gain confidence in the overall modeling features and techniques, such as simulating gusset plate or welded connection behavior; and (2) provide a baseline set of input parameters that technically capture experimental response under cyclic load and relate it to both modeling sensitivity analysis and ground-motion duration effects. Many of the iterations were concerned with the m and ε_0 values as these parameters can capture the onset of failure. Other iterations focused on the material model input parameters for *Steel02*.

The developed OpenSees models for diagonal-brace (HSS1) and X-brace (HSS31) frames were analyzed under same cyclic loading history as the experimental portion of the study. The analysis and tests results were compared to validate the accuracy of the OpenSees models and finalize model calibration. Comparable nonlinear displacements and drifts histories were obtained from both the proposed numerical model and the experimental tests; see Figure 3.5. Moreover, Figure 3.6(a) and (b) show the force-deformation relationships (hysteresis) for the final calibrated HSS1 and HSS31 models, respectively. Both figures show that both models successfully reproduced the observed behavior from the corresponding experimental test. To ensure that the compression response was accurately simulated in the numerical model in both tests, the out-of-plane buckling value was compared with the experimental tests and showed very close agreement.

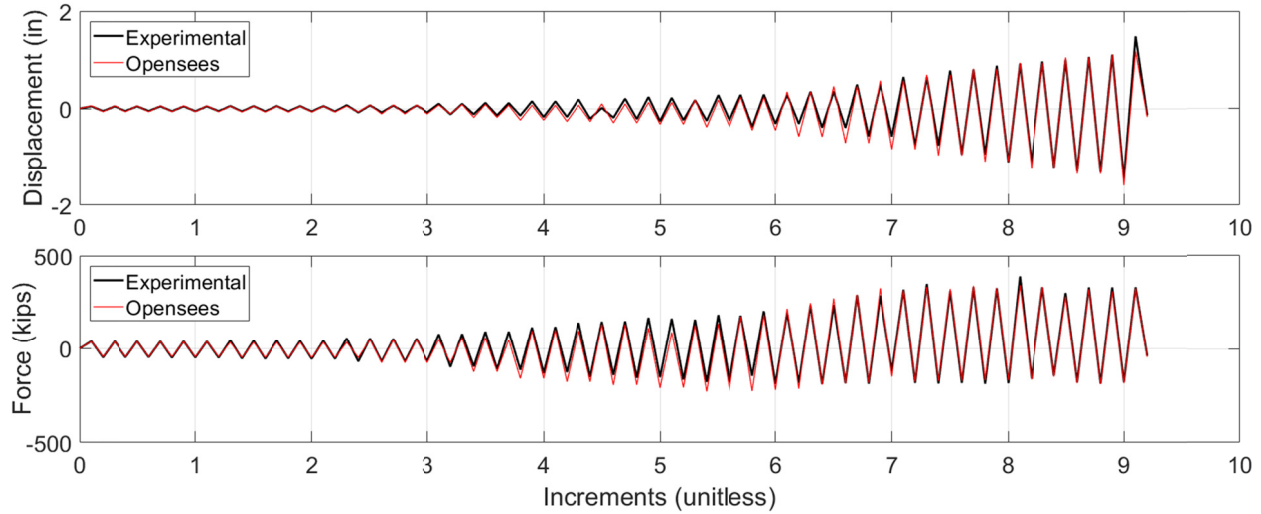


Figure 3.5 Simulated and measured responses of specimen HSS1: displacement history (top) and force history (bottom).

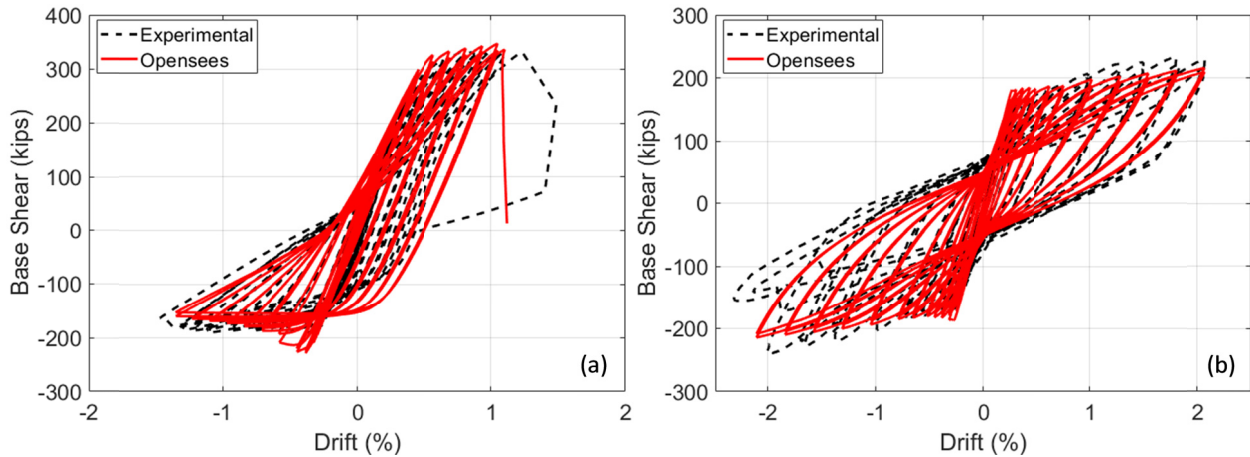


Figure 3.6 Simulated and measured force-drift responses of specimens: (a) HSS1 with diagonal single brace; and (b) HSS31 with double X-bracing.

3.3 GROUND-MOTION SELECTION

The main objective of this part of the study was to investigate the effect of varying modeling parameters on the seismic response of SCBFs under short- and long-duration ground motions. Two sets of long- and short-duration earthquakes (eight ground motions per set) were compiled and used for nonlinear time history analysis of the two calibrated braced frames models presented above. The ground motions from both sets were first scaled such that their mean response spectra match a representative target maximum considered earthquake (MCE) spectrum, referred to as the 100% scale. The objective of the analysis was to determine how the seismic capacity of the considered frames varied with modeling parameters and ground-motion duration. Thus, a target MCE spectrum for San Francisco, California, was used to obtain the so-called 100%-scale records for two reasons: (1) San Francisco is susceptible to typical crustal

short-duration earthquakes, which is the case for current design codes with no specific consideration for longer duration earthquakes; and (2) ground motions scaled to this MCE spectrum at the considered frames periods are likely to fail under the so-called 100% scale; less incremental analysis runs will be needed to capture the full failure in all cases.

With this in mind, for those cases where a failure (brace rupture) did not occur when subjected to the 100%-scale ground-motion intensity, the intensity was increased in 10% increments until the failure occurred, and both displacement and force capacities were obtained, as shown in the analysis results sections. A total of 16 records were chosen to cover a high range of duration from 13–119 sec based on the 5–95% significant duration definition. Table 3.4 shows the details of the selected ground motions used in this part of the study. Examples of the earthquake events considered in these sets include 1940 Imperial Valley, 1971 San Fernando, 1999 Chi-Chi (Taiwan), and 2011 Tohoku (Japan) earthquakes. Figure 3.7 shows the response spectra for the selected scaled short- and long-duration individual records along with their mean as compared to the target spectrum. The figure’s legends also indicates the significant duration of each record and shows the match between the mean spectrum and target spectrum in the vicinity of the fundamental period of both of the frames considered.

Table 3.4 Summary of ground motions used in the sensitivity analysis.

Type	GM #	Earthquake	Station name	D_s 5–95 (sec)
Short-duration set	1	1940 Imperial Valley	El Centro Array	24.20
	2	1952 Kern County	Santa Barbara Courthouse	22.10
	3	1952 Kern County	Taft Lincoln School	30.30
	4	1961 Hollister	Hollister City Hall	18.70
	5	1966 Parkfield	Cholame - Shandon Array	13.14
	6	1971 San Fernando	Lake Hughes	15.70
	7	1971 San Fernando	Pasadena - CIT Athenaeum	14.50
	8	1983 Coalinga	Cholame 3E	20.63
Long-duration set	1	2011 Tohoku, Japan	GNMH05	62.93
	2	2011 Tohoku, Japan	TKY007	81.03
	3	2011 Tohoku, Japan	IBR009	86.55
	4	2011 Tohoku, Japan	YMT015	106.01
	5	2011 Tohoku, Japan	SIT003	30.30
	6	1999 Chi-Chi, Taiwan	CHY079, E	37.57
	7	1999 Chi-Chi, Taiwan	CHY019, N	39.10
	8	2011 Tohoku, Japan	Matanzas	34.96

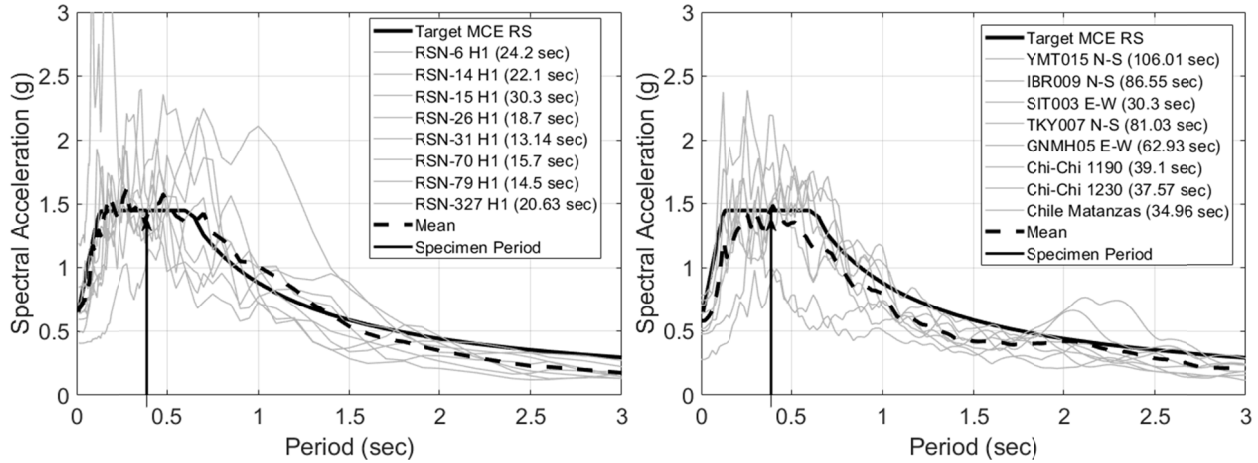


Figure 3.7 Mean response spectra for short-duration (left) and long-duration (right) ground motions compared to the target MCE response spectrum of San Francisco.

3.4 MODEL SENSITIVITY ANALYSIS

Using the validated OpenSees models for both of the diagonal and X-bracing frames discussed above, five modeling parameters were varied one at a time to conduct a sensitivity analysis and investigate the seismic response of such SCBFs under ground motions of different durations. The variation in the peak drift ratio and base shear capacity from the analysis results for both single-story diagonal and X-bracing SCBFs is the focus of this sensitivity analysis. The five varied parameters include: (a) *Steel02* input parameters; (b) low-cycle fatigue m and ϵ_0 ; (c) brace slenderness ratio; (d) number of brace elements (meshing); and (e) the number of integration points. When one parameter was varied, all other parameters were fixed at the “default” values as verified in the model. For each varied parameter, several values were selected as explained below and summarized in Table 3.6:

- **Material Model (*Steel02*):** Five sets of values were used to define the material model as summarized in Table 3.5. The table also shows the varied input arguments as defined in OpenSees. The five sets are meant to reflect the following cases: built-in default values, calibration against experiments, high-energy hysteretic behavior, increased compressive strength over tensile strength, and increased tensile strength over compressive strength.
- **Low-Cycle Fatigue (m and ϵ_0):** Eight different sets of values were selected to cover all the range of applicable values from published literature as previously summarized in Table 3.1.
- **Brace Slenderness Ratio:** Four values were chosen for the brace slenderness ratio (kL/r). The values were chosen to cover a high range of values ranging from 60 to 120. The slenderness ratio is varied to reflect how this variation alters the low-cycle fatigue input according to the Tirca and Chen prediction equation [2014].

- Number of Brace Elements (mesh discretization): Three different elements (6, 8, and 12) were considered to simulate the brace buckling behavior and in turn, brace capacity.
- Number of Integration Points: Four different values were used for the number of integration points per element (3, 5, 7, and 10) to investigate the nonlinear solver sensitivity if any.

Table 3.5 Summary of varied *Steel02* input parameters used for sensitivity analysis.

Set #	Varied input values; see Equation (3.4) above						
	$\$R_0$	$\$cR_1$	$\$cR_2$	$\$a_1$	$\$a_2$	$\$a_3$	$\$a_4$
Set 1	20	0.925	0.15	default built-in			
Set 2	20	0.97	0.15	0.003	0.01	0.002	0.01
Set 3	18	0.10	0.15	0	1	0	1
Set 4	20	0.925	0.15	1	1	0	1
Set 5	18	0.925	0.15	0	1	1	1

Table 3.6 Sensitivity analysis models parameters for diagonal (D) and (X-) brace SCBFs

CBF type	Model ID	Varied parameter	Parameters input values						
			m	ε_0	Steel02	KL/r	No. of elements	No. of int. points	
Diagonal Bracing	D-1	Steel02	-0.5	0.138	Set 1	80	12	5	
	D-2				Set 2				
	D-3				Set 3				
	D-4				Set 4				
	D-5				Set 5				
	D-6	# of elements	-0.5	0.138	Set 2	80	6	5	
	D-7						8		
	D-8						12		
	D-9	# of Integration points	-0.5	0.138	Set 2	80	12	3	
	D-10							5	
	D-11							7	
	D-12							10	
	D-13	m & ε_0	-0.5	0.047	Set 2	80	12	5	
	D-14								0.095
	D-15								0.138
	D-16								0.119
	D-17								0.09
	D-18								0.07
	D-19								0.19
	D-20								0.099
	D-21	KL/r	-0.5	0.105	Set 2	80	12	5	
	D-22								0.119
	D-23								0.123
	D-24								0.191
X- Bracing	X-1	Steel02	-0.5	0.152	Set 1	117	12	5	
	X-2				Set 2				
	X-3				Set 3				
	X-4				Set 4				
	X-5				Set 5				
	X-6	# of elements	-0.5	0.152	Set 2	117	6	5	
	X-7						8		
	X-8						12		
	X-9	# of Integration points	-0.5	0.152	Set 2	117	12	3	
	X-10							5	
	X-11							7	
	X-12							10	
	X-13	m & ε_0	-0.3	0.044	Set 2	117	12	5	
	X-14								0.095
	X-15								0.152
	X-16								0.1784
	X-17								0.0837
	X-18								0.09
	X-19								0.07
	X-20								0.19
	X-21	KL/r	-0.458	0.099	Set 2	80	12	5	
	X-22								0.0384
	X-23								0.0849
	X-24								0.1667

3.5 NONLINEAR TIME HISTORY ANALYSIS RESULTS

As previously mentioned, the two main objectives of this sensitivity analysis were to understand the effect of critical modeling assumptions, e.g., low-cycle fatigue, on the seismic response of SCBFs, and investigate the effect of earthquake duration on SCBFs when various modeling parameters were varied deterministically. To accomplish both objectives, a total of 768 nonlinear time history analysis cases were conducted (24 model variations \times 16 ground motions \times 2 frame configurations). Selected nonlinear time history analysis results are shown below along with a summary of the mean peak response values from the short- and long-duration ground motions; see Table 3.4.

3.5.1 Selected Response History

Presented below is a sample of the results and response histories obtained from different analysis cases, which was used to determine peak response values to estimate mean values from all ground motions (see Section 3.5.2) and the sensitivity analysis presented in Section 3.6. Figure 3.8 shows the force-displacement relationship and base shear force and top displacement histories of Model #D-23 (see Table 3.6 for model parameters and definition) under one of the long-duration ground motions. The hysteresis shows degradation in stiffness due to brace buckling and eventually complete rupture. Figure 3.9 shows same results for diagonal-brace configuration but with different model parameters (Model #D-7) and under one of the long-duration ground motions. Figures 3.10 and 3.11 show similar plots but for two X-bracing cases: Models #11 and #14 under selected short- and long-duration motions, respectively. The figures show that the analysis was valid until both braces ruptured; they illustrate the almost symmetric versus asymmetric behavior of X- and diagonal-brace configurations.

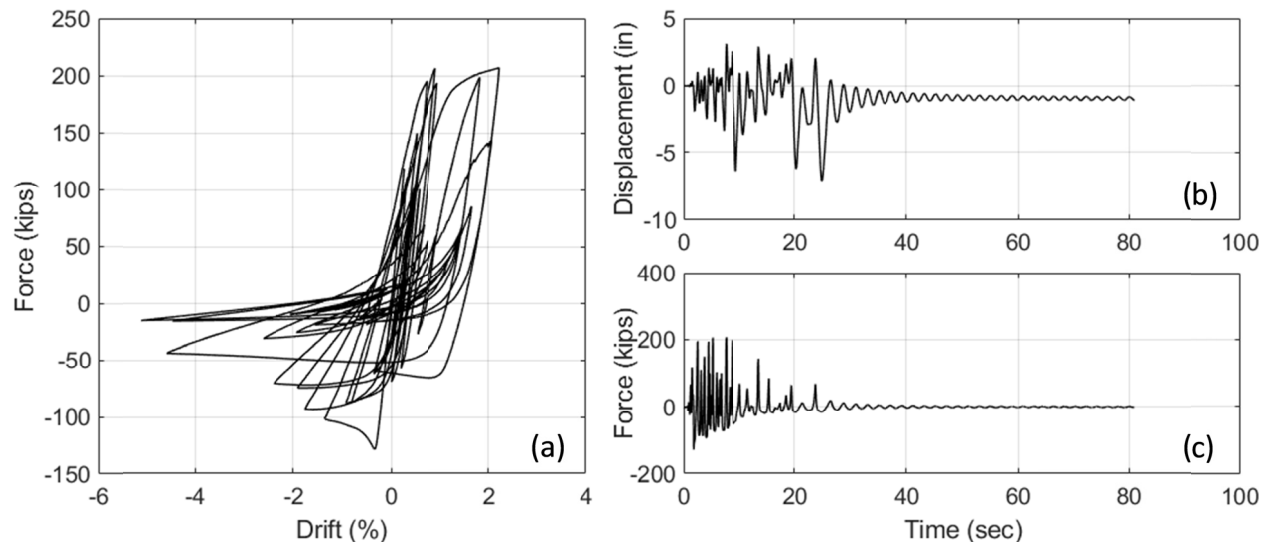


Figure 3.8 Diagonal-bracing frame, Model #D-23 under selected short-duration ground motion: (a) hysteresis, (b) displacement, and (c) force histories.

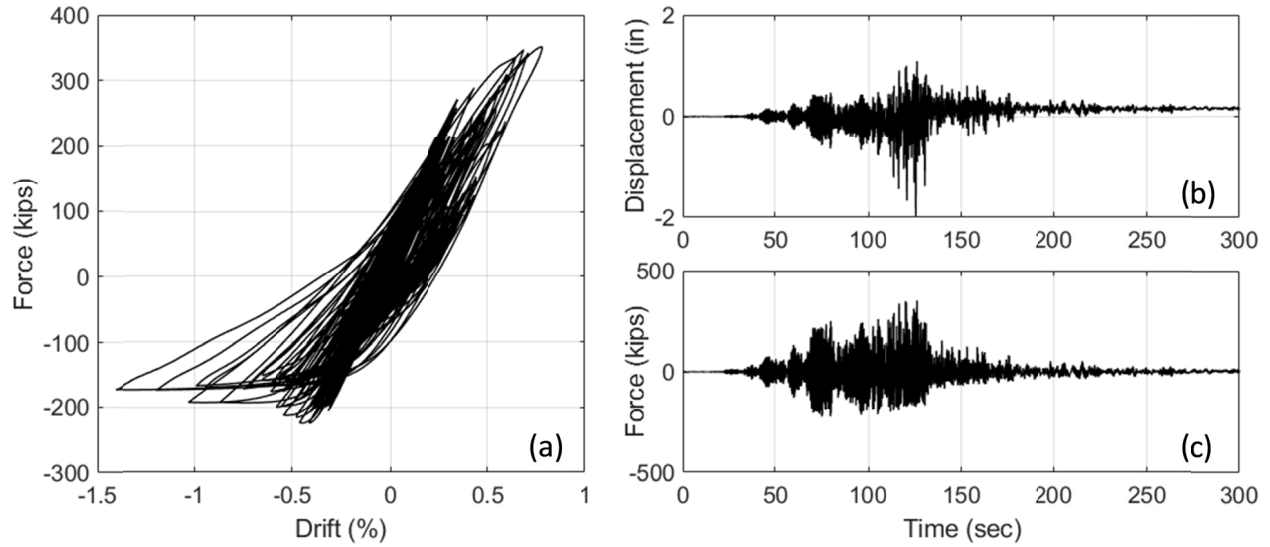


Figure 3.9 Diagonal-bracing frame, Model #D-7 under selected long-duration ground motion: (a) hysteresis, (b) displacement, and (c) force histories.

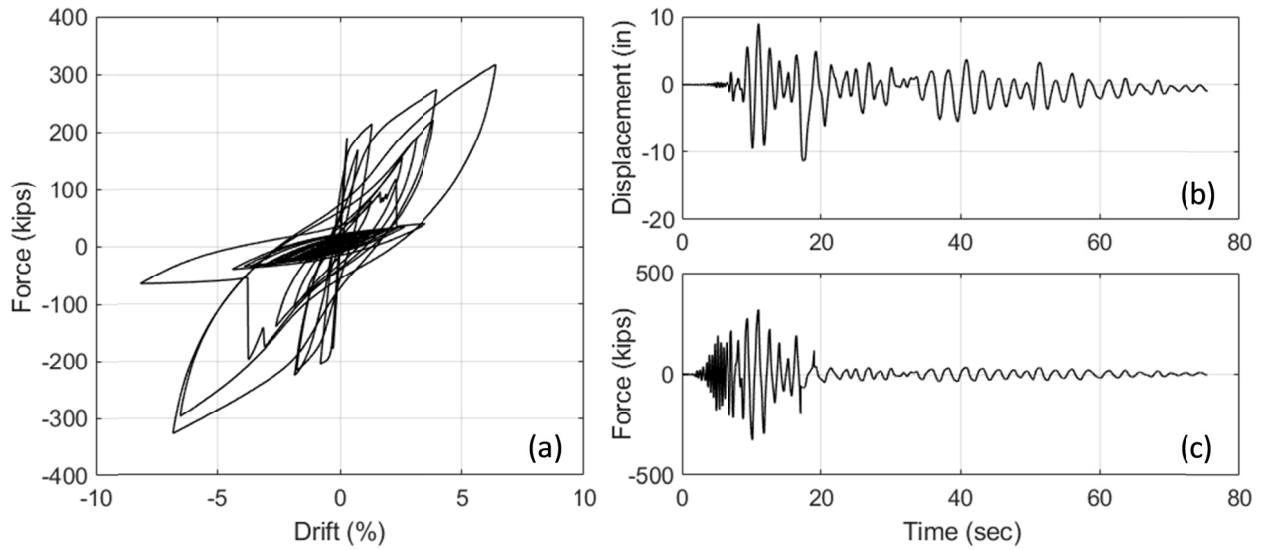


Figure 3.10 X-bracing frame, Model #X-11 under selected short-duration ground motion: (a) hysteresis, (b) displacement, and (c) force histories.

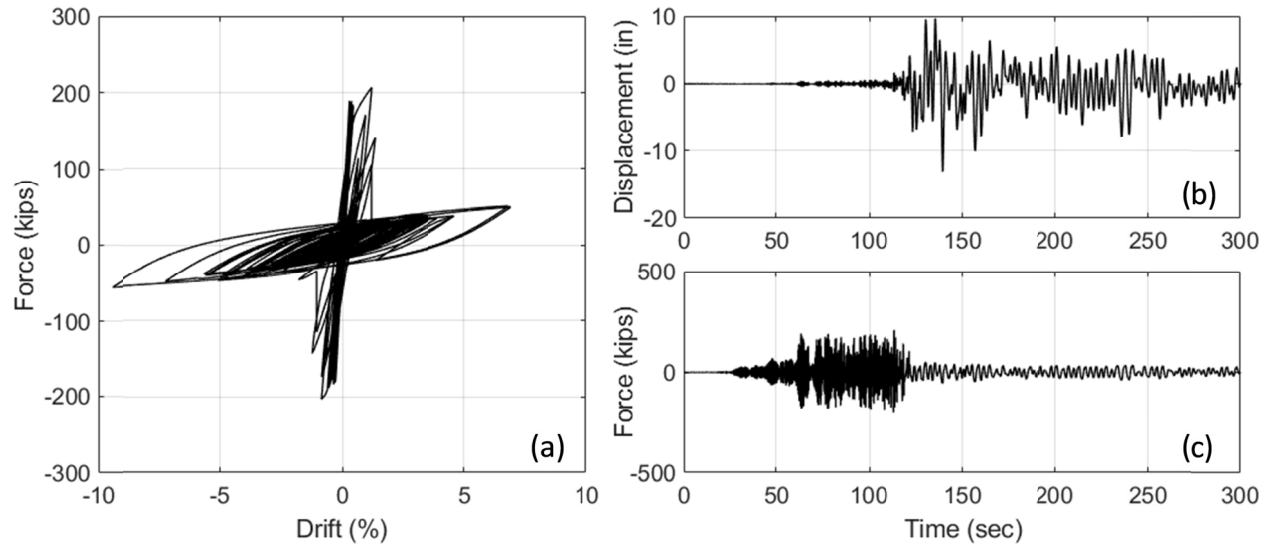


Figure 3.11 X-bracing frame, Model #X-14 under selected long-duration ground motion: (a) hysteresis, (b) displacement, and (c) force histories.

3.5.2 Summary of Mean Peak Response

Considering the two sets of short- and long-duration ground motions (eight records/set), the mean peak response values from the eight ground motions/set for all the different models (24 model variation/brace configurations) are summarized in Table 3.7. The shown peak response values include the frame top displacement, base shear, and top acceleration.

In most of the modeling cases shown in Table 3.6, the reported peak displacements, i.e., displacement capacity, is lower compared to those cases subjected to long-duration motions. This is attributed to the effect of low-cycle fatigue and damage accumulation associated with longer ground motions, which leads to earlier or pre-mature rupture when compared to short-duration ground motions. The same observation for duration effects is presented in two other different ways in Section 3.7. The variation between the different models is discussed in more detail in the sensitivity analysis results presented in Section 3.6.

Table 3.7 Summary of mean peak response values for all models from two motions sets.

Model no.	Varied parameter	Top displacement (in.)		Base shear (kips)		Top acceleration (g)	
		Short-duration	Long duration	Short-duration	Long duration	Short-duration	Long duration
Single (diagonal-) braced frame							
D-1	Steel02 input sets	3.56	2.08	334.5	337.5	1.18	1.11
D-2		4.04	2.35	367.0	361.5	1.22	1.19
D-3		2.64	1.92	338.0	345.0	1.29	1.18
D-4		9.85	10.71	417.5	427.0	1.57	1.35
D-5		12.58	12.01	534.0	522.5	1.42	1.28
D-6	No. of elements	3.05	2.02	374.0	363.0	1.30	1.17
D-7		3.31	1.93	363.5	358.0	1.20	1.17
D-8		4.04	2.35	367.0	361.5	1.22	1.19
D-9	No. of integration points	4.03	2.24	366.5	361.0	1.21	1.22
D-10		4.04	2.35	367.0	361.5	1.22	1.19
D-11		4.18	1.92	357.5	361.0	1.21	1.19
D-12		3.99	1.97	367.0	361.0	1.22	1.19
D-13	m and ε_0	1.45	1.38	346.5	342.0	1.07	0.96
D-14		2.89	1.73	359.5	350.0	1.17	1.01
D-15		4.04	2.35	367.0	361.5	1.22	1.19
D-16		3.24	1.97	357.5	361.0	1.24	1.13
D-17		1.96	0.73	349.5	331.0	1.15	0.79
D-18		1.95	1.29	350.0	342.0	1.16	0.91
D-19		6.51	3.61	385.0	378.5	1.33	1.31
D-20		2.34	1.96	363.5	357.0	1.07	1.03
D-21	K/lr	4.92	4.14	684.5	596.5	1.85	1.66
D-22		3.24	1.97	357.5	361.0	1.24	1.13
D-23		4.05	2.25	221.5	207.5	0.99	0.82
D-24		6.60	5.52	236.0	227.0	1.21	0.89
Double (X-) braced frame							
X-1	Steel02 input sets	4.90	6.15	295.00	265.00	0.98	0.77
X-2		5.15	9.90	288.50	236.00	0.87	0.75
X-3		4.40	6.75	287.50	263.50	0.93	0.82
X-4		14.65	9.25	460.00	348.50	1.52	0.99
X-5		11.55	6.90	680.00	562.50	1.47	1.11
X-6	No. of elements	5.60	8.20	296.50	272.50	0.89	0.81
X-7		9.50	8.85	232.50	202.50	0.80	0.76
X-8		5.15	9.90	288.50	236.00	0.87	0.75
X-9	No. of integration points	5.40	7.70	293.00	237.00	0.87	0.76
X-10		5.15	9.90	288.50	233.50	0.87	0.75
X-11		5.75	9.25	290.00	240.00	0.87	0.75
X-12		4.75	6.75	290.00	235.50	0.87	0.74
X-13	m and ε_0	7.10	9.95	222.50	200.00	0.75	0.75
X-14		7.05	10.10	276.00	202.50	0.86	0.72
X-15		5.15	9.90	288.50	236.00	0.87	0.75
X-16		5.10	4.20	295.00	246.50	0.87	0.79
X-17		8.16	8.90	235.50	192.50	0.83	0.67
X-18		9.96	8.31	247.50	194.50	0.83	0.67
X-19		8.06	6.26	312.00	240.00	1.14	0.78
X-20		7.78	8.69	266.50	206.00	0.86	0.75
X-21	K/lr	7.35	10.00	242.50	230.00	0.75	0.64
X-22		8.05	10.05	280.00	227.00	0.84	0.71
X-23		6.05	3.30	435.00	337.50	1.30	0.88
X-24		5.10	4.20	295.00	246.50	0.87	0.79

3.6 SENSITIVITY ANALYSIS

As previously discussed in Section 3.3 on ground-motion selection, the mean spectra of the short- and long-duration records match a target MCE spectrum at the considered frames periods. This means that, on average, the same seismic force demands were applied to the frames; however, different mean response values were reported at failure. The variation can be only attributed to the model or design in case of kl/r , parameters variability, and effect of the loading, i.e., cyclic versus realistic short- and long-duration earthquake loading. Note: the energy increment test was used in OpenSees with a tolerance of $1.0e-6$ and 200 iterations. When convergence was not achieved, a smaller step (Δt) was implemented in order to achieve convergence. In this section, the effect of modeling variability is isolated from loading protocol effects, and a deterministic tornado diagram analysis is used to present the range of the effect of each of the considered variables.

3.6.1 Tornado Diagram Analysis

Two types of response results or simply EDPs, i.e., drift ratio at failure and base-shear capacity, were used to study and rank the effect of modeling variability on SCBFs seismic response using tornado diagrams. The tornado diagram, commonly used in decision analysis, is an effective way of representing uncertainties. It has been used in sensitivity analysis in earthquake engineering (e.g., Porter et al. [2002]) and probabilistic seismic evaluation of structural components and systems (e.g., Lee and Mosalam [2005]). The tornado diagram consists of a set of horizontal bars, referred to as swings, one for each source of uncertainty (random variable). The length of each swing represents the variation in the output due to the variation in the respective parameter. Thus, a variable with larger effect on the output has larger swing than those with lesser effects. In a tornado diagram, swings are displayed in the descending order of the swing size from the top to the bottom. This wide-to-narrow arrangement of swings eventually resembles the shape of a tornado. Extensive review of the procedure of developing a tornado diagram analysis can be found in Lee and Mosalam [2005]. In this study, a total of 68 tornado diagrams were developed: two considered EDPs \times two brace configurations \times 17 loading cases (1 cyclic loading case as per original the experimental testing and the 16 short- and long-duration ground motions). To isolate the effect of ground-motion variability from modeling variations, the results presented herein are for the mean values as obtained from each set of ground motions, leading to a total of 12 tornado diagrams (two EDPs \times two brace configurations \times three loading protocols).

The OpenSees analysis was considered to be the deterministic function evaluation. In addition, each of the five groups of parameters that ranged between upper and lower bounds represented the input to the analysis. For instance, when one of the input parameters was set to a lower or upper bound, the rest of parameters were set to the values determined from model calibration as previously listed; see Tables 3.5 and 3.6. The absolute difference between these two values was the swing of the output corresponding to the selected input variable. The tornado diagram was then constructed by arranging the obtained swings in a descending order as mentioned above, and the sources of the tornado diagrams for the percentage of failure drift and base shear at failure outputs are shown next. Note: the results from each SCBF brace configuration is presented separately because the capacity dictated by rupturing one versus two braces may relate differently to the modeling parameters.

3.6.2 Variation in Drift (Displacement) Capacity

A compilation of 6 different tornado diagrams is shown in Figure 3.12 to present the variation in the obtained drift % of the single- (diagonal-) and double- (X-) braced frame under three loading scenarios: the first case considered the cyclic loading used in the experimental testing of the original frame; and the second and third cases reflect the variation in the mean drift % from all 8 short- and 8 long-duration ground motions. The tornado diagrams presented in this section and next one are a different way of presenting the results previously summarized in Table 3.7. The drift-capacity tornado diagrams illustrate several important observations. In general, the SCBFs models are less sensitive to the input parameters under cyclic loading when compared to the ground motions, as indicated by the tornado swings (bar width) that emphasize the fact that seismic performance needs to be assessed under realistic ground motions rather than cyclic or pushover analyses.

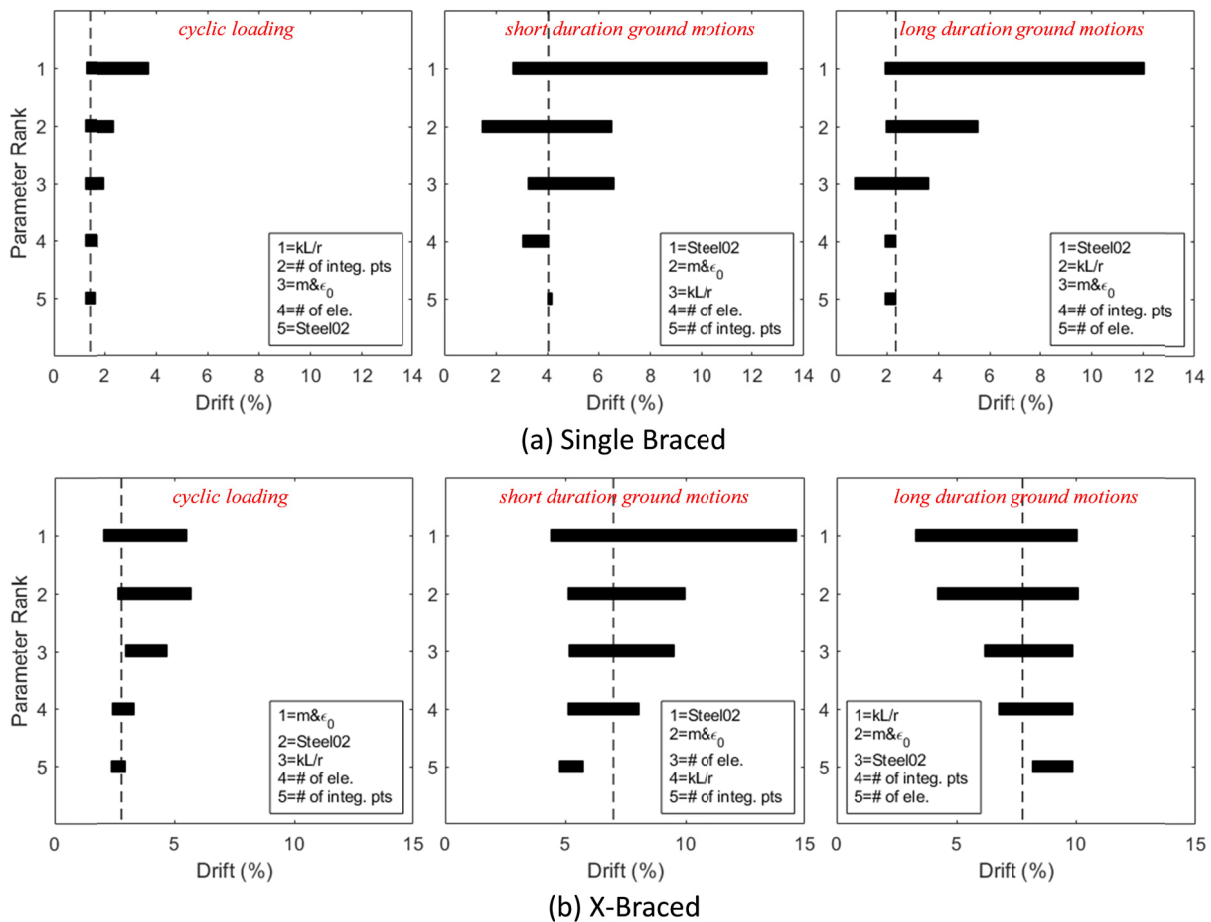


Figure 3.12 Tornado diagrams for drift ratio (%) for single- and x-braced frames under cyclic loading and mean responses from sets of short- and long-duration ground motions. Dashed lines represent results from calibrated model presented earlier.

Among the SCBFs modeling parameters, the slenderness ratio, and the low-cycle fatigue parameters using the material model (*Steel02*) lead to significant change in the interpreted drift capacity (variation between 1% and 12%), unlike the effect of the brace meshing and number of integration points. Note: given the sensitivity of low-cycle fatigue model in OpenSees when conducting an analysis of SBCFs, any analysis results and validation of a model should be viewed with caution when making any design decisions. Recall that there are at least seven pairs of values available in the literature to define the fatigue model for HSS used in SCBFs. Also note that the slenderness ratio variation indirectly varied the low-cycle fatigue input, but a single slenderness ratio value was used when m and ϵ_0 were varied. The brace configuration also results in different sensitivities to the modeling parameters because of the asymmetric capacity associated with single diagonal braces.

3.6.3 Variation in Base-Shear Capacity

Similar to before, the variation in the base-shear capacity of the SCBFs considered is presented in the form of tornado diagrams; see Figure 3.13. The most obvious observation gleaned from comparing the tornado diagrams for drift versus base-shear capacity is that the fatigue has much less effect on the base-shear capacity, which, in turn, is found to be highly sensitive to the material model input and slenderness ratio (which affects the strength of the brace, and, thus, the buckling behavior of the brace); this explains why this effect is more obvious in the case of single-diagonal braced frames compared to than double-braced frames. Obviously, the material model *Steel02* can significantly affect the base-shear capacity, especially considered that the selected input values cover a wide range for material behavior and affect the strength of the frame under lateral loading. Note: this also highlights the importance of the proper selection of input values for *Steel02* as it can skew the analysis results.

3.7 EFFECT OF EARTHQUAKE DURATION

Another objective of this study was to investigate the effect of earthquake duration on SCBFs but using an approach that considers critical modeling variables. The results from 768 analyses are presented below that averages out all considered modeling parameters in an attempt to isolate the effect of model sensitivity and provide insight into the effect of earthquake duration on collapse and fragility curves of the SCBFs considered.

3.7.1 Collapse Assessment

Using the same cases as analyzed earlier, the results were re-interpreted to quantify the effect of the duration rather than modeling sensitivity. In this regard, a preliminary regression analysis was conducted to determine whether the ground motion significant duration can be related to the drift capacity, which is expected to relate more to fatigue damage accumulation than strength or base shear capacity; see Figure 3.14. An inverse linear trend can be observed in the figure when results from all single-braced frame cases are considered (384 cases) altogether to average out the effect of modeling uncertainties. From Figure 3.14, the obtained drift capacity from analysis is reduced by about 7% on average for every 10 sec increase in ground motions duration. When a

similar relation is developed for the base shear capacity of single-braced frames, only a small reduction of about 1% corresponded to 10 sec increase in significant duration.

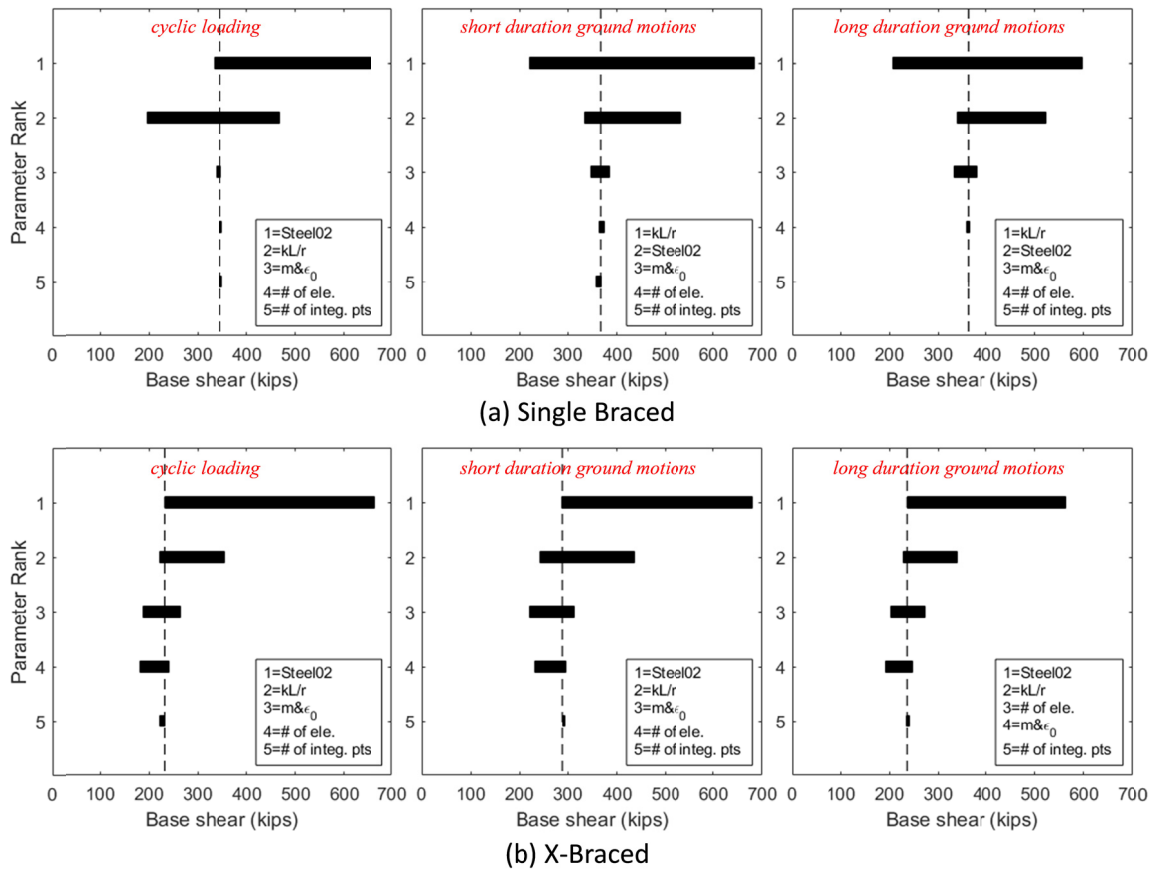


Figure 3.13 Tornado diagrams for base shear capacity for single- and x-braced frames under cyclic loading and mean responses from sets of short- and long-duration ground motions. Dashed lines represent results from the calibrated model.

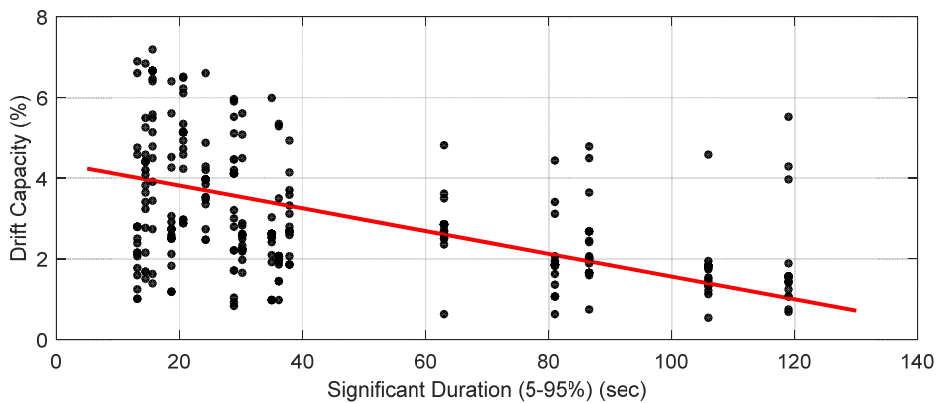


Figure 3.14 Fitted relationship between the significant duration and the single-braced frame drift ratio at failure (drift capacity) for all cases with varied modeling parameters.

This seems to agree with previous studies (e.g., Chandramohan et al. [2016a, b]) that demonstrated that when SCBFs are subjected to longer duration earthquakes they accumulate more damage and result in failures at lower displacement capacities than anticipated from the design. In addition, the study by Chandramohan et al. [2016a, b] also reported a clear trend between the spectral acceleration ratio (as an EDP) between and DS_{5-75} . The trend showed a smaller collapse capacity as a function of ground-motion duration. In contrast, it was not possible to find a meaningful trend for the X-bracing system due to the more progressive collapse nature of X-bracing associated with the sequence of brace failure and gradual loss of lateral capacity as braces alternate both tensile and compressive stresses after yielding. Moreover, the X-bracing dictates gusset plate connections at all joints unlike the case of the single-brace system where shear tab connections are used when no brace connection exists. The modeling of gusset plate connections usually contributes partially to the lateral frame capacity after brace buckling and fracture. In other words, the single-braced frame loses its entire capacity after brace failure; therefore, determining the trend for the duration effect can be better captured.

3.7.2 Fragility Curves

Fragility curves are conditional probability statements of the likelihood that a structure will meet or exceed a specified level of damage for a given ground-motion intensity measure (IM) [Padgett and DesRoches 2007]. Fragility curves are a powerful tool for seismic assessment of structures, and probabilistic methods are commonly used to account for different sources of uncertainties. For SCBFs, earthquake duration along with the uncertainty in crucial modeling parameters such as material input or low-cycle fatigue parameters have not been considered among other types of epistemic uncertainties when families of braced frames' fragility curves were developed (e.g., Roeder et al. [2012]). Based on the results presented herein regarding the effects such parameters may have on the seismic response of SCBFs, two sets of preliminary collapse fragility curves were developed using the short- and long-duration earthquakes. The fragility curves presented below considered the variability inherited in the 24 different model variations for each frame configuration along with 8 different ground motions per set. Various response values were used to estimate probability of collapse and a log-normal distribution was fitted to the scattered data from the analysis to develop the fragility curves; see Figure 3.15. Two response parameters, namely, the drift ratio and the peak top acceleration designated as spectral acceleration (S_a), were used to develop the collapse fragility curves under the short- and long-duration earthquakes. The results are shown in Figures 3.15 and 3.16, respectively.

As shown in Figures 3.15 and 3.16, the long-duration set leads to a higher probability of exceedance or collapse for a given IM. For single braced frames, the difference in the median fragility is about 45% of the drift capacity at failure, i.e., a reduction from 4% drift capacity to only 2.1% due to longer duration earthquakes. In contrast, about a 12% and 8% difference in the median spectral acceleration fragility can be observed in Figure 3.16 for the single- and double-braced frames, respectively. In the later, about a 20% difference in median fragility was found between the short- and long-duration cases. Overall, these trends agree to some extent as that reported in previous studies (e.g., Raghunandan et al. [2015] and Chandramohan et al. [2016a, b]). For instance, Chandramohan et al. [2016a, b] reported that the median displacement collapse capacity change by about 29% when longer duration earthquakes are applied to modern steel moment frames.

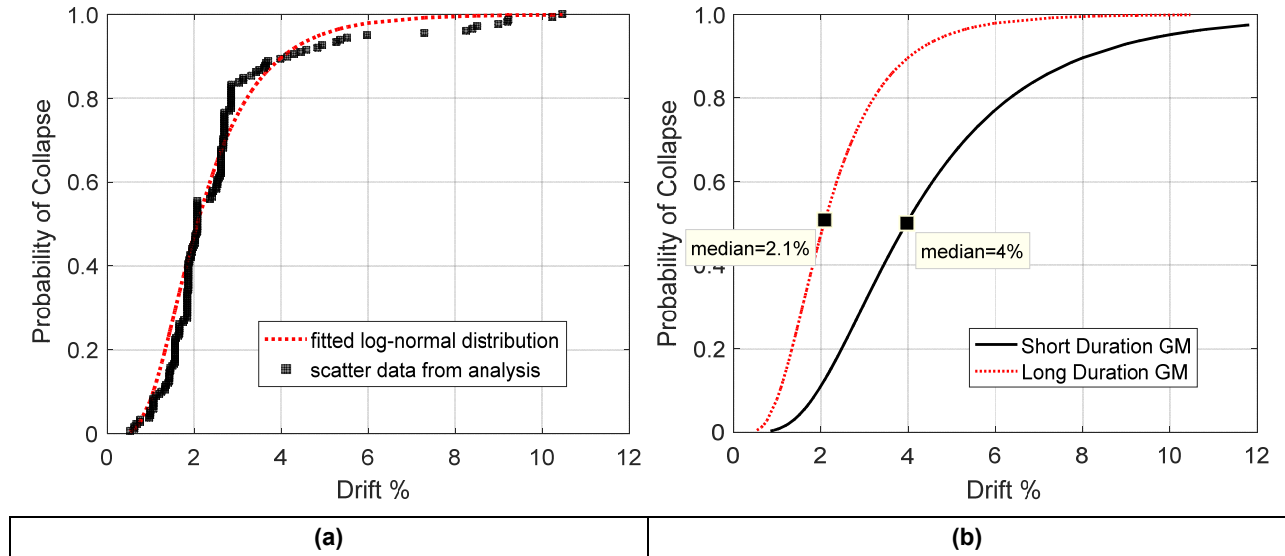


Figure 3.15 (a) Typical procedure for developing fragility curve: and (b) comparison of developed collapse fragility curves for single-braced frame under short- and long-duration ground motions.

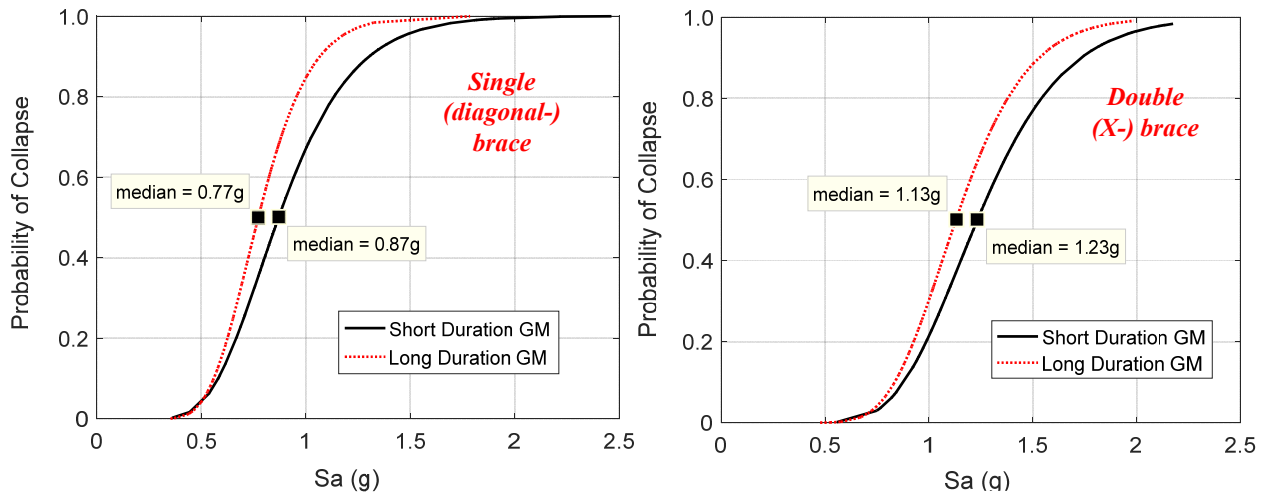


Figure 3.16 Developed fragility curves using spectral accelerations (S_a) for single- and double-braced frames under short and long-duration ground motions.

4 Experimental Program Development

This chapter presents the details of developing the shake table experimental program. A brief discussion on the current design practices and current code provisions as they apply to SCBFs as set forth by the American Institute of Steel Construction is presented first. Next, the design process used to design the three specimens is presented. Then, a discussion of the fabrication and material properties of the three identical test specimens follows. The experimental shake table test setup, instrumentation methods, and the ground motions used for the tests are also presented in details.

4.1 PROTOTYPE AND SPECIMEN

Three identical SCBFs were considered for the experimental program conducted in this study. The test specimens were adopted from a prototype building from the International Building Code's *Structural/Seismic Design Manual* [2006]. The building's footprint is 160 ft × 120 ft. Bracing is supplied on the four sides of the building. Figure 4.1 shows a 3D view of the building, with the general plan illustrated in Figure 4.2. The bracing orientation is shown in Figure 4.3. The basement panel was chosen to determine the design forces and configuration for the test specimens. According to the shake table dimensions available at University of Nevada, Reno, and the height of the mass rig attached to the specimen, a geometric scale of 1/2 was used to determine design forces. The test specimens followed the simple laws of similitude [Lu et al. 2008]; the main similitude scale factors are presented in Table 4.1. Figure 4.4 shows the final design specimen with all the dimensions and members used, with the details of the design of each member or connection provided in next two sections. Readers are also referred to Appendix A for the shop drawings and design details.

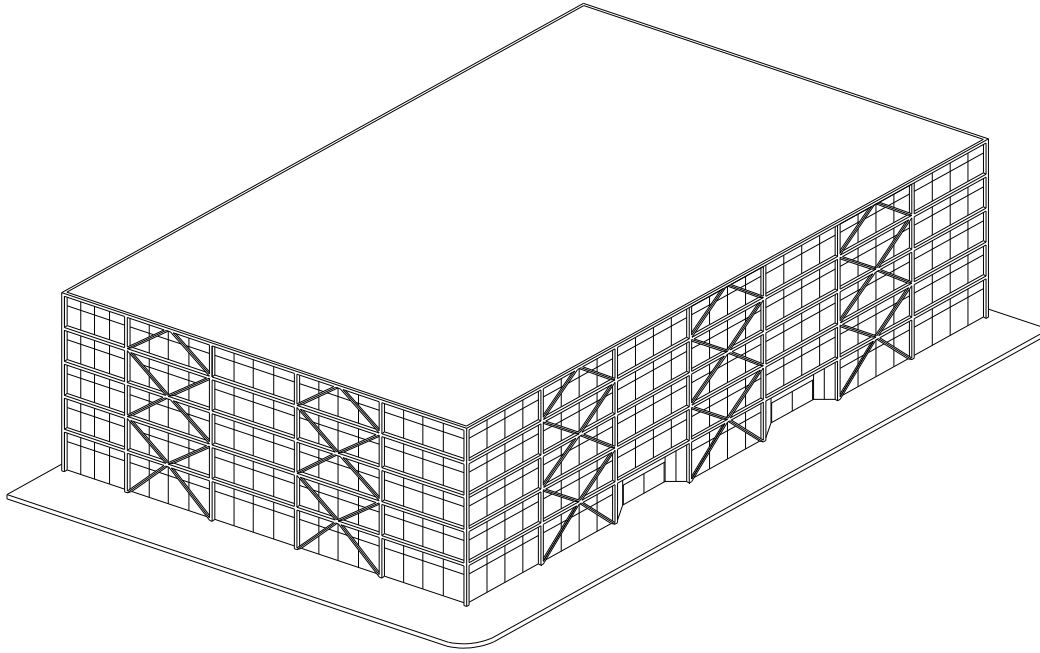


Figure 4.1 A three-dimensional view of the prototype building used to determine the test specimens design forces.

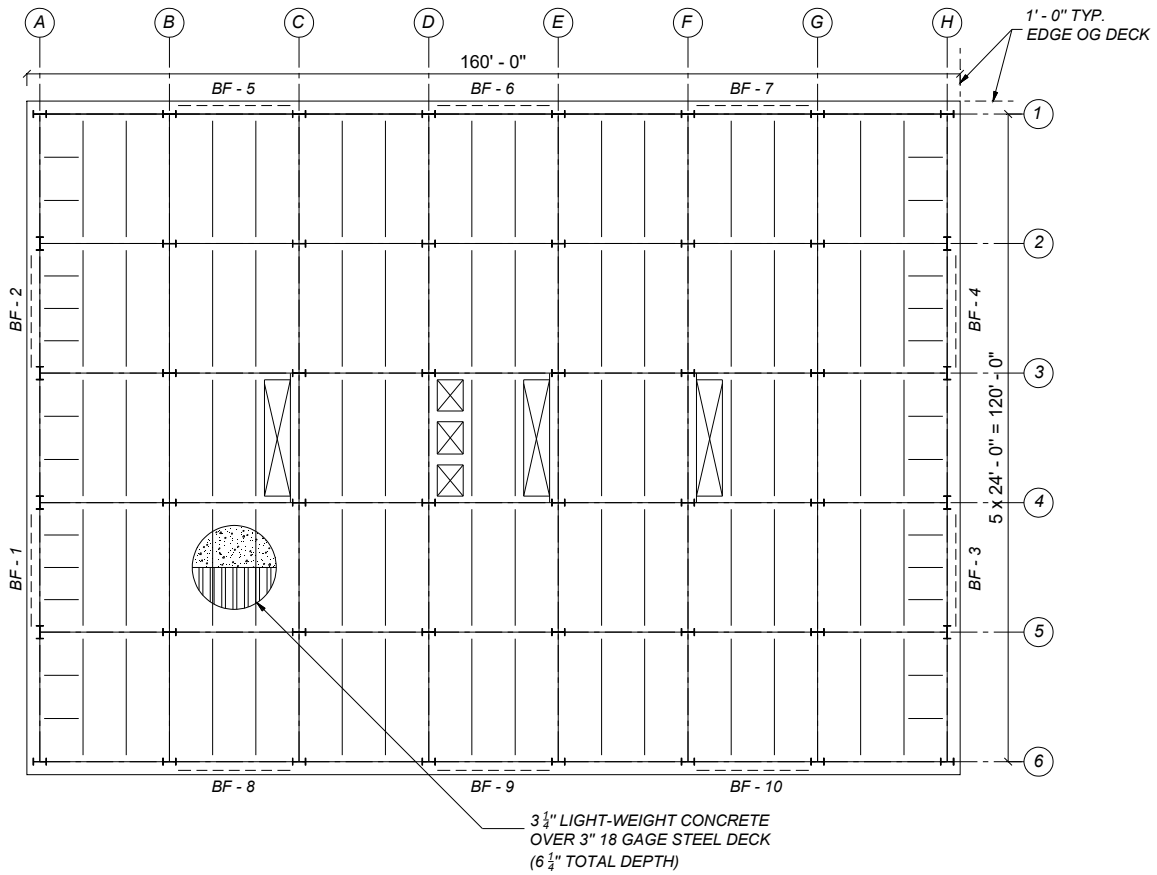


Figure 4.2 Plan view of the prototype building.

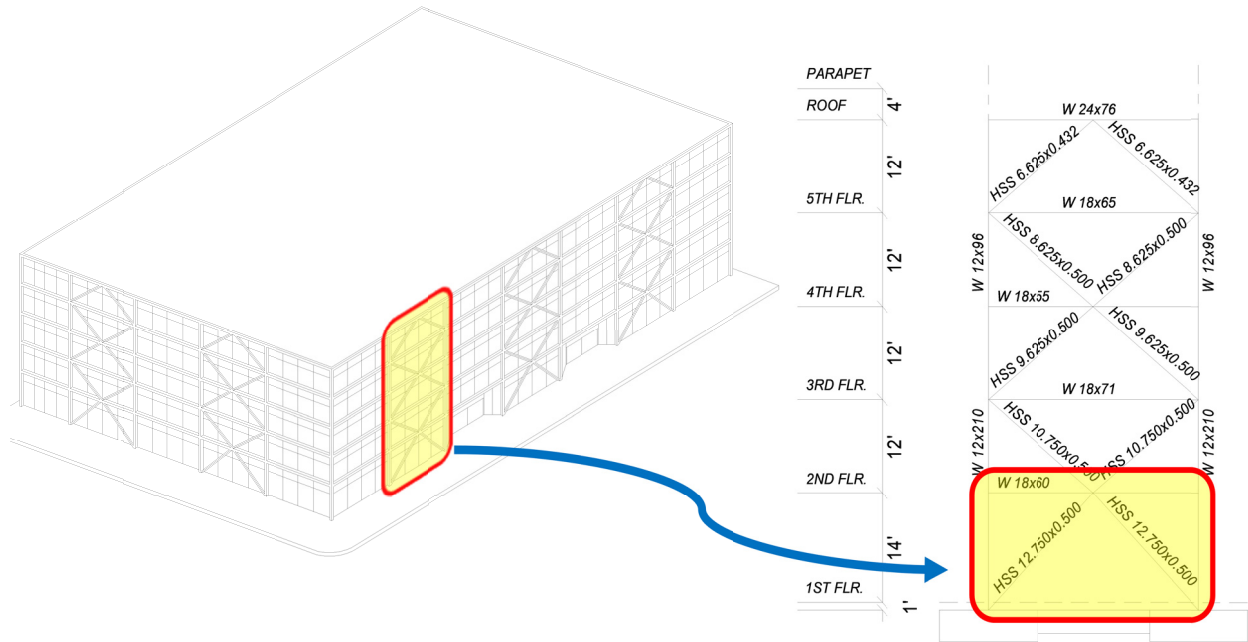


Figure 4.3 Prototype typical X-bracing geometry and illustration of the chevron braced frame consideration for determining reduced-scale specimens design forces.

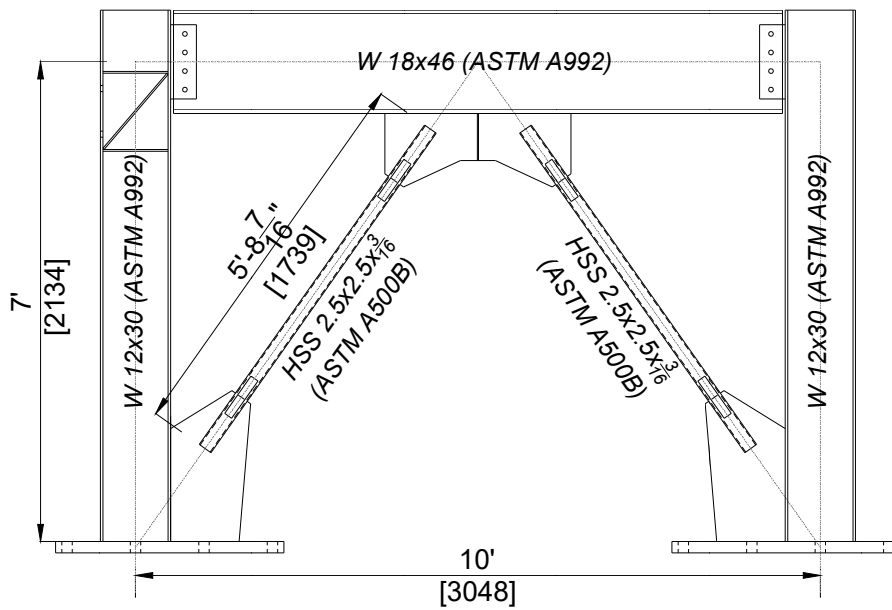


Figure 4.4 Details and designed sections for final test specimens [dimensions in both US units (in., ft) and metric (mm) are provided].

Table 4.1 Similitude scale factors used for the conducted shake table tests (after Lu et al. [2008]).

Parameter	Relationship	Model/prototype
Length (L)	S_L	$\frac{1}{2}$
Young's modulus (E)	S_E	1.0
Stress (σ)	$S_\sigma = S_E$	1.0
Strain (ϵ)	$S_\epsilon = S_\sigma / S_E$	1.0
Density (ρ)	$S_\rho = S_\sigma / S_L$	2.0
Force (F)	$S_F = S_L^2 \cdot S_\sigma$	$\frac{1}{4}$
Mass (m)	$S_m = S_\rho \cdot S_L^3$	$\frac{1}{4}$
Stiffness (k)	$S_k = S_E \cdot S_L$	$\frac{1}{2}$
Time (t) and period (T)	$S_t = (S_m / S_k)^{1/2}$	0.707
Displacement (d)	$S_d = S_L$	$\frac{1}{2}$
Velocity (v)	$S_v = S_L / S_t$	0.707
Acceleration (a)	S_a	1.0

4.2 DESIGN PHILOSOPHY

The specimens were designed carefully to be consistent and representative of current practice. Sources used during the design of the test specimens included current codes, the SAC model building [1997], and technical consultation with local consulting firms. The final design was based on testing constraints. The codes and design recommendations used include the following: AISC LRFD Manual [2010b], AISC LRFD Seismic Provisions for Structural Steel Buildings, and Steel TIPS [2016]. A special feature of SCBFs is the gusset plate connection. Several methods are discussed herein for designing gusset plate connections. The widely used Uniform Force Method (UFM) was chosen for use in this study based on input from local design firms.

4.3 DESIGN CALCULATIONS

4.3.1 General

Specimens were designed using AISC LRFD (2010b) in conjunction with LRFD seismic specifications. The prototype building used for determining the specimen forces was designed for a location in Seattle, Washington, using Seismic Design Category D with soil Site Class C. The building was designed to meet the ASCE-7 design spectrum. A response modification factor equals to 6 was used in the design. The calculated period was found to be 0.12 sec.

The design loads and calculations were based on a full-scale prototype, and then scaling factors were applied to obtain the corresponding design forces values for the scaled specimen. The gravity load used was 76 psf on the typical floor and 74 psf for the roof. Loads from the exterior curtain wall and steel studs were taken as 20 psf, with an exterior wall height of 13 ft.

The total mass on floor was approximately 1605 kips and was distributed along two sides of bracing; each specimen had three vertical bracing systems. The scaled mass on each frame was approximately 67 kips. To simulate this mass for the shake table test, two concrete blocks (each weighing approximately 20 kips) were added to the mass rig frame, which weighs about 60 kips. The additional mass along with the specimen weight and the rigid link that connects the mass rig to the specimen all together provide a very close equivalent to the required 67 kips.

The AISC Seismic Design Provisions [2002] require that the connection be designed for the plastic capacity of the brace. Therefore, the exact design checks for the connection are dependent on the members and connection types chosen. Therefore, in terms of this project, a brief discussion of the final frame design is presented below. The members chosen for the test specimens were: W18×46 for the beam, W12×30 for the columns, HSS 2.5×2.5×3/16 for the brace and a tapered gusset plate. These sizes were selected after designing the specimen. The selection of the brace was mainly controlled by considering buckling capacity, and then the selected brace size was checked for tension force.

4.3.2 Brace Selection

Member selection must be in accordance with AISC seismic provisions. The brace width-to-thickness (b/t) ratio selected was 11.4, which satisfied the current limit for SCBFs. This limits the b/t ratio for rectangular HSS sections subjected to axial compression to:

$$\frac{b}{t} \leq 0.64 \sqrt{\frac{E_x}{F_y}} \quad (4.1)$$

Note: the braces size used in this study might not be representative of full-scale braces typically used in actual buildings. While a brace size is known to affect its fatigue and fracture properties, it is believed that this limitation would not affect the overall objective of the study, i.e., the relative comparison of the tested SCBFs and small-scale brace behavior under short and long-duration ground motions.

4.3.3 Beam Design

The axial load capacity of the beam was designed considering the maximum axial load that could be delivered to the beams by the rigid link. Consistent with the AISC, the beam design considered a vertical unbalanced load from the braces, and a beam with the dimensions W18×46 was selected. The beam flanges satisfied current seismic requirements, but the beam web did not satisfy current height-to-thickness requirements for highly ductile sections.

4.3.3.1 Beam Strength

Due to the concentration of force applied from the gusset plate to the beam and column web, checks had to be made to ensure adequate strength of the web and flange. The design checks included: web local yielding and web crippling. In addition, flange local bending was checked. All of these checks are done in accordance with AISC [2002] and were found to be adequate.

4.3.4 Column Design

The columns were designed following the same basic load assumptions as before. Additional gravity loads attributed to the columns were considered for the design but were not applied during testing. Similar to the beam, although the column section satisfies seismic design requirements, the web and flanges did not satisfy current width-to-thickness requirements for highly ductile sections. The design was meant to represent real projects and construction limitations. As the brace had to be connected to a gusset plate, which in turn would be connected to the column flange and base plate, a large gusset plate footprint was required on the base plate. This resulted in a large base plate area with a large moment arm between the anchor bolts that was impractical for consideration as a hinged base connection. Therefore, this connection was designed to be fixed, which resulted in attracting around 20% of the horizontal load. These loads were taken in to account while designing the columns.

4.3.4.1 Column Strength

Due to the concentration of force applied from the actuator to the column flange, checks were made to ensure adequate strength of the web and flange. The web strength was found to be adequate against web yielding; however, column flanges needed strengthening plates when the design force reflected the 160 kips actuator force capacity. Strengthening plates, 3/16 in. thick, were used on both sides

4.3.4.2 Column–Base Plate Connection

The base connection was designed to carry the yield moment of the column, as the columns were not expected to exceed the elastic range. The thickness of the gusset plate was designed based on the overall dimensions of the plate and distribution of the anchor bolts. Anchor bolts were not allowed to carry any base shear as the shake table's limitations do not allow any lateral force on the table. This required having both base plates interact to increase the friction area. This was achieved by placing angles in the middle between the gusset plates to engage both base plates so that they would be able to carry all the base shear by friction rather than by anchors.

4.3.5 Brace-to-Gusset Plate Connection

The next step in designing the system was to design the brace-to-gusset plate joint. The brace was connected directly to the gusset plate by fillet welds with a slotted HSS tubular brace; see Figure 4.5. The weld size and connection length were determined using AISC [2001]. The design force used for the welds was $1.1R_yF_y$, which is the expected plastic capacity of the brace.

As a final design consideration for this connection, fracture of the net section of the brace was also checked because the brace was slotted and only connected to the gusset plate on two sides of the brace. Fracture of the net section was checked using AISC [2001], and the capacity of the net section was checked against the yield on gross section of the brace increased by 10% in accordance with AISC Seismic Provisions [2002]. A thickener plate was added to reinforce the net section of the brace at the slot. In this study, the plates were welded to the unslotted surfaces of the brace using fillet welds.

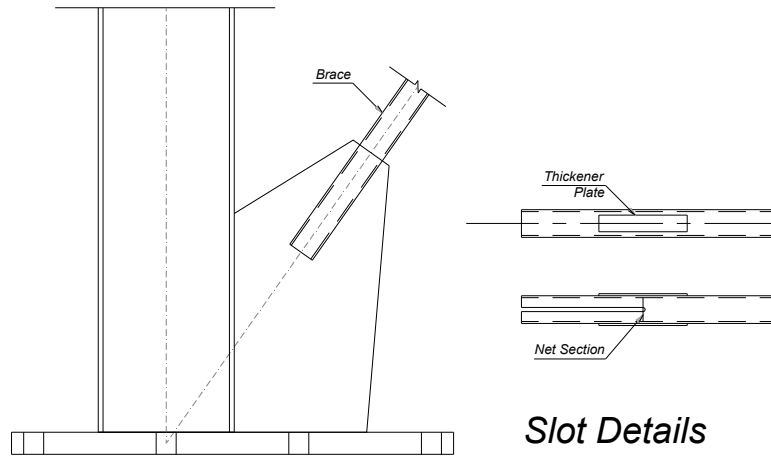


Figure 4.5 Brace-to-gusset-plate connection.

4.3.6 Gusset-Plate Design

The first step in designing the gusset plate was to determine its thickness. Four checks were necessary in determining the plate thickness: block shear, yielding of the Whitmore section, fracture of the Whitmore section, and buckling. The values of A_{gt} and A_{nt} for a fillet welded tubular section are equal to the width of the brace multiplied by the thickness of the plate. These areas are illustrated in Figure 4.6.

Yielding and fracture of the Whitmore section were computed using the concept of the “Whitmore width.” The Whitmore width is an assumed width over which the load can be treated as a uniform stress. The Whitmore width (B_w) was found by extending lines at 30° relative to the brace from the beginning of the brace -to-gusset plate connection to the end of the connection: see Figure 4.6.

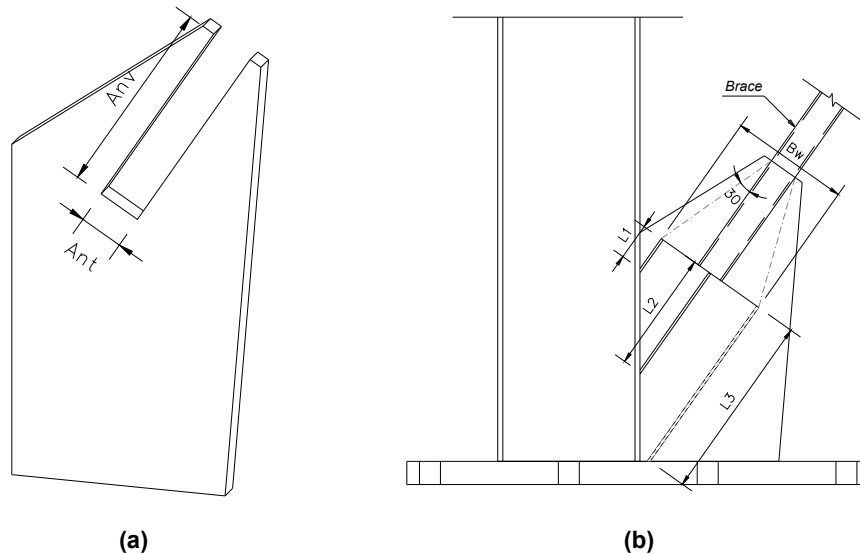


Figure 4.6 (a) Illustration of block shear, and (b) Whitmore width for gusset plates.

A report by Cheng et al. [1994] reported that the Modified Thornton method was the most accurate method in predicting the buckling capacity of rectangular gusset plates subjected to axial loading. Thus, this method was used herein in checking the buckling capacity of the gusset plates. The buckling capacity was calculated using the following expression in Equation (4.2):

$$P_{cr} = A_{gw} F_{cr} \quad (4.2)$$

where F_{cr} is the critical based upon the gusset plate slenderness as follows in Equations (4.3)–(4.5):

$$\text{For } \lambda \leq 1.5 \quad F_{cr} = 0.658^{\lambda^2} F_y \quad (4.3)$$

$$\text{For } \lambda \geq 1.5 \quad F_{cr} = \frac{0.877}{\lambda^2} F_y \quad (4.4)$$

where

$$\lambda = \frac{Kl}{t_p \pi} \sqrt{\frac{12F_y}{29,000}} \quad (4.5)$$

In Equation (4.5), several values of K have been recommended by various research studies, ranging from 0.5 to 1.2. The value l is found as either the average of l_1 , l_2 , and l_3 , or is the maximum perpendicular distance from the Whitmore section to the interior corner of the gusset plate.

4.3.7 Gusset Plate-to-Frame Joint Design

4.3.7.1 Interface Forces

Two design methods for finding the interface forces were considered. According to the UFM, the brace force is recharacterized into vertical and horizontal components at the beam and column interface. The forces are computed using equilibrium equations as found in AISC [2001]. The equations are provided below [Equations (4.6–4.10)] and illustrated in Figure 4.7.

$$V_{uc} = \frac{\beta}{r} P_u \quad (4.6)$$

$$H_{uc} = \frac{e_c}{r} P_u \quad (4.7)$$

$$V_{ub} = \frac{e_b}{r} P_u \quad (4.8)$$

$$H_{ub} = \frac{\alpha}{r} P_u \quad (4.9)$$

$$r = \sqrt{(\alpha + e_c)^2 + (\beta + e_b)^2} \quad (4.10)$$

The second method, commonly referred to as the “KISS” method, involves recharacterizing the brace forces into a horizontal force at the beam and a vertical force at the column. The forces and moments found using this method are illustrated in Figure 4.7.

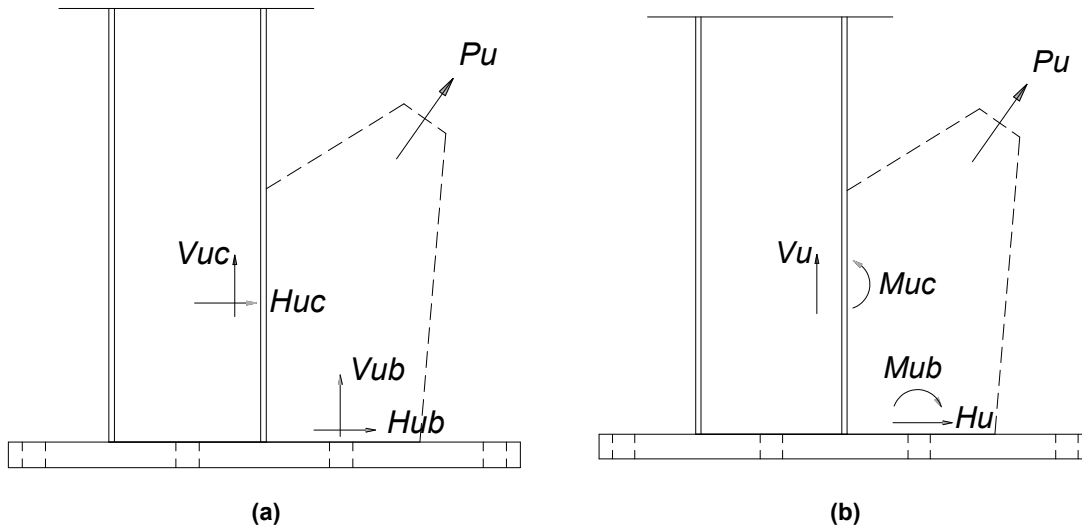


Figure 4.7 Recharacterized forces: (a) UFM method and (b) KISS method.

4.3.7.2 Gusset-to-Frame Weld Design

One method recommended in AISC [2001] is to size the welds using the vertical and horizontal interface forces in conjunction with AISC’s Table 8-5. First, resultant forces, P_{uc} and P_{ub} , are found using the two components of force and for the column forces are as follows [Equation (4.11)]:

$$P_u = \sqrt{(H_{uc})^2 + (V_{uc})^2} \quad (4.11)$$

The angle at which this resultant force acts is found using Equation (4.12):

$$\theta = \tan^{-1}\left(\frac{H_{uc}}{V_{uc}}\right) \quad (4.12)$$

The minimum weld size is then calculated using the provided equation in the table, which is:

$$D_{\min} = \frac{1.4P_u}{CC_1l} \quad (4.13)$$

where D_{\min} is the number of sixteenths-of-an-inch in the fillet weld size; l is the length of the joint; and C_1 is a tabulated coefficient. The 40% increase of the design force P_u is recommended in AISC [2001] Section 13. The increase of the force is to ensure adequate force redistribution in the weld group.

4.3.8 Beam-to-Column (Simple Shear)

4.3.8.1 Initial Design

The beam-to-column connection was designed as a simple shear connection, which is common design practice. The shear force used to design the connection was related to the plastic moment capacity of the beam. This is not specified by AISC, but is commonly done by local design firms. The shear force was found using Equation (4.14):

$$V = \frac{1.5M_p}{l_b} = \frac{1.5F_y Z_b}{l_b} \quad (4.14)$$

where the length l is the length between both shear connections. Then, using this shear force, the initial plate size and bolt size is found.

4.3.8.2 Bolt Strength

The strength of the bolts was checked for bolts subject to single shear. Then, using AISC [2001] Table 7-10 the bolt strength can be found for a single bolt. All bolts for this study were designed as A325 threads.

4.3.8.3 Bearing Strength

Bearing strength of the plate and beam web was checked next. For this check, deformation at the bolt hole was considered. In addition to this, the shear plate was assumed to be A572 steel.

4.3.8.4 Shear Strength of the Plate

For this check, the net area of the plate was taken as the gross area of the plate in the direction of shearing minus the area of the bolt holes. Next, the shear yielding strength of the plate was checked using Equation (4.15):

$$\phi R_n = \phi(0.6) \left(\frac{2}{3} \right) t_p l F_y \quad (4.15)$$

In this equation, the value ϕ is 0.75 according to AISC [2001]. The quantity two-thirds is the result of assuming a parabolic shear stress distribution as shown in Figure 4.8. Assuming this distribution, Equations (4.16) and (4.17) were used to express the stress. The final shear check of the plate was to check the block shear rupture strength, which was done in accordance with AISC [2001] Section J4.3.

$$\frac{3}{2} \tau_{\text{ave}} = 0.6 F_y \quad (4.16)$$

$$\tau_{\text{ave}} = 0.6 \left(\frac{2}{3} \right) F_y \quad (4.17)$$

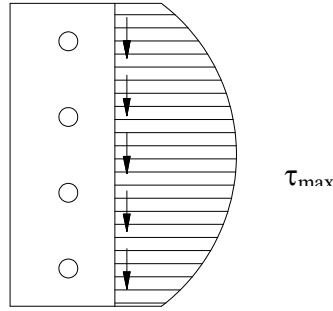


Figure 4.8 Shear tab plate shear distribution.

4.3.8.5 Plate Bending

The bending capacity of the plate was checked next. For this check, the moment capacity of the plate, based on the section modulus of the plate, was checked against the applied moment caused by the applied shear force at a distance, e , away from the column face. Therefore, the check was done according to Equations (4.18) and (4.19) as follows:

$$\phi R_n \geq V(e) \quad (4.18)$$

where

$$R_n = \phi \frac{t_p l^2}{6} F_y \quad (4.19)$$

In this equation, ϕ is 0.9, t_p is the thickness of the plate, and l is the height of the plate.

4.3.8.6 Shear Plate Welds

As a final check, the capacities of the fillet welds that connect the shear plate to the column face were checked.

4.4 CONSTRUCTION OF SPECIMENS

The construction of the specimens was done by a fabricator in the Reno–Tahoe area, YAJIMA USA, by a group of experienced steel construction workers. The frames were constructed in several steps as follows: (1) cut beams, column and brace to length; (2) complete weld preparations; (3) complete beam and column connections; (4) connect column stiffener plates; (5) cut gusset plates to appropriate dimensions; (6) weld gusset plates to frame; (7) weld the brace to gusset plates; and (8) weld the brace thickener plates.

As mentioned, each SCBF component was first cut to the needed size. Beams and columns were flame cut, and the cut surfaces were ground to length. The gusset plates were flame cut to size, and the edges were ground smooth using an angle grinder. The brace was cut to length using a band saw. In order to slot the brace, a hole was first drilled at the end of the slot; see Figure 4.9. Brace slots were then flame cut slightly oversized with a small taper in order to compensate for local shrinkage due to heat effects and to simplify placement of the brace.

Shear tabs were fillet welded to the column at each end. The beams were then fit up and clamped in place while bolt holes were drilled. Appendix B provides several photographs documenting the different fabrication procedures, with additional details on the shear tab welded to column flange, and how the stiffener plates are attached to the column web in order to increase the web capacity and prevent column flange bending; note, this column was the column attached to the mass rig). All the plates were laser cut from a big plate to ensure the most economic fabrication and the least amount of remaining steel. Figure 4.10 shows the three specimens after fabrication was completed. All welds were completed by an experienced welder certified in the FCAW process for all weld sizes in all positions in both groove and fillet welds. Once the beam and column connections were completed, the gusset plates were set in place and fillet welded to the frame elements. The braces were then fit into place, achieving the weld length specified in design from each gusset plate side. Thickener plates were then welded to the brace. Finally the specimens were shipped to the laboratory at the University of Nevada, Reno.

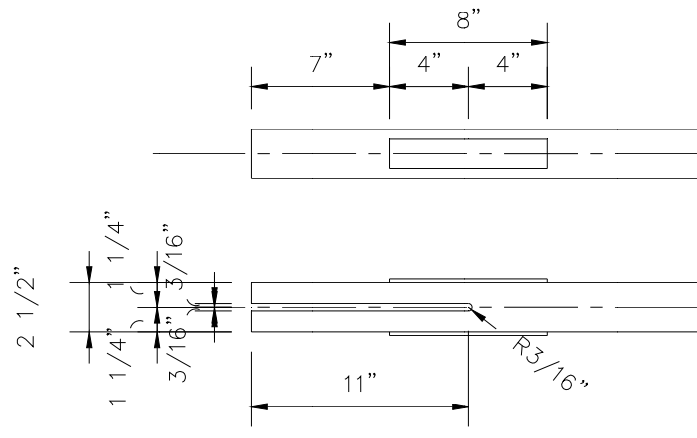


Figure 4.9 Brace slot details.



Figure 4.10 The three fully fabricated test specimens before shipping to UNR.

4.5 MATERIAL PROPERTIES

Each specimen contained both welded and bolted connections. All welded connections were made using 1/16 in. dual shield 7100 Ultra-E71T-9 Flux Cored ESAB weld wire. A325 3/4 in.-diameter bolts were used to connect framing elements to each other. All bolted connections were pre-tensioned connections (in accordance with RCSC Specifications), with threads excluded for the shear plane. The grade of steel used for the specimen elements is shown in Table 4.2. Theoretical values of F_y and F_u were used for design calculations according to the grade of steel. Theoretical values for member geometries were also used in calculations for the design of the specimens.

Table 4.2 Steel grades.

Element	Steel grade
Beams	A992
Columns	A992
Brace	A500-B
Plates	A572

4.6 TEST SETUP

The three SCBFs were tested on one of the biaxial shake tables at the Earthquake Engineering Laboratory at UNR. Figure 4.11 shows schematic details of the complete shake table test setup, and Figures 4.12 and 4.13 show the actual setup. In order to represent the inertial mass, each specimen was attached laterally with the mass rig system. This inertial mass system was designed by Laplace et al. [1999]. The mass rig was connected to the column flange using a rigid link to apply the lateral force to the specimen. A special link was designed and fabricated to connect the mass rig to the column flange. Four threaded high-strength rods were used to connect the special link with the mass rig. The total inertial mass was 60 kips, which was represented by two concrete blocks—weighing approximately 20 kips each—were added to the mass rig (which weighs about 20 kips).

An important aspect of the test setup was the out-of-plane restraining system. All the tested frames had fixed-base connections in two directions, but additional safety frames were added to prevent any out-of-plane movement or vibrations. The out-of-plane restraints were developed to simulate the typical out-of-plane restraints provided by additional framing components but still provide a smooth and almost friction-free resistance to in-plane movement of the frames during the tests. The restraining system consisted of two columns, each was aligned with the main frame column, that were in turn connected to the main frame column with two pipe sections that connected the flanges at two different levels. In order to allow the translation in the excitation direction and prevent the out-of-plane translation, a special joint was added. The details of the restraining system are illustrated in Figure 4.14. This system was chosen, because it is economical and allowed for unobstructed in-plane translation of the frame. See Appendix C for several photographs of the different setup stages and close-ups of major instrumentation.

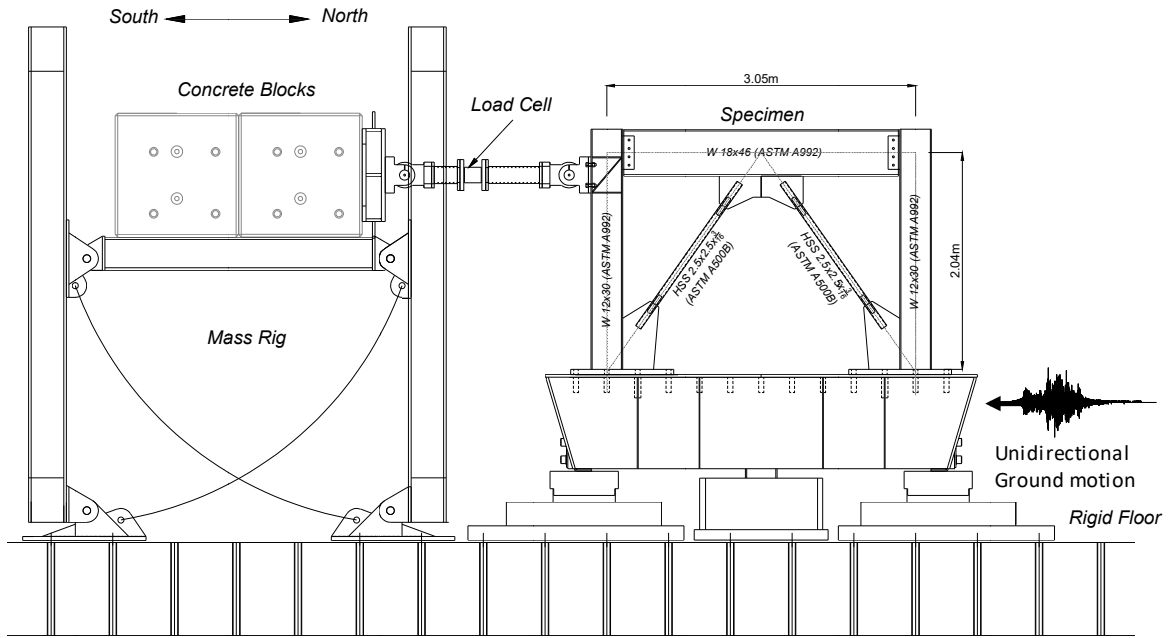


Figure 4.11 Schematic diagram showing the details of the shake table test setup.

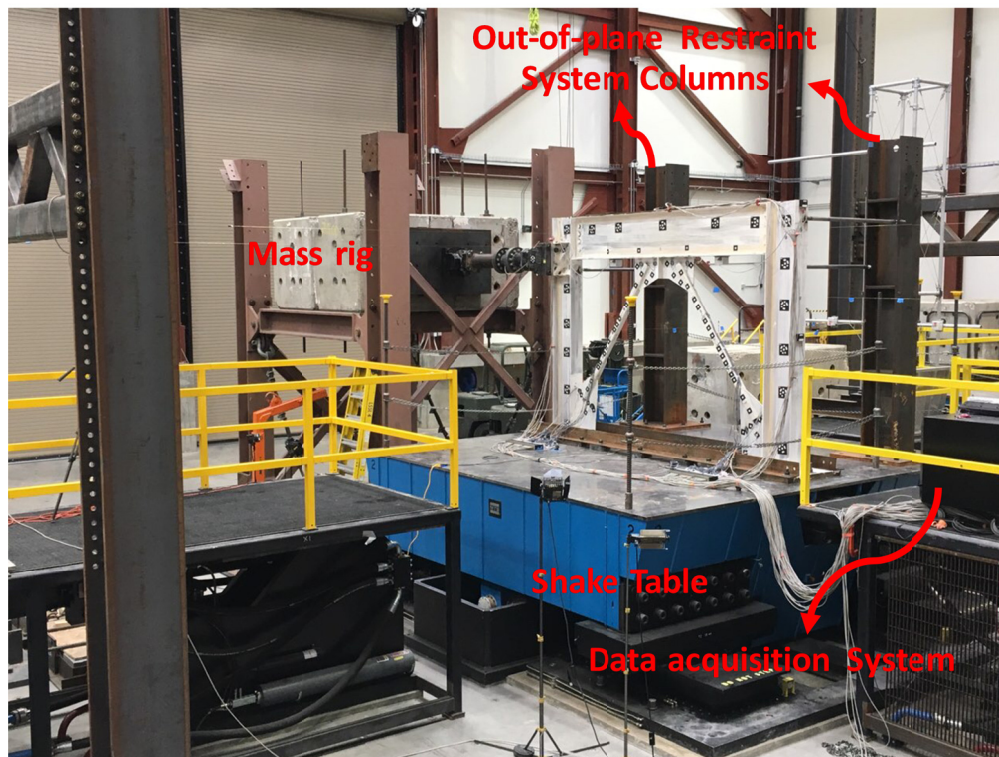


Figure 4.12 General layout and components of shake table test setup.

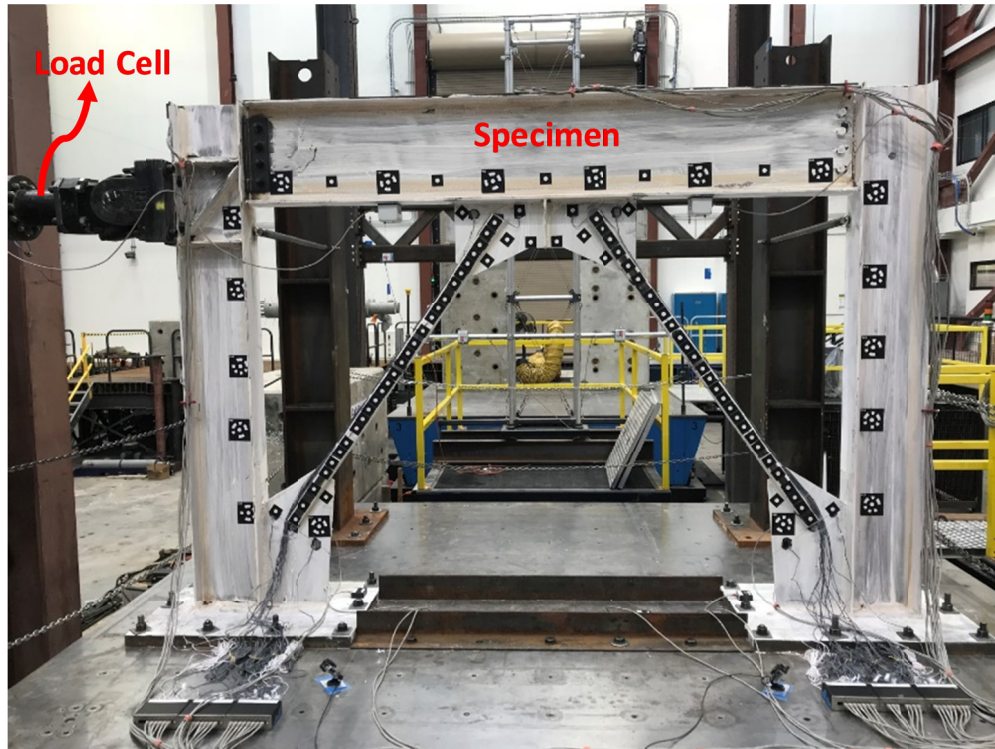
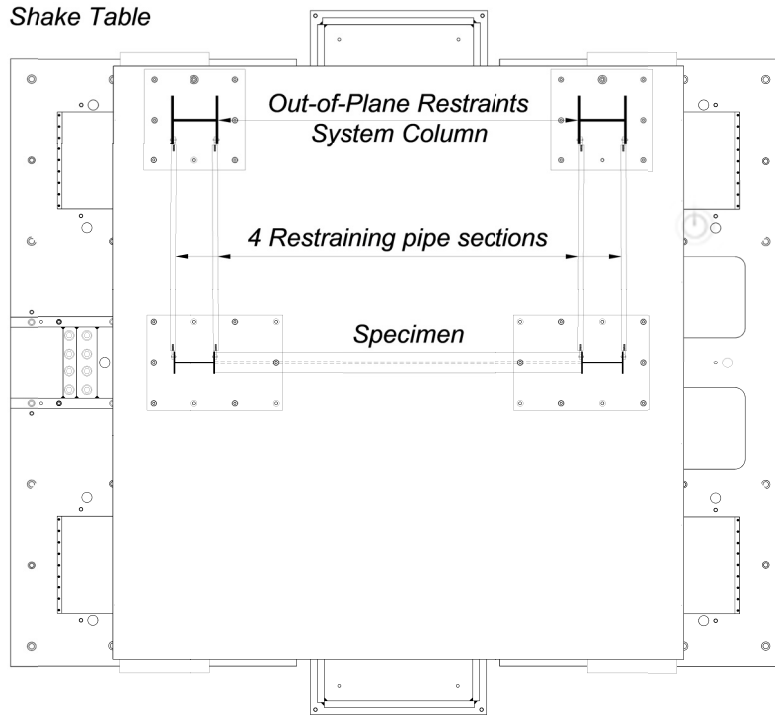
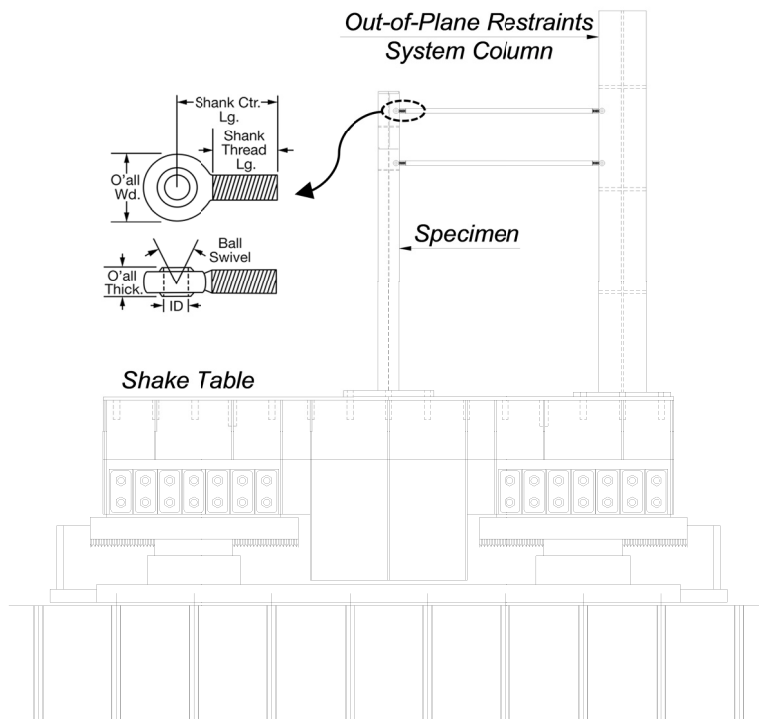


Figure 4.13 Elevation of actual test setup.

Whitewash was applied to the HSS braces and gusset plates in areas where yielding was expected to help with the visual observations. The whitewash consisted of a mixture of approximately 2.5 parts water to 2 parts Beadex Silverset 40. Once dry, this mixture bonds to the mill scale of the steel, and yielding of the steel can be emphasized by flaking of the whitewash. The whitewash was proven to be less effective on the brace than on the other elements of SCBFs [Johnson 2005]. This is attributed to the method in which the brace was formed, namely, that it is hot rolled into a flat plate and then cold-formed into the hollow tube section. This process limits the amount of “mill scale” present on the surface of the brace. This type of surface does not allow the whitewash mixture to bond as well to the surface of the steel. As a result, the whitewash flakes off in large chunks rather than showing areas of localized yielding; however, the whitewash did provide some indication that the brace underwent inelastic behavior.



PLAN VIEW



SIDE VIEW

Figure 4.14 Schematic diagram showing the details of out-of-plane restraint system.

4.7 INSTRUMENTATION

Multiple measurement techniques were used for each specimen during the tests. The specimens were instrumented to measure forces, displacements, strains, and accelerations. In addition, high-definition video cameras were used to capture damage propagation. A summary of the instrumentation and layout is presented next.

4.7.1 Load, Displacement, and Acceleration Measurement

A load cell was inserted within the lateral rigid link connecting the specimen with the mass rig and used to measure total force applied to the specimen during testing. Measuring the total force applied to the specimen was important and used for capacity estimation. External lateral displacement of the frame was measured using one string potentiometer connected to the top of the frame at the north column. Each brace had two string potentiometers attached mid-span to measure both in-plane and out-of-plane displacements, and buckling during testing. In addition, a string potentiometer was attached along each brace to measure the amount of elongation occurring due to buckling. To capture the deformation of the bottom gusset plates, three linear variable displacement transducers (LVDTs) were attached to the gusset plates. Figure 4.15 shows the orientation and layout of all of the string potentiometers and LVDTs.

Eight accelerometers were used to measure the accelerations for each specimen and distributed as follows: two were installed on the column top, two were installed on the mid-height of the column, one was mounted on the beam mid-span, two were mounted on the two base plates, and one was mounted on the table; see Figure 4.15. In addition, all shake table actuators provide force, displacement, and acceleration feedback, which were used to compare measurements obtained from the other instrumentation used in all tests.

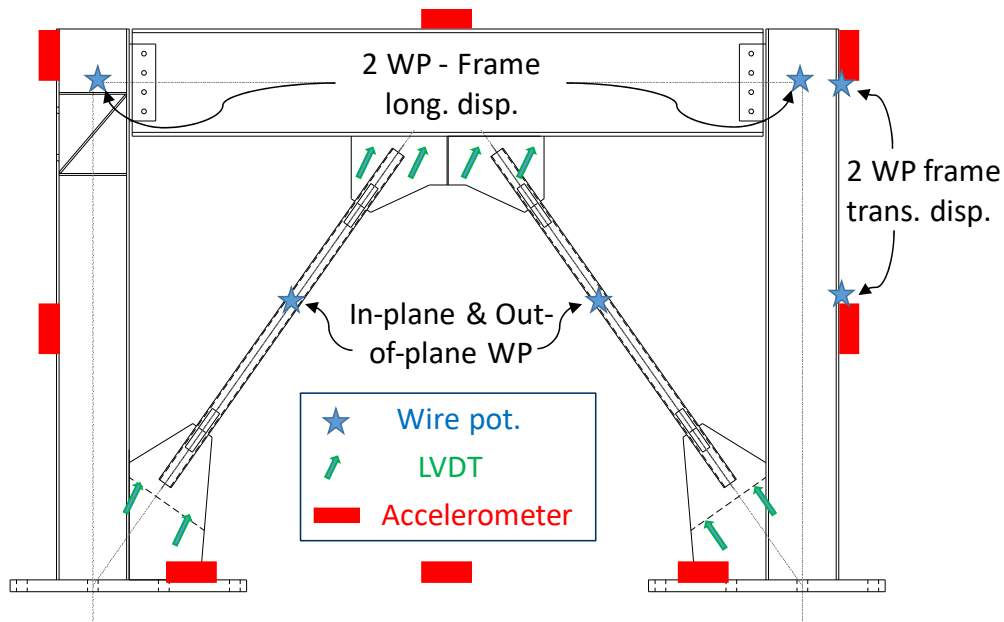


Figure 4.15 String Pots, LVDTs layout, and location of accelerometers..

4.7.2 Strain Measurement

Several strain gages were used for each specimen at various locations. All strain gages used in this study were manufactured by Tokyo Sokki Kenkyujo Co. Ltd. Strain was measured only in the braces and gusset plates, using YEFLA-5 gauges. All gages had a nominal gauge factor of 2.14 with a 6-mm gauge length. Strain gages with high elongation were used in the HSS brace elements. Several rosette strain gages were also used in the gusset plates to measure strains in two directions. Figure 4.16 shows the layout of the different strain gages for each specimen.

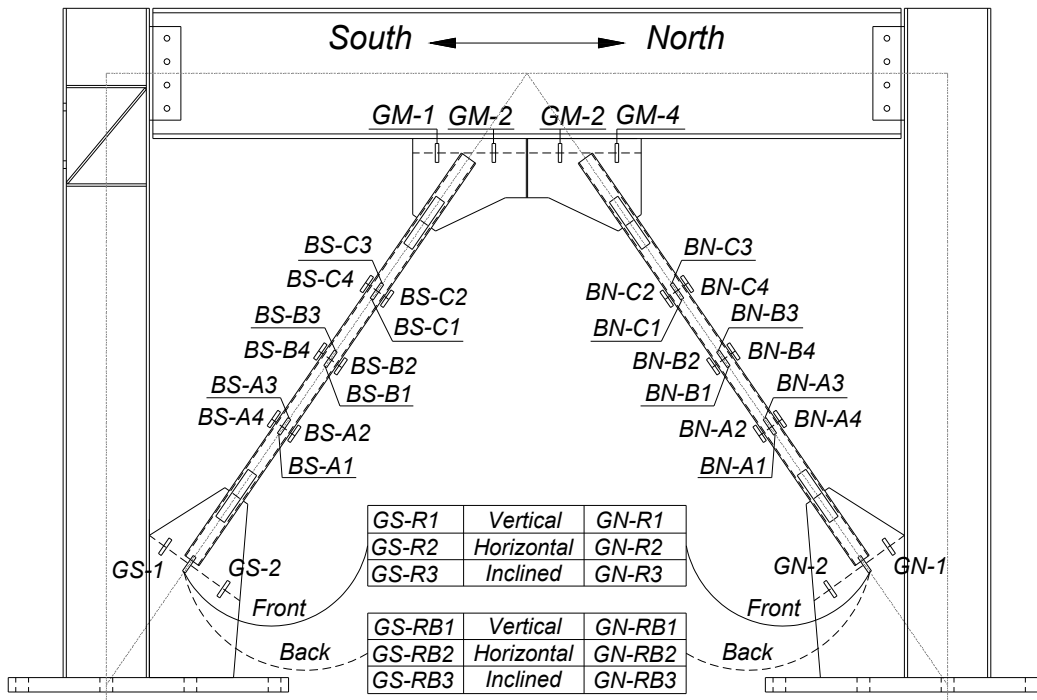


Figure 4.16 Strain gages locations and distribution for each test specimen.

4.7.3 Cameras

During the tests, cameras were used to capture damage of the specimens. Two high-definition cameras were installed on the east and west side of the specimens, and go-pro cameras were used near the bottom gusset plates to capture any cracking or yielding that may occur. Note: target-tracking digital image correlation (DIC) was applied for the tested SCBFs, which explains the black and white targets previously shown in Figures 4.12 and 4.13. The DIC work was part of another study that aimed at verifying DIC techniques for dynamic response monitoring and structural system identification [Ngeljaratan and Moustafa 2017; 2018]. Thus, results from DIC are not part of the scope of this study and are not shown in this report. However, the distribution of DIC targets and coordinate identification for one of the SCBFs is shown in Figure 4.17 as an example for clarification; more details are provided in Ngeljaratan and Moustafa [2017; 2018].

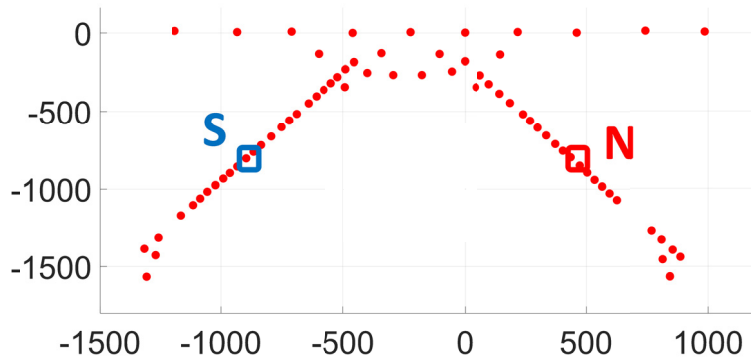
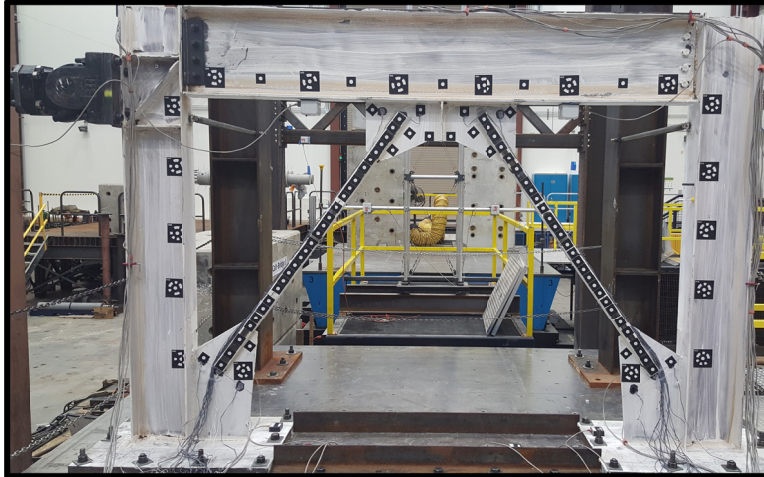


Figure 4.17 DIC targets attached to one of the tested SCBFs and the corresponding 2D coordinates (mm) for the spatial target locations.

4.8 GROUND-MOTION SELECTION

The experimental program involved three identical specimens tested under different ground motions. The overall goal of this research was to study the effect of ground-motion duration on the seismic response of SCBFs and, specifically, the low-cycle fatigue capacity of the braces; therefore, one short crustal and two long-duration subduction ground motions were selected. The intensity (scale) of each ground motion was increased until both braces ruptured. No particular number of runs was specified for each specimen as the criteria was to start from 100% of the ground motion and incrementally increase the scale until failure occurred; the final number of runs and testing scales are discussed in Chapter 5. To directly determine whether earthquake duration affects the seismic capacity of the tested specimens, the short-duration ground motion was spectrally matched to one of the two long-duration ground motions. This was to test the frames under approximately similar force and acceleration demands, and leave it for the low-cycle fatigue accumulated damage to determine the force and displacement capacity of the frames. Note: the specimens were designed according to downtown Seattle response spectrum; however, rupture of the SCBF braces was dictated mainly by the low-cycle fatigue damage accumulation rather than force demands, which is the typical design philosophy for SCBFs. The third specimen was tested under another long-duration ground motion to provide more data on

seismic performance of SCBFs under long-duration subduction earthquakes. Both long-duration ground motions were adopted from the 2011 Tohoku, Japan, earthquake.

For the two spectrally-matched ground motions, an original record from Tohoku was used for the long-duration case and a short-duration record from the PEER NGA West 2 database [PEER 2011] was selected and matched in two steps. First, the online PEER NGA matching tool was used to get a close matching record to the selected long-duration record. Then, SeismoMatch [2016] was used to alter the frequency content of the short-duration record such that the response spectrum would closely match the one for the long-duration record such that the response spectrum would closely match the one for the long-duration record within the period ranges of interest: 0.05 to 0.6 sec, which well encompassed the specimen’s fundamental period. The actual records and characteristics are listed in Table 4.3. Figure 4.18 shows the acceleration histories of the short- and long-duration ground motions used for testing after time scaling for similitude; see Table 4.1. Figure 4.19 shows the response spectra of the original and matched short-duration record as compared to that of the long-duration record.

For the third test, a second long-duration Tohoku ground motion was used, but the record was selected such that the velocity and/or displacement pulses—if they existed—were shifted from the peak acceleration or pulse. There was not a specific objective for such a selection other than to demonstrate the effects of another long-duration record with different characteristics, and to see whether the shifted displacement pulse affected the low-cycle fatigue damage accumulation. Figure 4.20 shows the acceleration, velocity, and displacement time histories of the third ground motion where the anticipated shift in the pulses or simply peak values occurred. A final note is that the two long-duration records were handpicked using several trials and extensive pretest analysis to follow these simple criteria: (1) to determine the feasibility of adopting a reasonably scaled short-duration ground motion as a means of comparison for this study, and (2) to maintain the expected force and acceleration demands all the way through brace rupture within the allowable shake table and actuators limits, i.e., 160 kips and 4.0g.

Table 4.3 Characteristics of the selected ground motions for all three test specimens.

Test ID	Earthquake event	Station name	PGA (g)	Significant duration (sec), scaled	Notes
S1	Japan, Tohoku 2011	YMTH04 NS2	0.57	70	Spectrally matched
S2	USA, San Fernando 1971	Santa Anita Dam	0.75	7.8	
S3	Japan, Tohoku2011	IWT005 NS	0.48	64	Shifted pulses

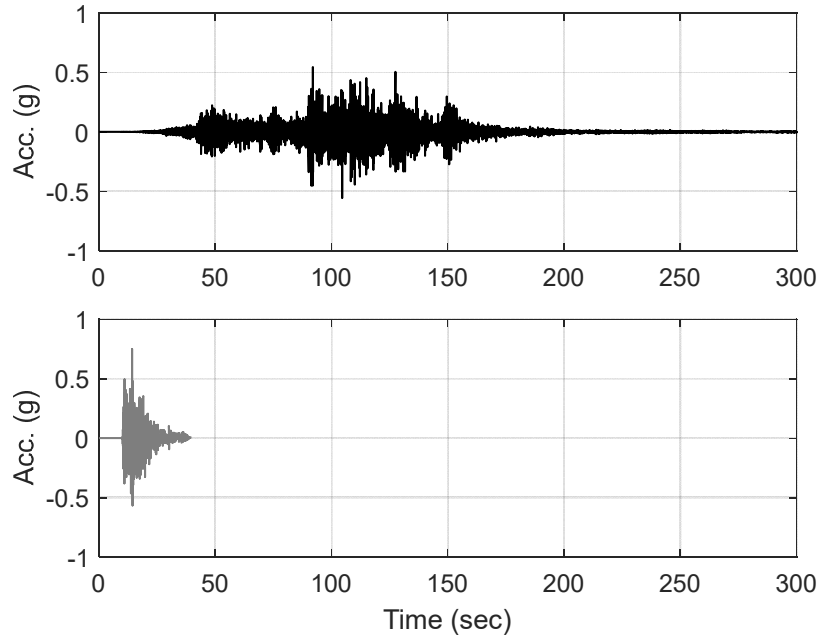


Figure 4.18 Acceleration time histories of the long- and modified short-duration records.

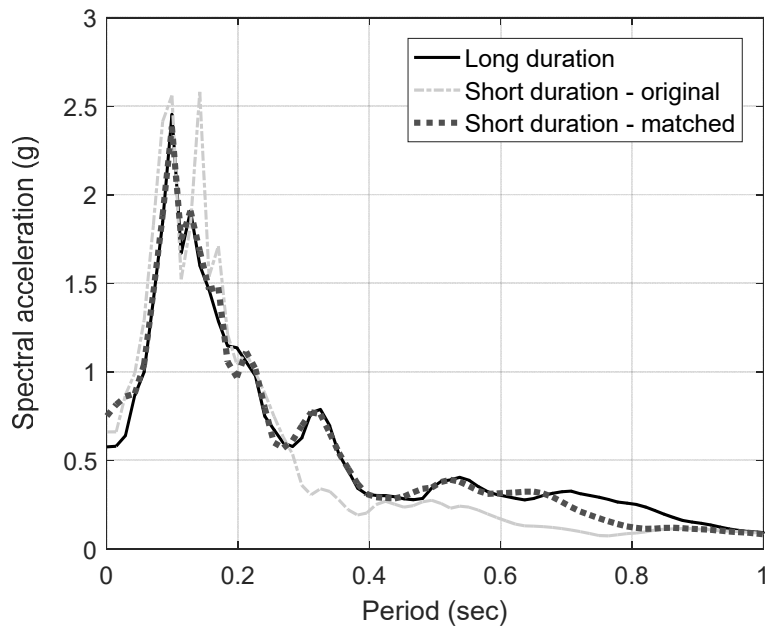


Figure 4.19 Acceleration response spectra of the original and matched short-duration record versus the long-duration record.

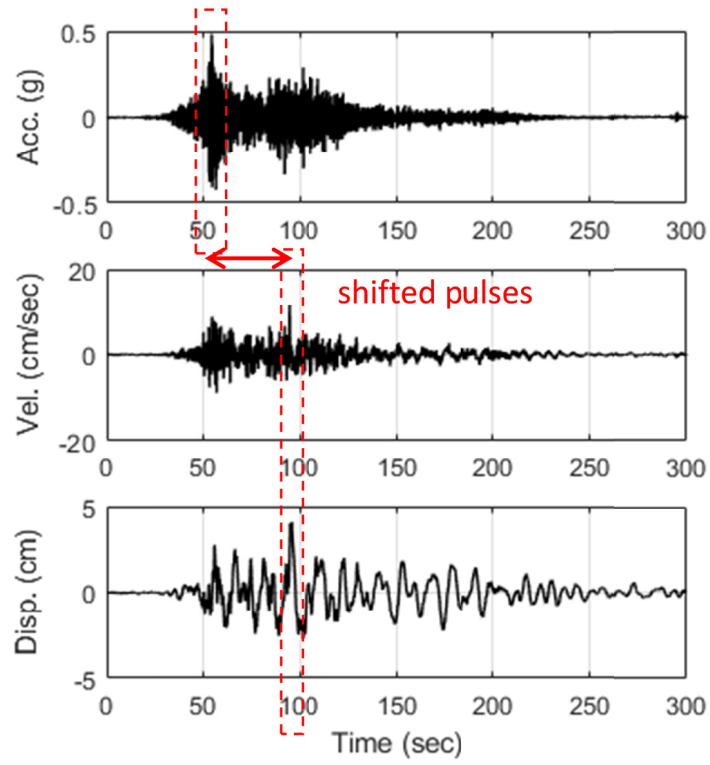


Figure 4.20 Time histories of the third specimen ground motion (velocity and displacement pulses shifted from peak acceleration).

5 Experimental Results and Discussion

This chapter summarizes the results of the shake table tests of the three specimens. The progression of testing and the damage sequence is documented. The global behavior of Specimens S1, S2, and S3, in terms of lateral forces, displacements, stiffness, and changes in period is presented first. Then, the localized behavior of the braces in terms of strains, and damage accumulation is discussed.

5.1 GLOBAL RESPONSE

5.1.1 Test Progression and Mode of Failure

The exact number of runs and scales until brace rupture for each specimen tested was difficult to determine before the tests. In addition, every ground-motion test that occurred after the onset of buckling would directly contribute to the fatigue life and, thus, needed to be properly assessed. Optimally, it was desired to achieve brace buckling around the original 100% ground motion level so that the following larger scale runs would have meaningful contribution to the fatigue life, and, in turn, rupture could be achieved within few number of runs. One challenge associated with the fixed base of the columns of the frames was the distribution of the lateral dynamic forces between the columns and braces. Thus, it was not easy to determine what percentage of the force should be allocated to the braces to calculate buckling loads for estimating the best ground-motion scale. Accordingly, a small scale of the long-duration ground motion was conducted first. Using the strain gages attached to each brace at three different sections, the force in the braces was estimated and related to the total lateral force measured in the rigid link. Next, the equivalent total link force was back calculated and related to the original ground motion to find the intensity scale. This procedure was adopted mainly for the first long-duration ground motion, and similar scale factors were used for other tests for direct comparison purposes.

For the purpose of the overall discussion of the test results, the first run reported herein is the first run to cause inelastic buckling. It was assumed that the contribution from the few small-scale trials were conducted primarily to properly tune the shake table and adjust the scale;

therefore, any contribution towards the fatigue life of the braces was neglected. This assumption is justified in that low-cycle fatigue is usually sensitive to small amount of cycles in the inelastic range, unlike the high-cycle fatigue that depends on large number of cycles in the elastic range. The testing procedure was successfully achieved and inelastic buckling was observed at the intended intensity levels that were adjusted as part of the ground-motion selection process. The inelastic buckling is simply referred to the residual buckling or the “end state” after the completion of a given earthquake run. Figure 5.1 shows the inelastic brace buckling and the complete brace rupture for one of the specimens.



Figure 5.1 Typical test progression: (a) inelastic buckling, and (b) complete brace rupture

5.1.2 Force-Displacement Response

The first aspect of the seismic response reported herein is the number of runs and ground-motion amplification scale required to reach failure. Regardless of the scale values, this was a comparative study, so whatever scale factors were needed to fail the SCBF under the first long-duration earthquake were applied in same order when subjecting the specimens to the short-duration one. The first specimen tested under the first long-duration earthquake, designated as Specimen S1 throughout the rest of this discussion, required seven incremental runs until the complete brace rupture was reached at 200% scale of the original ground motion. For S1, the north brace ruptured at 190% scale, and the south brace ruptured at 200% scale. Note: the lateral force capacity of the tested frames was reached early in the first few runs of testing when brace buckling took place. Increasing the ground-motion scale after that point did not cause an increase in the force demands but induced larger displacements; testing continued until the ultimate displacement capacity was captured. Figure 5.2 shows the force history for Specimen S1 throughout the seven ground-motion runs.

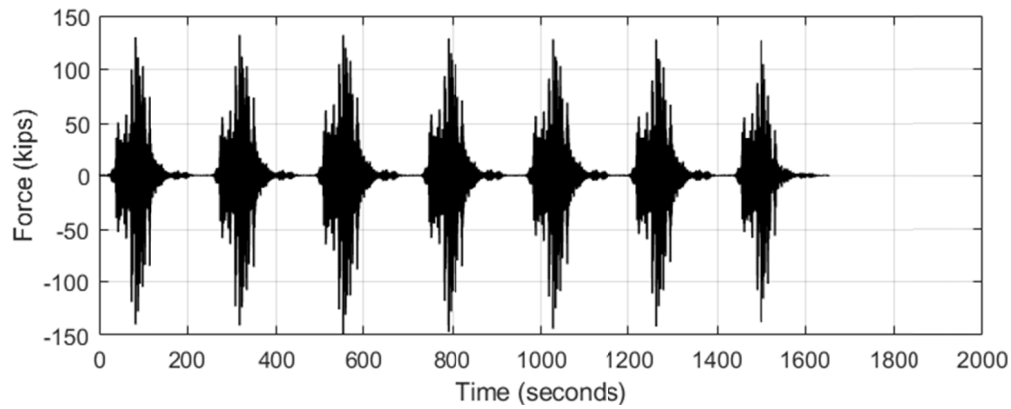


Figure 5.2 Specimen 1 force history.

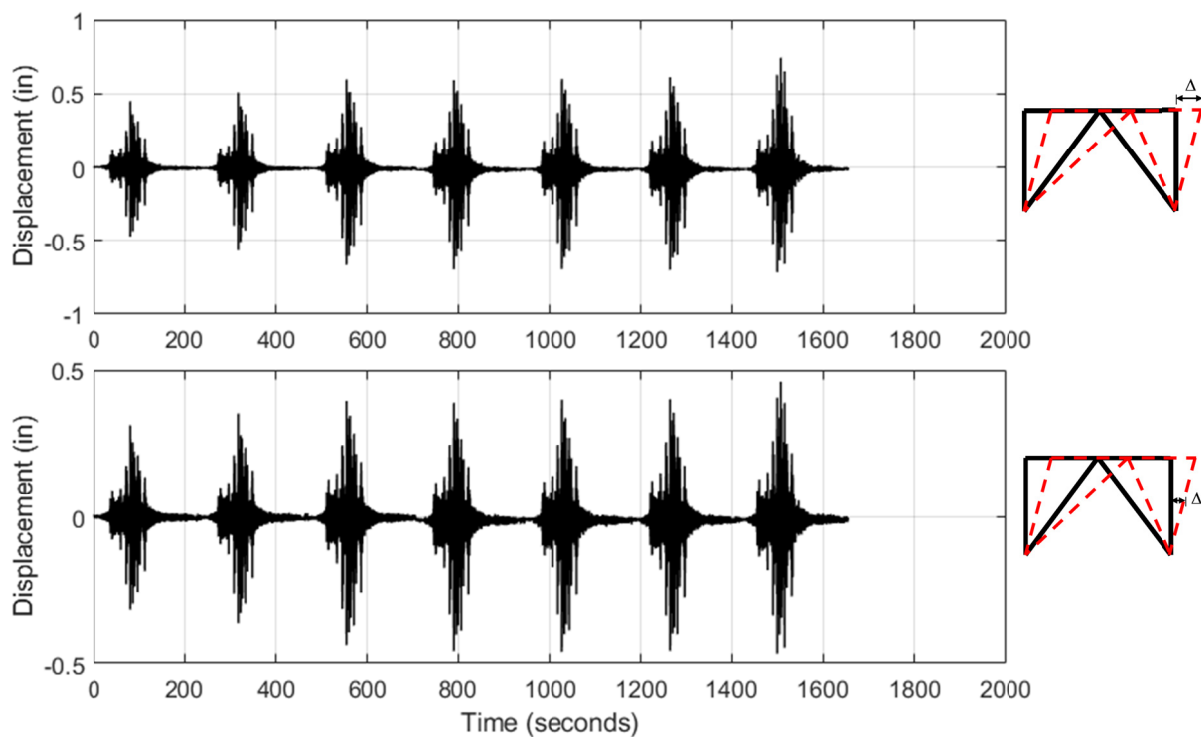


Figure 5.3 Specimen 1 displacement histories at top and mid-height of frame.

Figure 5.2 demonstrates that the lateral force capacity was capped and all scaling of the ground motions scaling was reflected in terms of larger lateral displacements. Figure 5.3 shows the lateral displacements at two points; top frame and mid-column displacements, respectively.

In comparing S1 and S2, the response to the ground-motion scaling was similar, and only the equivalent runs and sequence that caused failure was important. In other words, the problem at hand is a low-cycle fatigue problem and, in turn, the same ground-motion scale that caused buckling could have been applied as many times as needed until brace rupture. For Specimen S2 tested under the matched short-duration ground motion, reaching an equivalent 200% scale as the long-duration ground motion did not accumulate enough damage and no rupture was observed. Testing of S2 continued until brace rupture did not occur until the ground motion was scaled up

to 225%. Figure 5.4 shows the force histories for Specimen S2 for all the ground motions back-to-back. As the frames were identical, the frames lateral capacity was the same. Once the ground motion demand hit that frame capacity, the forces were capped. Figure 5.5 shows the displacements for Specimen S2 at two points along the frame height.

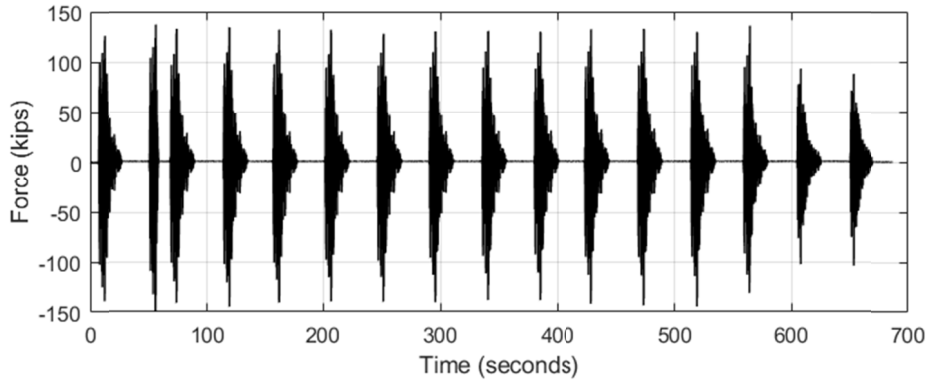


Figure 5.4 Specimen 2 force history.

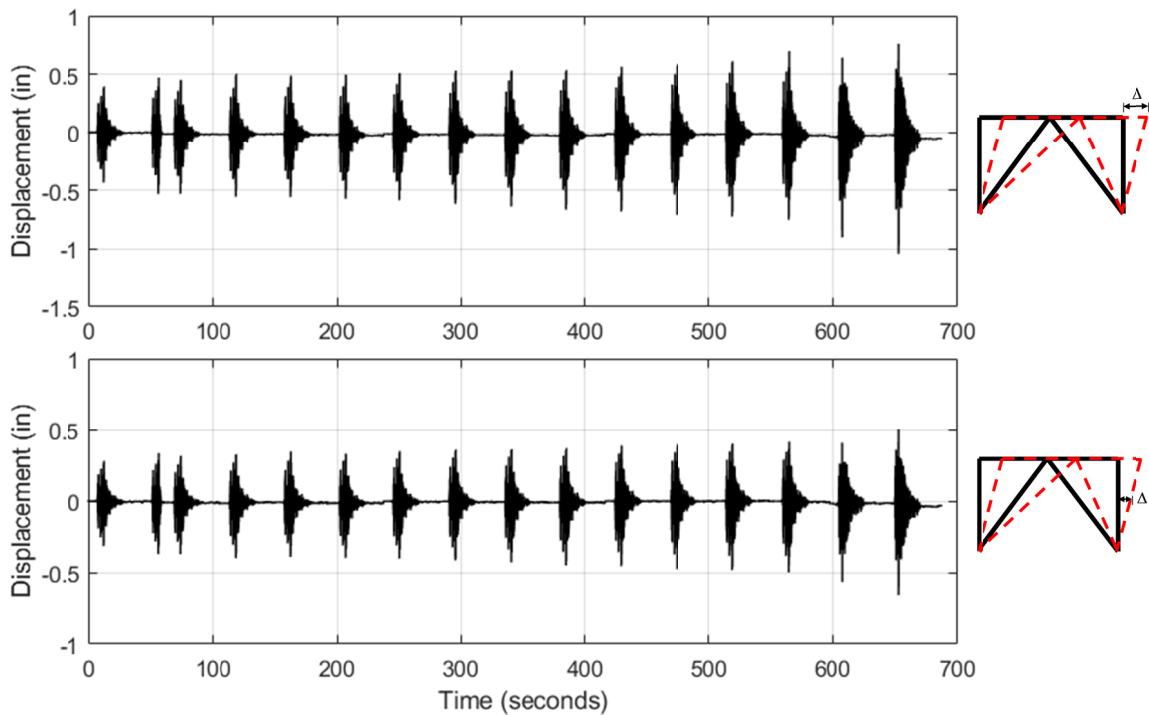


Figure 5.5 Specimen 2 displacement histories at top and mid-height of frame.

The overall force versus the drift ratio, i.e., the hysteretic relationship, for S1 and S2 along with the displacement history at the SCBF top are shown in Figure 5.6. The backbone curves for both specimens are shown in Figure 5.7, with the sequence of brace buckling and rupture identified. Figures 5.6 and 5.7 demonstrate that failure in case of the long-duration

earthquake occurred at lower drift ratio compared to the short-duration ground motion, which is about 0.8% versus 1.25% for long and short-duration cases, respectively, i.e., that about 40% reduction in the intended displacement capacity was observed due to the effect of the longer duration earthquake. This is also the first time such an observation was found experimentally for SCBFs tested under short- and long-duration earthquakes.

Specimen S3 was tested under the second long-duration record, with shifted velocity and acceleration peaks/pulses. Figure 5.8 shows the force history, and Figure 5.9 shows the frame lateral displacements as previously shown for S1 and S2. The force versus drift ratio for the third specimen is shown in Figure 5.10. The figure shows that similar to S1, a lower displacement capacity was observed at 1% drift ratio. This is slightly higher than the 0.85% capacity for S1, but it is still much lower than the 1.25% observed for S2, again confirming that the reduction in displacement capacity was due to the duration effect.

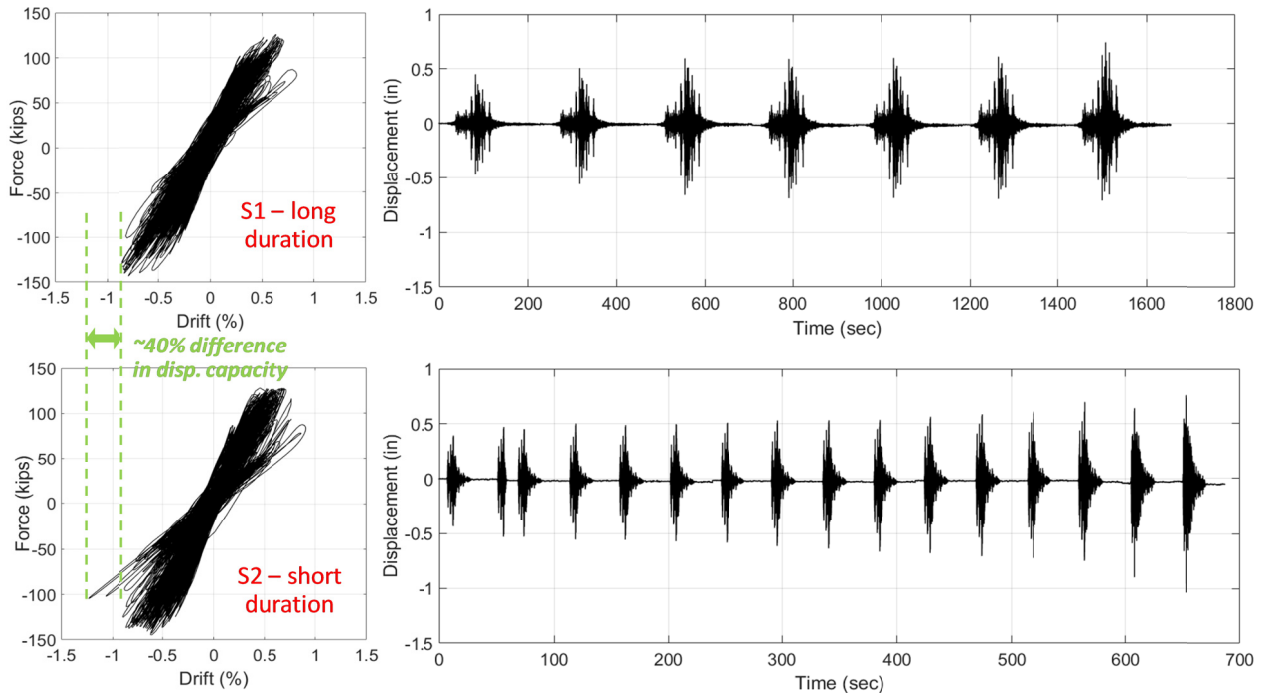


Figure 5.6 Force versus drift ratio for S1 and S2 (left), and top displacement history for both tests (right).

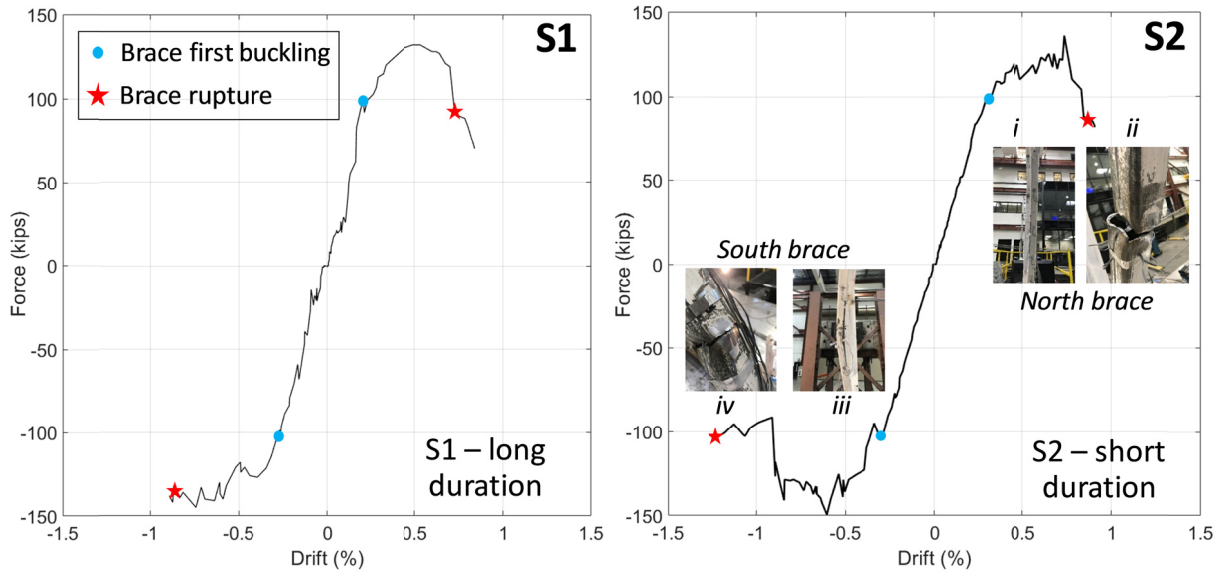


Figure 5.7 The backbone curves for S1 and S2 with both braces buckling and rupture identified.

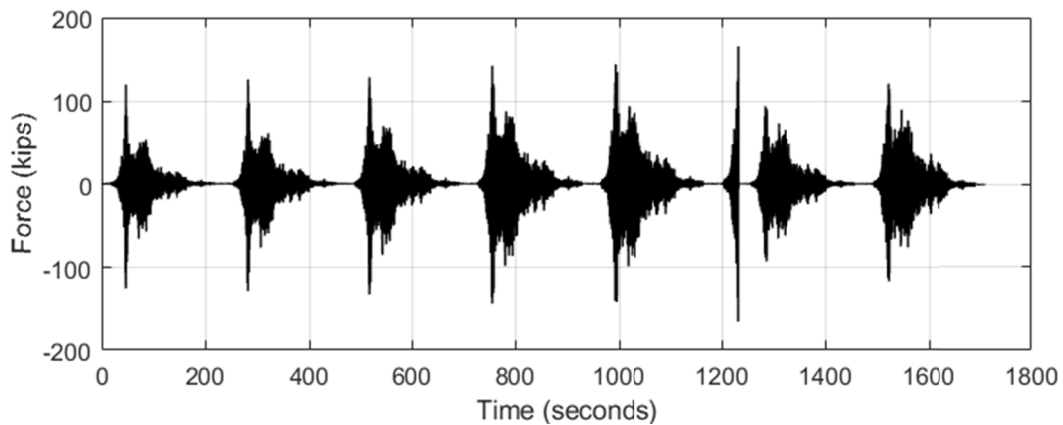


Figure 5.8 Specimen 3 force history.

During the tests of S3, after the force demand was capped when the frame reached its ultimate force capacity, one of the larger scale runs caused a sudden increase in the shake table actuator force, and the table interlocked—see Figure 5.10—which caused a large displacement cycle. As discussed later, this displacement was accounted for as part of the fatigue-life estimations or any model calibration. Thus, a relatively smaller test scale was applied to ensure the shake table actuator force was back within its proper limits, and the shake table was retuned in the displacement values of the 7th run that followed the interlock; see Figure 5.10. Note: that for S3, the final force demand recorded when the failure occurred was only about half of the frame force capacity.

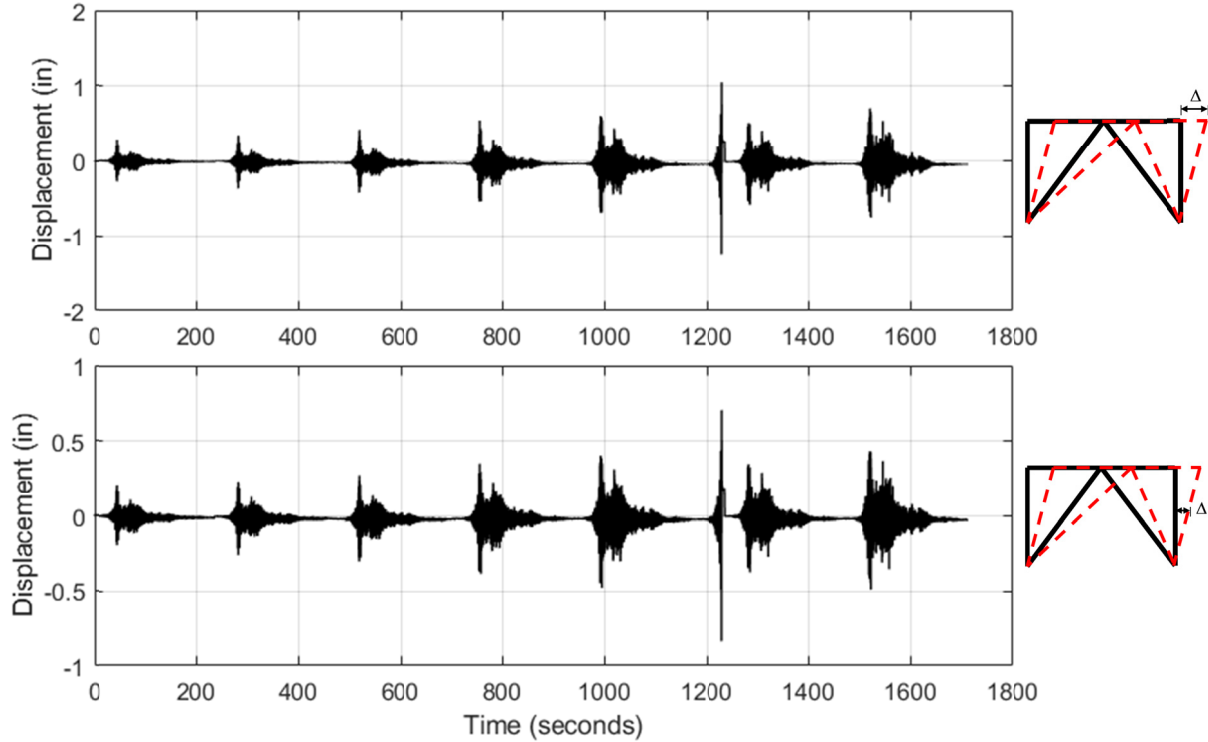


Figure 5.9 Specimen 3 displacement histories at top and mid-height of frame.

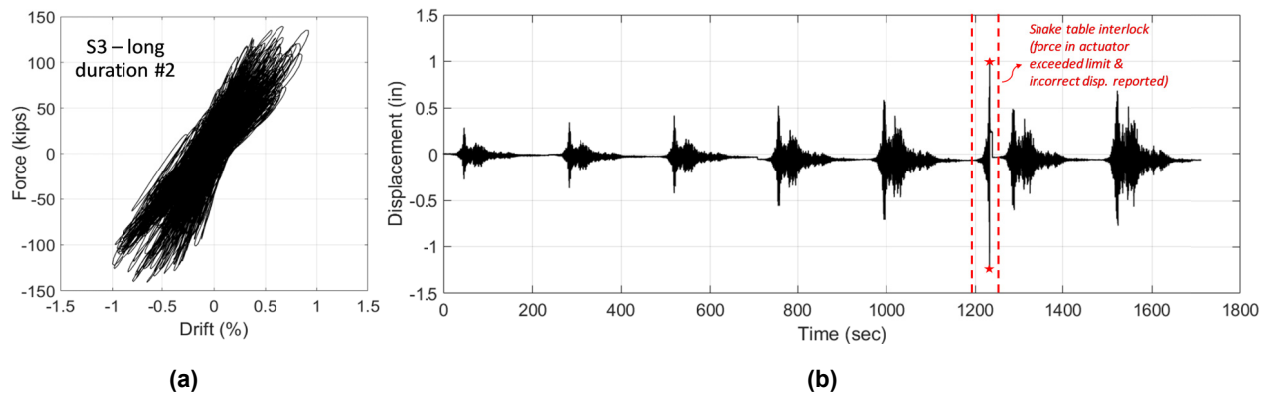


Figure 5.10 (a) Force versus drift ratio (hysteretic behavior) for S3; and (b) top displacement history.

5.1.3 Acceleration Response

During the tests, the acceleration at different locations were measured to better understand the specimen–shake table dynamics and interaction, and how the input motion changed or amplified along the specimen height. Figures 5.11 through 5.13 show the accelerations at the base, mid-height, and top of the tested frames S1, S2, and S3, respectively. The same frame dynamics were noted for all three frames. The input motion was slightly amplified at the frame top but largely suppressed at the mid-height, which was expected and has been evident in numerous tests.

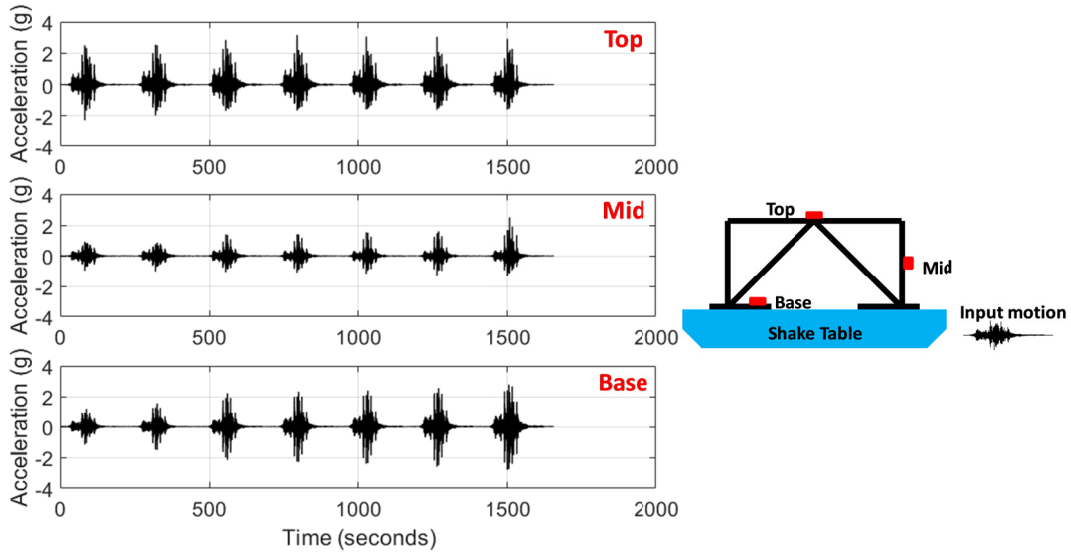


Figure 5.11 Specimen 1 acceleration histories at different locations and heights.

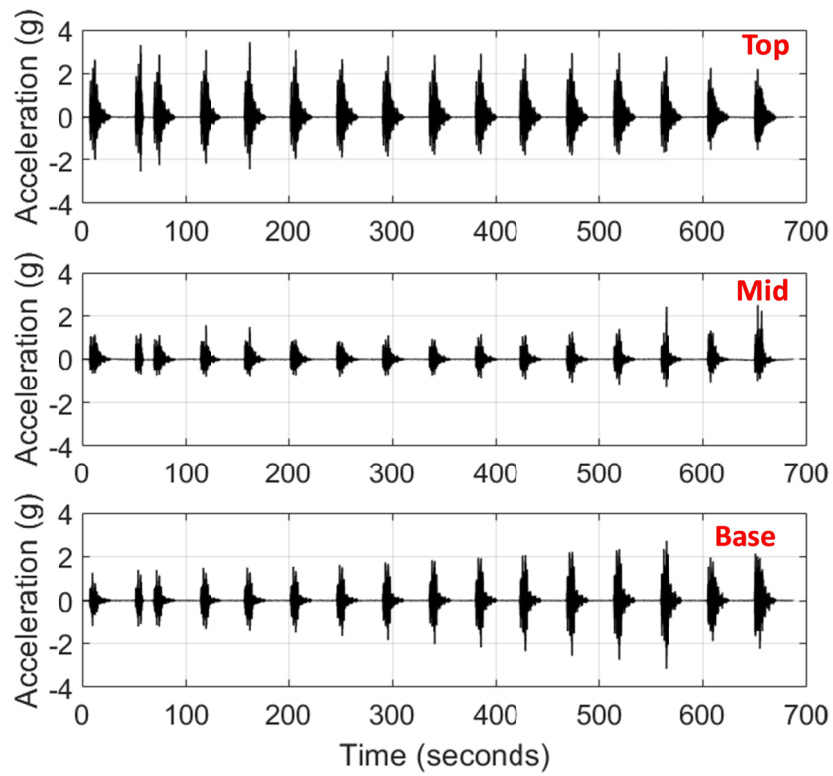


Figure 5.12 Specimen 2 acceleration histories at different locations and heights.

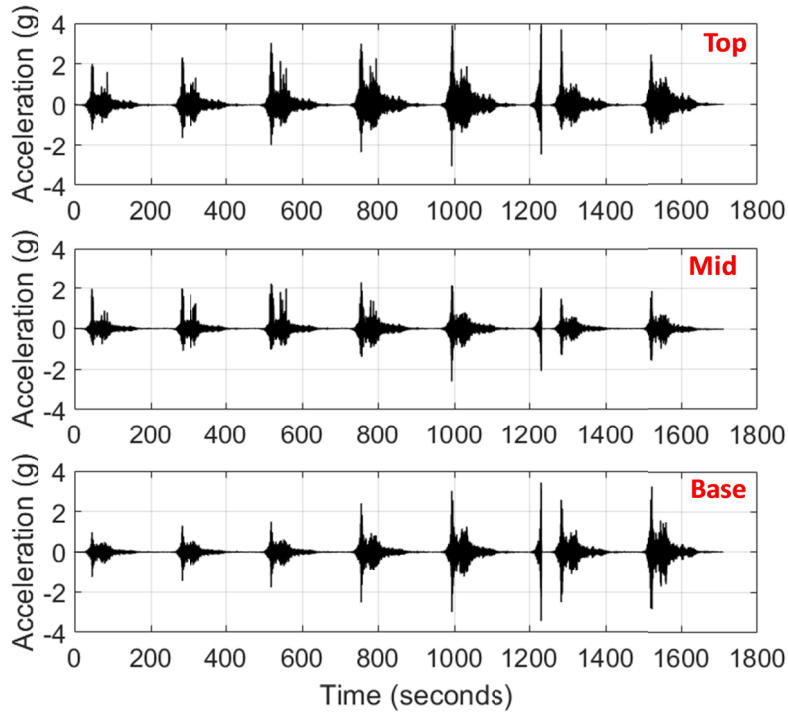


Figure 5.13 Specimen 3 acceleration histories at different locations and heights.

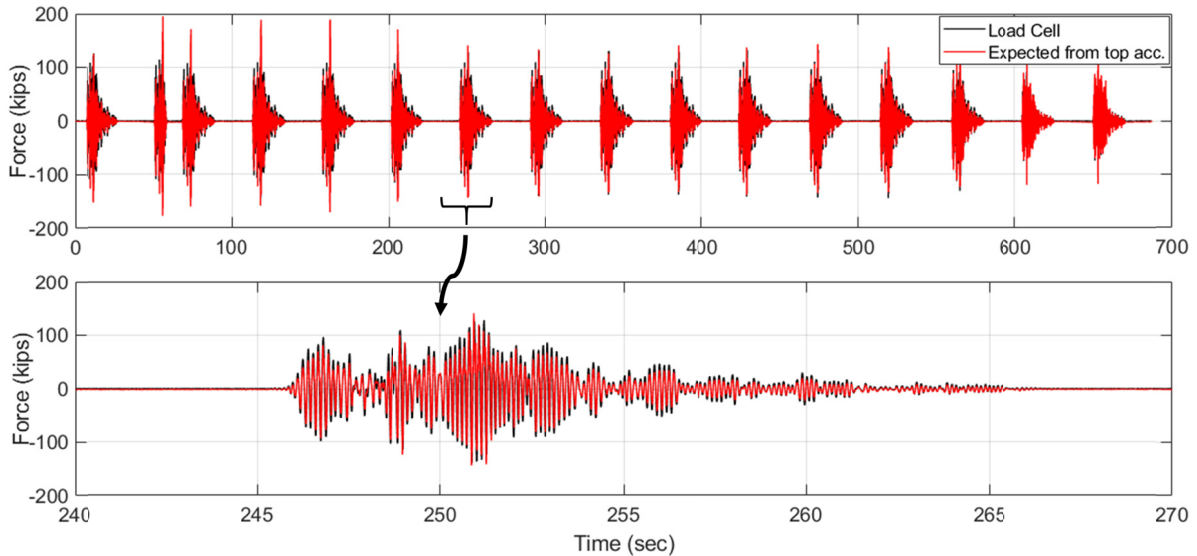


Figure 5.14 Measured force versus estimated (expected) force as deduced from the measured top acceleration for Specimen S2.

To further check the measured forces and accelerations, a comparison between the force directly recorded in the load cell and an estimate for the force based on the top acceleration and inertia mass was obtained; see Figure 5.14. The comparison shows high consistency between the measured acceleration when related to the mass and the force transferred to the frame, and provides confidence in the recorded acceleration values for interpreting test results or analytical model calibrations.

5.1.4 Stiffness Degradation/Period Elongation

As the tests progressed and the braces of a given specimen buckled, the overall frame's stiffness degradation was observed, with a changing contribution from a buckled brace depending on whether it was in tension or compression. Typically, SCBFs suffer major stiffness loss with the first brace(s) buckling, then after complete brace rupture, the frame loses most of the lateral stiffness, given that all other components, e.g., columns, remain elastic.

Stiffness degradation can be quantified in two ways. The first method is indirect by capturing the change in the specimens' fundamental period as testing progress. A white noise is applied after each seismic test and the recorded accelerations are used to calculate the frequency response function (FRF). The FRF is a frequency-based measurement function used to identify the resonant frequencies of a physical structure by relating an output acceleration to the input; FRF is sometimes referred to "transfer function." Figure 5.15 shows the FRF for the three specimens from three different white noise tests: an initial test before any seismic runs (Run #1), a test after both braces buckled, and a test after rupture was observed. The reduction in the detected fundamental frequency, illustrated in Figure 5.15, means period elongation and reflects stiffness reduction or degradation. The figure shows a similarity in the trend and values for the three specimens.

Another way of presenting the stiffness degradation is to estimate the stiffness from the slope of best fitted linear regression from each seismic test, which is then plotted against the corresponding measured period; see Figure 5.16. The figure shows the stiffness degradation for all three specimens and confirms that the identical frames had very comparable stiffness estimates and vibration periods, which are mainly governed by brace buckling and rupture, and are independent from the earthquake duration. This is another key observation: it suggests that accurate numerical models for SCBFs will need to properly capture the buckling and damage accumulation through fracture rather than considering macro-models or hysteretic degradation models.

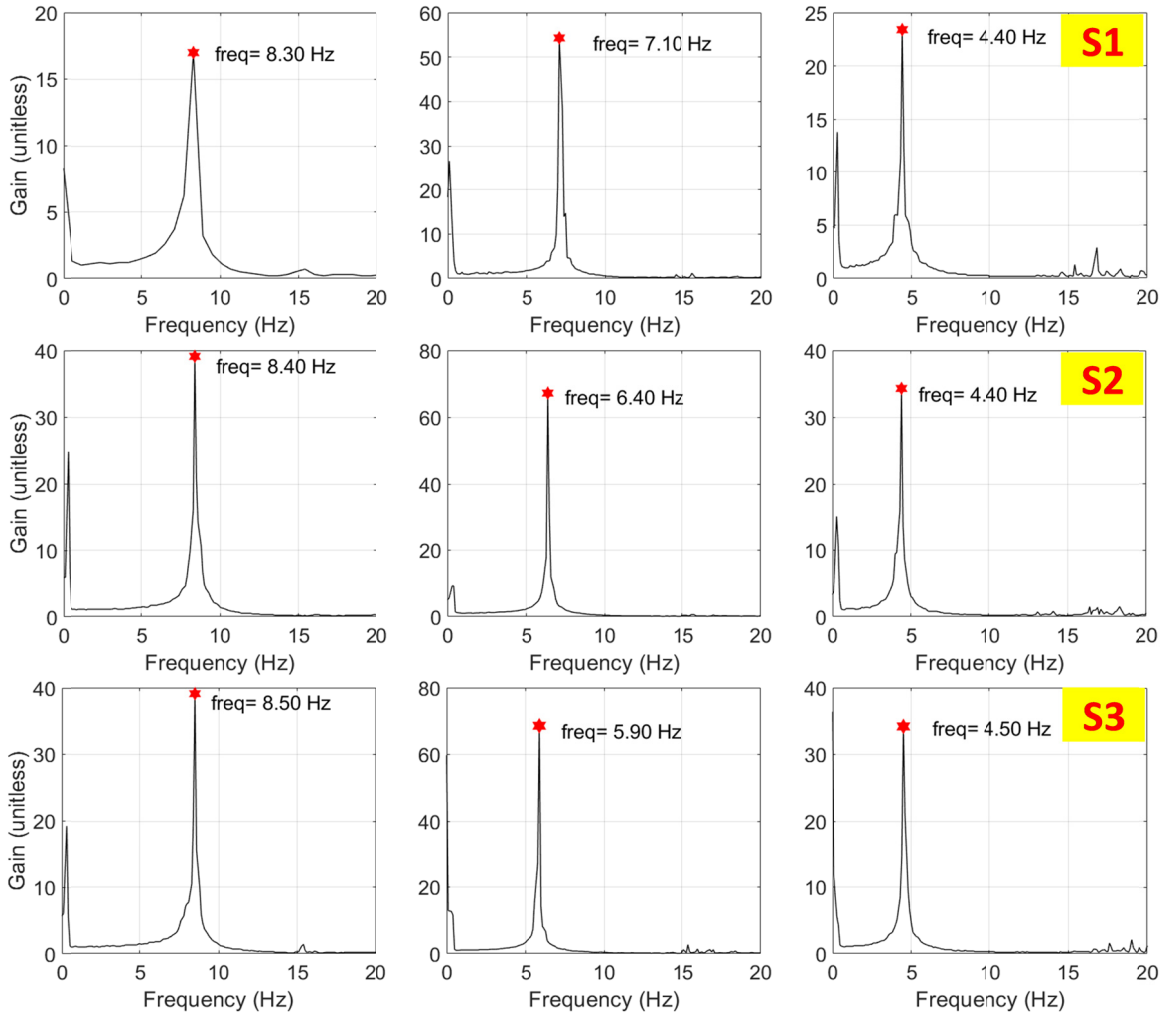


Figure 5.15 The frequency response function and identified fundamental frequency for the three specimens from white noise tests.

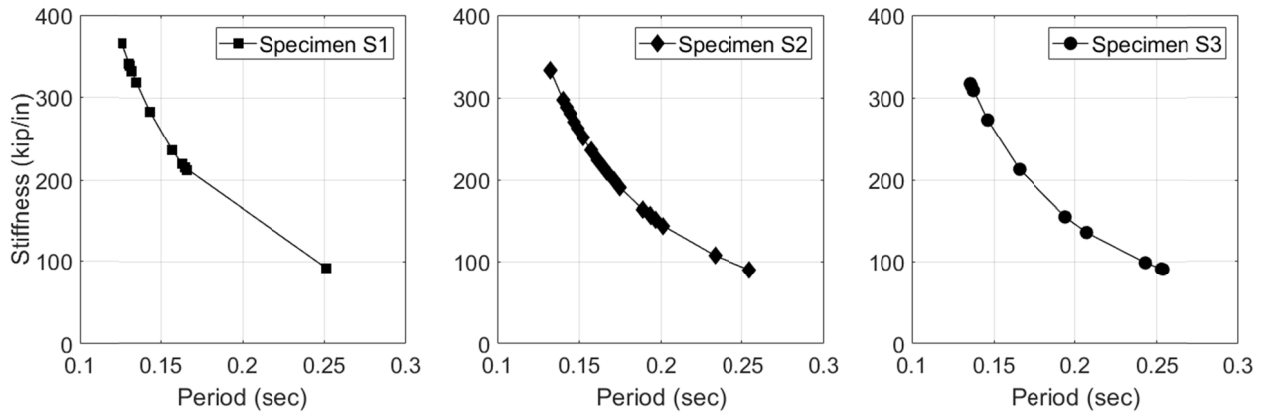


Figure 5.16 Stiffness degradation with respect to fundamental period for all tested specimens, S1, S2, and S3.

5.1.5 Summary of Key Test Results

A comprehensive summary of key test results is provided in Table 5.1 for all runs for all three specimens. These results can be used in future studies to validate numerical models to properly capture the effect of earthquake duration. Values for the peak top accelerations, peak force demand in each run, frame displacements, brace out-of-plane buckling, and the residual displacements are presented. The force and displacement capacities for each specimen are highlighted in the table as well. It is shown that force capacity is approximately the same for all three specimens. Because it is dictated mainly by the inelastic brace buckling, it is insensitive to earthquake duration; since the displacement capacity is mainly dictated by the brace rupture, i.e., dictated by the low-cycle fatigue, it is sensitive to earthquake duration.

Table 5.1 Summary of key test results for all runs and specimens.

Run #	PGA (g)	Global Response			Brace				Notes
		Peak acc. (g)	Peak force (kip)	Top Disp. (in)	North brace (in.)		South brace (in.)		
					Peak	Resid.	Peak	Resid.	
SPECIMEN 1									
1	0.91	2.58	140	0.51	2.80	0.04	---	---	Both braces buckled, SB wire pot. cut
2	0.97	2.65	141	0.60	3.90	-0.46	4.68	-0.69	
3	1.08	2.74	149	0.70	3.44	0.50	5.77	0.37	
4	1.08	2.58	147	0.73	3.18	0.20	4.67	0.24	
5	1.08	2.49	144	0.73	3.34	-0.12	---	---	SB wire pot. Cut
6	1.11	2.45	142	0.73	3.31	0.11	---	---	SB wire pot. Cut
7	1.14	2.35	138	0.75	---	---	---	---	Both braces complete rupture, NB & SB wire pt. cut
SPECIMEN 2									
1	1.28	2.53	139	0.43	1.51	-0.17	1.31	-0.17	Both Braces Buckled
2	1.35	2.69	152	0.53	1.49	-0.33	1.92	-0.32	
3	1.28	2.64	141	0.53	2.05	-0.02	1.77	-0.03	
4	1.35	2.63	145	0.55	3.25	-0.35	2.39	-0.18	
5	1.35	2.48	141	0.56	2.22	-0.26	1.91	-0.15	
6	1.35	2.58	140	0.57	1.81	-0.09	4.08	1.44	
7	1.43	2.47	140	0.58	1.95	-0.01	2.65	0.22	
8	1.46	2.44	140	0.62	1.85	-0.04	3.39	0.20	
9	1.39	2.43	138	0.64	2.28	-0.05	4.68	0.14	
10	1.50	2.39	138	0.66	2.18	-0.16	4.65	-0.10	
11	1.58	2.43	142	0.68	1.92	-0.03	6.22	-0.17	
12	1.65	2.45	144	0.71	2.24	-0.09	4.63	-0.07	
13	1.69	2.39	145	0.72	2.10	-0.05	4.41	-0.43	
14	1.69	2.22	136	0.75	2.58	-0.10	6.81	-0.64	South Brace Complete Rupture
15	1.65	1.82	103	0.90	3.07	-0.56	3.11	0.07	
16	1.65	1.88	104	1.04	2.82	0.69	5.44	0.25	North Brace Complete Rupture
SPECIMEN 3									
1	0.91	2.22	126	0.29	0.58	-0.13	0.32	-0.01	
2	1.06	2.85	129	0.37	1.23	-0.22	0.49	0.06	Both Braces Buckled
3	1.18	2.44	133	0.43	1.75	-0.24	1.55	0.15	
4	1.54	2.81	144	0.56	1.95	-0.39	2.63	0.42	
5	1.68	2.56	144	0.71	2.10	-0.80	3.87	0.25	
6	1.80	2.89	166	1.26	2.24	0.07	5.19	1.85	Table Interlock, * values not representative of frame
7	1.06	1.58	94	0.61	1.71	-0.06	1.81	-0.06	
8	1.18	1.89	121	0.78	2.13	-0.03	2.37	0.00	Both Braces Complete rupture

5.2 LOCAL RESPONSE

This section focuses on local behavior in terms of brace buckling and damage propagation, fatigue life until failure (as estimated based on the outer most fiber of the brace), and gusset plate behavior during loading.

5.2.1 Brace Buckling

Deformation of the gusset plates was observed during the tests and reported after the out-of-plane brace buckling occurred. Both the gusset plates connecting the braces to the beam and the columns deformed; see Figure 5.17. According to the AISC design criteria [REF], the gusset plates should stay elastic during extreme events, which was observed in these tests even after the inelastic brace buckling. Figures 5.17(b) and 5.17(c) show deformation of upper and lower gusset plates that followed the out-of-plane brace buckling; see Figure 5.17(a). Figure 5.17(d) shows a line crack that can approximately represent the rotation axis for the buckling brace.

Figures 5.18–5.20 show the out-of-plane brace buckling for Specimens S1, S2, and S3, respectively, as measured at the brace mid-span using wire potentiometers. For S3, which was tested under the second long-duration earthquake, the two braces buckled in opposite directions; see Figure 5.20. Note: towards the end of S1 tests, the brace wire potentiometers slipped and the string wires were cut, so reliable brace buckling data were not recorded towards the end of the test.

Figure 5.21 shows the deformed shape for the out-of-plane buckling of the three tested specimens. The direction of buckling is highly dependent on the initial imperfection of the brace member and on the welding line location of the HSS section. In terms of damage propagation for braces, Figure 5.22 shows the different stages of brace failure. First, local brace buckling occurs, then tiny cracks start to form at the buckled face near the HSS edges. The crack propagates continuously until it makes a complete rupture in the brace cross section. Figure 5.23 shows both north and south braces ruptured; the rupture occurred right at the location of the strain gauges. Figure 5.24 shows the elevation of Specimen S1 after the rupture of both braces. Figure 5.25 shows the locations where cracking initiates and rupture eventually occurred for Specimen S2, and Figure 5.26 shows the rupture for Specimen S3.

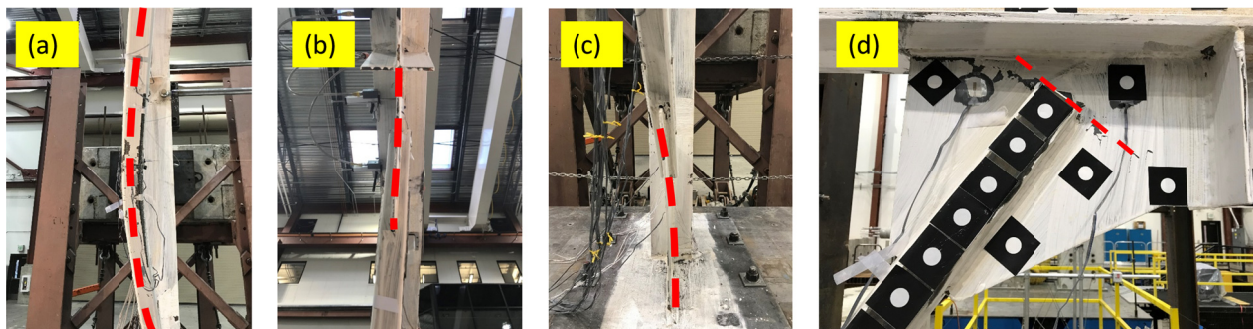


Figure 5.17 (a) Out-of-plane brace buckling; (b) upper gusset deformation; (c) lower gusset deformation; and (d) upper brace white wash flakes.

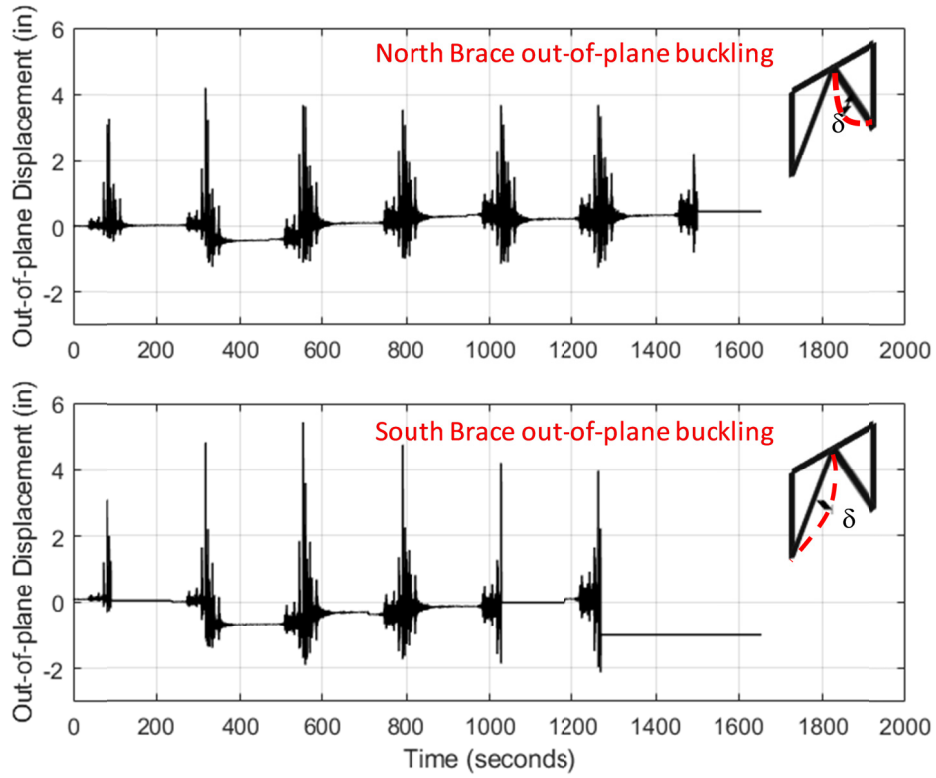


Figure 5.18 Specimen 1 braces out-of-plane displacement.

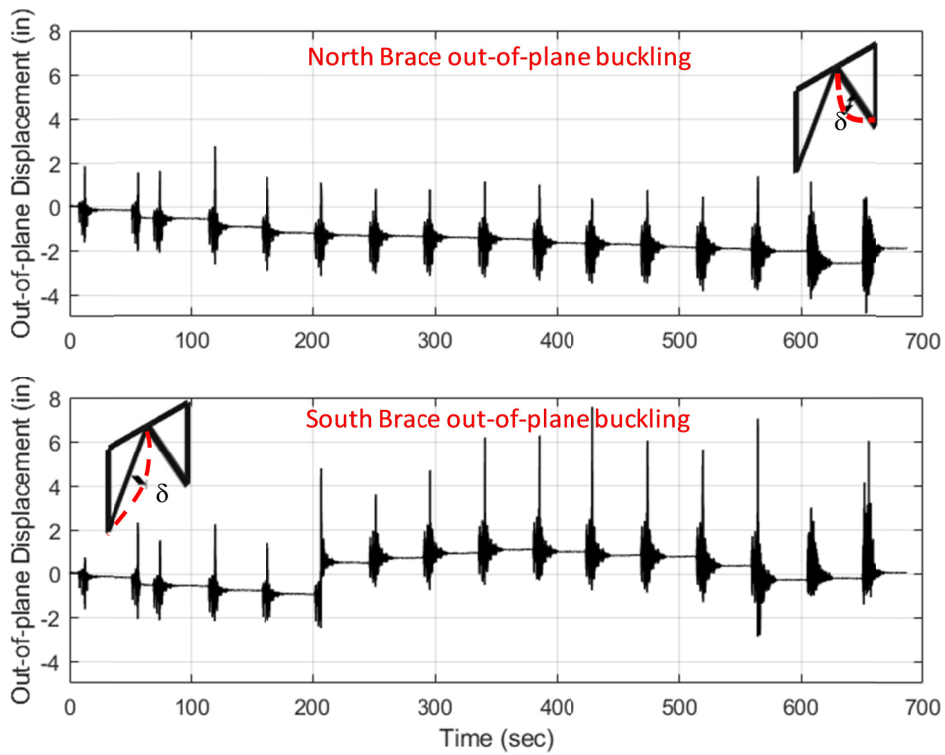


Figure 5.19 Specimen 2 braces out-of-plane displacement.

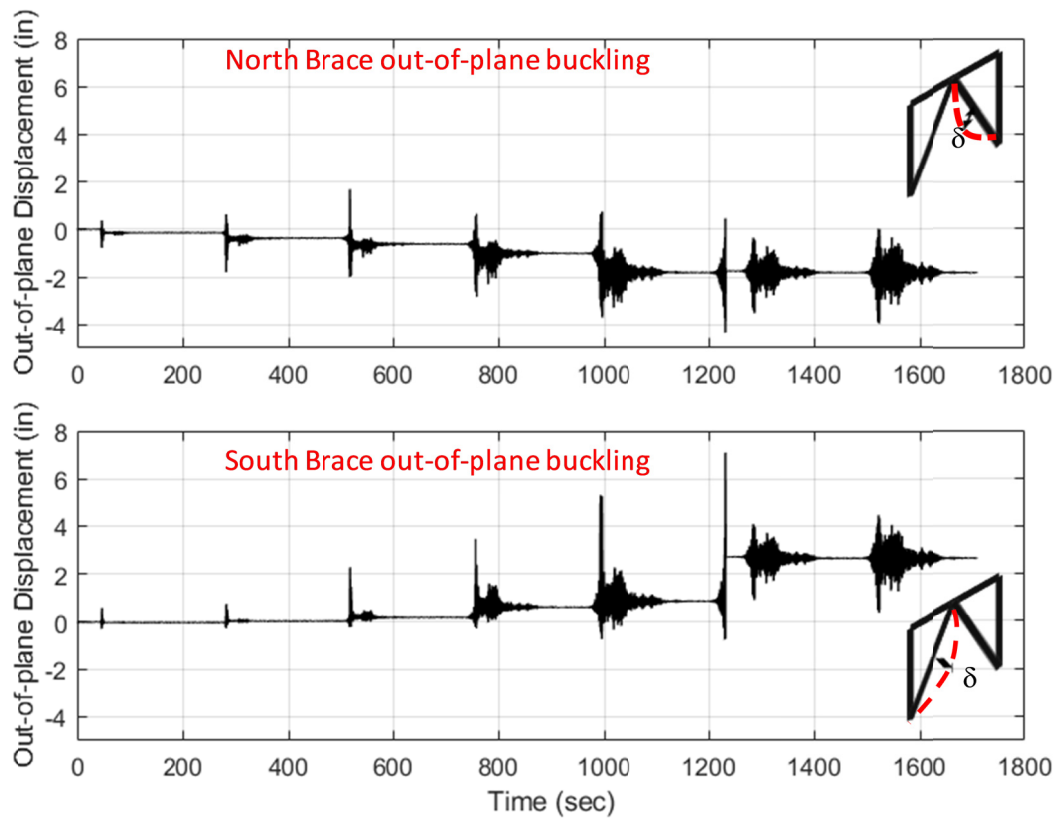


Figure 5.20 Specimen 3 braces out-of-plane displacement.

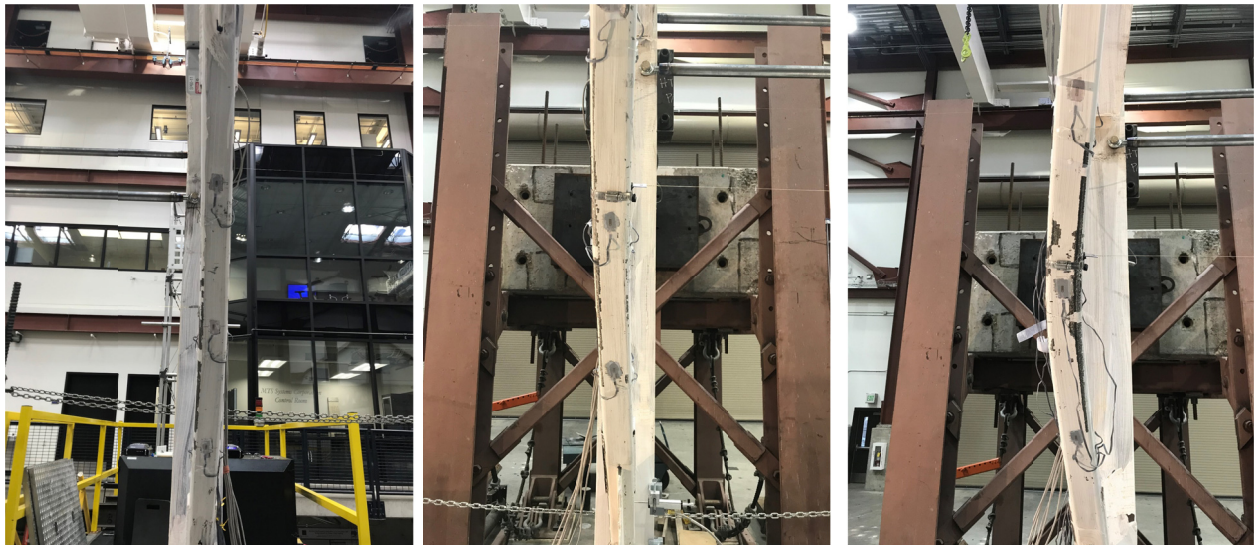


Figure 5.21 Specimens 1, 2, and 3 braces out-of-plane deformed shape, respectively.



Figure 5.22 Stages of brace failure: (a) local buckling, (b) crack initiation, (c) crack propagation, and (d) fracture.

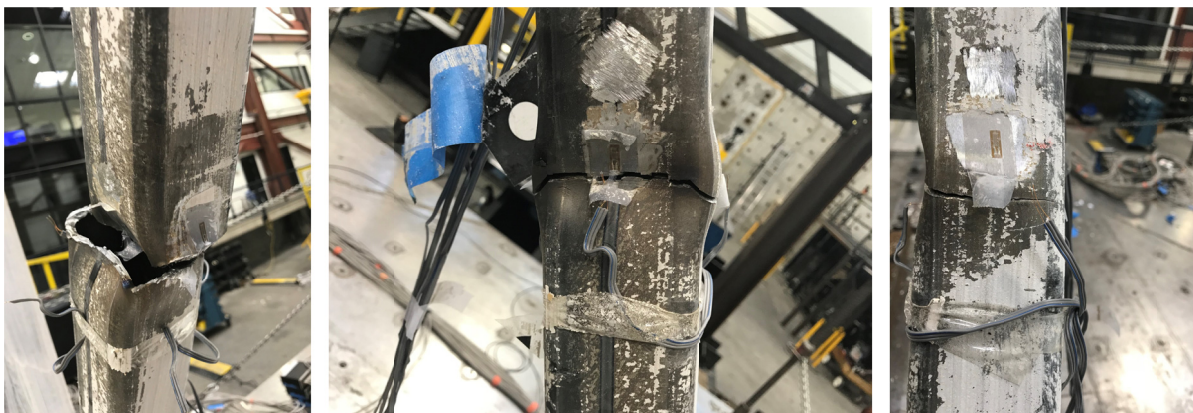


Figure 5.23 Specimen 1 ruptured braces locations.

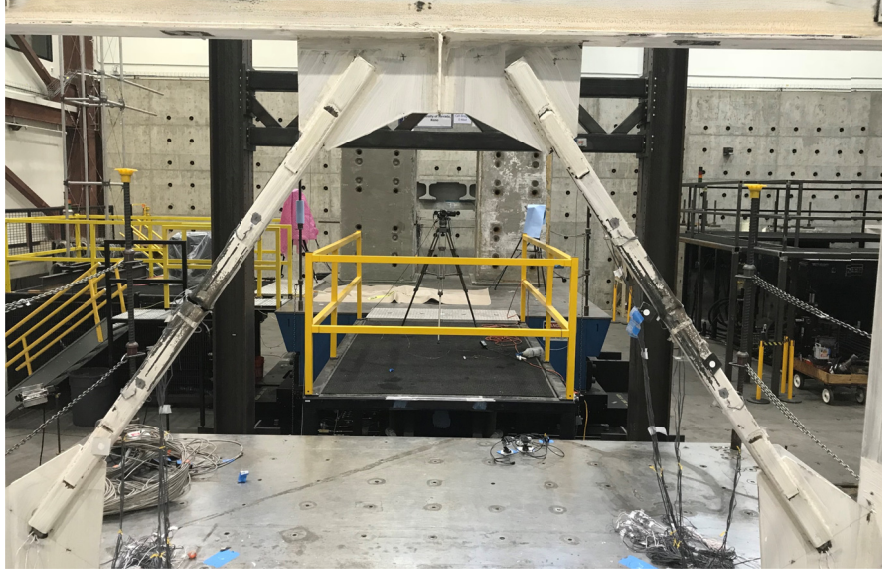


Figure 5.24 Specimen 1 elevation with both braces ruptured.



Figure 5.25 Specimen 2 ruptured braces locations.

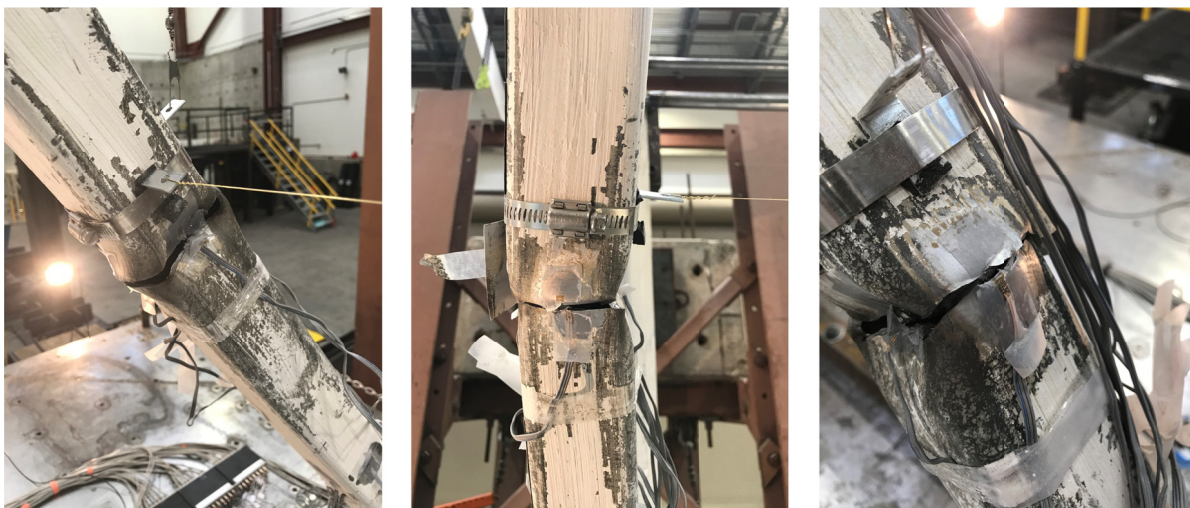


Figure 5.26 Specimen 3 ruptured braces locations.

5.2.2 Low-Cycle Fatigue and Brace Rupture

Chapter 2 provided a literature review of the development of models for capturing the effect of low-cycle fatigue for steel braces. Results from the global response suggest that low-cycle fatigue-induced rupture can be related to the duration of earthquakes. Accordingly, the objective of this section is to utilize the strain data measured in the tests to provide greater understanding of fatigue life. First, all strain data obtained for both braces at several locations are presented for all specimens. Then, the strains measured from Specimens S1 and S2, tested under two spectrally matched records, were compared.

Four strain gages were used at three different locations for each brace and distributed around the HSS 4 sides to accurately measure the outer-most strains; see Figure 5.27. Note that at the brace mid-span (location B in Figure 5.27), fibers 1 and 3 experienced the largest strain values, and experienced the initial fatigue cracks that led to the full rupture, as shown in the strain histories in following figures.

Figures 5.28–5.30 show the strain histories in the north brace for Specimen S1 under the long-duration earthquake at the three locations A, B, and C, and at each face of the HSS brace, respectively. Figures 5.31–5.33 show the strains but in the south brace of Specimen S1 at the three locations A, B, and C at all four faces of the HSS brace, respectively.

As before, Figures 4.34–4.36 and Figures 4.37–4.39 show the strain histories at brace locations A, B, and C in the north and south braces of Specimen S2, respectively. For completeness, Figures 4.40–4.42 and Figures 4.43–4.45 show the strain histories at brace locations A, B, and C in the north and south braces of Specimen S3, respectively.

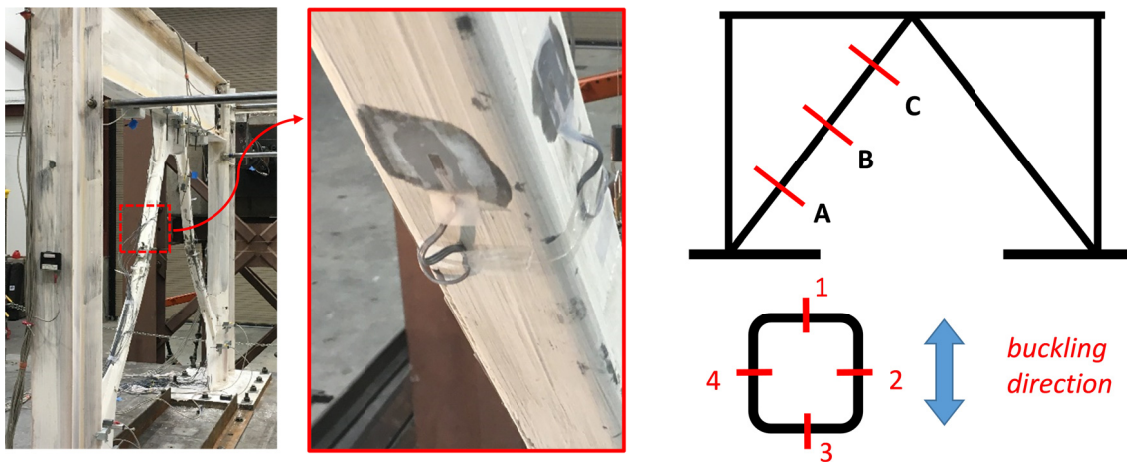


Figure 5.27 Strain gages locations along the brace length (A, B, and C) and around the HSS brace four faces (1, 2, 3, and 4).

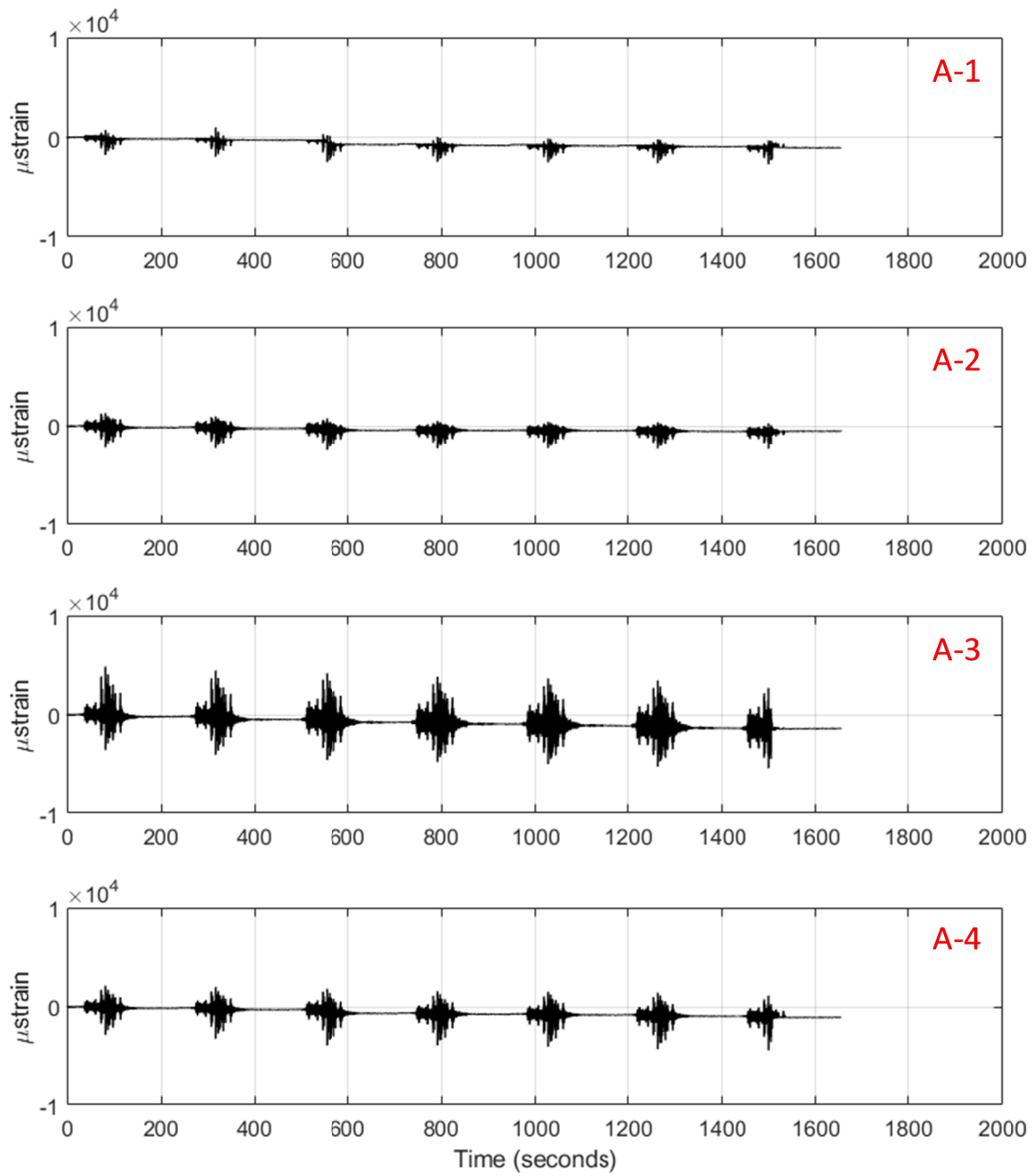


Figure 5.28 Specimen 1 north brace strains at section A.

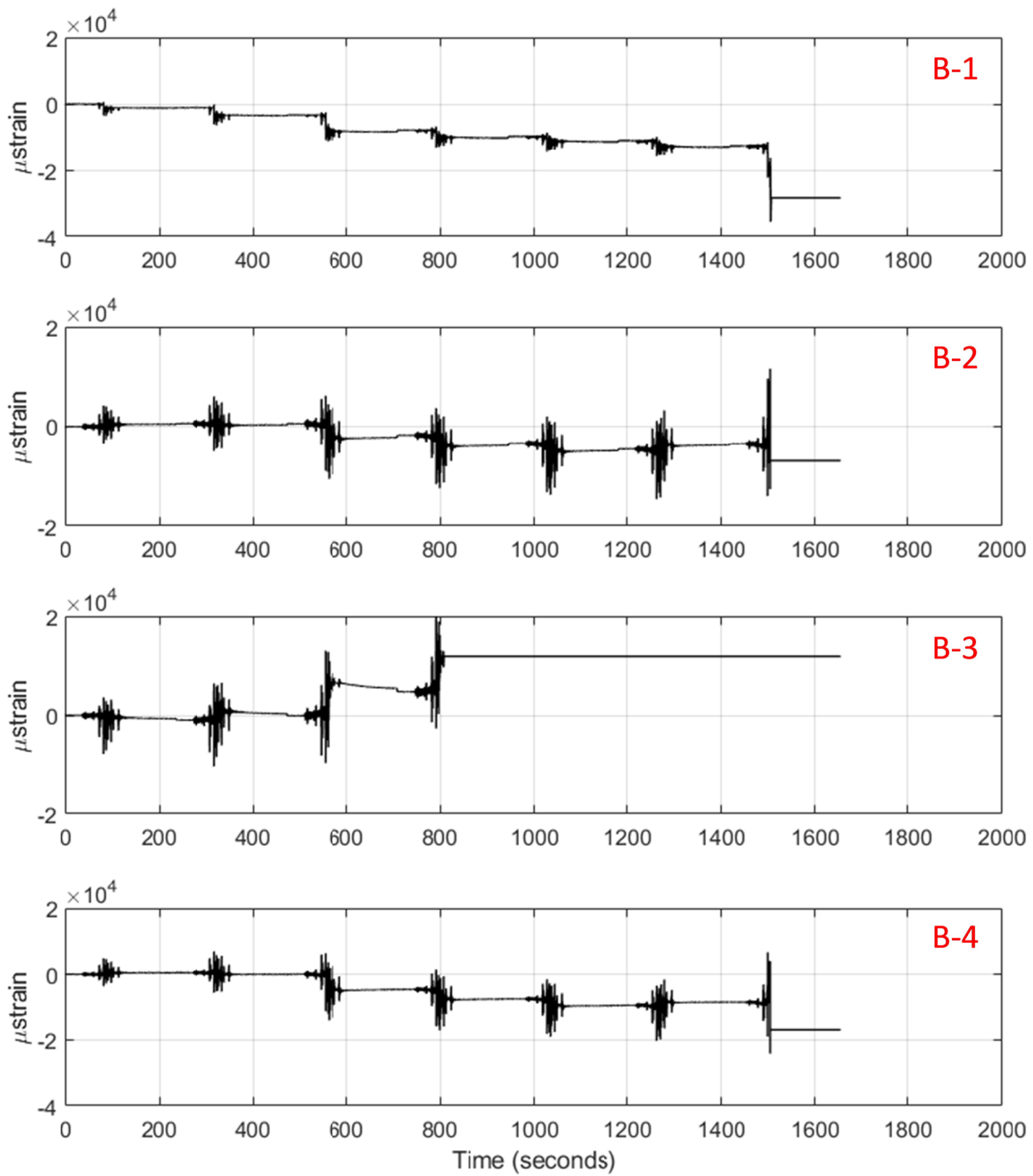


Figure 5.29 Specimen 1 north brace strains at section B.

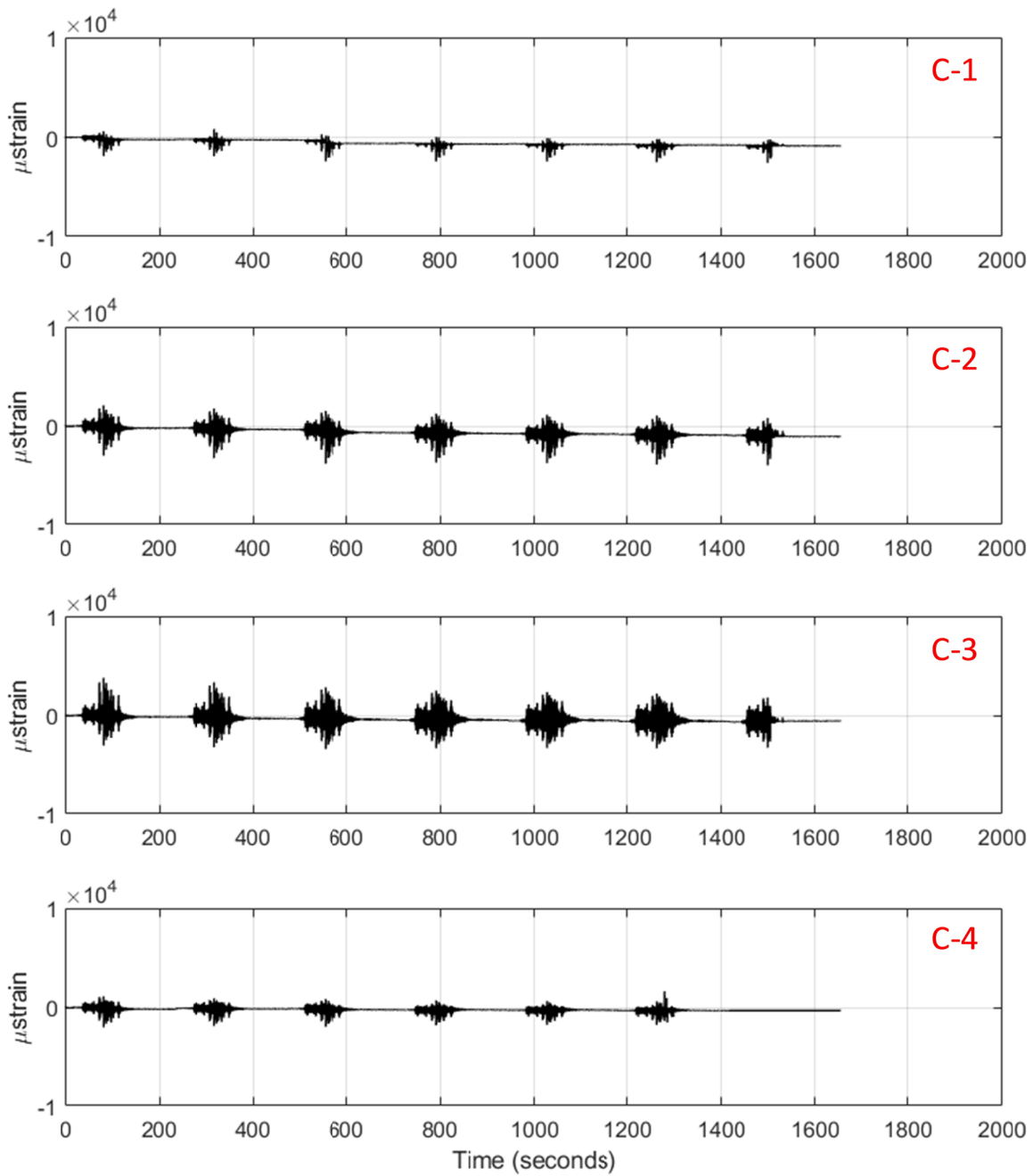


Figure 5.30 Specimen 1 north brace strains at section C.

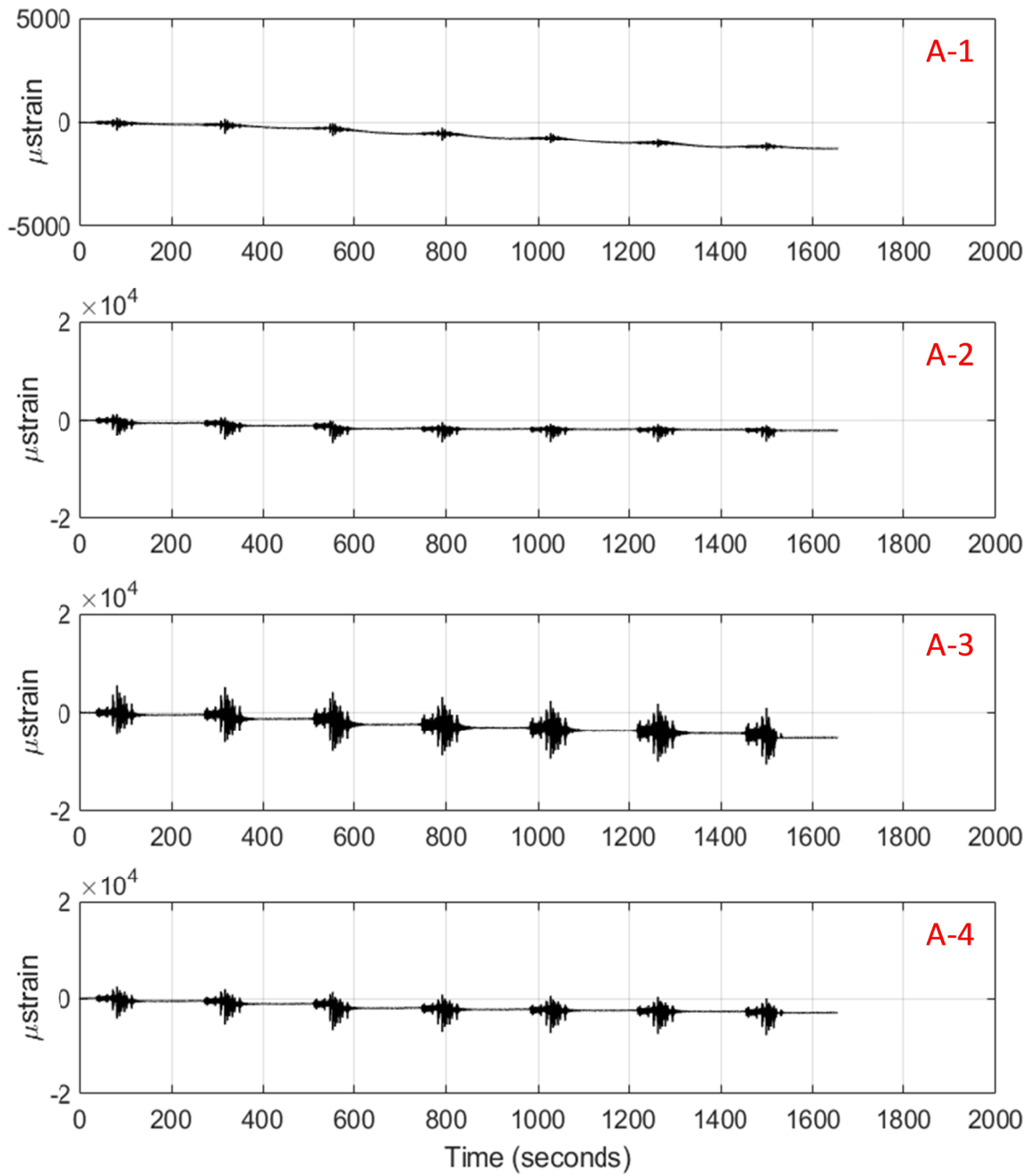


Figure 5.31 Specimen 1 south brace strains at section A.

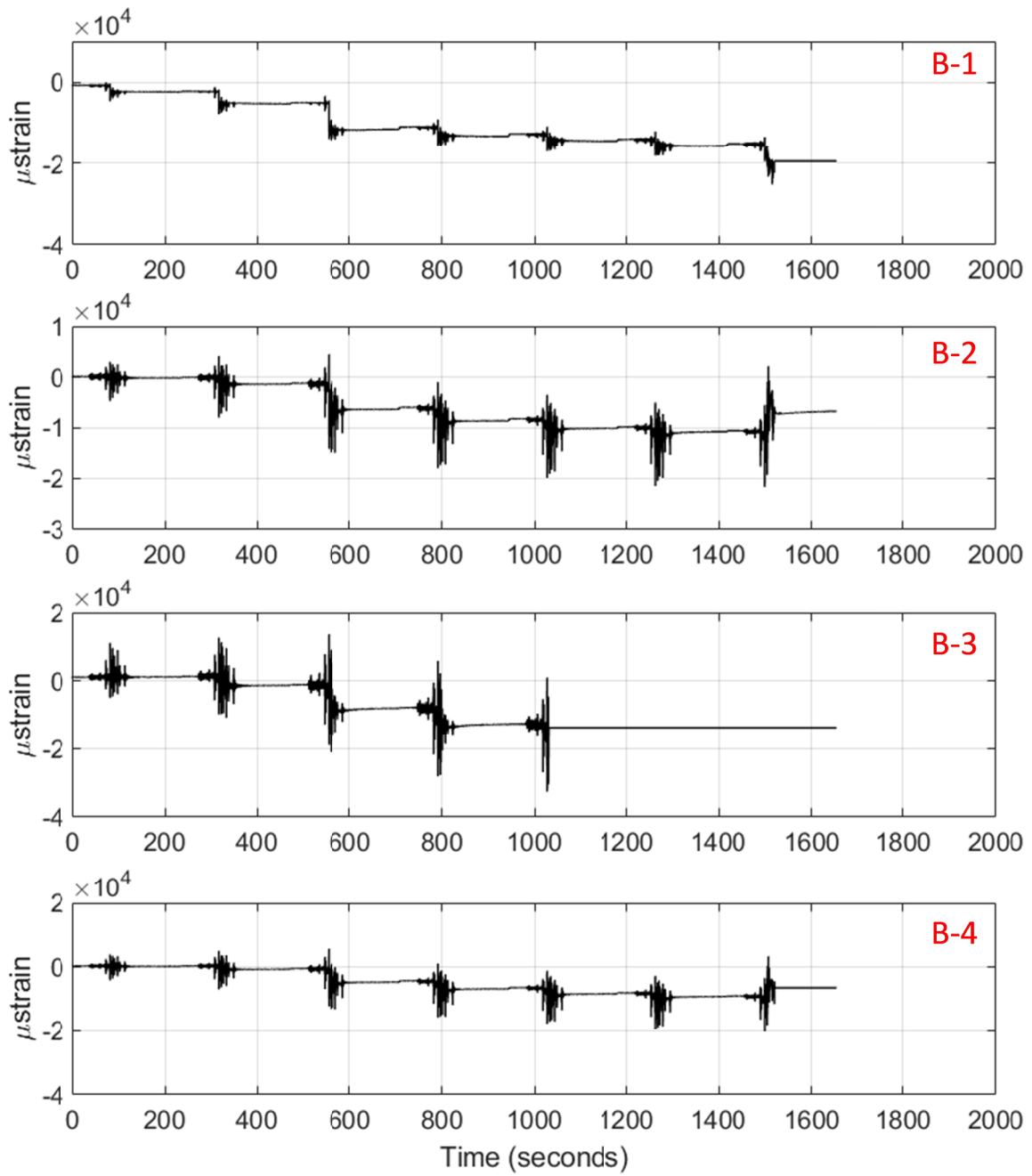


Figure 5.32 Specimen 1 south brace strains at section B.

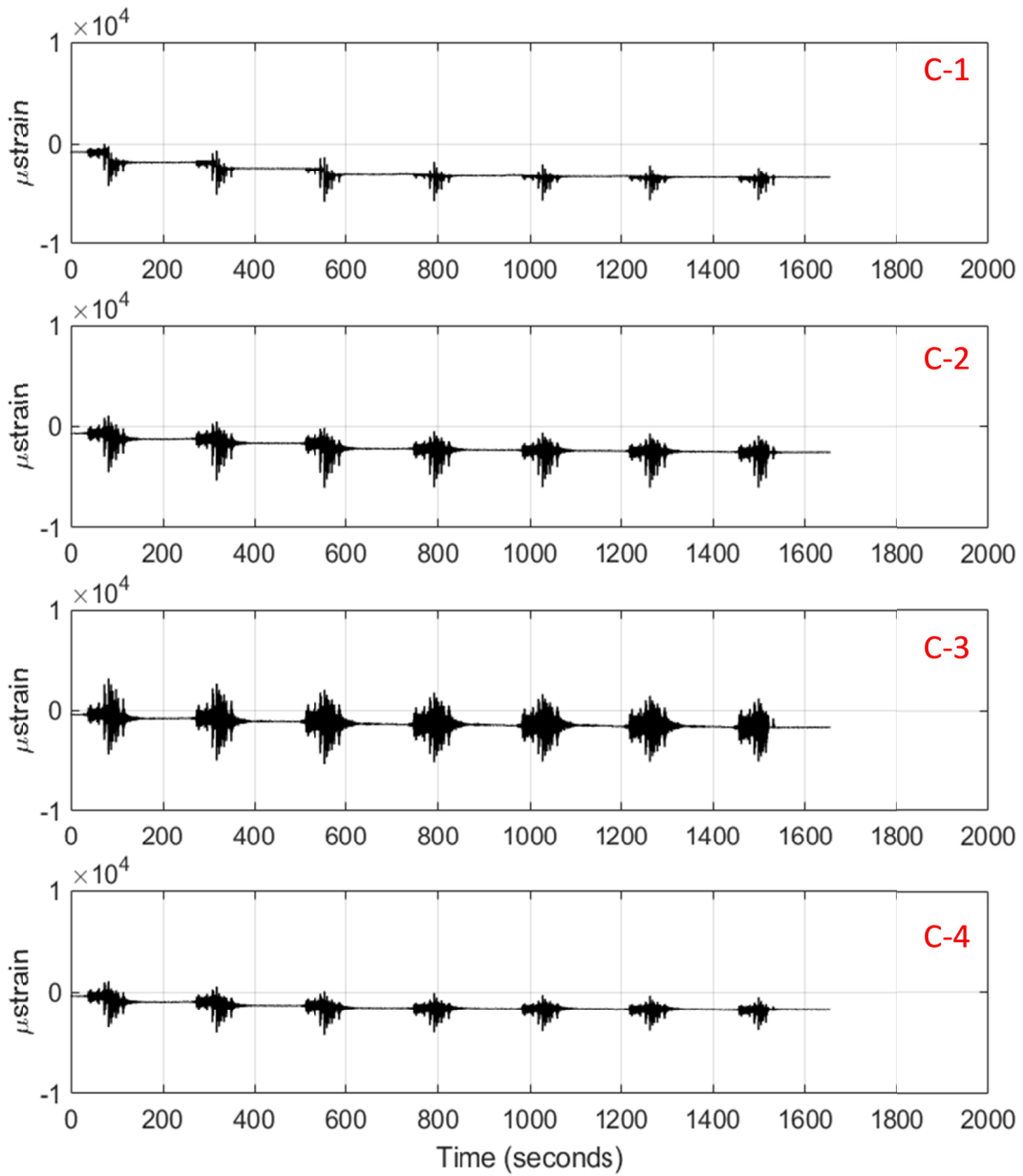


Figure 5.33 Specimen 1 south brace strains at section C.

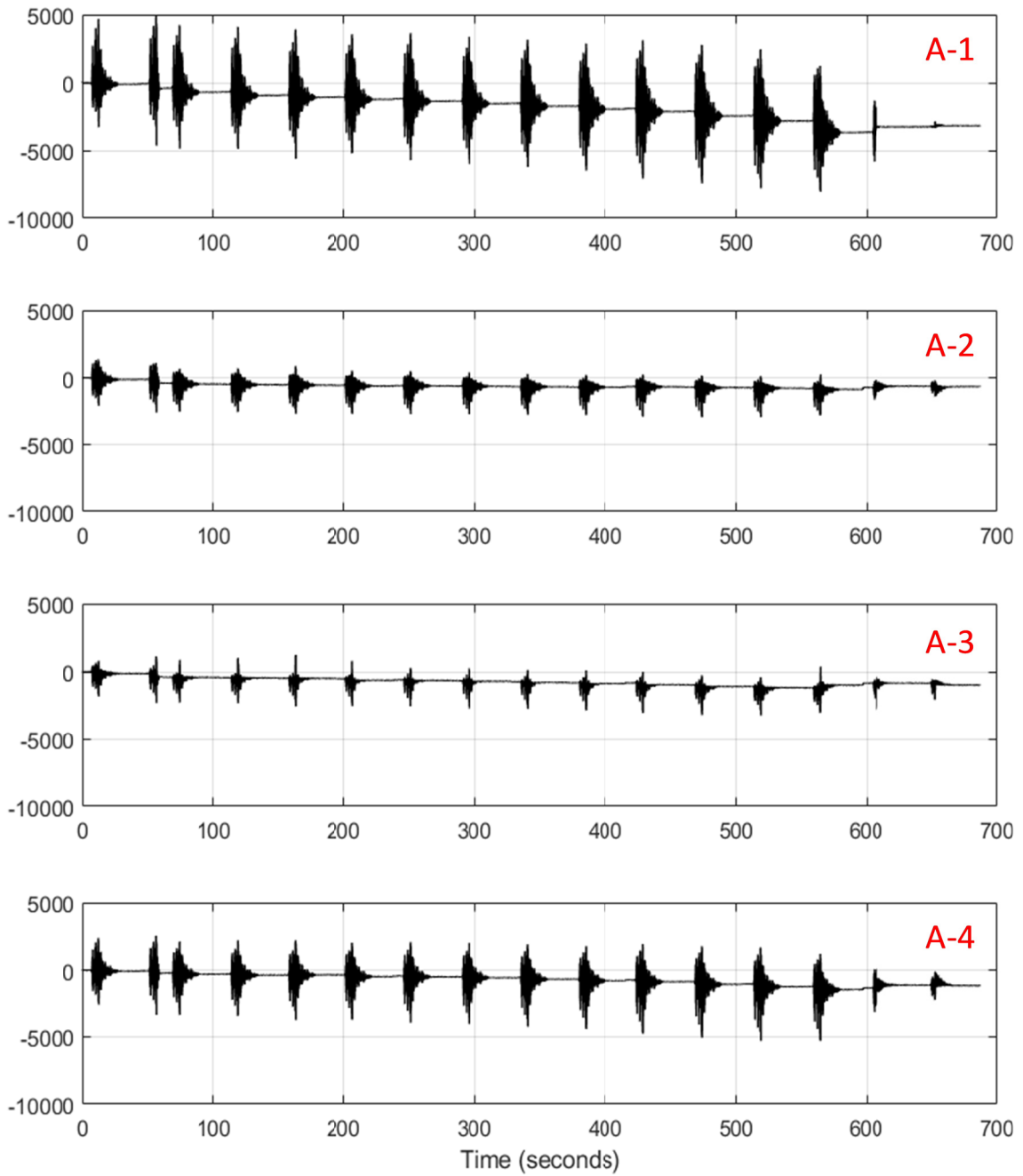


Figure 5.34 Specimen 2 north brace strains at section A.

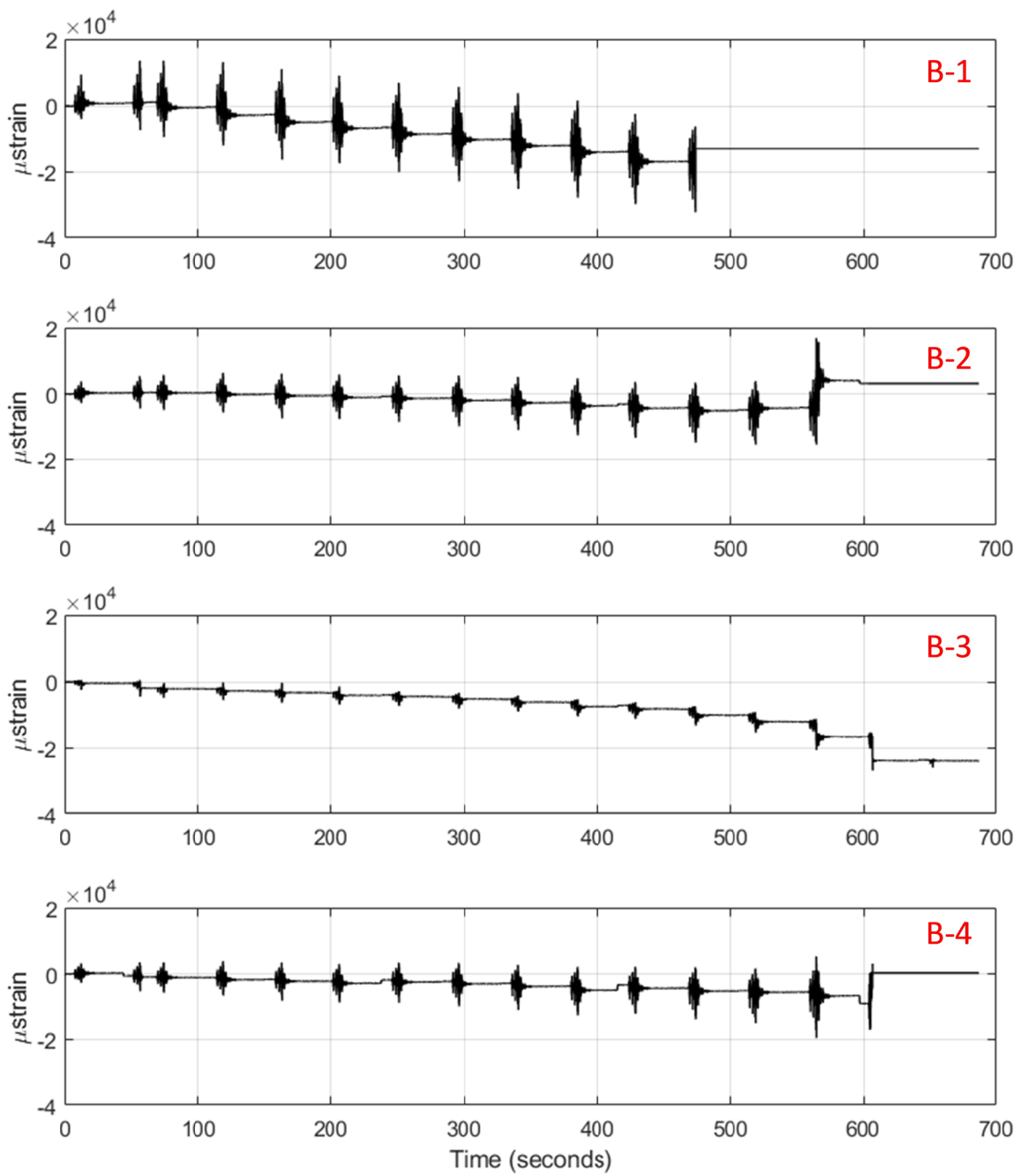


Figure 5.35 Specimen 2 north brace strains at section B.

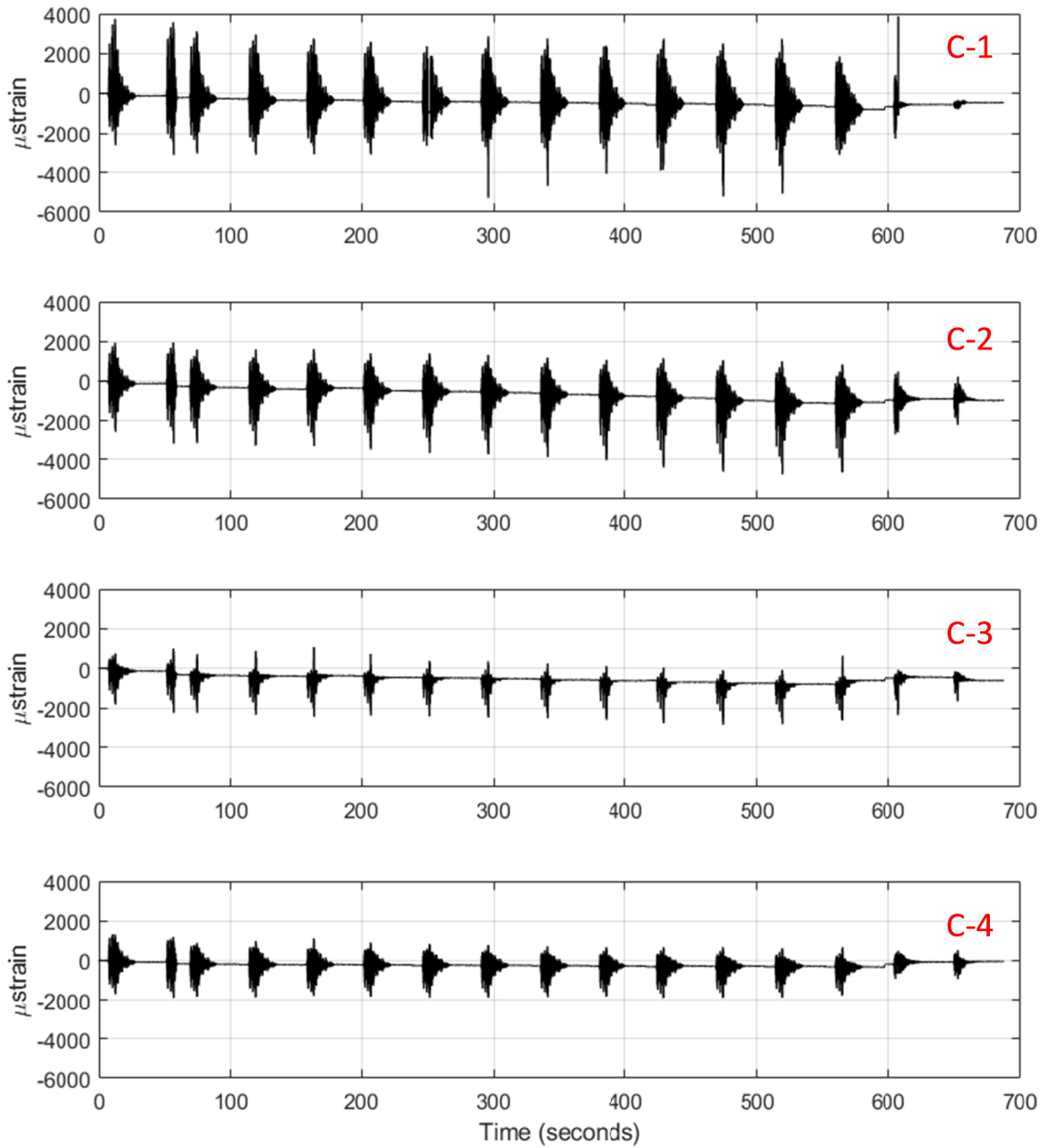


Figure 5.36 Specimen 2 north brace strains at section C.

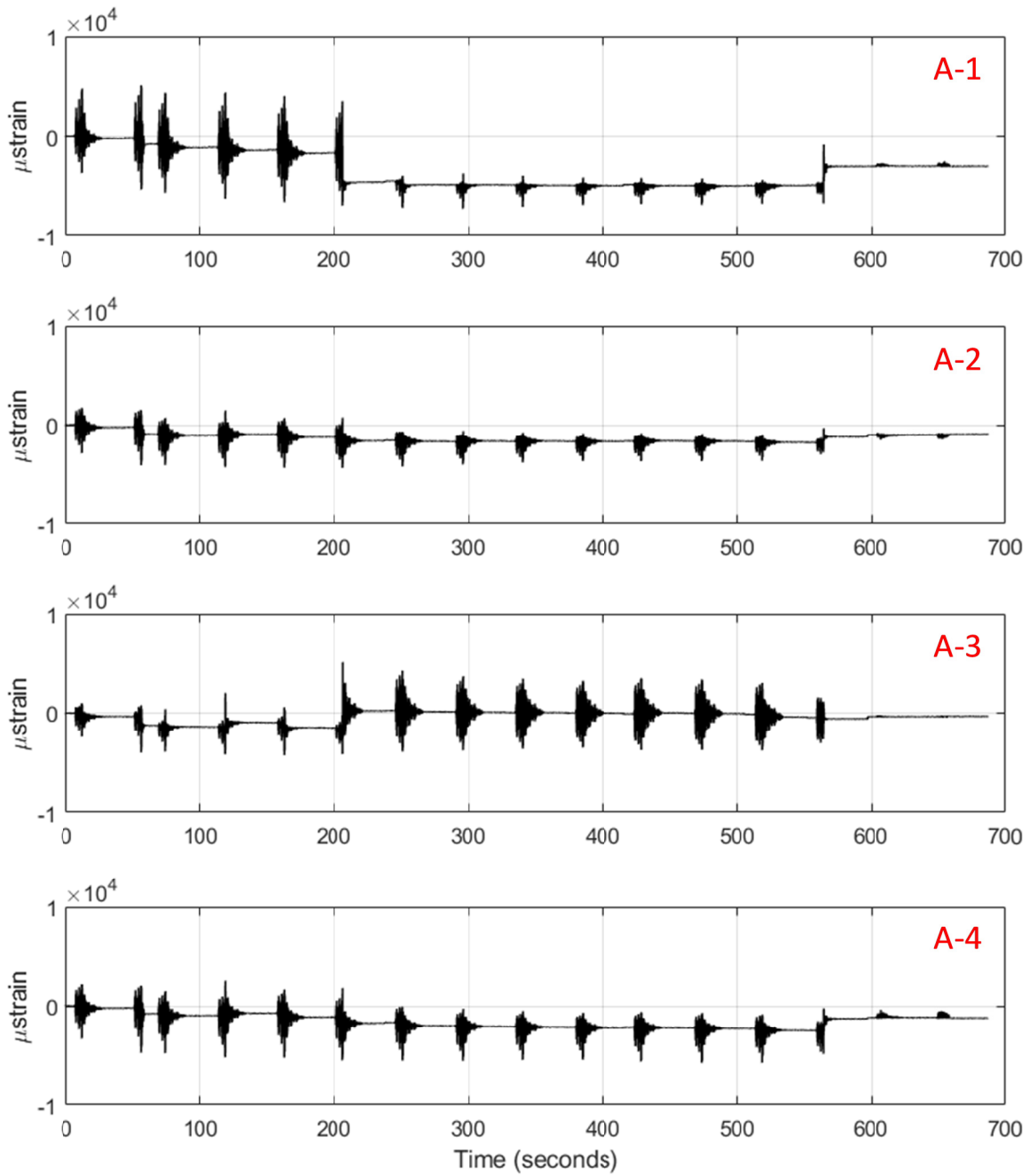


Figure 5.37 Specimen 2 south brace strains at section A.

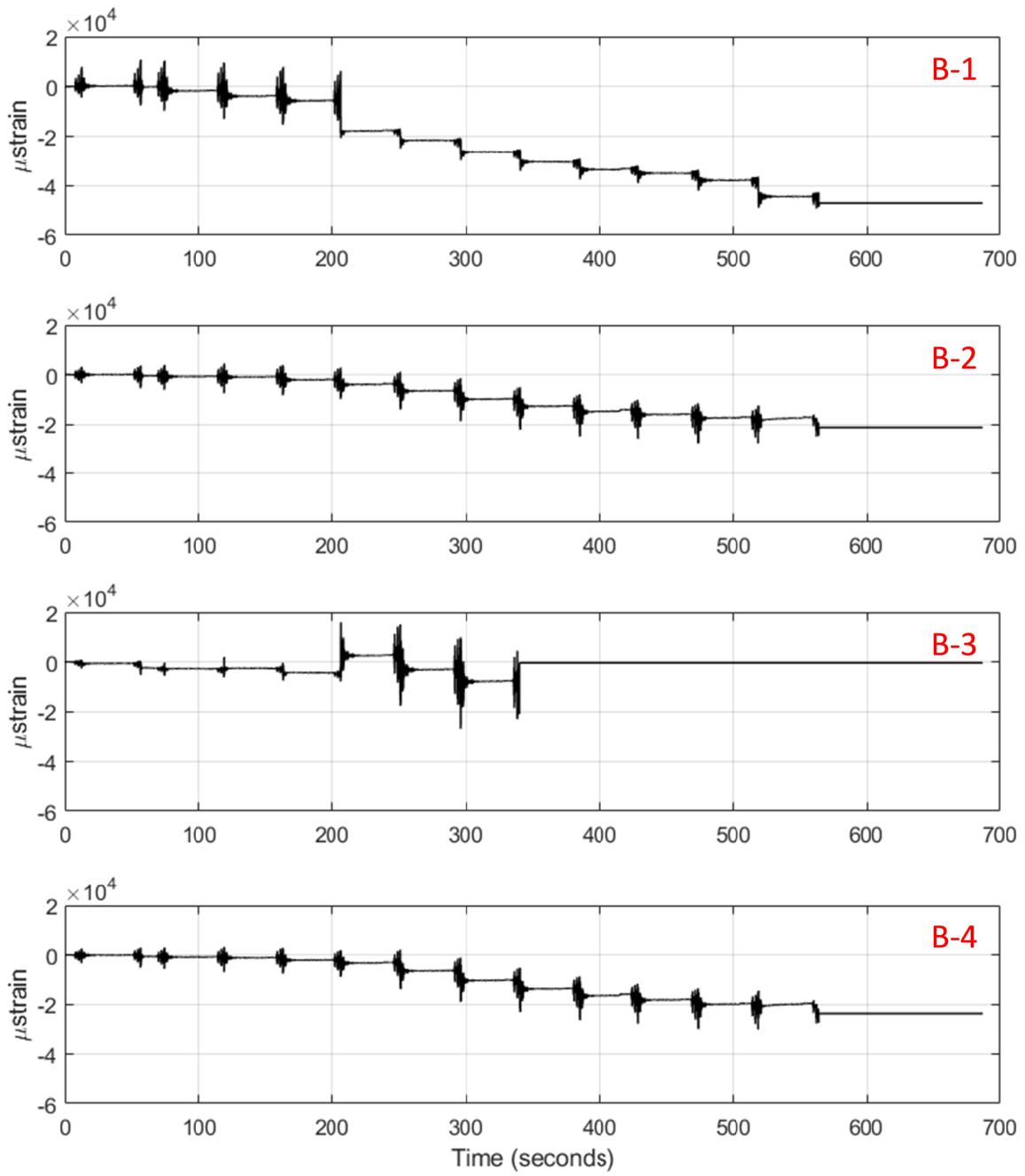


Figure 5.38 Specimen 2 south brace strains at section B.

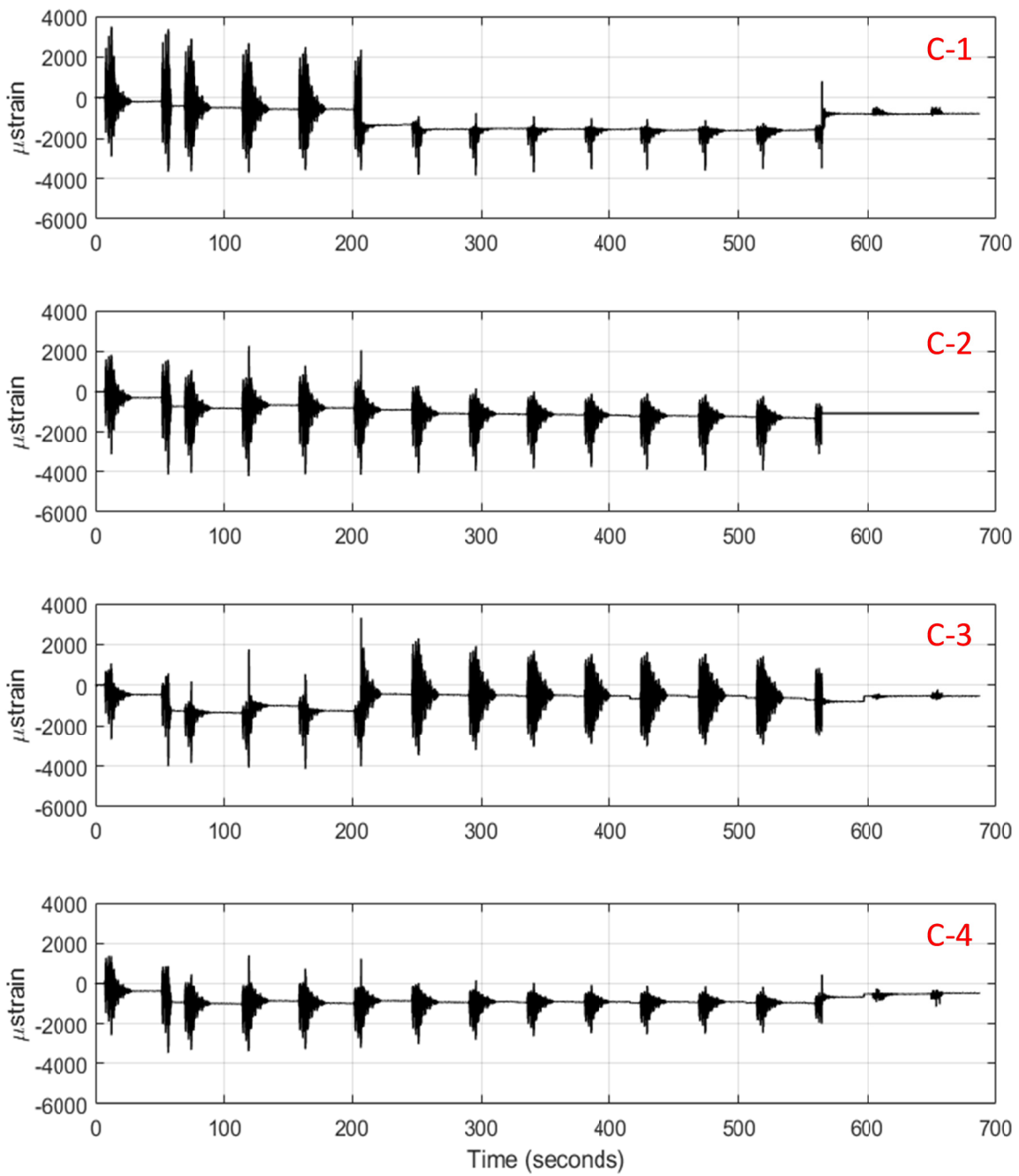


Figure 5.39 Specimen 2 south brace strains at section C.

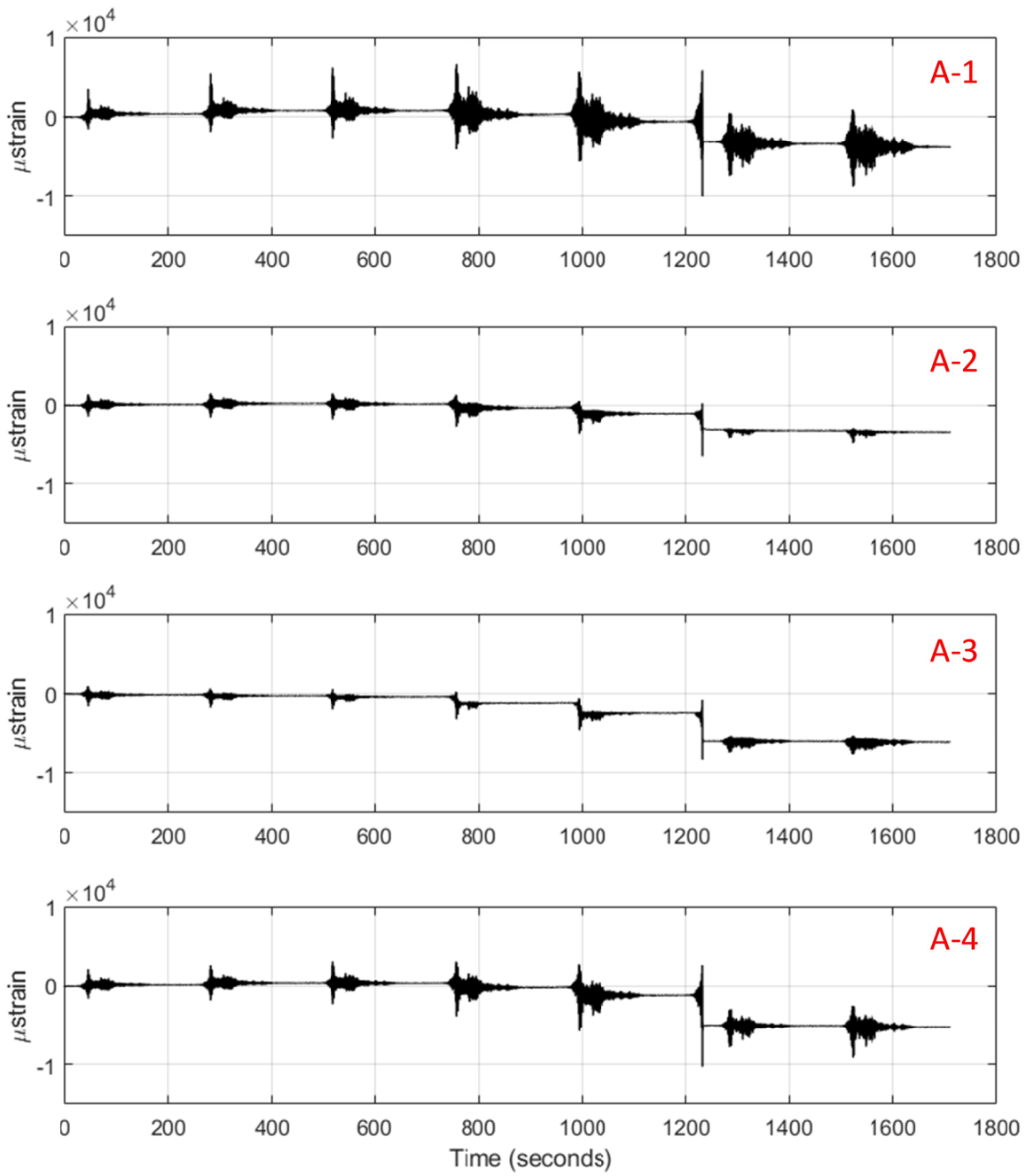


Figure 5.40 Specimen 3 north brace strains at section A.

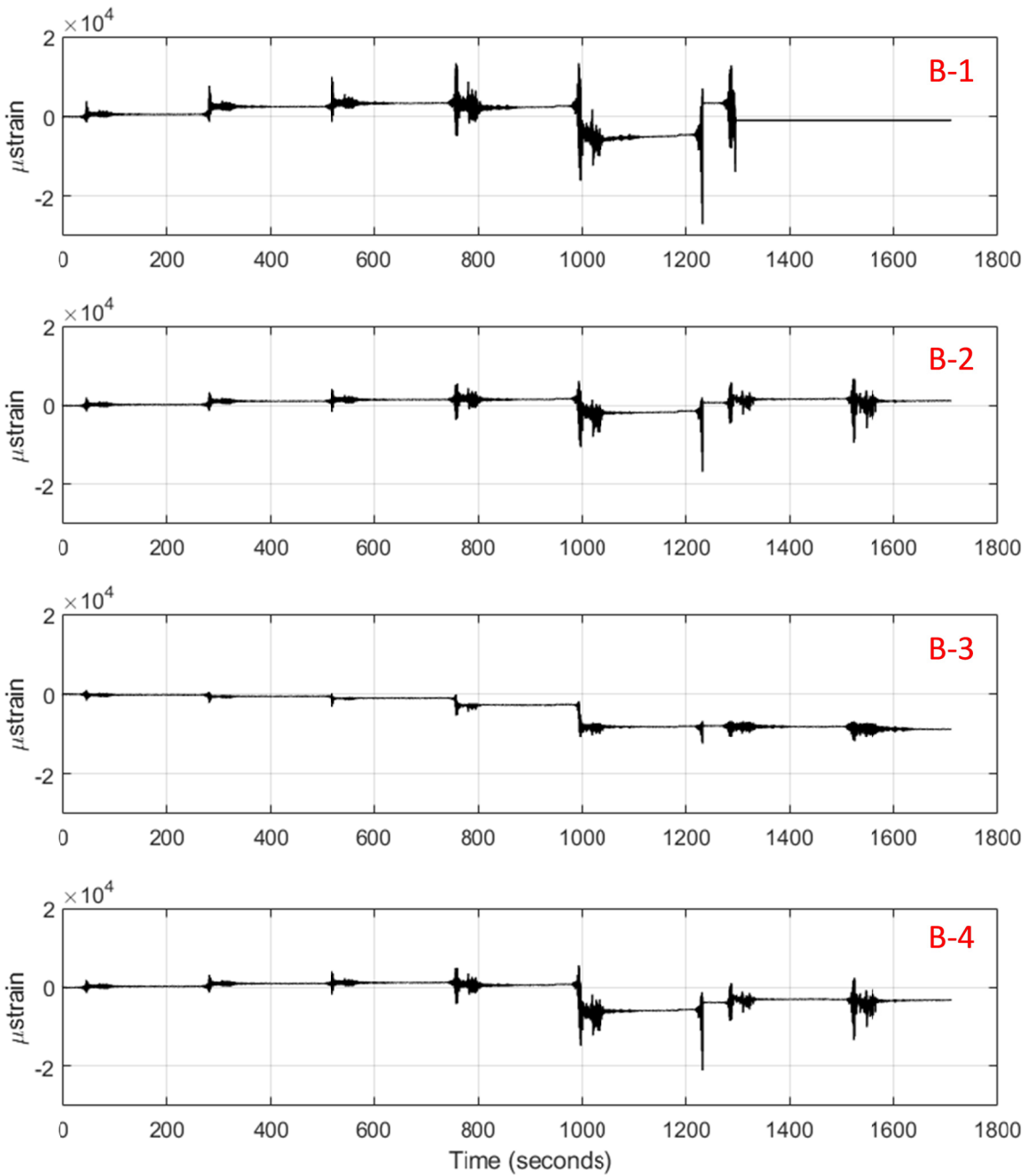


Figure 5.41 Specimen 3 north brace strains at section B.

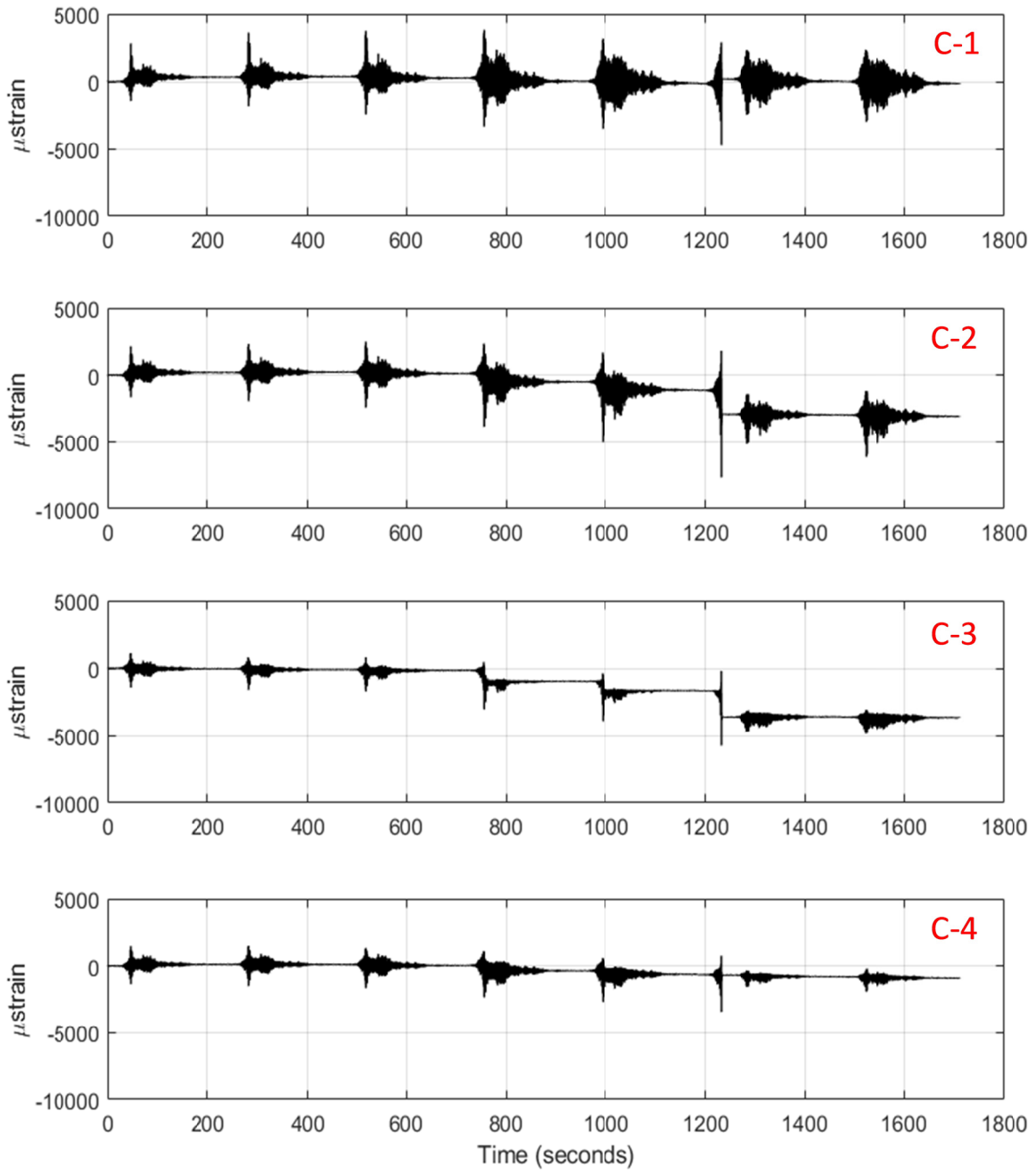


Figure 5.42 Specimen 3 north brace strains at section C.

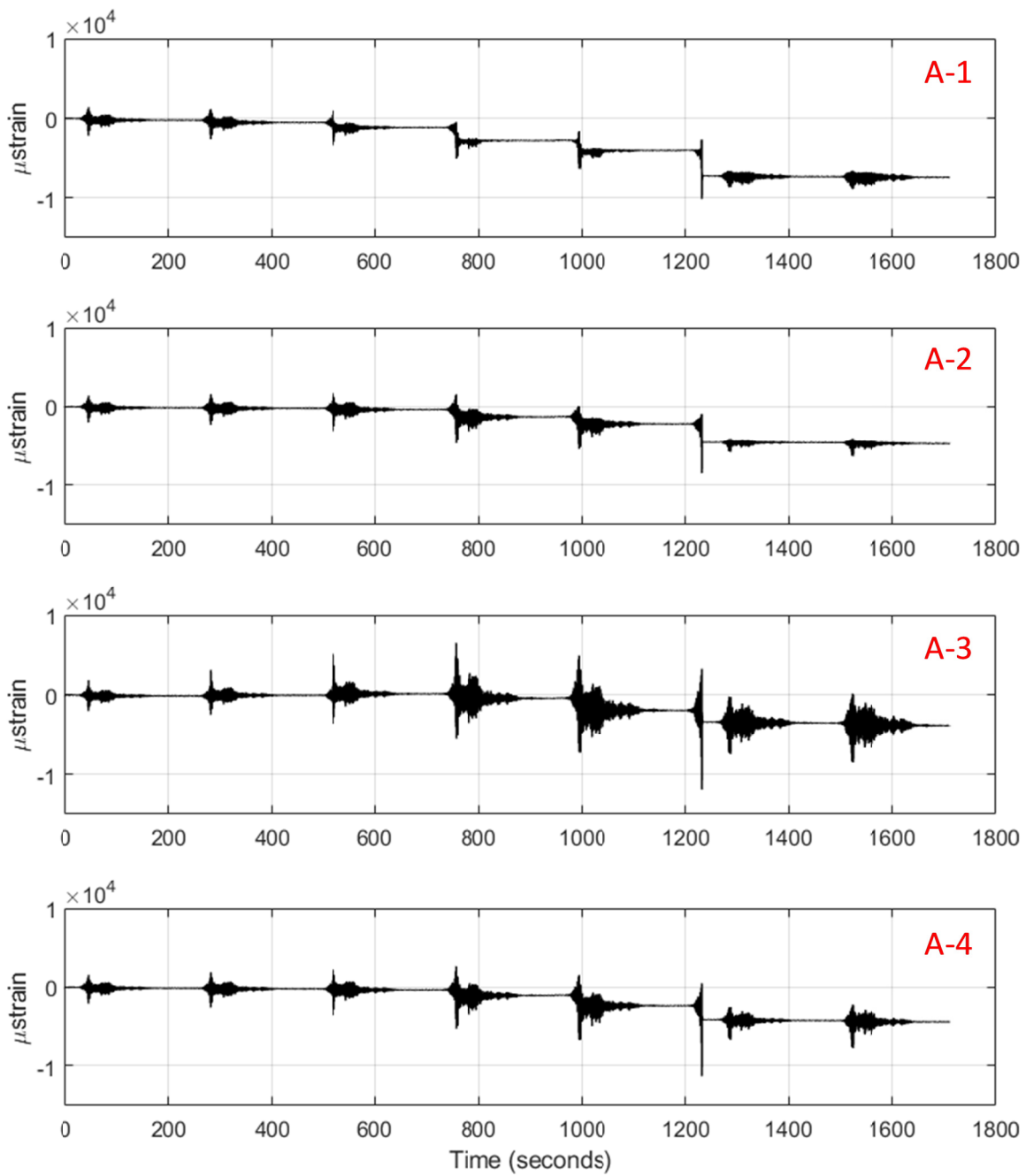


Figure 5.43 Specimen 3 south brace strains at section A.

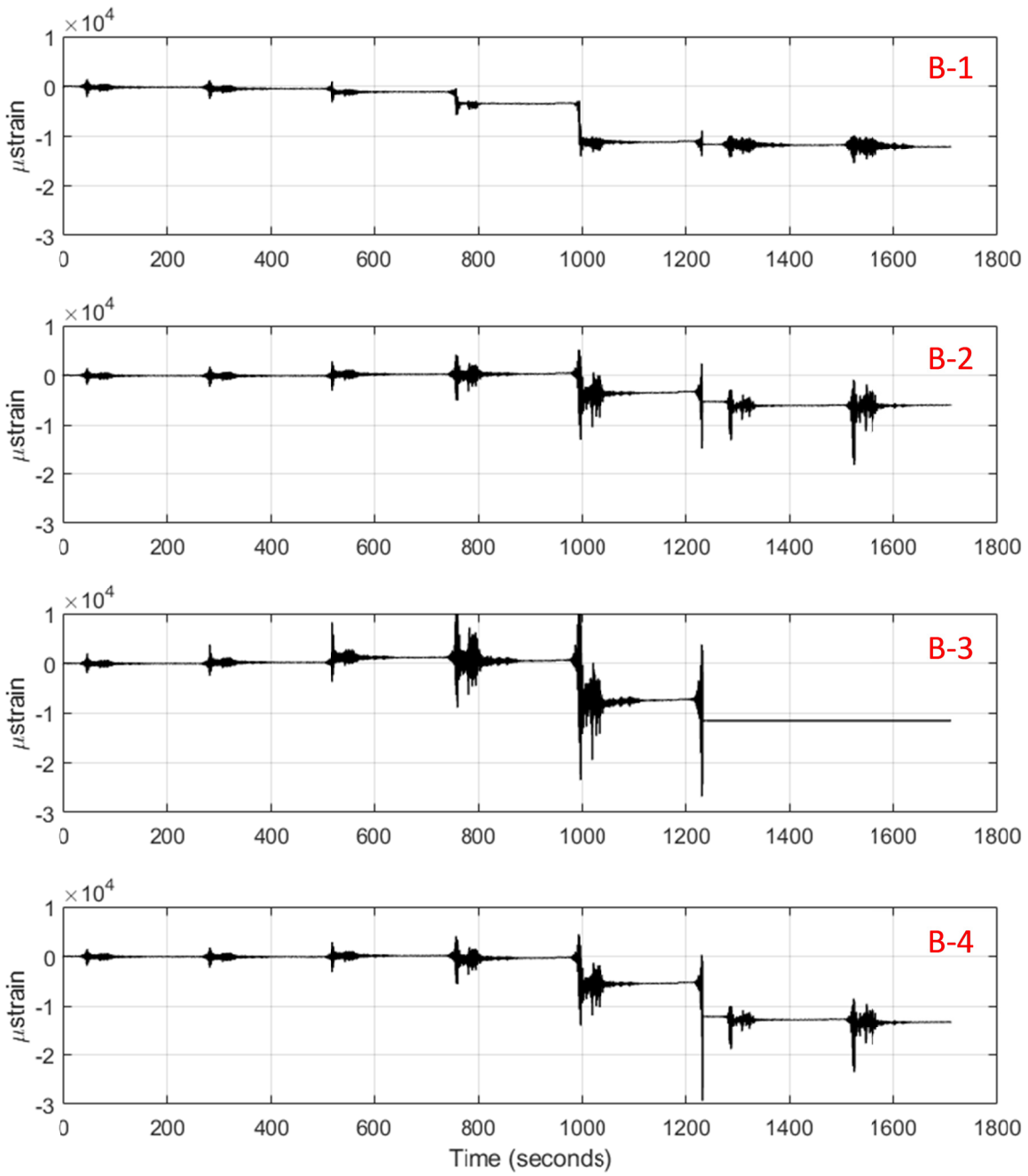


Figure 5.44 Specimen 3 south brace strains at section B.

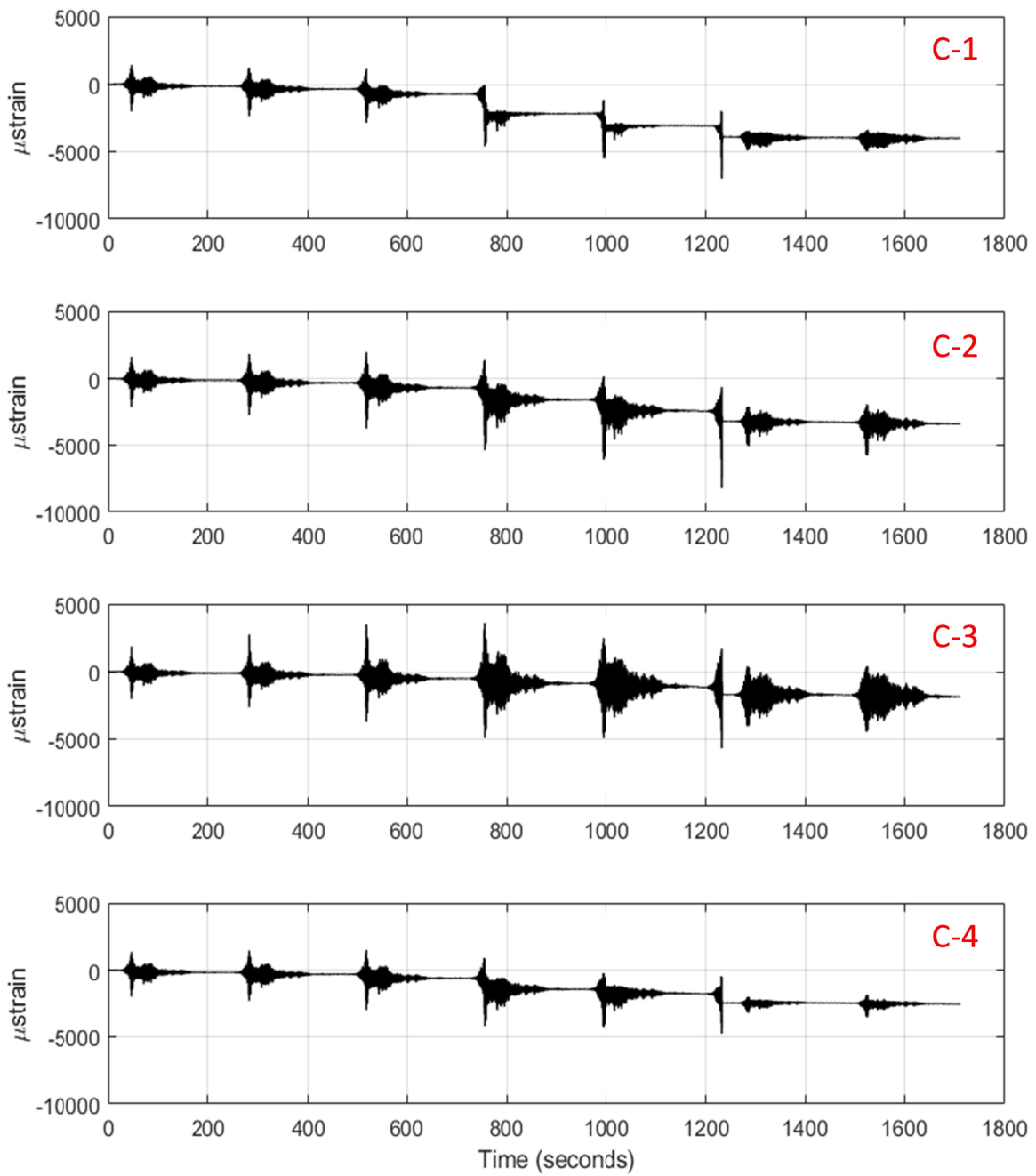


Figure 5.45 Specimen 3 south brace strains at section C.

As shown in Figures 5.28–5.45, the strain values at sections A and C, which were located at one-third and two-thirds of the brace length, were not significantly large or significantly exceeded the yield strains. Section B was the location where all the braces experienced the largest strains. In some cases; the brace ruptured exactly at a location of a strain gage where the strain gages reported extremely high values of strains indicating the cut and loss of the gage. Note: in Figures 5.28 –5.45, when a strain gage was cut or lost during one of the test runs, all the data from that point onwards was represented by a constant strain value for the last recorded strain value before the gage was cut.

All the strains measured during S1 and S2 tests were used to populate a rainflow scheme as one way of interpreting fatigue life as it relates to the earthquake duration effects. The number of cycles corresponding to different strain ranges was calculated for the two specimens tested under the spectrally matched short- and long-duration earthquakes; see Figure 5.46. These numbers were counted from the accumulated strain from all runs until failure and using different strain ranges that exceeded the yield strain value. Figure 5.46 illustrates that the long-duration runs generated significantly larger number of strain cycles than the short-duration runs, mainly in the low strain ranges. This explains why failure occurred at a lower ground-motion scale for the long-duration record relative to the short-duration record: 200% versus 225%. In other words, the lower displacement capacity observed in the long-duration test can be interpreted as premature failure. In a case of a multi-story SCBR, this can be alarming as the damaging effect of the large number of low-range strain cycles associated with longer duration earthquakes could induce brace rupture at lower interstory drifts than what would be anticipated from the seismic design or performance-based assessment.

For an alternative way of assessing fatigue life and damage accumulation, Figure 5.47 compares the estimated damage index (DI) as it built up with the different strain ranges for S1 and S2. The DI was calculated by running each strain range with its equivalent number of cycles, as shown in Figure 5.46, through the Coffin–Manson relationship, at which point Miner’s rule is applied to reach failure, i.e., $DI = 1$. As explained earlier, Coffin–Manson requires input for m and ϵ_0 , which was estimated based on the empirical values obtained from calibrating the OpenSees numerical models used in Chapter 3 in the sensitivity analysis against the respective experimental results from the UW tests. The goal here was not to validate whether these values were correct or valid for the shake table tests as well, but to use same values for the purpose of comparison between S1 and S2. The figure confirms that S1 accumulated more damage (a higher DI) at the lower strain ranges than S2; Specimen 1 reached full failure ($DI = 1$) earlier than S2. The difference in the strain range at $DI = 1$ between S1 and S2 confirms again that long-duration earthquakes can cause failure before the full anticipated displacement or strain capacity from a typical short-duration earthquake is reached. In summary, the above results show, preliminarily, that it is not a matter of how severe the ground motion is in terms of ground accelerations; it is the accumulated “low-range” strain cycles with longer duration earthquakes that could adversely affect the seismic performance of SCBFs.

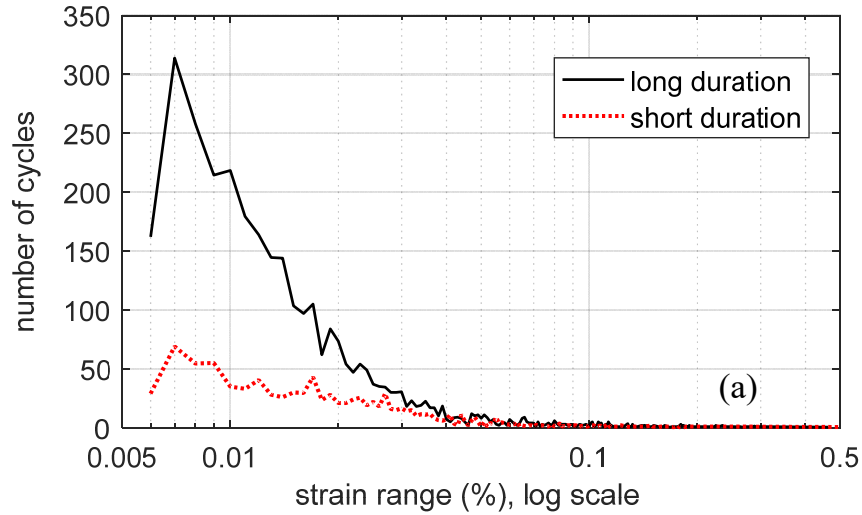


Figure 5.46 Number of cycles for different strain ranges as accumulated from all S1 and S2 runs until failure.

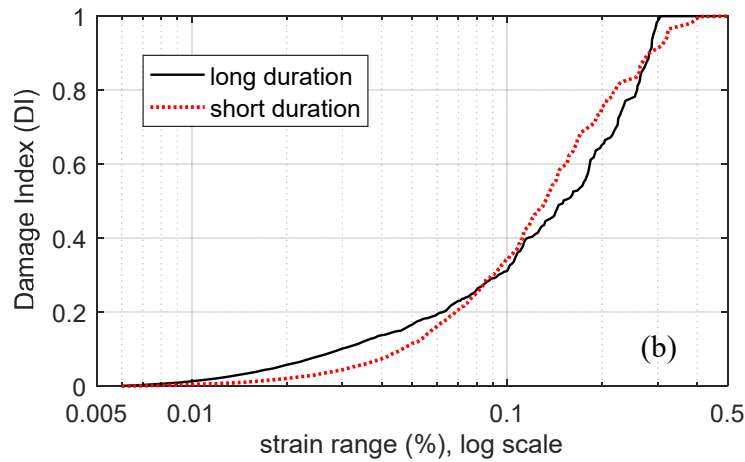


Figure 5.47 Representation of how outermost brace fiber accumulated damage from different strain ranges for all S1 and S2 runs until failure.

5.2.3 Gusset Plates Strain Data

Gusset plates play an important role in the design criteria of SCBFs as they ensure system ductility through an extreme event when the braces experience inelastic phases and act as the fuse for the structural system. Elastic deformations of upper and lower gusset plates were recorded during all shake table tests. Figures 5.48 and 5.49 show the strain data recorded for the upper and two lower gusset plates in Specimen S1 at the various locations indicated in each figure. Figures 4.50 and 4.51 and Figures 4.52 and 4.53 show same strain data but for Specimens S2 and S3, respectively. The figures and all the recorded strain data confirm that all gusset plates remained elastic during all the tests, meeting AISC design criteria; only the braces acted as fuse elements in the system.

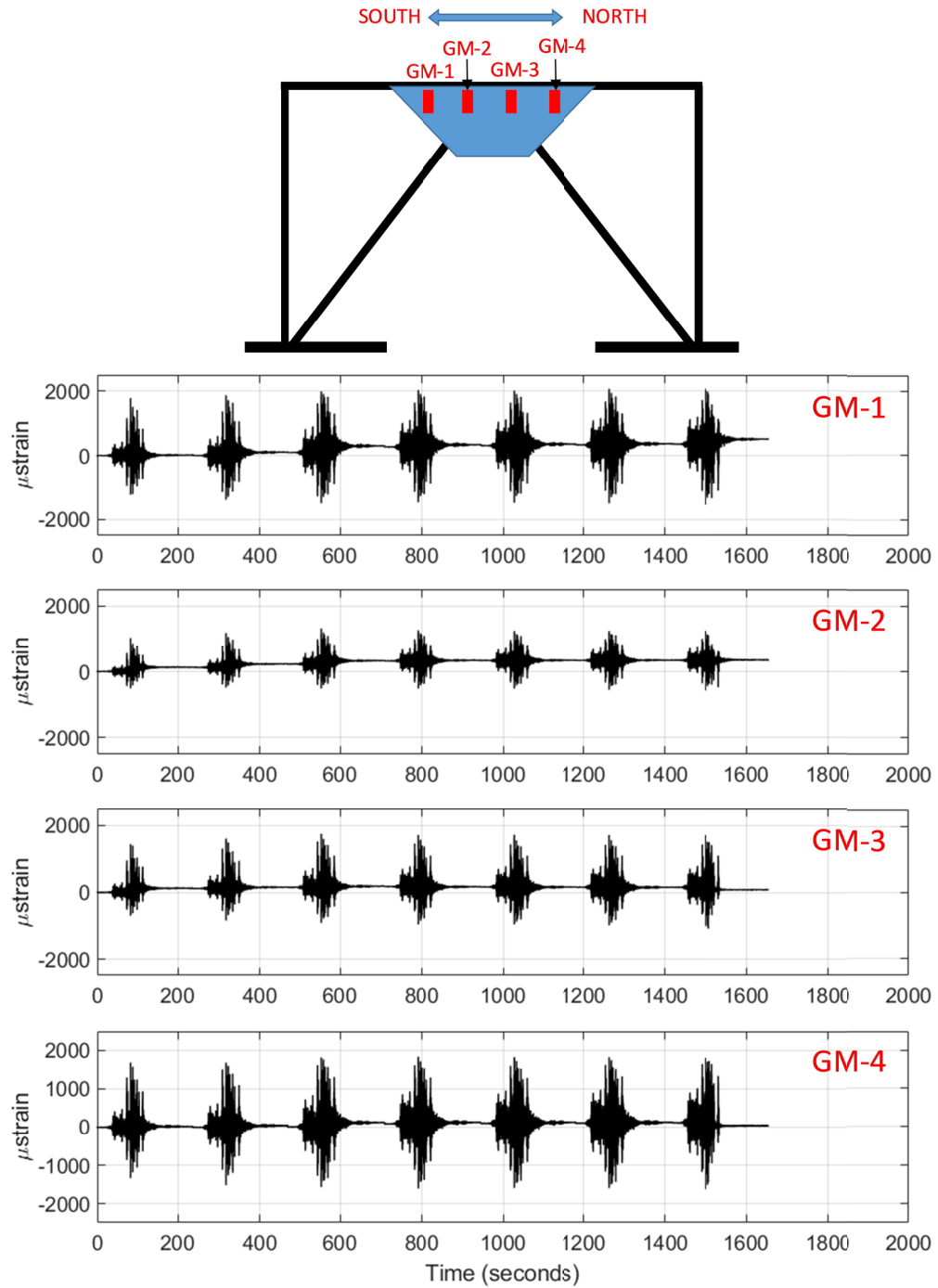


Figure 5.48 Strains in Specimen S1 middle top gusset plate at four identified locations.

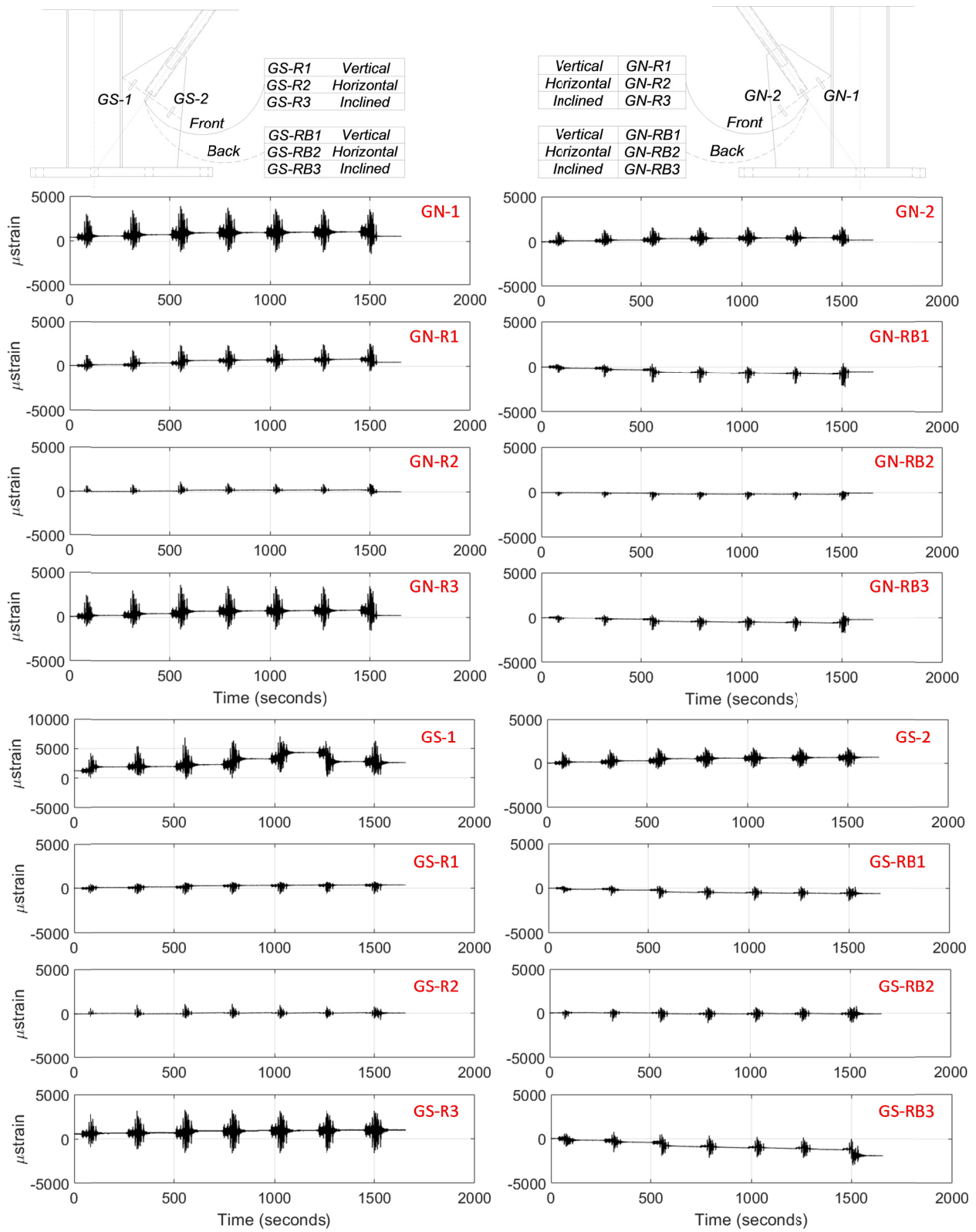


Figure 5.49 Strains in Specimen S1 lower gusset plates at the several identified locations.

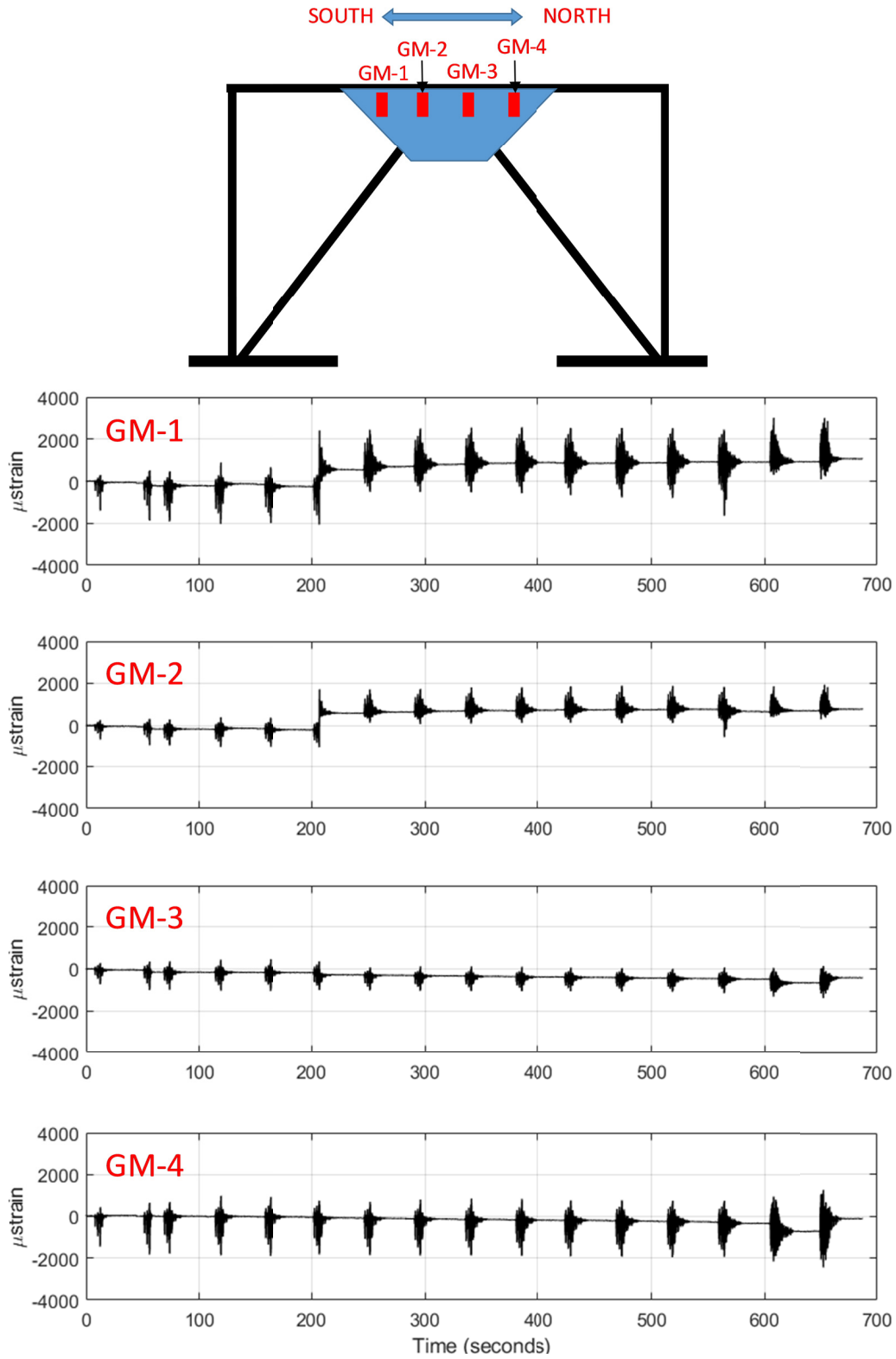


Figure 5.50 Strains in Specimen S2 middle top gusset plate at four identified locations.

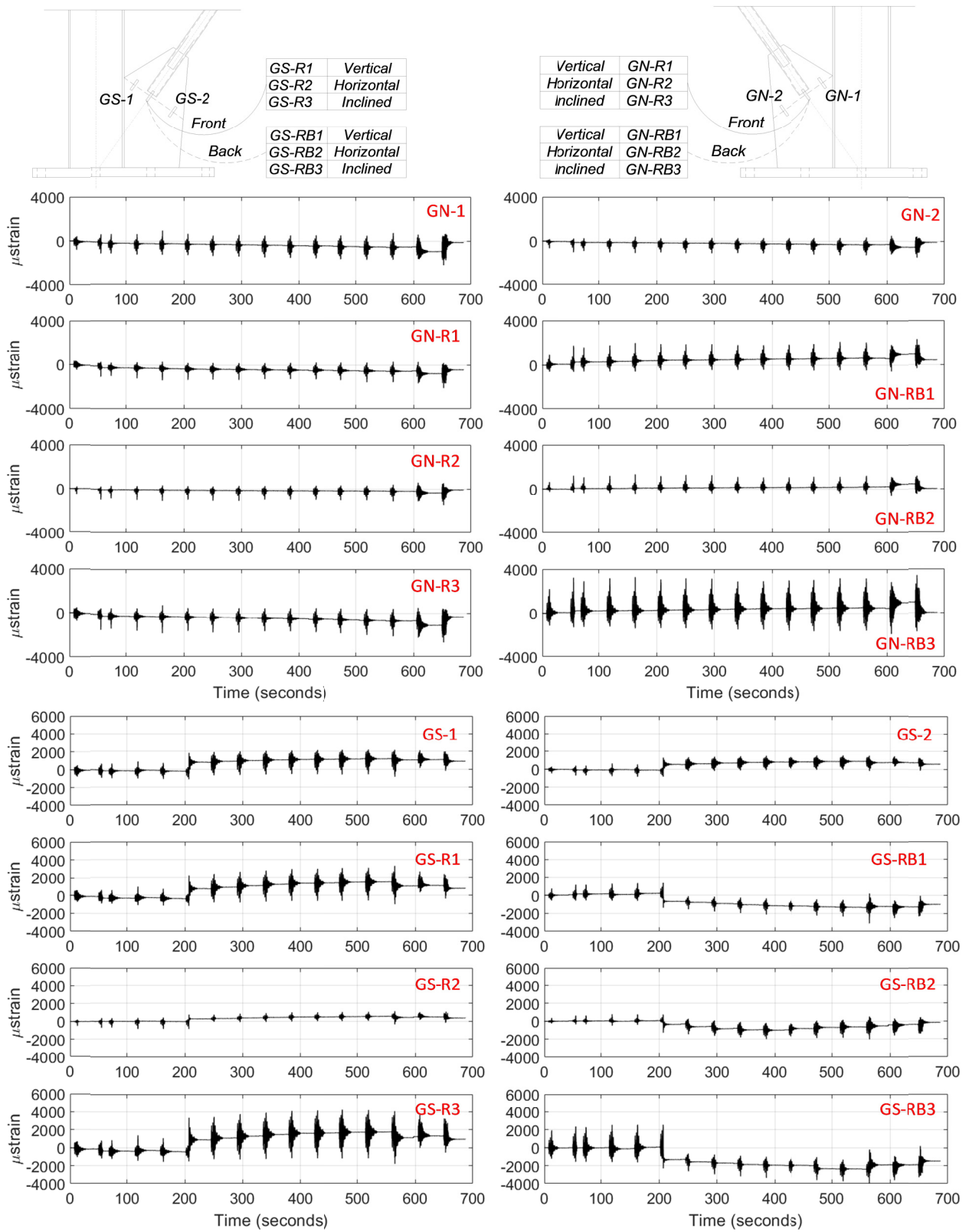


Figure 5.51 Strains in Specimen S2 lower gusset plates at the several identified locations.

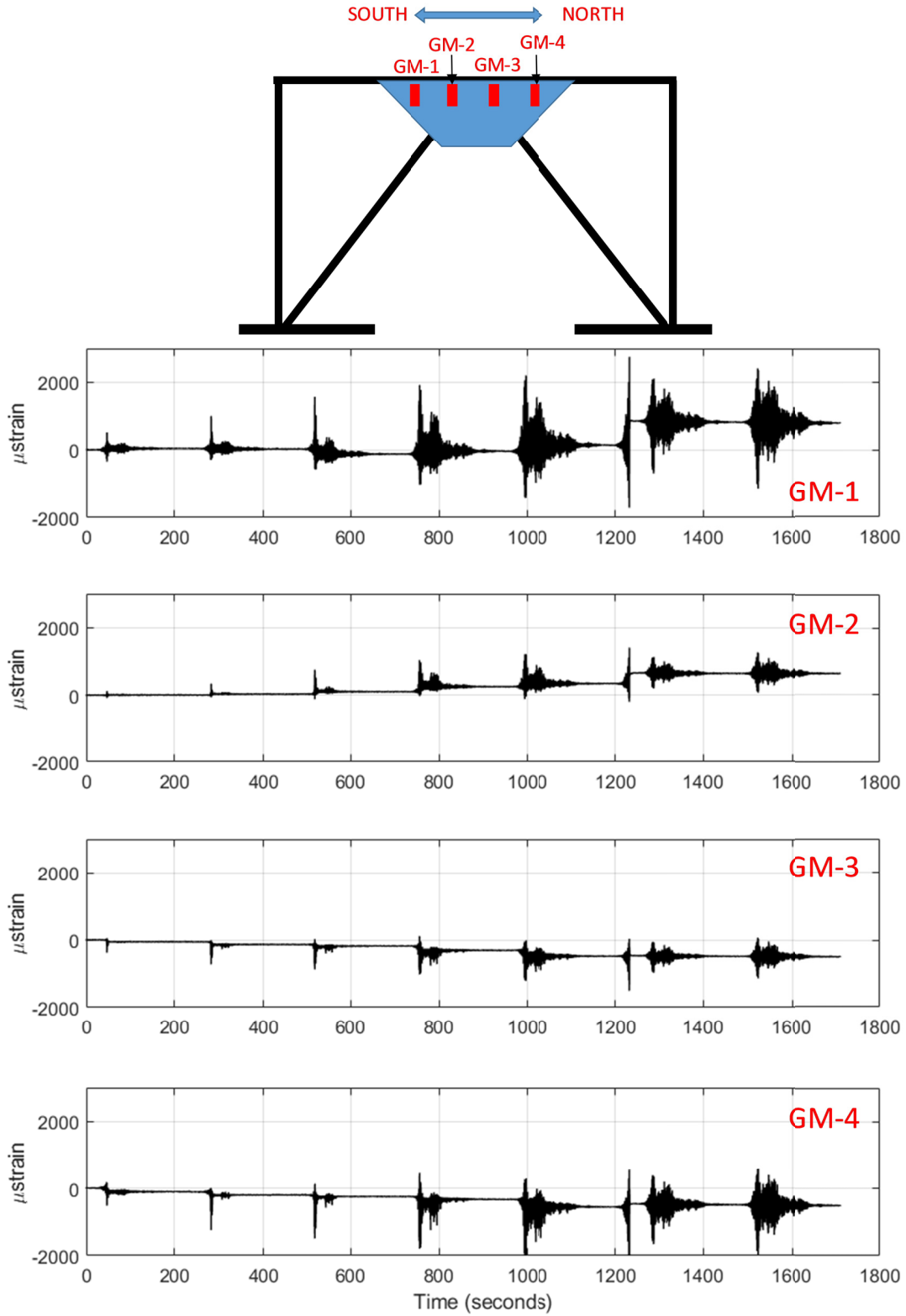


Figure 5.52 Strains in Specimen S3 middle top gusset plate at four identified locations.

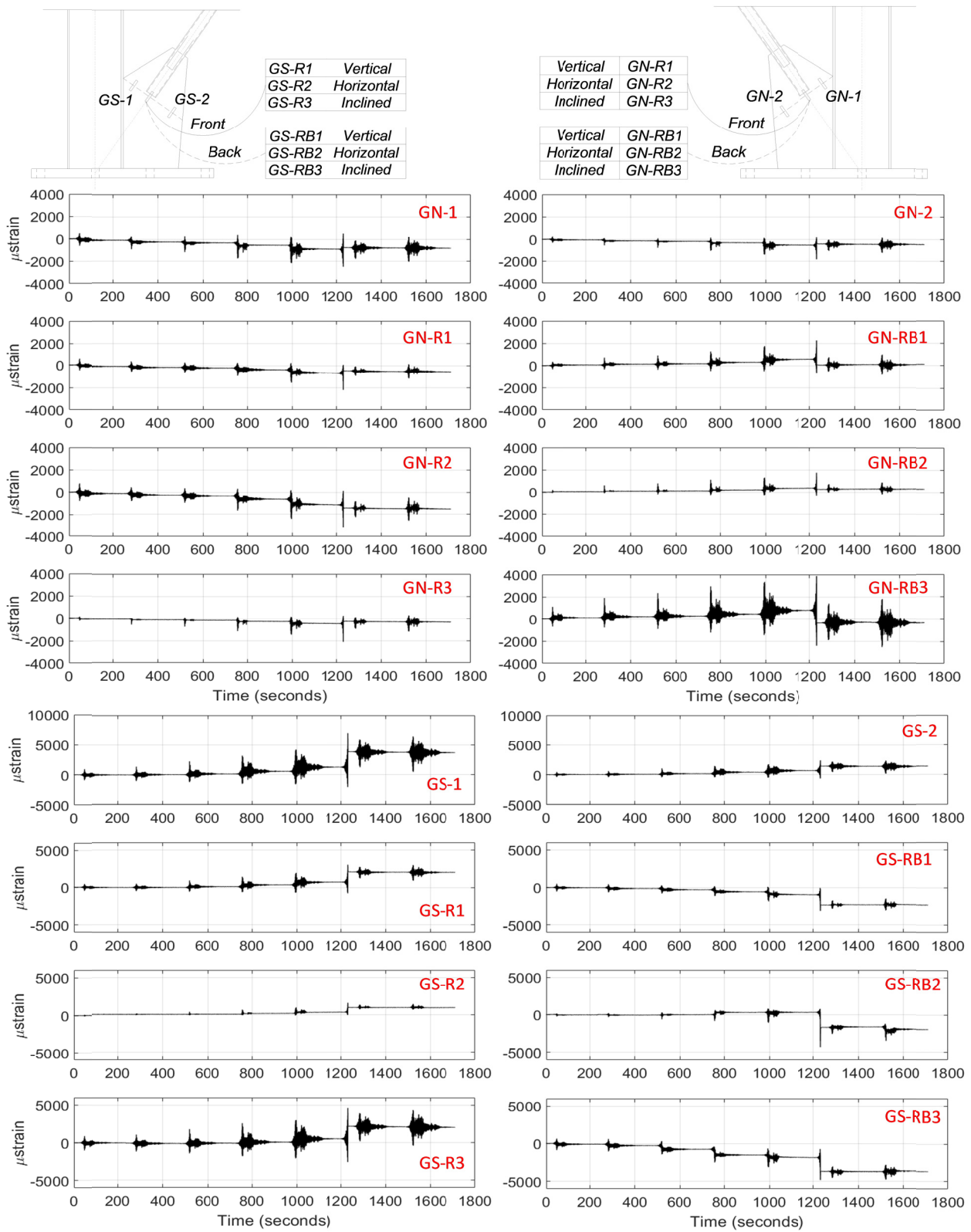


Figure 5.53 Strains in Specimen S3 lower gusset plates at the several identified locations.

5.3 GENERAL NOTES

Below are a few general notes regarding post-test observations:

- No yielding or flaking or any signs of deformation was reported in the beam at the location of the unbalanced forces of the braces. This confirms that the SCBF beams remained elastic even after the brace rupture as required by design.
- Deformation near the column connect to the base occurred; see Figure 5.54(a).
- Cracks in the welds were reported at the edge of the weld line of the bottom gusset plate with the column at one location; see is shown in Figure 5.54(b).
- At the mass rig to the south-column rigid-link connection, some hair lines appeared in the white wash at the column flange at the location of the stiffening plates; see Figure 5.54(c).

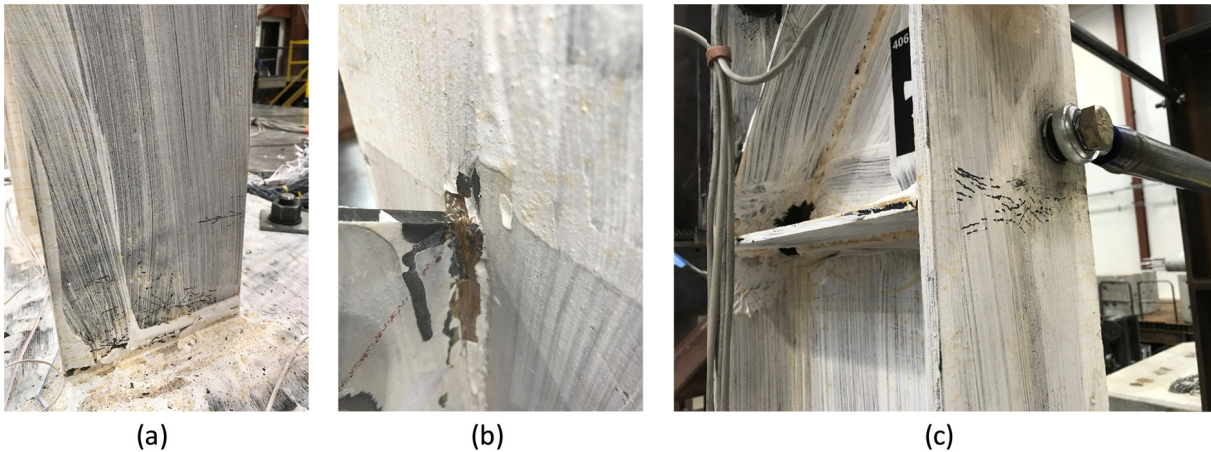


Figure 5.54 (a) Column deformation at base; (b) bottom gusset-to-column edge weld crack; and (c) yielding evidence at the link-to-column connection location.

6 Post-Test Analysis

6.1 OVERVIEW

Using results from the three 1/2-scale tested SCBFs, detailed finite-element models were calibrated as part of the post-test analysis phase and used for extensive nonlinear time history analysis. The purpose of this chapter is to use the calibrated models to generate larger number of data points on ground-motion duration effects in order to generalize and solidify the conclusions regarding the ground-motion duration effect on the structural response of SBBFs. The first part of the chapter presents the numerical model calibration for the tested specimens using OpenSees. Then, IDA was conducted using large number of short and long-duration ground motions to provide more insight on how earthquake duration effects could be addressed in future designs. For this purpose, results from the IDA were used to develop seismic fragility curves for the tested SCBFs to show the probability of collapse from the two suites of ground motions. This chapter focuses only on the tested SCBFs, where low-cycle fatigue modeling, those parameters that had been determined to affect analysis results, and seismic response of SCBFs were calibrated to gain confidence in the model's validity.

6.2 NUMERICAL MODEL CALIBRATION

To develop numerical models in OpenSees, the same details and modeling procedures, and techniques as discussed in Chapter 3 were followed. Figure 6.1 shows all the modeling details and the locations of the rigid elements used to model the one-story one-bay SCBF with a chevron-brace configuration. The figure shows all the spring locations and the spring materials used for modeling in OpenSees. Twenty nonlinear force-based elements were used to model the braces. Fiber sections were implemented for all the nonlinear frame elements in the model. While all the geometric modeling assumptions, e.g., for gusset plates, were previously verified against the UW experimental program (see Chapter 3), the new calibrations were done here because of the concern with the fatigue parameters m and ϵ_0 . Comparisons of the calibrated models results with the respective experimental data for all three specimens is presented next.

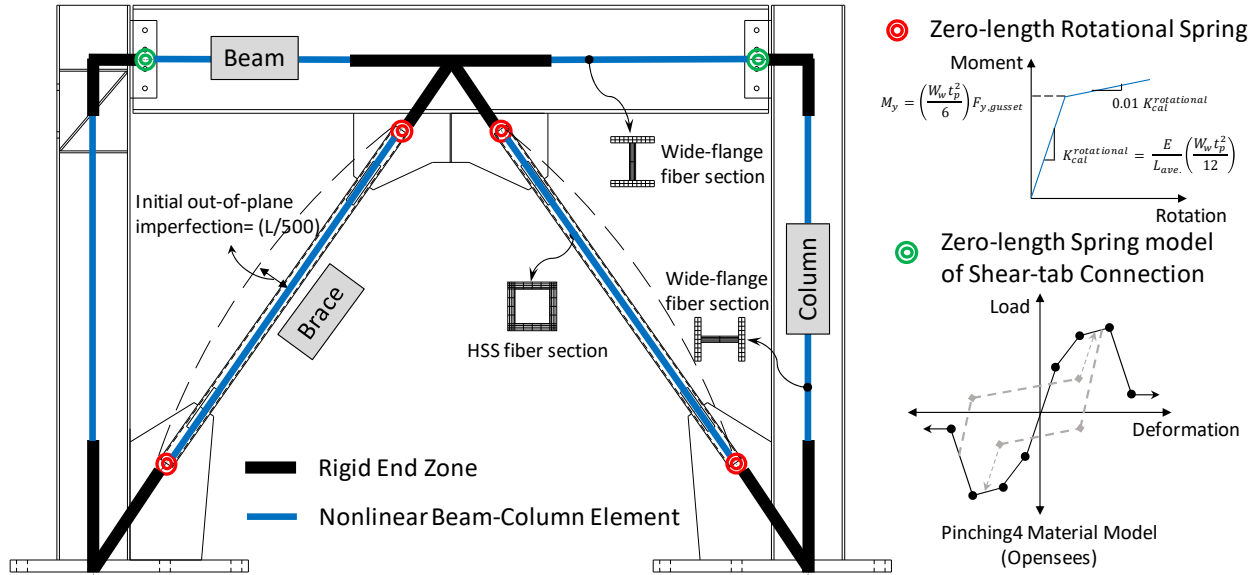


Figure 6.1 Schematic representation of the OpenSees numerical model.

To calibrate the numerical model, several results obtained from the experiments and the models were compared, which included: the frame base shear, frame top displacement, frame stiffness degradation, and the overall force-drift hysteresis. These results were thought to represent both the global and local behavior of the specimen, and capturing such response guarantees that the model accurately represents the actual frame behavior. As previously mentioned, only the fatigue parameters were varied at this stage of the research to complete the calibration process, with most of the selected values based on trial and error. Different values from the literature were considered, but none captured the onset of failure, which is known to be highly dependent on the fatigue life of the braces. After several iterations that considered all three specimens, the values found to best capture the onset of brace rupture correctly based on the three shake-table tests were $m = -0.5$ and $\varepsilon_0 = 0.23$. Note: these values were consistent for the three tests and not based on averaging.

6.2.1 Specimen S1

Specimen S1 was subjected to one of the two long-duration ground motions used in the experimental program; see Chapter 4. Using the calibrated modeling parameters for low-cycle fatigue and other modeling assumptions, the force and displacement histories from the model were obtained and compared to the experimental results; see Figures 6.2 and 6.3, respectively. The figures also present close up views or zoom-in for a range of data to better show the match between the results.

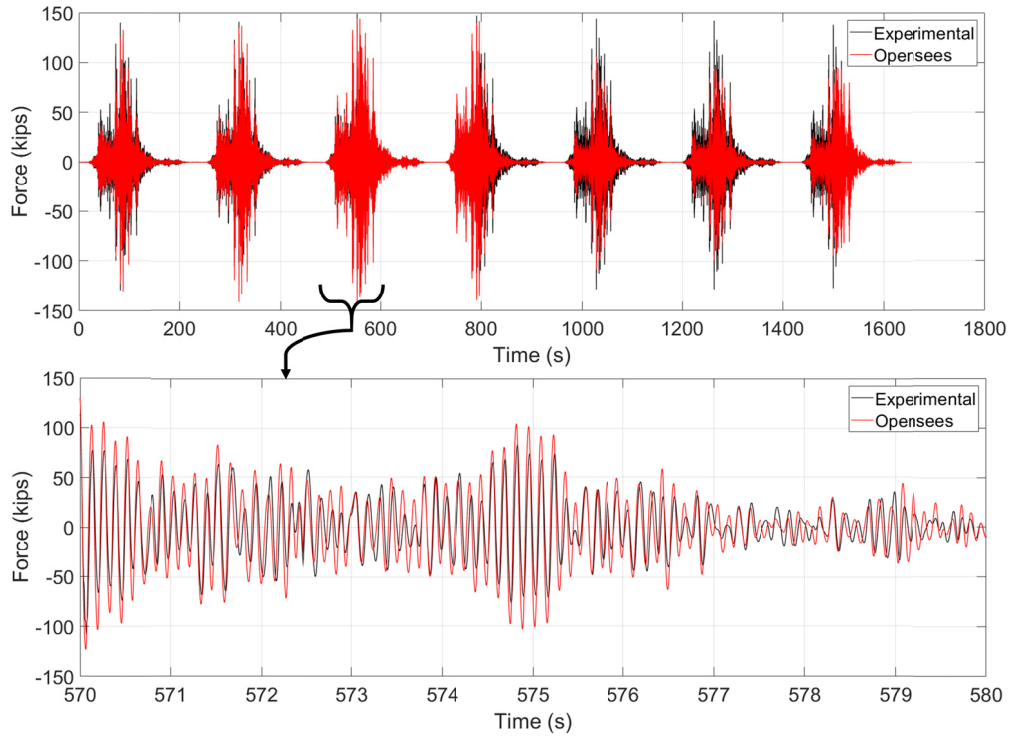


Figure 6.2 Comparison of base shear history for Specimen S1 obtained experimentally and from the OpenSees model.

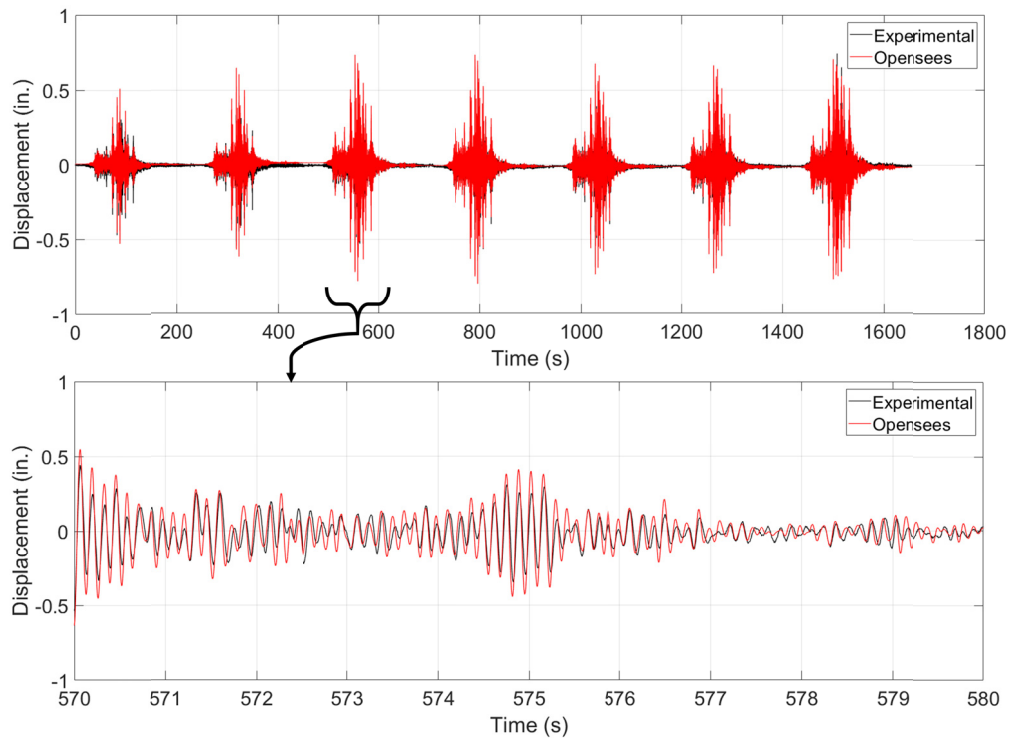


Figure 6.3 Comparison of the relative displacement history at the top of the frame as obtained for Specimen S1 obtained experimentally and from the OpenSees model.

Typically, chevron-style SCBFs experience stiffness degradation due to lateral loading that pass through several stages. The first significant drop in stiffness occurs after the first brace buckles, at which point only the brace in tension fully contributes to frame lateral capacity, while the buckled brace contributes with about 30% of its axial stiffness capacity. When the second brace buckles, the next significant drop in stiffness is associated with brace fracture. A good numerical model should capture such phases accurately with respect to both degraded stiffness values and the loading demand causing such degradation. Figure 6.4 compares the stiffness degradation as obtained from test results and that obtained from the calibrated numerical model. For ultimate verification of the calibrated model, the force-drift relationship (hysteresis) and the equivalent backbone curves for both the experimental and numerical models are shown in Figure 6.5. The force-drift curves confirm that the low-cycle fatigue induced-rupture was properly captured by the model as indicated by sudden drop in force. Other figures previously shown also demonstrate good agreement between the experimental and numerical results, validating the model and provide confidence in extending the model for IDA.

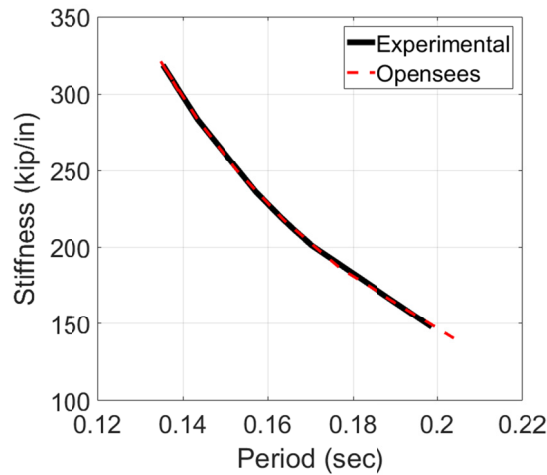


Figure 6.4 Comparison of Specimen S1 stiffness degradation obtained experimentally and from the OpenSees model.

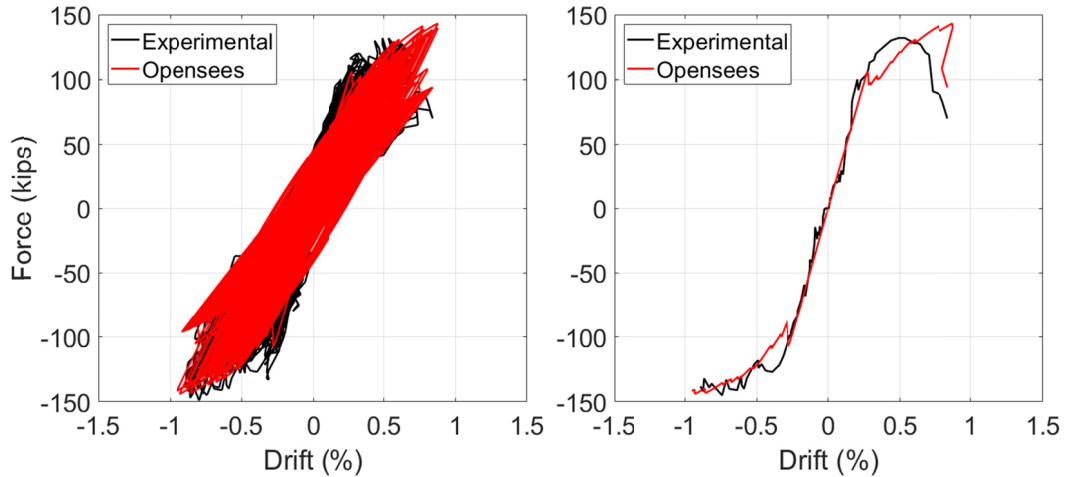


Figure 6.5 Comparison of Specimen S1 force-drift relationship (hysteresis) and backbone curves obtained experimentally and from the OpenSees model.

6.2.2 Specimen S2

Specimen S2 was tested under the spectrally-matched short-duration ground motion; see Chapters 3 and 4. Similar to what was presented for specimen S1 above, Figures 6.6 and 6.7 show the force and relative displacement at the top of the frame histories for both the experimental and numerical model results, respectively. Close up views are presented in these figures as well to better show the match between the results. Both figures show that the numerical model was able to properly capture the trends and most of the peak values, as well as other smaller values at the beginning and at the end of the test. Figure 6.8 compares the stiffness degradation obtained experimentally and from the numerical results. Figure 6.9 shows the hysteresis and backbone curves where the capability of the numerical model to capture the drop in force, which is reflected the south brace rupture, is demonstrated. Capturing brace ruptures was one of the most important calibration aspects considered an important factor in this study because it is highly dependent on the fatigue model.

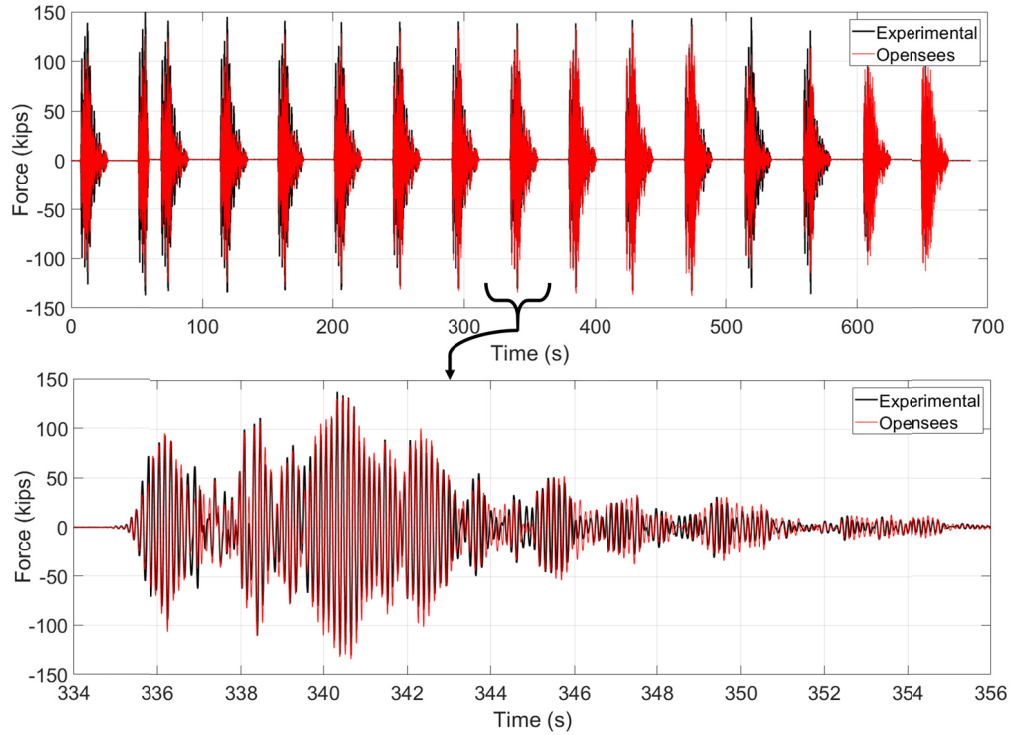


Figure 6.6 Comparison of base shear history for Specimen S2 obtained experimentally and from the OpenSees model.

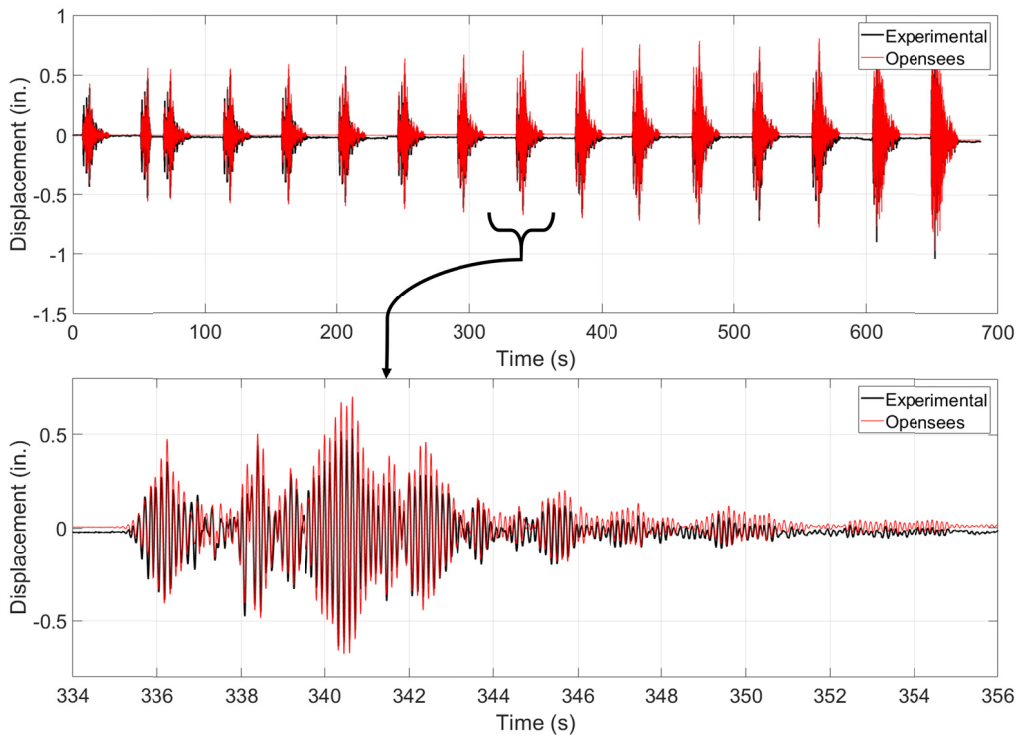


Figure 6.7 Comparison of the relative displacement history at the top of the frame as obtained for Specimen S2 obtained experimentally and from the OpenSees model.

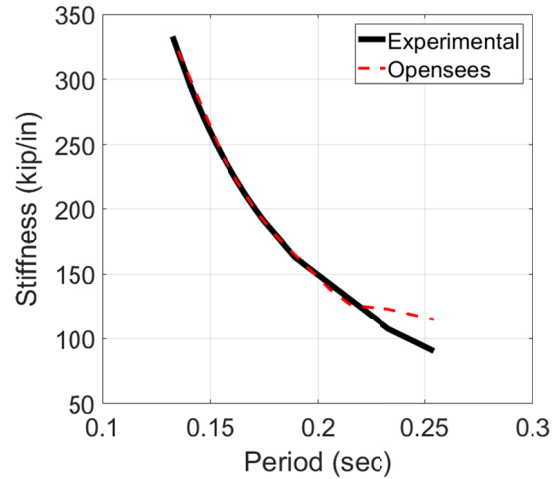


Figure 6.8 Comparison of Specimen S2 stiffness degradation obtained experimentally and from the OpenSees model.

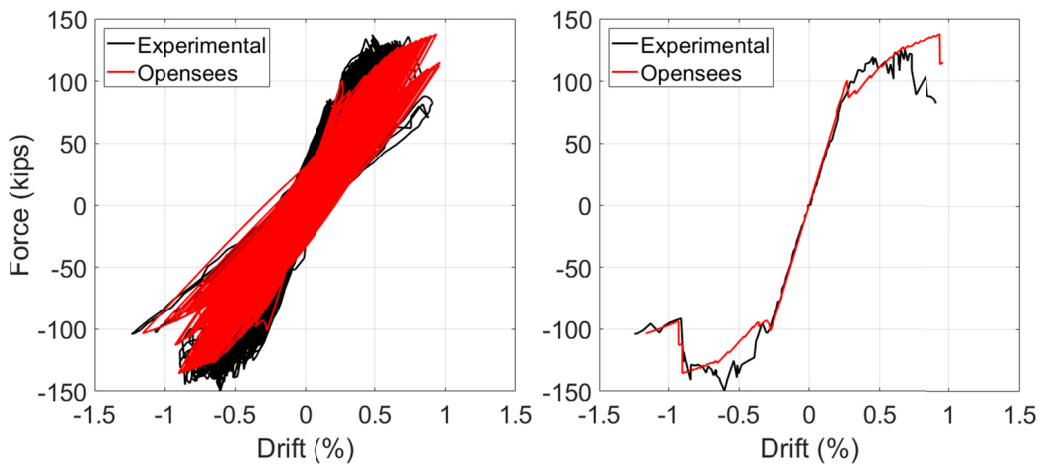


Figure 6.9 Comparison of Specimen S2 force-drift relationship (hysteresis) and backbone curves as obtained experimentally and from the OpenSees model.

6.2.3 Specimen S3

This section will validate the OpenSees model for Specimen S3, which was tested under the other long-duration ground motion where the velocity and displacement peaks shifted from the acceleration peak. Figure 6.10 shows the force history for both the experimental and numerical model results. Figure 6.11 compares the displacement histories of the experimental and numerical models. Both figures are in good agreement.

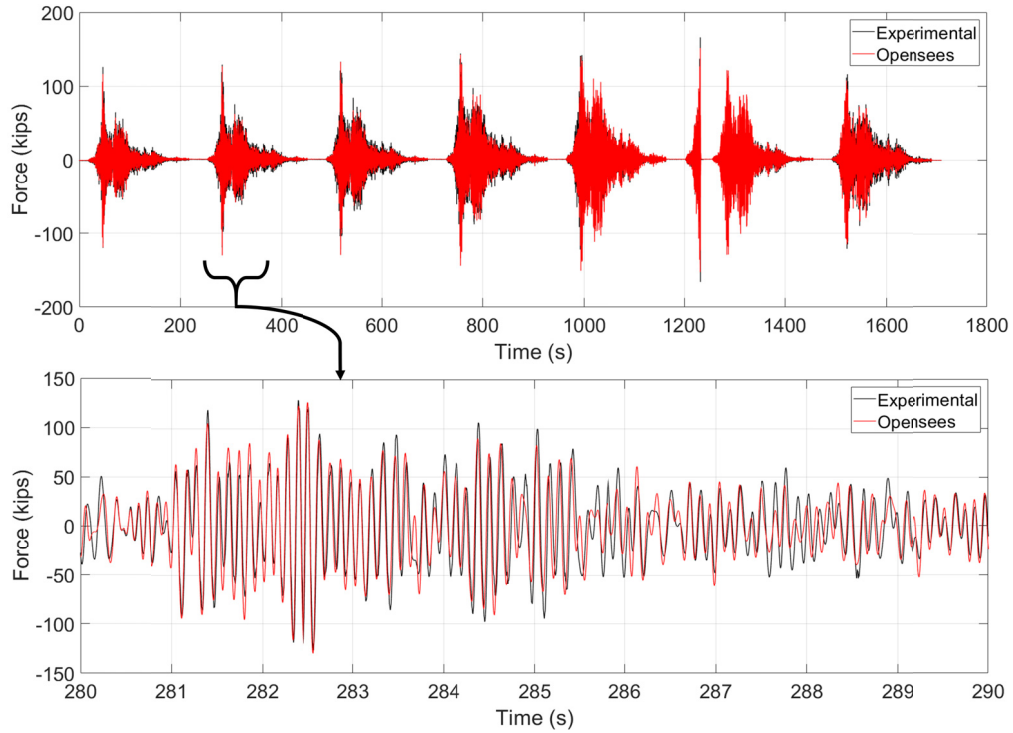


Figure 6.10 Comparison of base shear history for Specimen S3 experimentally and from the OpenSees model.

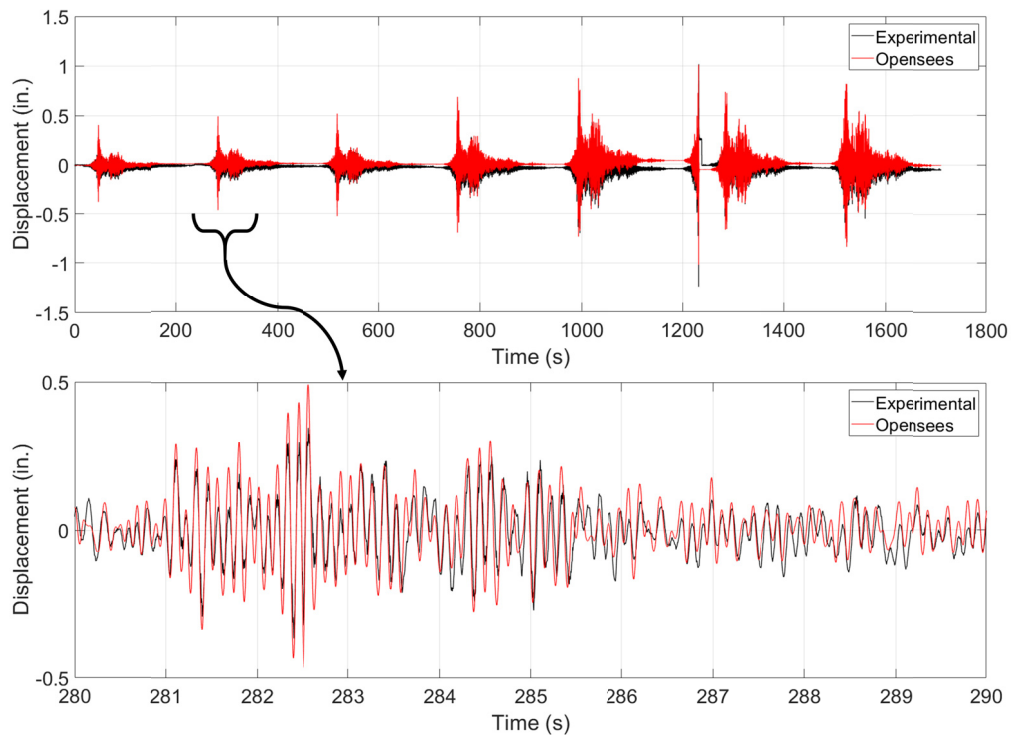


Figure 6.11 Comparison of the relative displacement history at the top of the frame obtained for Specimen S3 experimentally and from the OpenSees model.

Figure 6.12 compares of the stiffness degradation determined from the experimental and numerical results. Similar to before, this figure validates the calibrated model and indirectly indicates that the buckling and rupture of both braces were captured by the models at the correct instances. Figure 6.13 shows the hysteresis and backbone curves. Again, the backbone is in very good agreement between the onset of failure for the south brace.

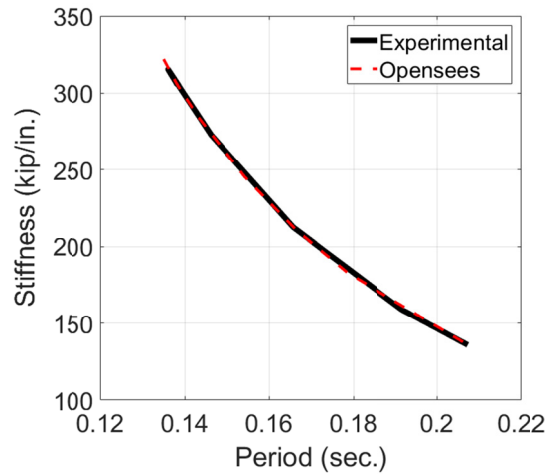


Figure 6.12 Comparison of Specimen S3 stiffness degradation obtained experimentally and from the OpenSees model.

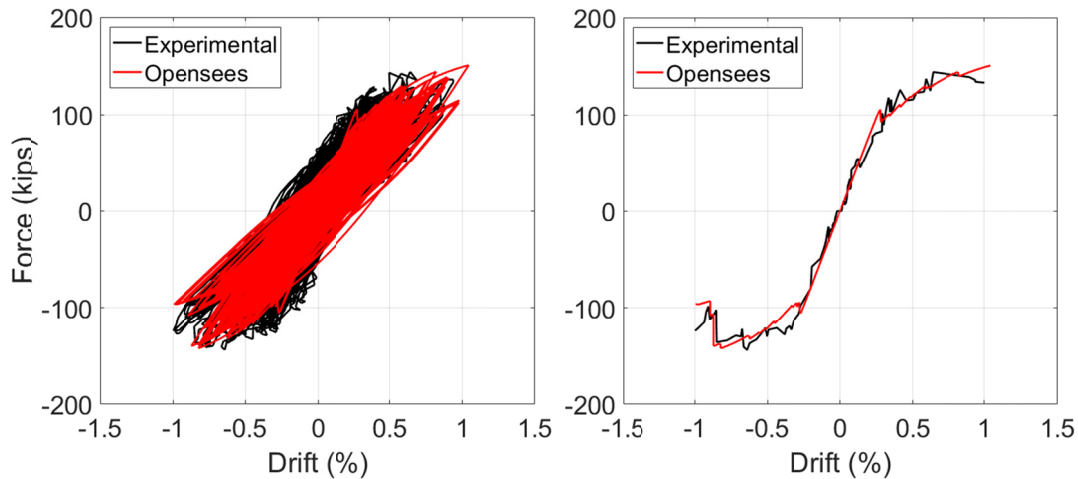


Figure 6.13 Comparison of Specimen S3 force-drift relationship (hysteresis) and backbone curves obtained experimentally and from the OpenSees model.

6.3 FATIGUE PARAMETERS ANALYSIS

The previous section confirms that the calibrated model that used trial and error to determine best values for the low-cycle fatigue model properly captured brace buckling and rupture and stiffness degradation. Worthy of further exploration is to understand further how the seismic response can vary with the other empirical low-cycle fatigue modeling parameters currently

available in the literature. The main objective of this section is to investigate the effect of the fatigue parameters, i.e., m and ε_0 previously explained in Chapter 3, on the analysis results. This exercise can be mainly used to assess the validity of such fatigue parameters reported in the literature (summarized in Table 3.1) to capture dynamic response of SCBFs, especially as it relates to earthquake duration. The assessment used results from all three experimentally tested specimens. Note: a similar comparative analysis was done as part of the sensitivity analysis discussed in Chapter 3. The comparative analysis discussed below was done for the tested specimen so that the assessment of the models can be based on the experimental results.

The previously calibrated model was used again in this part of the study with one difference where the m and ε_0 input values were varied eight times to represent the different values reported by other researchers for low-cycle fatigue modeling (Table 3.1). Given that the onset of failure and ultimate rupture is mainly attributed to the fatigue capacity of the braces, reporting and comparing the onset of failure of the braces using the different fatigue parameters was the goal of this analysis. It is important to be reminded that the empirical fatigue parameters shown in Table 3.1 were calibrated using mostly individual braces cyclic loading tests, i.e., calibration using results when braces were tested as parts of full systems or under realistic earthquake loading is missing. In addition, the reported fatigue parameters originally used mostly 20 finite elements for brace meshing, and allow using finer meshes, except for Lignos and Karamanci [2013] who used eight elements.

The results obtained from this analysis are presented in Figure 6.14–Figure 6.16 which show the force-drift backbone curves as obtained for specimens S1, S2, and S3 using a similar model with varying fatigue parameters. The figures compares the analysis results to the experimental results as well as the numerical results from the fully calibrated model demonstrated in Section 6.2 above. As seen in the figures, the different models led to different results, which highlights how the fatigue parameters can affect the inferred seismic response of SCBFs under different earthquake loading scenarios. Most of the models predicted brace rupture at lower drift values. Thus, it is important to note that even though there is large variability in the results, yet all the variation is on the conservative side where force or displacement capacities are underestimated.

To properly report the results for the sought assessment of the different models from the literature, Table 6.1 provides a summary of the obtained force and drift capacities at brace rupture in both loading directions for all different models. The table also provides the difference (%) in the analysis results relative to the experimental results for all the three specimens. Moreover, the results from comparison against all three tests were used to calculate the absolute (no signs) average variation from experiments as presented for force and drift capacities in Tables 6.2 and 6.3, respectively. Overall, the values provided by Salawdeh and Goggins [2013] can be considered the most relatively accurate in predicting the observed experimental behavior with an average variation of 6.8% and 7.3% in force and drift capacity, respectively. On the other hand, values reported by Chen and Mahin [2010] seem to give the largest variation from the experimental results with an average variation of 15% and 39.83% in force and drift capacity, respectively. The tables also quantify the variation in case of the calibrated values obtained from trial and error with an average variation of 6.5% and 1.7% in force and drift capacity, respectively.

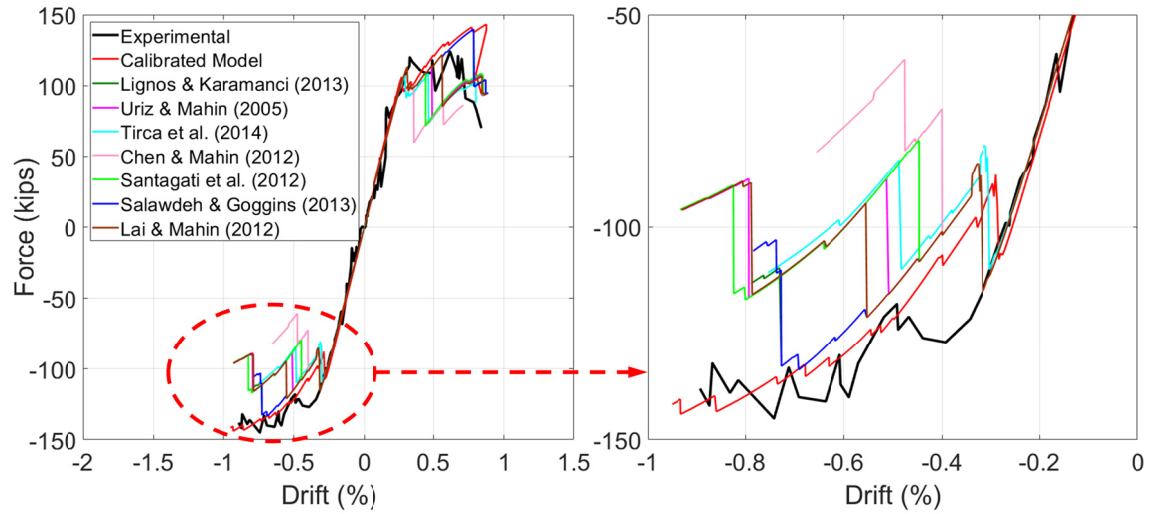


Figure 6.14 Force-drift backbone for Specimen S1 modeled using different low-cycle fatigue parameters.

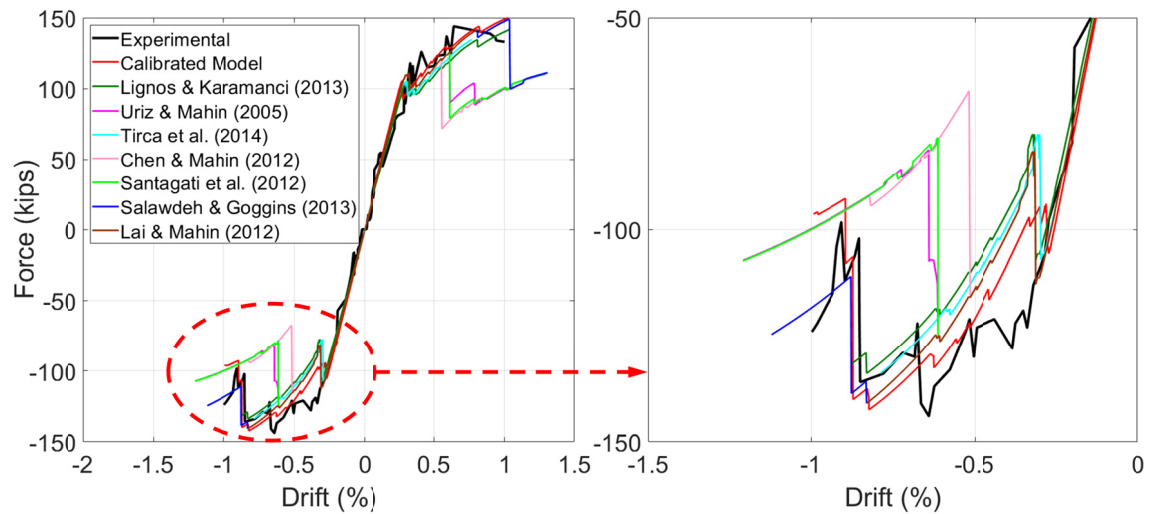


Figure 6.15 Force-drift backbone for Specimen S2 modeled using different low-cycle fatigue parameters.

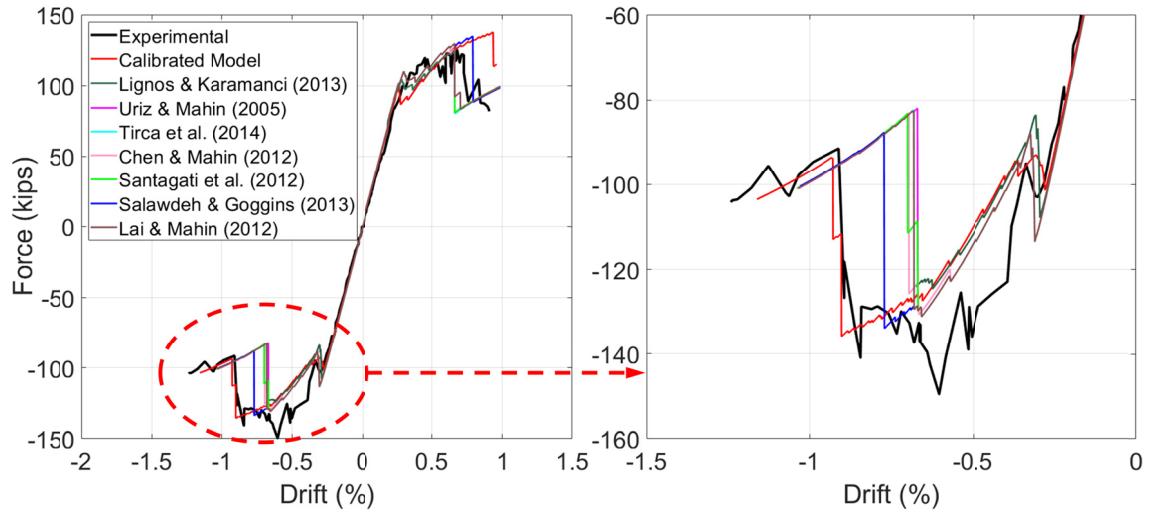


Figure 6.16 Force-drift backbone for Specimen S3 modeled using different low-cycle fatigue parameters.

Table 6.1 Summary of analysis results for varying low-cycle fatigue model parameters (m and ϵ_0) as compared to experimental results.

Basis for fatigue model parameters	North results at rupture		South direction (results at rupture)		Difference relative to experiments (%)			
	Force (kips)	Drift (%)	Force (kips)	Drift (%)	North direction		South direction	
					Force	Drift	Force	Drift
Specimen S1								
Experimental	125	0.82	145	0.85	N/A	N/A	N/A	N/A
Lignos and Karamanci [2013]	140	0.79	132	0.76	12.0	-3.7	-9.0	-10.6
Uriz and Mahin [2000]	115	0.50	115	0.50	-8.0	-39.0	-20.7	-41.2
Tirca and Chen [2014]	109	0.44	110	0.47	-12.8	-46.3	-24.1	-44.7
Chen and Mahin [2010]	99	0.38	102	0.40	-20.8	-53.7	-29.7	-52.9
Santagati et al. [2012]	109	0.42	108	0.45	-12.8	-48.8	-25.5	-47.1
Salawdeh and Goggins [2013]	140	0.79	132	0.76	12.0	-3.7	-9.0	-10.6
Lai and Mahin [2012]	122	0.56	121	0.55	-2.4	-31.7	-16.6	-35.3
Calibrated model (this study)	143	0.83	142	0.87	14.4	1.22	-2.1	2.4
Specimen S2								
Experimental	125	0.90	141	0.92	N/A	N/A	N/A	N/A
Lignos and Karamanci [2013]	124	0.66	125	0.70	-0.8	-26.7	-11.4	-23.9
Uriz and Mahin [2000]	127	0.66	130	0.69	1.6	-26.7	-7.8	-25.0
Tirca and Chen [2014]	126	0.66	129	0.70	0.8	-26.7	-8.5	-23.9
Chen and Mahin [2010]	126	0.66	131	0.71	0.8	-26.7	-7.1	-22.8
Santagati et al. [2012]	126	0.66	129	0.70	0.8	-26.7	-8.5	-23.9
Salawdeh and Goggins [2013]	134	0.80	133	0.78	7.2	-11.1	-5.7	-15.2
Lai and Mahin [2012]	126	0.66	131	0.69	0.8	-26.7	-7.1	-25.0
Calibrated model (this study)	137	0.93	136	0.92	9.6	3.33	-3.6	-0.5
Specimen S3								
Experimental	143	1.00	137	0.83	N/A	N/A	N/A	N/A
Lignos and Karamanci [2013]	141	0.81	133	0.81	-1.4	-19.0	-2.9	-2.4
Uriz and Mahin [2000]	125	0.61	125	0.62	-12.6	-39.0	-8.8	-25.3
Tirca and Chen [2014]	134	0.78	135	0.79	-6.3	-22.0	-1.5	-4.8
Chen and Mahin [2010]	121	0.57	115	0.50	-15.4	-43.0	-16.1	-39.7
Santagati et al. [2012]	125	0.61	125	0.62	-12.6	-39.0	-8.8	-25.3
Salawdeh and Goggins [2013]	149	1.02	141	0.84	4.2	2.0	2.9	1.2
Lai and Mahin [2012]	141	0.81	141	0.81	-1.4	-19.0	2.9	-2.4
Calibrated model (this study)	151	1.02	142	0.84	5.6	2.0	3.7	0.6

Table 6.2 Summary and average value for variation (%) in force values from experimental results associated with varying low-cycle fatigue model parameters.

Basis for fatigue model parameters	S1		S2		S3		Average
Lignos and Karamanci [2013]	12.0	9.0	0.8	11.4	1.4	2.9	6.3
Uriz and Mahin [2000]	8.0	20.7	1.6	7.8	12.6	8.8	9.9
Tirca and Chen [2014]	12.8	24.1	0.8	8.5	6.3	1.5	9.0
Chen and Mahin [2010]	20.8	29.7	0.8	7.1	15.4	16.1	15.0
Santagati et al. [2012]	12.8	25.5	0.8	8.5	12.6	8.8	11.5
Salawdeh and Goggins [2013]	12.0	9.0	7.2	5.7	4.2	2.9	6.8
Lai and Mahin [2012]	2.4	16.6	0.8	7.1	1.4	2.9	5.2
Calibrated model (this study)	14.4	2.1	9.6	3.6	5.6	3.7	6.5

Table 6.3 Summary and average value for variation (%) in drift values from experimental results associated with varying low-cycle fatigue model parameters.

Basis for fatigue model parameters	S1		S2		S3		Average
Lignos and Karamanci [2013]	3.7	10.6	26.7	23.9	19	2.4	11.9
Uriz and Mahin [2000]	39	41.2	27	25	39	25.3	32.7
Tirca and Chen [2014]	46.3	44.7	27	23.9	22	4.8	28.1
Chen and Mahin [2010]	53.7	52.9	27	22.8	43	39.7	39.8
Santagati et al. [2012]	48.8	47.1	27	23.9	39	25.3	35.1
Salawdeh and Goggins [2013]	3.7	10.6	11	15.2	2	1.2	7.3
Lai and Mahin [2012]	31.7	35.3	27	25	19	2.4	23.4
Calibrated model (this study)	1.22	2.4	3.3	0.5	2	0.6	1.7

6.4 INCREMENTAL DYNAMIC ANALYSIS

Incremental dynamic analysis (IDA) [Vamvatsikos and Cornell 2002] is a common analysis method where structures are analyzed using incrementally scaled ground motions until structural collapse occurs. IDA is frequently conducted using generic ground-motion sets such as the FEMA P695 [2005] far-field set, which was developed to be structure and site independent, and do not represent the seismic hazard at any particular site. Although IDA can be conducted using site-specific ground motions, the additional effort involved in selecting these ground motions makes unattractive [Chandramohan 2016]. Even if site-specific ground motions are used, using the same set of ground motions scaled to different intensity levels has been shown to produce inaccurate, hazard-inconsistent structural collapse risk estimates, since ground motions of different intensities are inherently expected to possess different characteristics. A procedure to compute a hazard consistent median collapse capacity by iteratively conducting a modified version of IDA using ground motions selected to match targets conditional on different successive intensity levels is described in FEMA P-58 [FEMA 2018, Appendix J], but this

method is limited and cumbersome. Most of the recent work at Stanford University [Chandramohan 2016] that incorporated ground-motion duration and response spectral shape used generic record sets to compute hazard-consistent collapse fragility curves using IDA. For such studies, two suites of short- and long-duration ground motions were used, which were the same ground motions used for this part of study as explained below.

In this section, selected ground motions were used to conduct an IDA on the structural model of the single-bay/single-story building. Each ground motion was scaled to incrementally higher intensity levels until structural collapse, indicated by both braces rupturing. The collapse intensity of each ground motion, expressed in terms of the spectral acceleration at fundamental period, i.e., $S_a(T_1)$ value when scaled to the lowest intensity level required to cause structural collapse, was recorded similar to several previous studies (e.g., Chandramohan [2016]). The same previously calibrated model discussed in Section 6.2 was used with the fatigue parameters found from trial and error to best match the experimental results.

6.4.1 Ground-Motion Selection

In order to further study the ground-motion duration effect, a large number of ground motions was used to conduct IDA. For the purpose of determining the duration effect, it is important to establish a comparative reference—such as using spectrally-matched ground motions—that vary only in the duration. Thus, 44 pairs of ground motions were used in this study. Each pair has one short- and one long-duration motion, both are having the same spectral shape to guarantee that the only difference is the duration. Previous studies have used different criteria to define long-duration motions. Chandramohan et al. [2013] used motions with significant duration, $D_s(5-95\%) > 45$ sec. Chandramohan [2016] used ground motions with significant duration, $D_s(5-75\%) > 25$ sec. Ou et al. [2014] differentiated between short- and long-duration motions based on the number of times the 5% of a given PGA level is crossed. Ground motions with a number of crossings exceeding 600 (approximately) were considered as long-duration motions. In this study, the 5–75% was used with the definition proposed by Chandramohan et al. [2016(a); (b)], i.e., $D_s(5-75\%) > 25$ sec.

A generic set of 88 recorded ground motions was selected to analyze the structure, which was adopted from the previous work by Chandramohan [2016] and is listed in detail in Appendix D. The selected motions do not represent the hazard at any specific site. The 88 records is composed of two suites of ground motions, Forty-four of these ground motions were taken from the FEMA P695 far-field set, which contains relatively short-duration ground motions [with $D_s(5-75\%) < 25$ sec], recorded from shallow crustal earthquakes. The remaining 44 records were selected from long-duration ground motions [with $D_s(5-75\%) > 25$ sec] recorded from both large magnitude interface earthquakes such as the 2011 Tohoku (Japan), 2010 Maule (Chile), and 1985 Michoacan (Mexico) earthquakes, and large-magnitude crustal earthquakes such as the 2008 Wenchuan (China) and 2002 Denali (U.S.) earthquakes.

The ground-motion selection per Chandramohan [2016] was done so that the 88 selected records had a wide range of $D_s(5-75\%)$ values that covers the broad range of ground-motion durations anticipated in Seattle, which is located near the Cascadia subduction zone and at great risk from a large magnitude, long-duration earthquake. In addition, each of the 44 long-duration ground motions was selected to have a similar response spectrum to one of the short-duration

ground motions. Readers are referred to Chandramohan [2016] for details of the selection and scaling procedure along with full information on the selected records' response spectra and time series. For convenience, the list of all 88 ground motions used in this study is provided in Appendix D and presented in 44 pairs to show the one-to-one record match. Figure 6.17 shows the response spectrum of each ground motion in each set along with their mean spectrum. Then, the means of each of the short and long-duration suites are compared in Figure 6.18 to show the anticipated match.

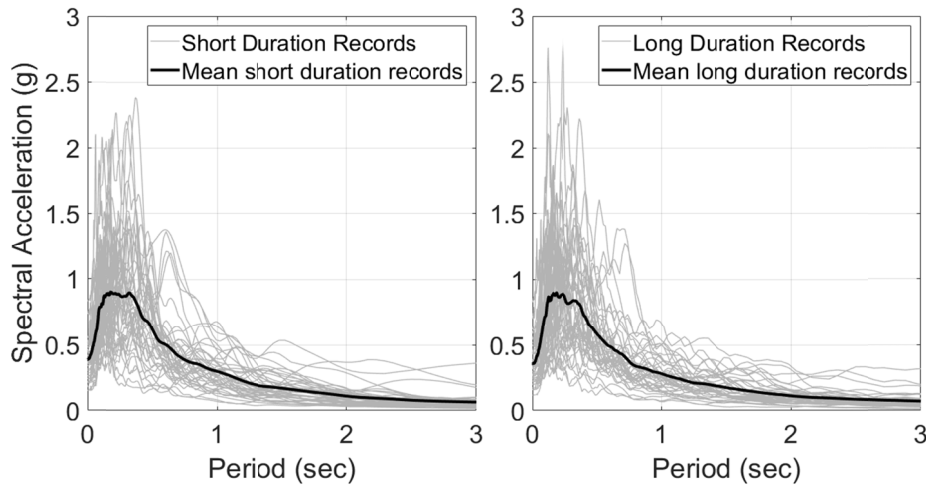


Figure 6.17 Short- and long-duration ground-motion response spectrum and their mean.

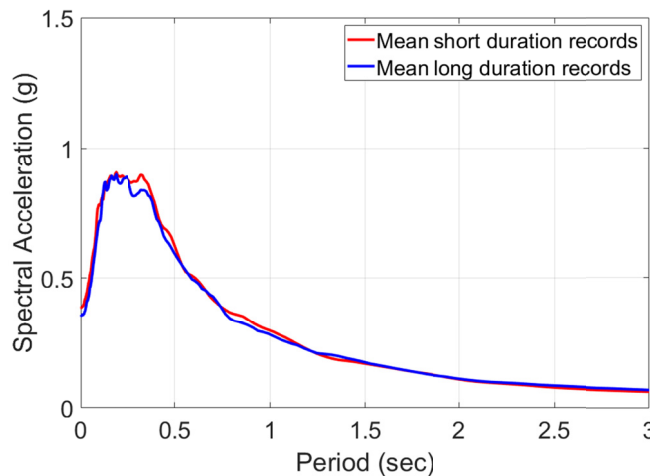


Figure 6.18 Mean response spectrum for short- and long-duration ground-motion suites.

6.4.2 Development of Collapse Fragility Curve

As previously explained, IDA is an analysis method used to apply ground motions incrementally until collapse occurs. Results from IDA are typically used to develop fragility curves, which is an objective of this study. Two sets of IDA analyses were conducted: one under the 44 short-

duration ground motions and the other set used the 44 long-duration ground motions. All analyses were conducted on the tested specimens using the calibrated OpenSees model. Figures 6.19 and 6.20 show the IDA results from the incremental nonlinear time-history analysis when the percentage of drift is related to either the peak ground acceleration (PGA) or spectral acceleration (S_a) as an IM, respectively. In general, lower drift capacities can be seen in case of long-duration records (parts b in both figures). The effect of the long-duration earthquakes is explained as accumulating more fatigue damage in the braces at lower drift ratios because of larger number of loading cycles in long-duration earthquakes, which can cause complete brace rupture.

The results from IDA analysis were used to develop two types of collapse fragility curves based on which IN is used. Figures 6.21(a) and (b) compare the developed collapse fragility curves from the short- and long-duration earthquakes for PGA and S_a IMs, respectively. As shown in Figure 6.21, the long-duration set led to a higher probability of exceedance or collapse for a given IM. The difference in the median fragility is about 45% in the drift capacity at failure, i.e., a reduction from 1.20% drift capacity to only 0.82% due to longer duration earthquakes. Note that the difference in the median fragility is about 10% in the spectral acceleration at failure, i.e., a reduction from 1.75g spectral acceleration to 1.58g due to longer duration earthquakes. Overall, these trends agree to some extent with what was reported by Raghunandan et al. [2015] and Chandramohan et al. [2016a; 2016b]. For instance, Chandramohan et al. [2016a; 2016b] reported that the median displacement collapse capacity changed by about 29% when longer duration earthquakes are applied for modern steel moment frames. Note: the median drift % values shown in the results of the IDA almost match the results obtained from the experiments, specifically Specimens S1 and S2.

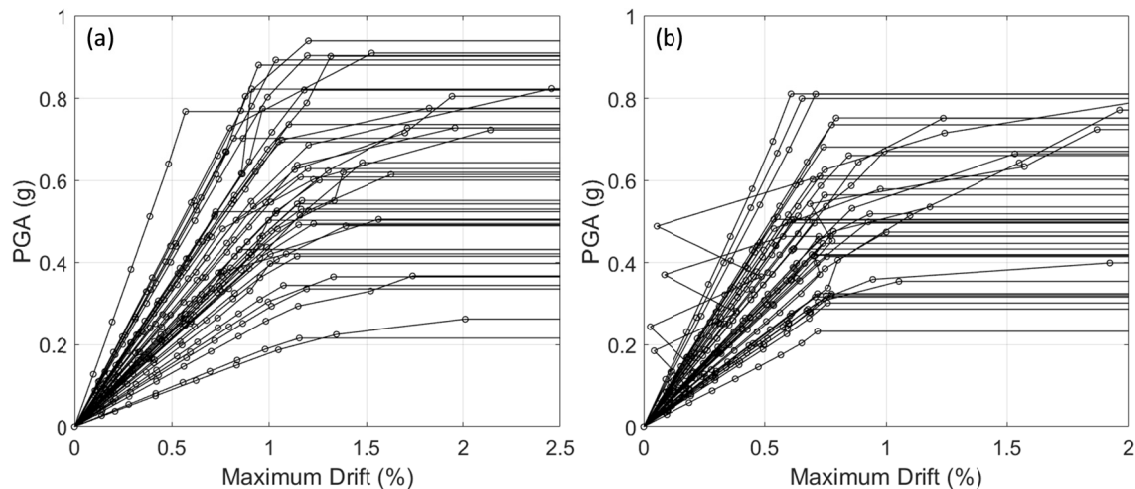


Figure 6.19 IDA results for story drift as relates to PGA as the intensity measure.

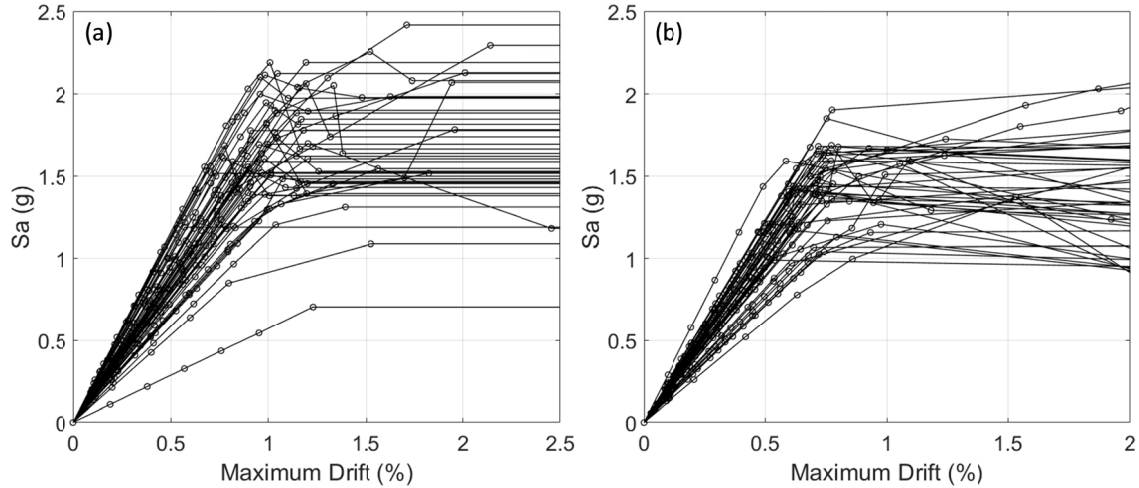


Figure 6.20 IDA results for story drift as relates to S_a as the intensity measure.

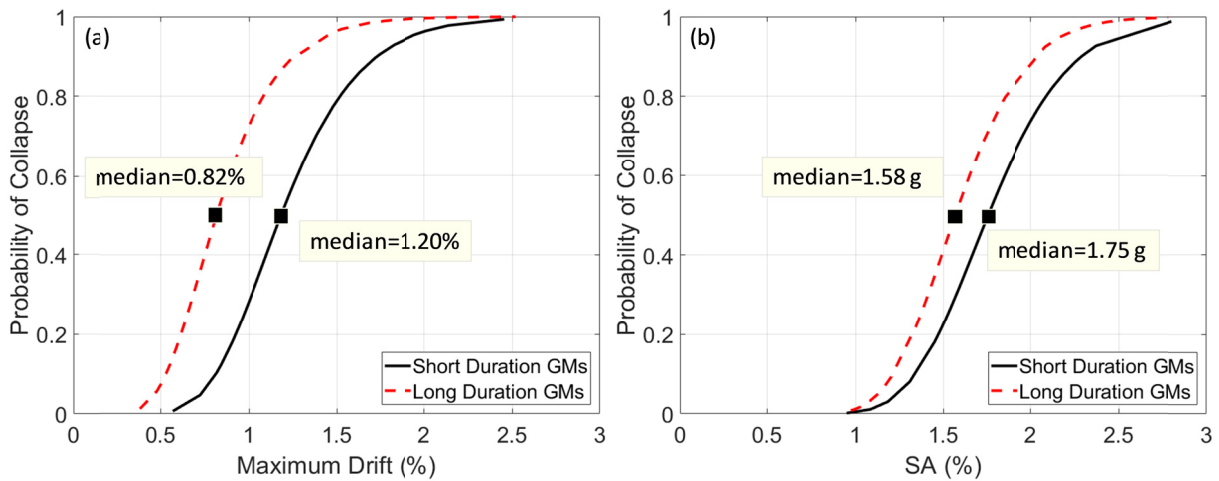


Figure 6.21 Developed fragility curves for one-story one-bay SCBF with chevron braces (test specimens) using two intensity measures: (a) drift %, and (b) spectral acceleration.

6.4.3 Collapse Assessment

Using the same nonlinear time-history analyses cases previously obtained from IDA, results were interpreted differently to further understand the effect of duration. In this regard, a preliminary regression analysis was conducted to determine if there is a relationship or trend between the ground-motion significant duration and the drift capacity; see Figure 6.22. An inverse linear trend can be observed in the figure where results from all 88 analyses done for the tested specimen OpenSees model were considered altogether. As shown in Figure 6.22, the best fitted linear regression shows that the obtained drift capacity from analysis is reduced by about 8% on average for every additional 10 sec in ground-motion significant duration. Similarly, Figure 6.23 shows the relationship between the ground-motion significant duration and the spectral acceleration where an inverse trend is obvious. The reduction is about 5% on average for every 10 sec in ground-motion significant duration.

The trends observed from Figures 6.22 and 6.23 seem to agree with the recent study by Chandramohan et al. [2016a; 2016b], who reported a clear trend between the spectral acceleration ratio as an EDP, and significant duration D_s (5–75%). The trend showed a smaller collapse capacity as a function of ground-motion duration. This finding supports previous studies in demonstrating that not only higher intensity ground motions would lead to damage or might lead to collapse, but lower spectral acceleration accompanied by other effects—such as longer durations—may have similar effects and lead to structural members failure or full collapse. This highlights once again the importance of future consideration of ground-motion duration as part of design codes, at least for specific sites where long-duration ground motions are expected such as the Pacific Northwest.

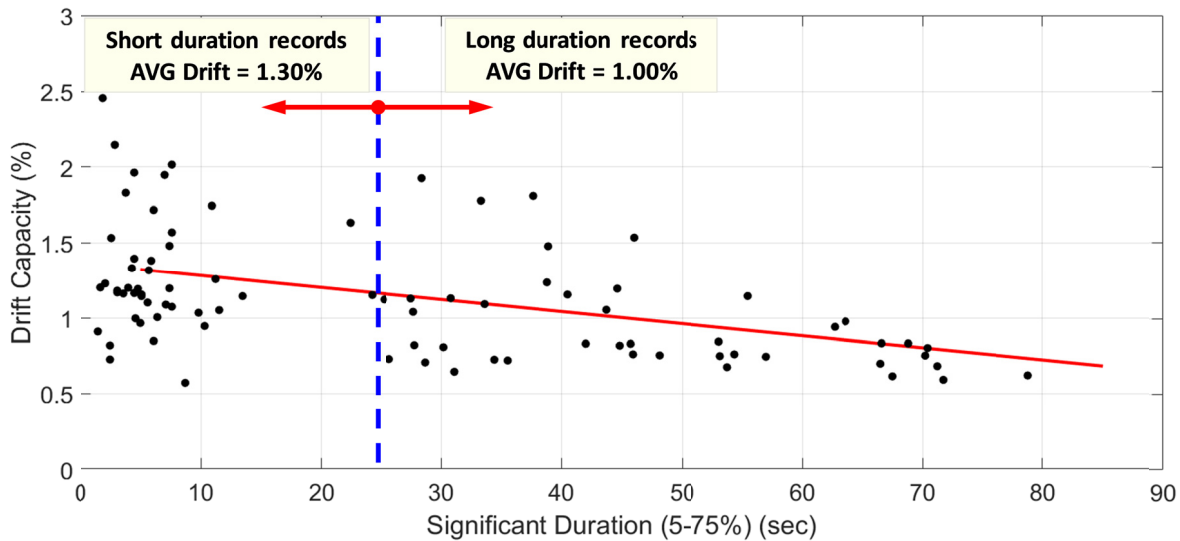


Figure 6.22 Fitted relationship between the significant duration and frame drift capacity.

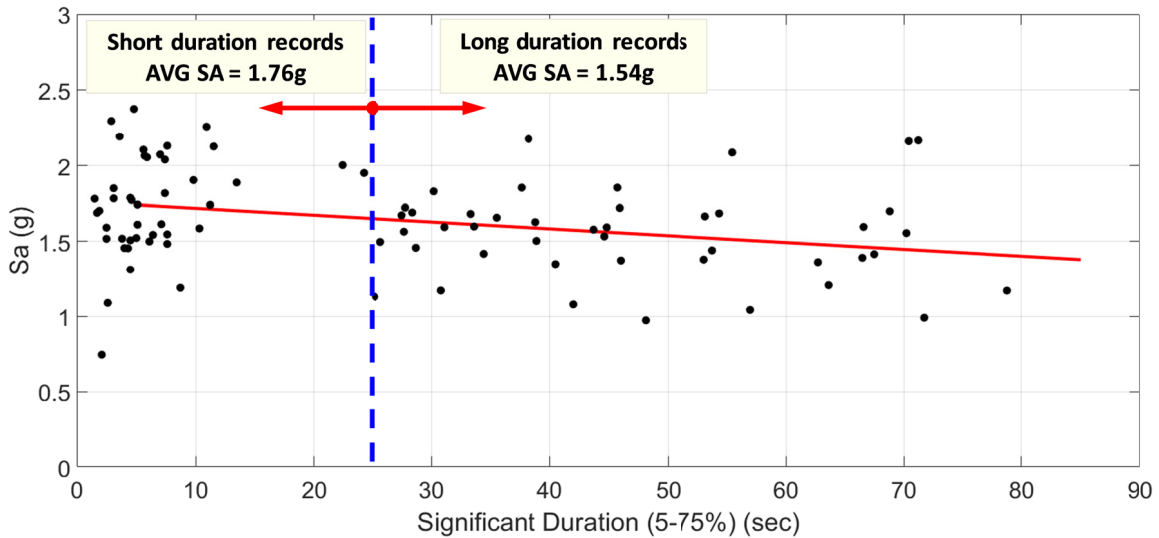


Figure 6.23 Fitted relationship between the significant duration and frame spectral acceleration.

7 Effect of Duration on Archetype SCBF Buildings

In Chapter 5, the effect of ground-motion duration on SCBFs was evaluated based on the results obtained from shake table tests. Due to the limitations of the shake table, half-scaled specimens were used. In Chapter 6, the effect of duration was further studied on the tested specimens but using analytical methods. To increase the “fictitious” number of tests to include more ground-motion variability and better generalized conclusions, a detailed OpenSees model was calibrated and used to conduct IDA using 88 ground motions. Based on the scope of both Chapters 5 and 6, only the reduced-scale frames were considered. Thus, the main goal of this chapter is to complement what was previously presented and discussed on reduced-scale frames and investigate the effect of long-duration ground motions on full-scale archetype SCBF buildings. Two multi-story archetype buildings were selected—a three-story and a nine-story SCBF—and analyzed using OpenSees. Both buildings were analyzed under the same 88 short and long-duration ground motions previously used. The ground motions were scaled to specific hazard level and deterministic analysis was conducted rather than IDA. Although no fragility curves were developed for the archetype frames, their seismic performance was compared under short and long-duration earthquakes. This chapter provides the details of the archetype buildings, the modeling procedure, ground-motion scaling for the deterministic analysis, and a discussion of the results obtained from the analysis.

7.1 ARCHETYPE BUILDINGS

Two archetype buildings were used in this study. The three- and nine-story buildings were adopted and based on the model buildings used as part of the SAC Steel project [FEMA 2000]. These designs adopted the basic floor plan, story height, and gravity loads. Appropriate modifications were made to transform the buildings from special moment-resisting frames to SCBFs. The new design details were taken after Hsiao et al. [2012]. The buildings were designed using the equivalent lateral force procedure [ASCE/SEI 7-10 [2013]; AISC [2002]]. Figures 7.1 and Figure 7.2 show the typical floor plan and elevation of the three-story building; Figures 7.3 and 7.4 show same details for the nine-story building considered herein.

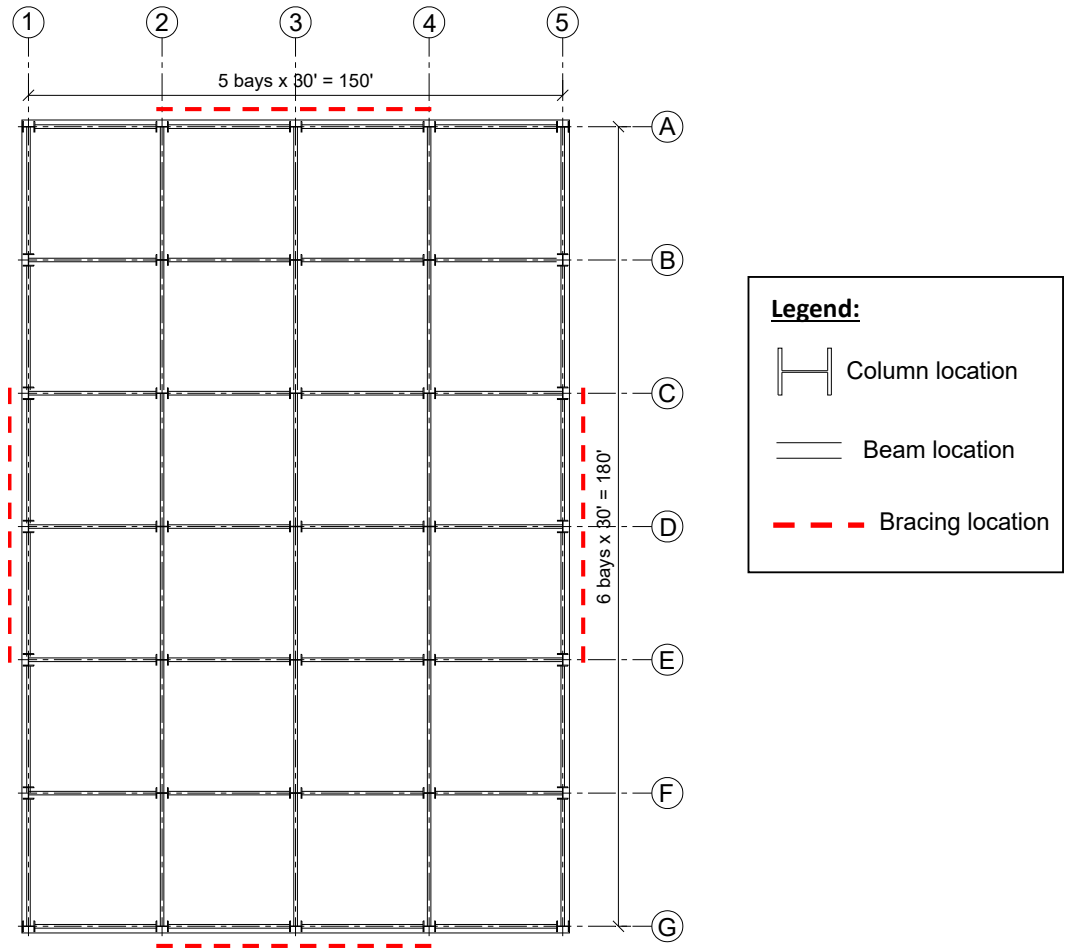


Figure 7.1 Floor plan of the considered three-story archetype building.

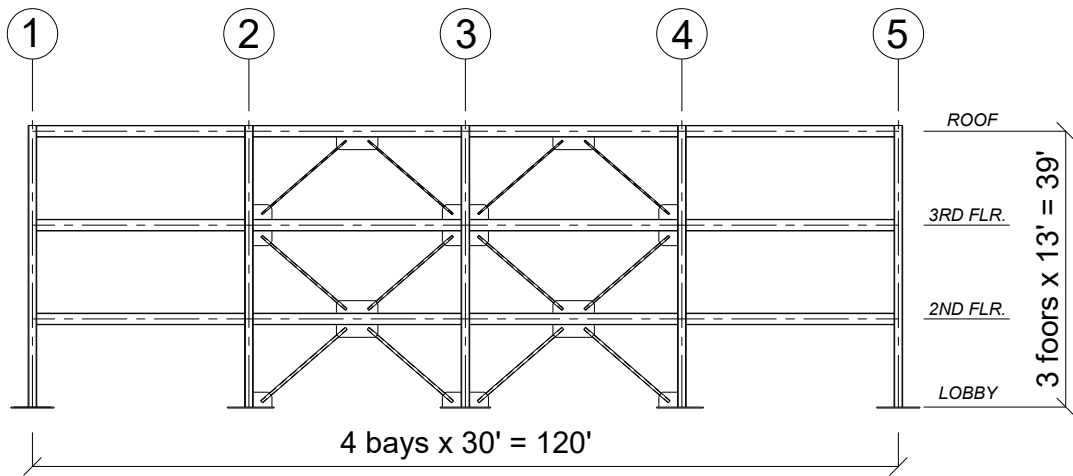


Figure 7.2 Elevation and brace configuration of the three-story archetype building.

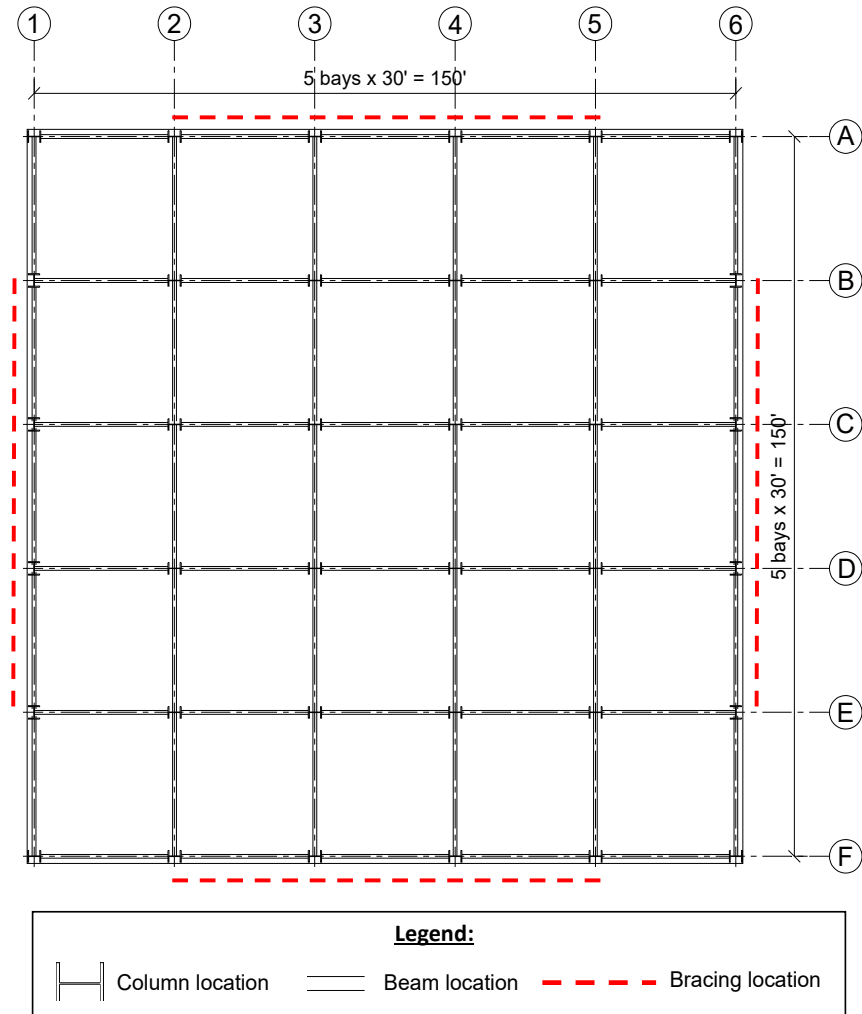


Figure 7.3 Floor plan of the considered nine-story archetype building.

A brief discussion of the design basis of the archetype buildings is presented next; the reader is referred to [Hsiao 2012] for additional details. The basic design R value used to adjust the design spectrum was 6. All of the buildings were designed for a location in Seattle, Washington, using Seismic Design Category D with soil Site Class C. The three-story building included 4×6 story braced bays identical in height. The nine-story building had 5×5 story braced bays, with a taller bottom story to reflect typical mid-rise construction, see Figure 7.4. The braced bays were placed on the perimeter of the buildings in a symmetric plan configuration using a multi-level X-bracing configuration; see Figure 7.4. The buildings were designed to meet the ASCE-7 design spectrum using the updated 2008 United States Geological Survey’s (USGS) [2018] mapped spectral acceleration values at 2% in 50-years hazard level for the building site. The short-period spectral acceleration, S_S was 1.4g and spectral acceleration at the 1.0-sec period, S_I was 0.53g. The site class coefficients F_a and F_v are 1.0 and 1.3, respectively, and the damped spectra were adjusted to 2% of critical damping by applying damping adjustment factor β_s and β_1 of 0.8 [FEMA 273 1997]. The resulting design spectral acceleration parameters were S_{DS} of 1.17g and S_{DI} of 0.57g. The buildings were considered to be general office buildings, and an occupancy importance factor, I , of 1.0 was used. According to Hsiao [2012], Table 7.1 gives the

resulting design member sizes of the three- and nine-story buildings. Rectangular HSS were used for all brace sections and satisfied the AISC seismic compactness criteria [AISC 2010b]. For the current code design based on $R = 6$, the fundamental periods of the resulting frames were 0.38 and 0.87 sec for the three- and nine-story buildings, respectively.

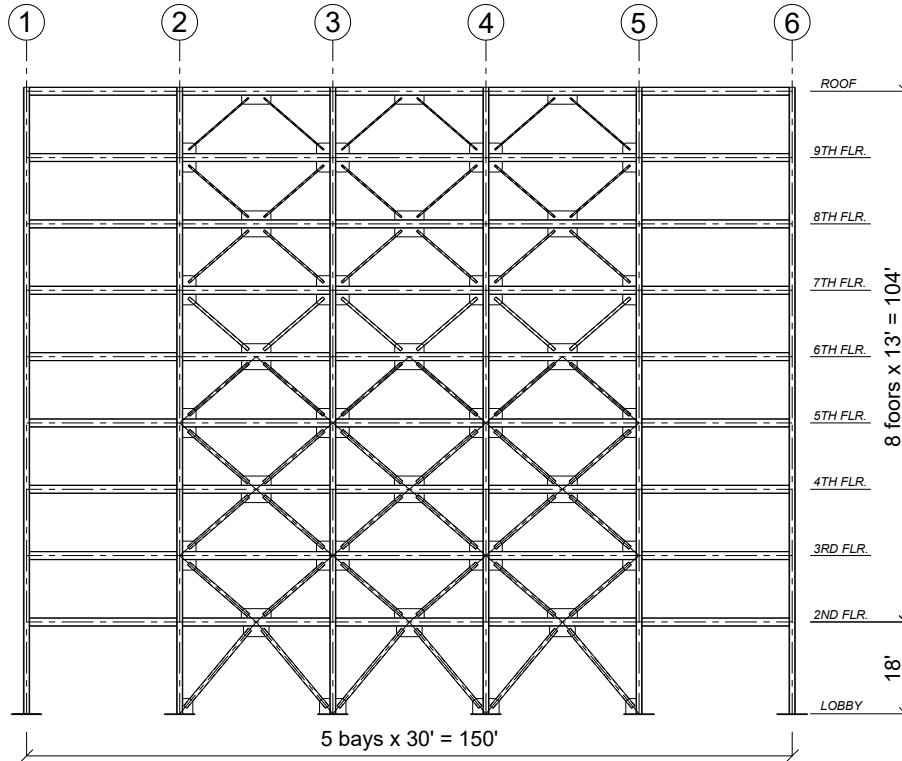


Figure 7.4 Elevation and brace configuration of the nine-story archetype building.

Table 7.1 Member sizes of the three- and nine-story archetype buildings with representative frames used for the analysis.

Building	Story	Brace	Beam	Exterior col.	Interior col.
three-story	1	HSS 6x6x5/8	W21x93	W14x90	W14x90
	2	HSS 6x6x1/2	W21x93	W14x90	W14x90
	3	HSS 5x5x1/2	W24x104	W14x90	W14x90
nine-story	1	HSS 8x8x1/2	W21x93	W14x283	W14x283
	2	HSS 7x7x1/2	W21x83	W14x283	W14x283
	3	HSS 7x7x1/2	W21x83	W14x283	W14x283
	4	HSS 7x7x1/2	W21x83	W14x193	W14x193
	5	HSS 6x6x5/8	W21x83	W14x193	W14x193
	6	HSS 6x6x1/2	W21x83	W14x120	W14x120
	7	HSS 6x6x3/8	W21x83	W14x120	W14x120
	8	HSS 5x5x1/2	W21x83	W14x74	W14x74
	9	HSS 5x5x5/16	W24x104	W14x74	W14x74

7.2 SYSTEM MODELING

To assess the seismic performance of SCBFs under long-duration ground motions, comprehensive nonlinear dynamic analyses are needed, especially since full system testing is not feasible. The models needed for such purposes must include every yield mechanism and failure mode that impacts the seismic response of the overall frame, and must be capable of simulating the response beyond initial fracture. These requirements can be met by incorporating the various modeling techniques presented herein. Two representative planer (two-dimensional) frames from each building (see Figures 7.2 and 7.4) were considered herein and modeled using same approaches presented in Chapter 3. The gravity loads and second-order (P -delta) effects were included in the simulation by employing a leaning column connected to the frame by rigid links; see Figure 6.5. The gravity frame was modeled using shear-connection springs to simulate the total rotational strength and stiffness of gravity beam–column connections (shear-tab connections), which were located between the rigid link and the leaning column. The gravity loads at each floor level were placed on the gravity frame. The technique used herein was similar to that adopted by Hsiao [2012].

The properties of the shear-connection springs were based upon Liu’s model of shear tab connections with composite slabs [Liu and Astaneh-Asl 2004]. The springs were simulated using the *Pinching4* material model in OpenSees. Each spring element had a stiffness and strength equivalent to the number of the gravity bays contributing to the seismic weight. The rigid beams used in the gravity frame model, which had the same length of the gravity bay, were supported by rollers. The nodes at the end of the rigid beams were slaved to the nodes at the middle of the braced frame in horizontal translation at each level; see Figure 7.5. The base of the leaning column was pinned. Wide-flange sections W10×49 and W12×65 were used for the gravity columns of the three- and nine-story buildings throughout the height, respectively. To represent the overall contributions, such as initial axial and bending stiffness and strength, of the gravity columns to the lateral-load resisting system, a particular cross section of the leaning column was adopted with a cross-sectional area, moment of inertia, and plastic moment capacity equal to the total of the gravity columns contributing to the seismic weight.

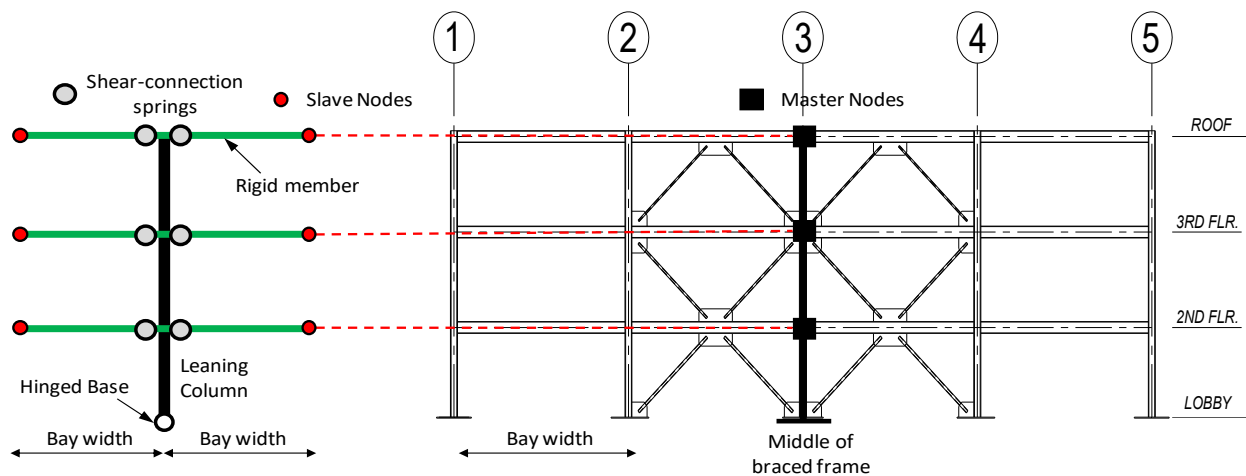


Figure 7.5 Leaning column modeling.

7.3 GROUND-MOTION SELECTION

In order to study the duration effect on the two frames adopted from the archetype buildings described above, nonlinear dynamic analysis was considered under a large number of ground motions. The same suites of ground motions previously used in Chapter 6 were used in this particular study but with different scaling factors. For the IDA previously conducted in Chapter 6, no specific scaling was required as each ground motion was applied incrementally until collapse occurred. This chapter uses a deterministic analysis rather than IDA and a fragility analysis.

For this analysis, the mean of each suite of ground motions was linearly scaled to represent a specific hazard level; see Appendix D for more detailed information regarding the 44 pairs of ground motions. The information presented in Appendix D also includes the respective scaling factors used to match each pair of ground motions. Figure 7.6 shows the response spectrum and the mean of each suite (short- and long-duration) based only on matching scales and not a specific hazard level. Figure 7.7 shows both response spectra but after scaling to represent a 10%/50-years and 2%/50-years hazard-level response spectra. The linear scaling used for each desired hazard level considered a range of periods around the fundamental periods of the two frames of interest. For completeness, Figure 7.7 indicates the fundamental period for each of the three- and nine-story buildings.

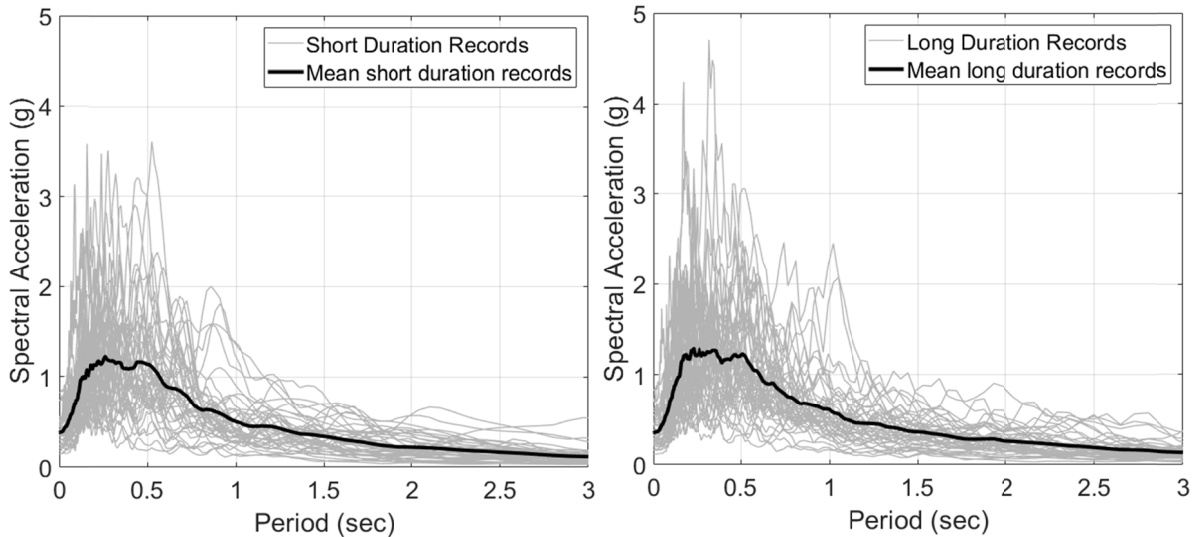


Figure 7.6 Short- and long-duration ground-motion sets and their mean.

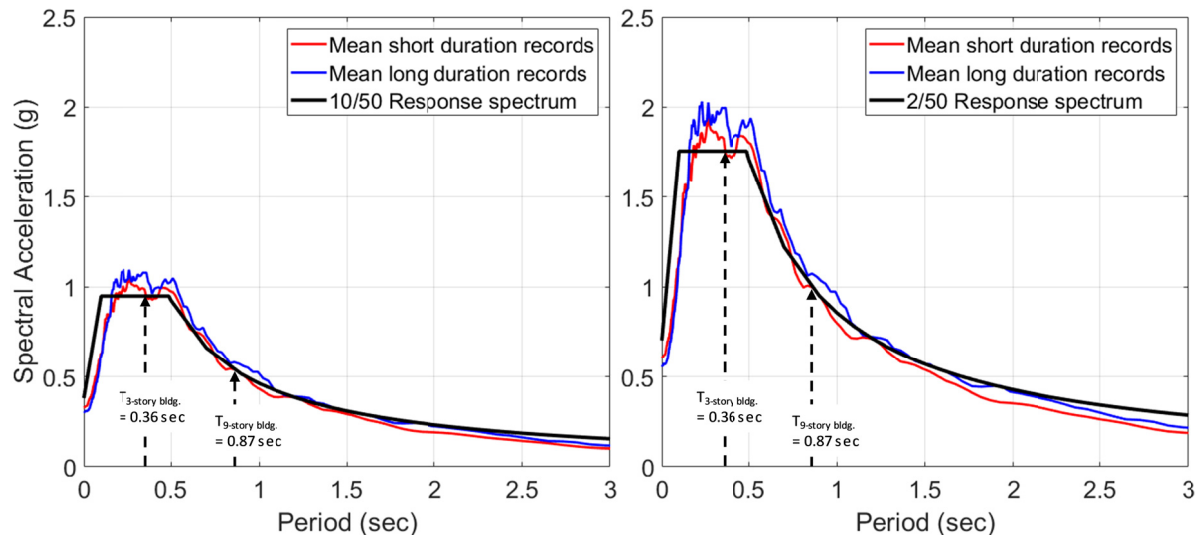


Figure 7.7 Comparison of short- and long-duration ground-motion mean for the 10%/50-years and 2%/50-years hazard level.

7.4 RESULTS AND DISCUSSIONS

This section presents the results obtained from two sets of nonlinear time history analysis conducted for both the three- and nine-story archetype SCBFs. Each set included analysis under 88 ground motions (44 short-duration records and 44 long-duration records) that were scaled to a specific hazard level, i.e., 10% in 50 years and 2% in 50 years. The results include percentage of story drift, percentage of interstory drift, maximum story displacements, residual displacements, and floor accelerations. The results are compared, where each demand parameter is presented for the individual and mean of 44 short versus 44 long-duration ground motions.

7.4.1 Three-Story Building Results

The scaled ground motions based on 10% and 2% in 50-years (10/50 and 2/50) hazard levels were used to compute the nonlinear response of the three-story SCBF model. Results from this analysis are presented and discussed below.

7.4.1.1 10%/50 years ground-motion set

Presented below are the results of four different types of results are presented here and repeated for all other cases. These include the percentage of maximum story drift, percentage of interstory drift, residual displacement, and floor accelerations as obtained from both short and long-duration suites of ground motions. All figures show results from individual records as well as average results from all 44 ground motions for better comparison. Figure 7.8 shows the average maximum story drifts (MSD) computed for the three-story SCBF for the 10/50-years hazard level. The average MSDs over the frame height varied between 0.3% and 0.4% for both suites of ground motions. The results show that both suites of earthquakes at this hazard level caused very limited deformation and little concentration of inelastic deformation over the building height. The ground-motion duration also does not have any specific adverse effects on

MSD, which is attributed to the fact that the duration sensitive effects, i.e., low-cycle fatigue-inducing brace rupture, did not occur at this intensity level.

Figure 7.9 shows the interstory drift distribution in response to short- and long duration earthquakes along the frame height of the three-story building. The figure shows that no large interstory demands are expected at this hazard level, which is less than the typical hazard level for design. All interstory values obtained from the analysis satisfy the ASCE 7-10 [2013] percentage of drift limits. At this low-intensity hazard level, the long-duration records show slightly higher demands compared to those resulting from short-duration motions. Figure 7.10 shows the frame residual displacement at the end of the analysis, i.e., after each ground-motion record was completely applied. Consistent with the observation that no damage (e.g., significant brace buckling) was reported at this hazard level, it can be seen that residual displacements are almost zero. This means that building can be still considered fully functional after an earthquake of this level.

Figure 7.11 shows the floor accelerations at different stories for both the short and long-duration ground-motion cases. The accelerations are shown to vary along the building height and between the two suites of ground motions. Although ground motions pairs were matched, the average results from short and long-duration earthquakes reflect different structural dynamic responses, and, in turn, force and acceleration demands were obtained.

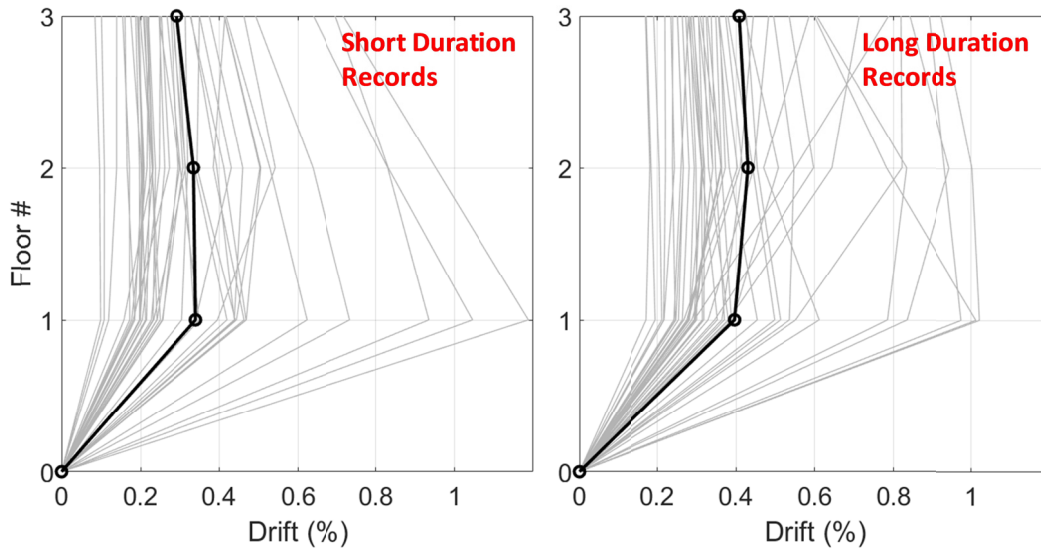


Figure 7.8 Comparison of the distribution of maximum story drift along three-story SCBF height at the 10%/50-years hazard level for short- and long-duration earthquakes.

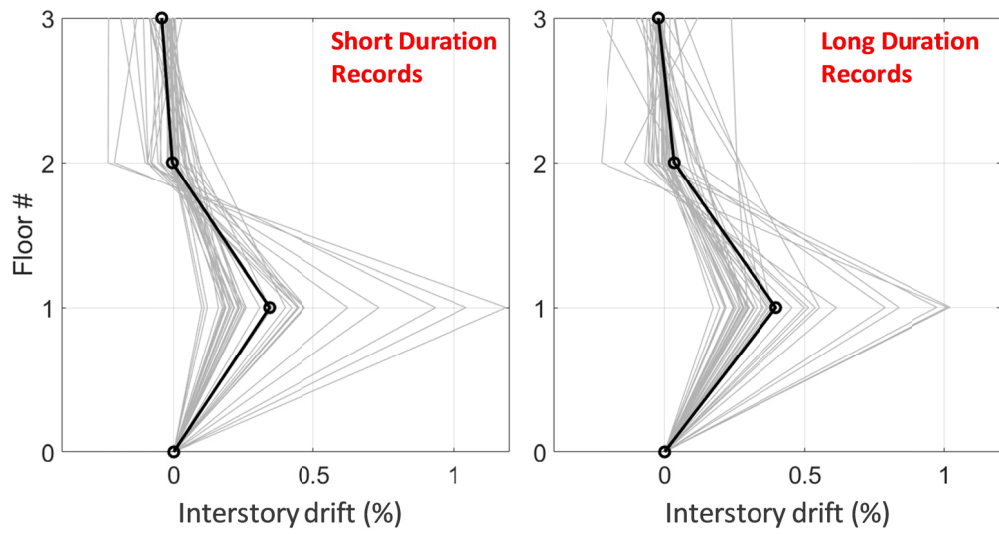


Figure 7.9 Comparison of the distribution of interstory drift along three-story SCBF at the 10%/50 years hazard level for short- and long-duration earthquakes.

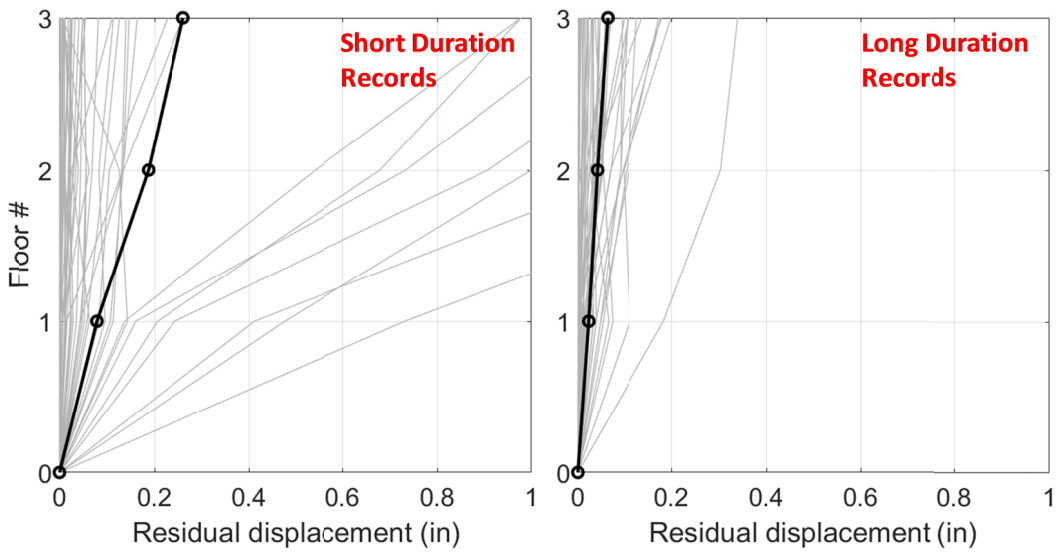


Figure 7.10 Comparison of the distribution of residual displacement along three-story SCBF at the 10%/50 years hazard level for short- and long-duration earthquakes.

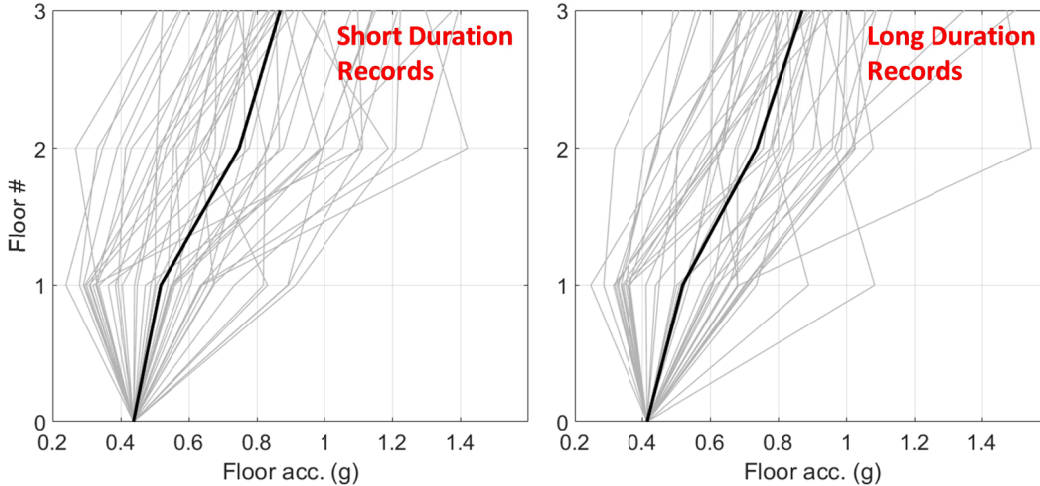


Figure 7.11 Comparison of the distribution of floor acceleration along three-story SCBF height at the 10%/50 years hazard level for short and long-duration earthquakes.

7.4.1.2 2%/50 years ground-motion set

For the 2/50 level analyses, the average MSD values increased significantly, and severe concentration of deformation occurred in most cases. Figure 7.12 shows the individual records results and the average MSD computed for the three-story SCBF for the 2%/50-years hazard level. The long-duration suite of ground motions caused relatively more damage compared to short-duration ground motions. The damage included severe brace buckling that exceeded three times the brace width and complete brace ruptures in many cases. In some cases, a soft-story mechanism was reported where all the braces within a certain floor ruptured. Figure 7.13 shows the interstory drift for the same building type. It is clear that the values increased significantly for this hazard level compared to the 10%/50-years hazard level. Some values were noted to be high, which resulted from those cases when soft-story mechanisms were reported.

Figure 7.14 shows the building residual displacement after the end of the ground motion. Figure 7.15 shows the floor accelerations for both the short and long-duration ground motions. In general, close acceleration values were reported from both suites of ground motions.

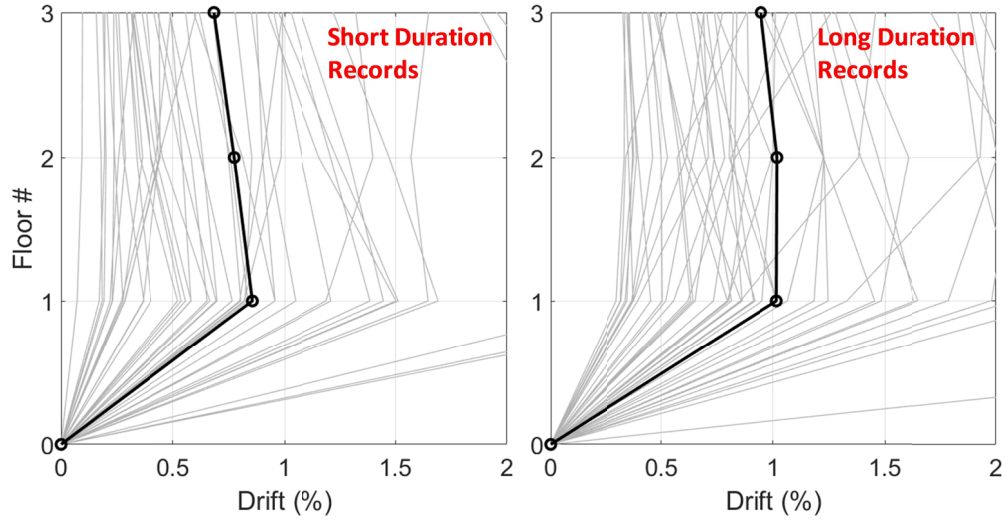


Figure 7.12 Comparison of the distribution of maximum story drift along three-story SCBF at the 2%/50-years hazard level for short- and long-duration earthquakes.

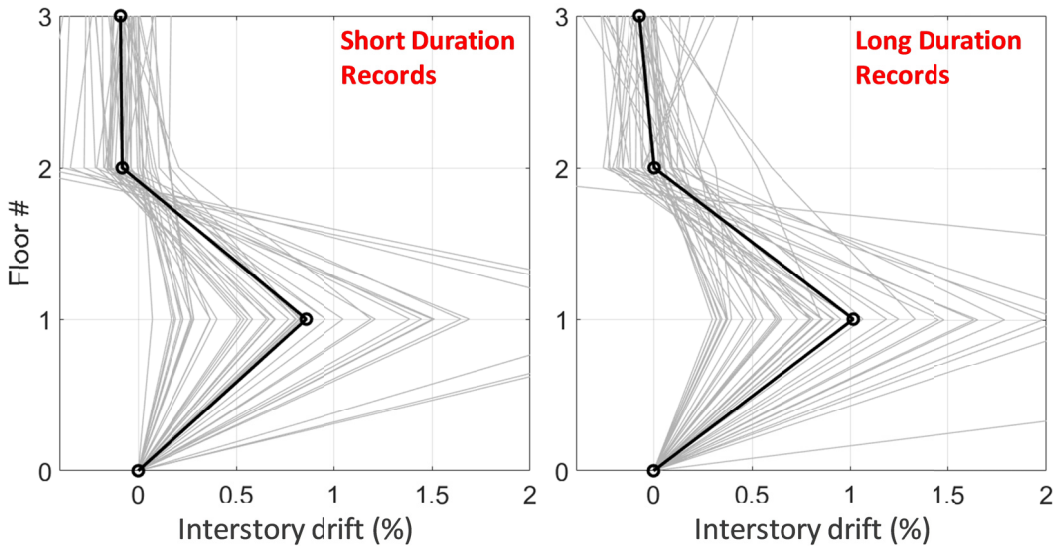


Figure 7.13 Comparison of the distribution of interstory drift along three-story SCBF at the 2%/50-years hazard level for short- and long-duration earthquakes.

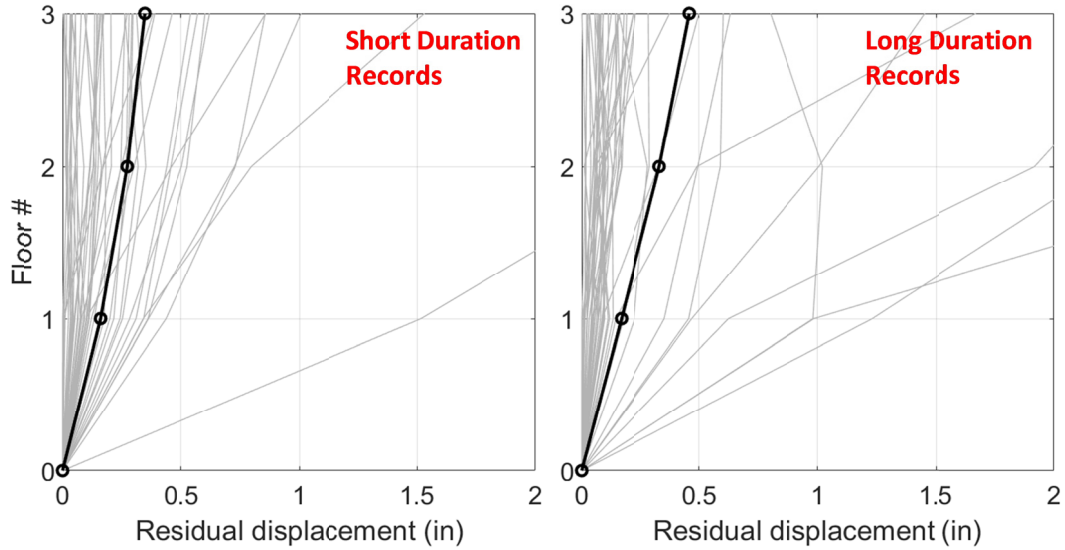


Figure 7.14 Comparison of the distribution of residual displacement along three-story SCBF height at the 2%/50-years hazard level for short- and long-duration earthquakes.

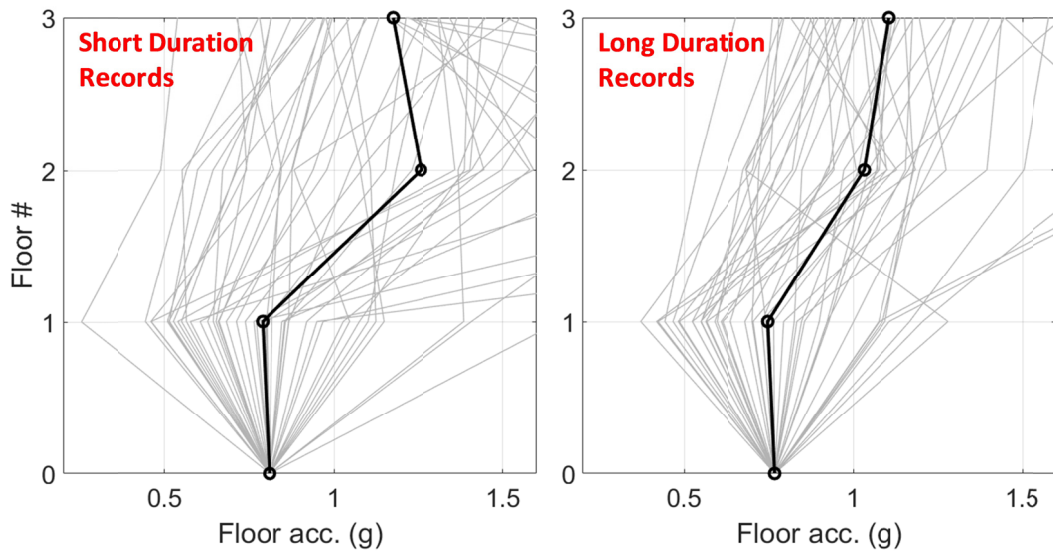


Figure 7.15 Comparison of the distribution of floor acceleration along three-story SCBF at the 2%/50-years hazard level for short- and long-duration earthquakes.

7.4.2 Nine-Story Building Results

Similar to the three-story SCBF analysis, two hazard levels, i.e., 10% and 2% in 50 years, were used to scale the two suites of ground motions for nonlinear time history analysis of the nine-story SCBF model.

7.4.2.1 10%/50 years ground-motion set

Figure 7.16 shows the average maximum story drifts computed for the nine-story SCBF for the 10%/50-years hazard level under both short and long-duration earthquakes. The difference between the response of the nine-story SCBF under both suites of ground motions was not significant at that hazard level. This is because none or only few number of ground motions caused failure in either case. Worth mentioning is that the long-duration suite caused an average higher percentage of drift concentrated at the first floor. The variation between the average results from both suites of ground motions is around 25% higher in case of long-duration records. Figure 7.17 shows the maximum story displacement for the same building type. At this hazard level, no damage was been reported and only limited brace buckling was observed in some braces, which did not exceed three times the brace width.

Figure 7.18 shows the interstory drift for the same building type with concentration of the interstory drift at the first floor level, which was expected because this is where the highest shear demand are typically observed under a given ground motion. Figure 7.19 shows the building residual displacement at the end of applying each ground motion. Residual displacements are negligible at this hazard level as no damage or soft-story mechanism was reported. Figure 7.20 shows the floor accelerations for both the short- and long-duration ground motions. Floor accelerations for the nine-story building were found to be very similar for both short and long-duration motions. Unlike the analysis for the three-story building at same hazard level, the nine-story SCBF had a more consistent dynamic response under the matched pairs of short- and long-duration ground motions.

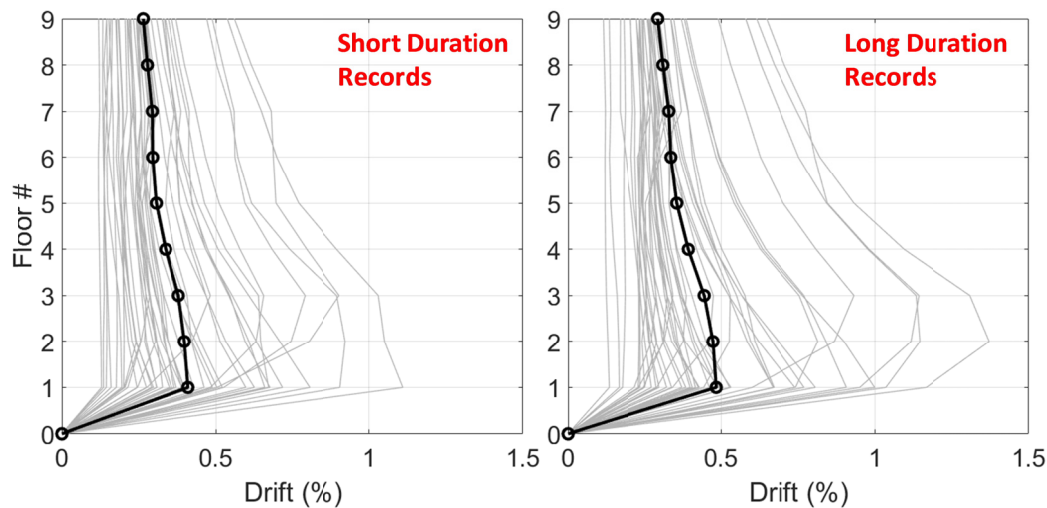


Figure 7.16 Comparison of the distribution of maximum story drift along nine-story SCBF at the 10%/50-years hazard level for short- and long-duration earthquakes.

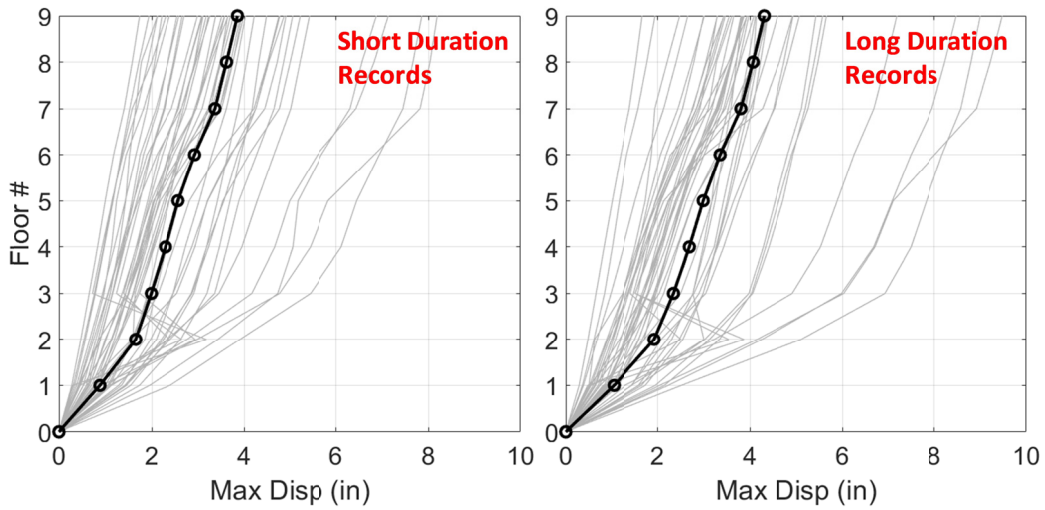


Figure 7.17 Comparison of the distribution of maximum story displacement along nine-story SCBF height at the 10%/50-years hazard level for short- and long-duration earthquakes.

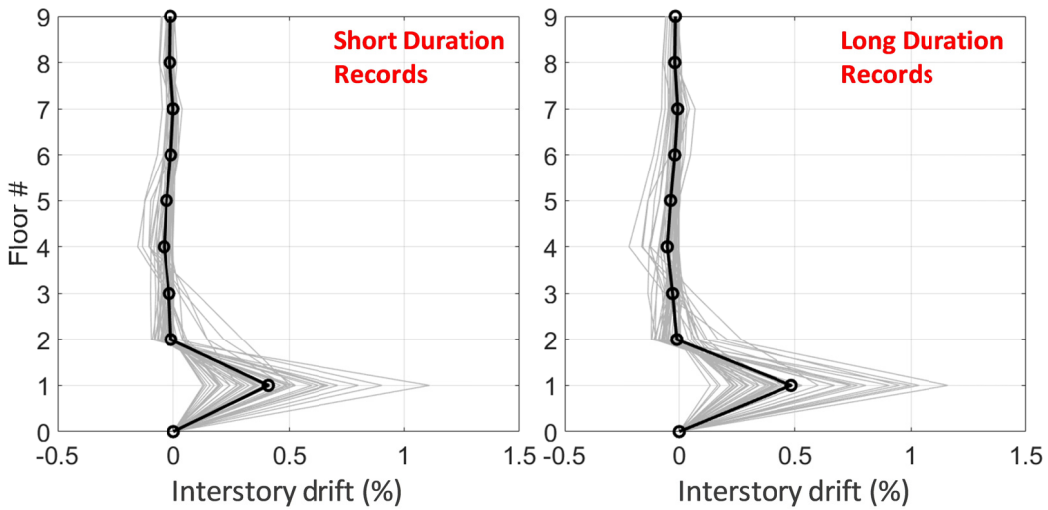


Figure 7.18 Comparison of the distribution of interstory drift along nine-story SCBF height at the 10%/50-years hazard level for short- and long-duration earthquakes.

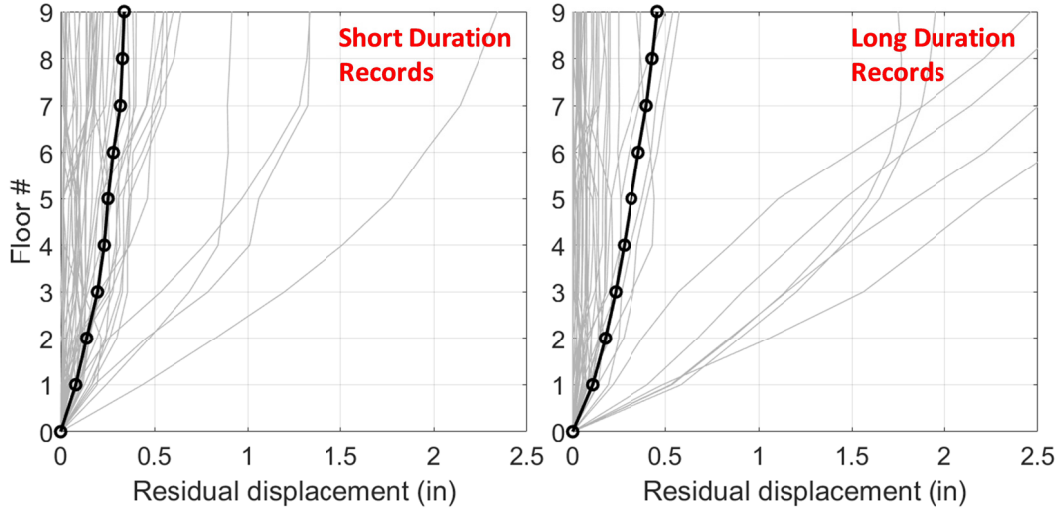


Figure 7.19 Comparison of the distribution of residual displacement along nine-story SCBF at the 10%/50 years hazard level for short- and long-duration earthquakes.

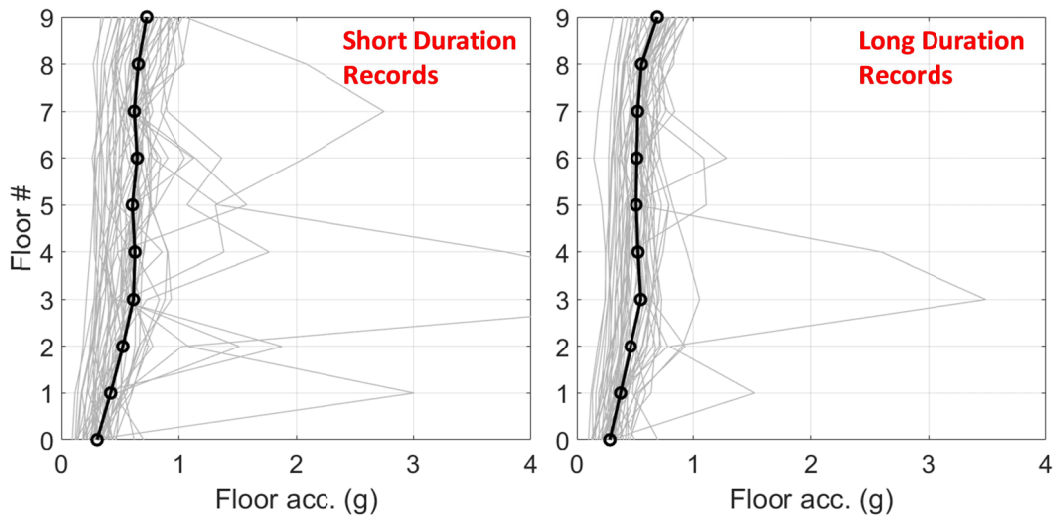


Figure 7.20 Comparison of the distribution of floor acceleration along nine-story SCBF at the 10%/50-years hazard level for short- and long-duration earthquakes.

7.4.2.2 2%/50 years ground-motion set

Figure 7.21 shows the average maximum story drifts computed for the nine-story SCBF for the 2%/50-years hazard level. Note: a significant difference is observed between the average results from the short and long-duration suites at this hazard level. Although both suites are composed of spectrally-matched pairs, the longer duration records led to more accumulation of damage. The observed difference is around 50% in the case of maximum drift ratios, which is a significant difference, especially when a larger number of soft-story mechanisms were reported in the case of long-duration earthquakes. More details about brace ruptures and mechanisms are presented in the next section on limit states.

Figure 7.22 shows the maximum story displacement for the same building type. As the damage increased at this hazard level, the maximum displacements increased with, again, larger average displacements observed compared to the long-duration suite of ground motions. Figure 7.23 shows the interstory drift for the SCBF under both suites of ground motions. The difference is around 50% more compared to the long-duration ground motions. As before, the analysis showed concentration of damage in the first story.

Figure 7.24 shows the building residual displacement at the end of each ground motion. The values are significant at this hazard level, indicating that severe damage took place, which is interpreted more properly in next section. Figure 7.25 shows the floor accelerations for both the short- and long-duration ground motions. Unlike drift and residual displacements, floor accelerations were not significantly different between the average results from short and long-duration ground motions.

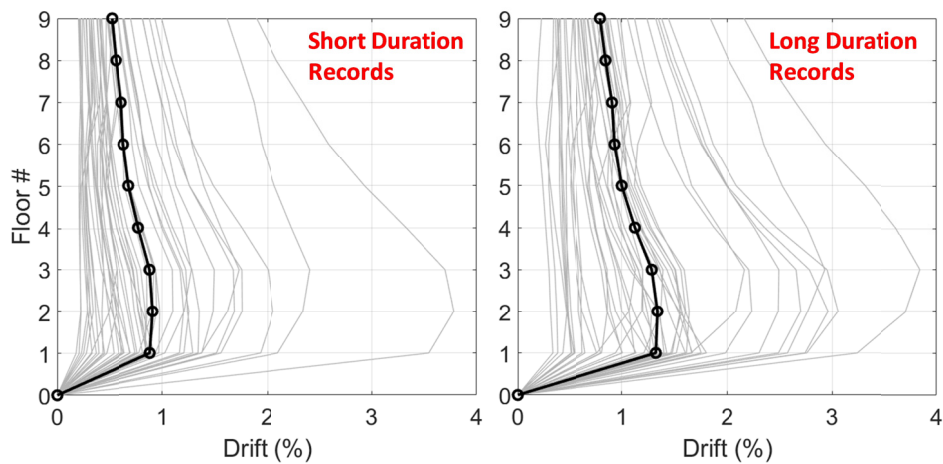


Figure 7.21 Distribution of maximum story drift along nine-story SCBF height at the 2%/50-years hazard level as compared for short- and long-duration earthquakes.

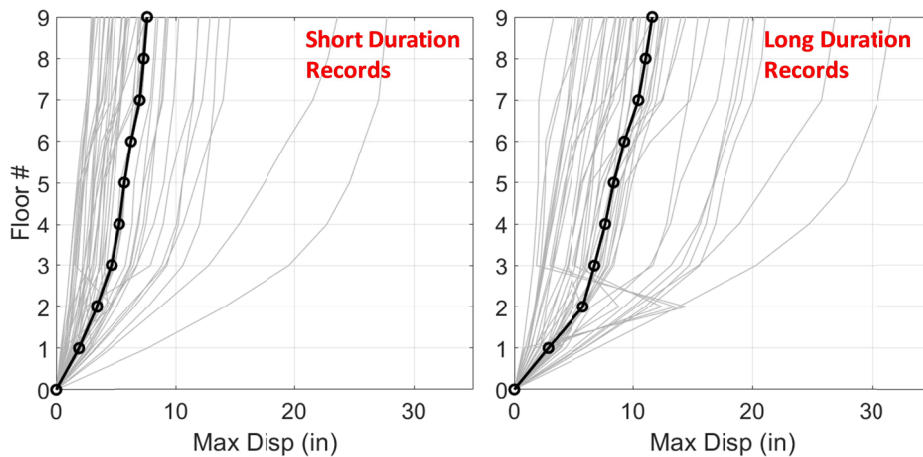


Figure 7.22 Distribution of maximum story displacement along nine-story SCBF height at the 2%/50-years hazard level as compared for short- and long-duration earthquakes.

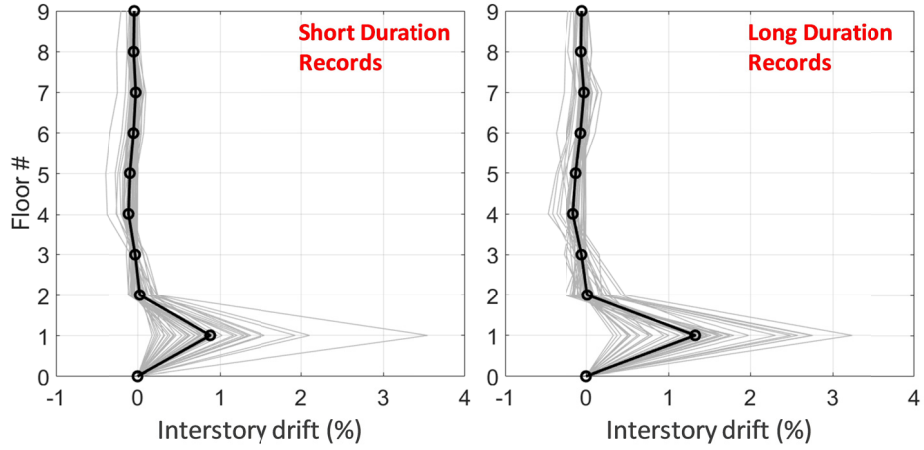


Figure 7.23 Distribution of interstory drift along nine-story SCBF height at the 2%/50-years hazard level as compared for short- and long-duration earthquakes.

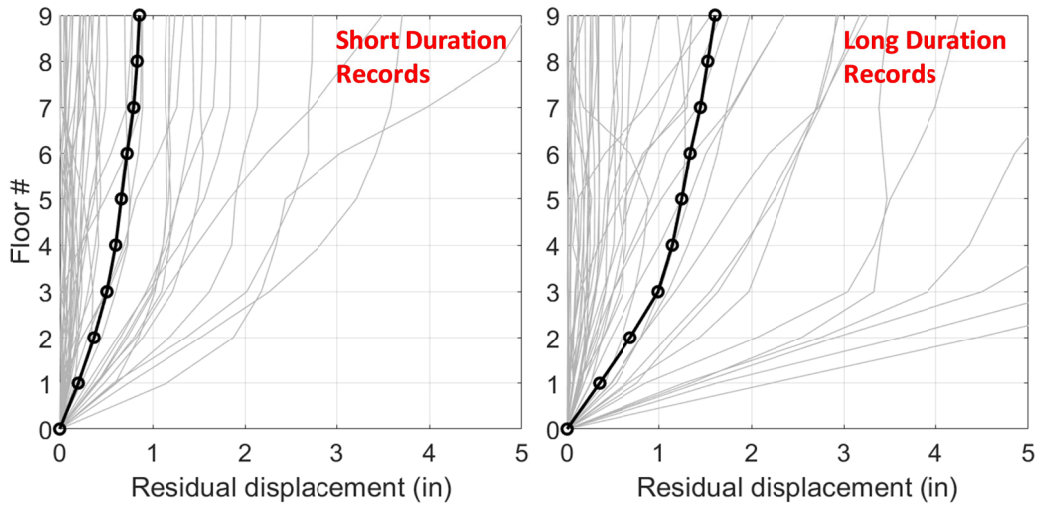


Figure 7.24 Distribution of residual displacement along nine-story SCBF at the 2%/50-years hazard level as compared for short- and long-duration earthquakes.

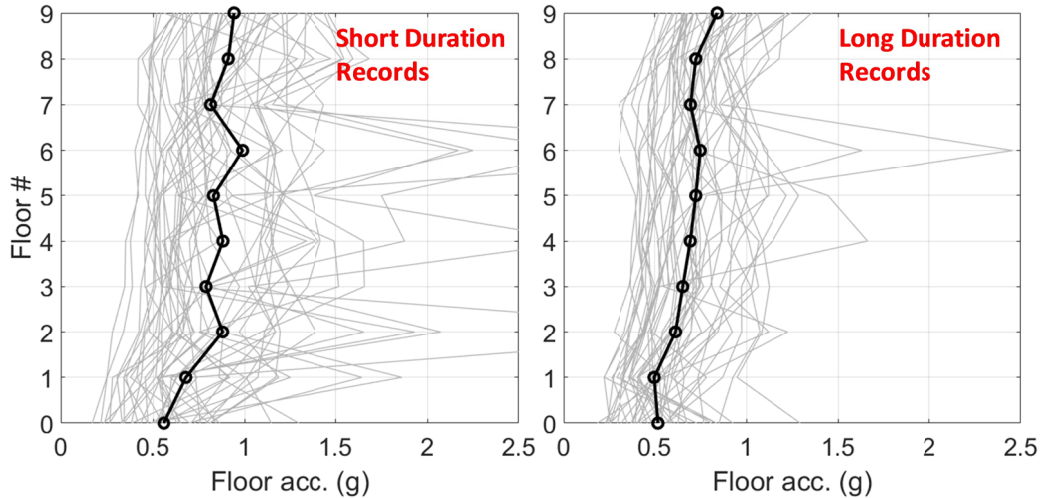


Figure 7.25 Distribution of floor acceleration along nine-story SCBF at the 2%/50-years hazard level as compared for short- and long-duration earthquakes.

7.5 LIMIT STATES

Four performance limit states were considered to further evaluate the effect of earthquake duration on SCBFs based on comparisons of the results obtained in previous section for both short and long-duration ground motions. These limit states were selected to reflect the significant key stages in SCBF nonlinear response. These limit states were adopted in part after the study by Hsiao [2012] and with some modifications proposed by the author. A brief description of the four different limit states used to interpret the archetype SCBFs analysis results is as follows.

1. Initial brace buckling: Brace buckling was reported for each brace in the SCBFs in every analysis. Following prior experiments, initial brace buckling typically occurs at approximately 0.3% story drift [Hsiao 2012], which is the value used to report brace buckling in this study.
2. Excessive brace buckling requiring replacement of the brace: Requirements for possible replacement of the brace are defined as: (a) the maximum out-of-plane displacement of the brace exceeded three times the brace depth, or (b) prediction of brace fracture. These damage states related to definitions developed in a prior study for developing fragility curves for concentric braced frames [ATC-58 2009].
3. Brace fracture: The fracture was predicted by the OpenSees model as interpreted from reported damage index values (Chapter 3 provided the basis for interpreting damage index results).
4. Soft Story: This limit state is introduced by the author and refers to the case when all braces at a given floor ruptured according to the analysis. This case can be considered vulnerable to forming a soft-story mechanism if the residual floor lateral stiffness and force resistance from columns and beams are significantly lower than the braced frame before brace rupture.

As discussed in Section 7.4, all results from extensive analysis were compiled together to determine the probability of occurrence for each of the four performance limit states defined above. The probability of meeting a certain limit state is expressed in a simplified way through determining what percentage of the braces experienced a given limit state relative to total number of braces in the analyzed SCBF. Figure 7.26 shows such percentages for the three-story building at the 10%/50-years and 2%/50-years (MCE level) hazard levels as obtained from separate short- and long-duration analyses conducted. For the 10%/50-years hazard level, almost all braces buckled but no damage was reported according to the limit states defined above. For the 2%/50-years hazard level, the long-duration ground motions caused more damage when the possible brace replacements, brace rupture, and soft-story mechanism were considered than the short-duration ground motions in the case of the three-story building; that said, the difference between short and long-duration cases was not significant. This might be attributed in part that because of the short period of the three-story building, high force demands were expected in the frame regardless of the duration effect.

Figure 7.27 shows similar damage levels for the 10%/50-years and 2%/50-years hazard levels for the nine-story building. The results for the 10%/50-years hazard level, show that brace buckling occurred at 100% of the analysis cases, but no additional damage was observed at this hazard level; for the 2%/50-years hazard level, long-duration earthquakes are shown to cause more significant damage either for excessive brace buckling (expressed as possible replacement limit state) or brace fracture. The soft-story mechanism was reported only in the case of long-duration records.

The results obtained from the archetype SCBFs analysis, especially those pertaining to the story mechanisms or possible brace ruptures, are yet another means of highlighting the importance of considering ground-motion duration in future designs or performance-based assessment. Overall, it was demonstrated in different analysis cases throughout this study that severe structural damage or even full collapse might have a larger probability of occurrence only because of the larger damage accumulation in SCBF braces associated with longer duration effects.

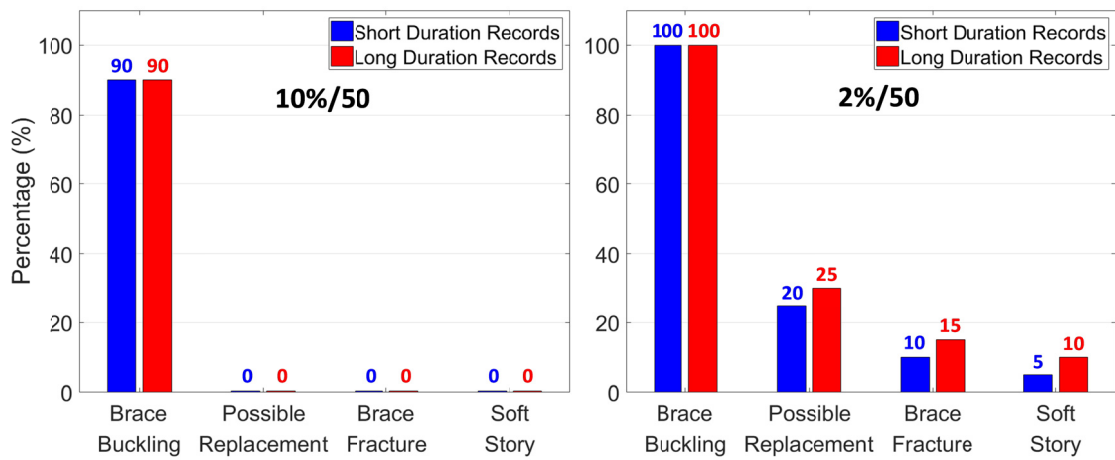


Figure 7.26 Percentage of braces meeting a given limit state as related to total number of braces in the three-story SCBF as obtained from analysis results under the short- and long-duration ground motions scaled at 10%/50-years and 2%/50-years hazard levels.

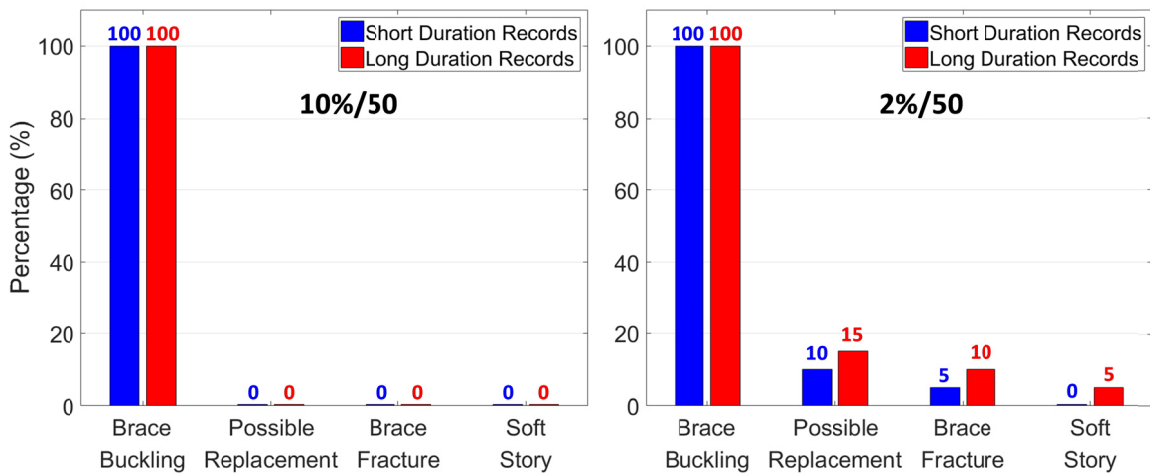


Figure 7.27 Percentage of braces meeting a given limit state as related to total number of braces in the nine-story SCBF as obtained from analysis results under the short- and long-duration ground motions scaled at 10%/50-years and 2%/50-years hazard levels

8 Summary and Conclusions

8.1 SUMMARY

Experimental and analytical investigations were conducted to study the effect of earthquake duration on SCBFs. In particular, the effect of long-duration ground motions on SCBFs' collapse capacity was evaluated. The analytical part of the study consisted of two phases: (1) modeling sensitivity and pre-test analysis, and (2) post-test analysis for test specimens and archetype SCBFs. The experimental program involved shake table testing of three identical SCBFs subjected to long and short-duration motions. The test specimens for this study were adopted from a prototype building taken from the SEAOC Design Manual; one-half-scale single bay-single story frames were used for the tests.

Current seismic design codes are based on site-specific response spectra and do not consider duration effects. Based on the literature (see Chapter 2), most previous studies on earthquake duration effects on seismic performance of structures considered numerical methods, and only few considered experimental testing. Moreover, many of the studies were related to concrete structures with less focus on steel structures and specifically SCBFs. The lack of experiments and consensus in critical modeling features such as low-cycle fatigue in SCBFs motivated this study. First a sensitivity analysis to understand modeling effects was performed and then shake table testing of the SCBFs were conducted to verify the models.

The first phase of the analytical investigation performed a detailed sensitivity analysis using OpenSees models that were preliminarily calibrated against previous experimental results for different configurations of SCBFs. This analysis aimed at finding and ranking the model parameters with greatest effects on analysis results that pertained to seismic behavior under short and long-duration earthquakes. The sensitivity analysis was conducted for two SCBFs configurations: a single diagonal brace and double X-bracing under cyclic loading, subjected to two sets of ground motions covering a wide range of significant durations.

The experimental program was the core of this study, which included three large-scale shake table tests of identical single-story single-bay SCBFs with a chevron-brace configuration tested under different ground motions. Two specimens were tested under a set of spectrally-matched short and long-duration ground motions. The third specimen was tested under another long-duration ground motion. All tests started with a 100% scale of the selected ground motions, then testing continued with increasing ground motion until failure, i.e., until both braces ruptured. The obtained test results were not only used to understand the effect of the duration but

provide valuable input for numerical model calibration and existing fatigue modeling parameters assessment in the post-test analysis.

The post-test analysis was then conducted where an OpenSees model for the tested specimens was developed to capture the experimental response of the three specimens. First, the calibration matched the initial stiffness and overall global response, then the low-cycle fatigue parameters were fine-tuned to properly capture the experimental local behavior, i.e., brace buckling and rupture. The calibrated model for the test specimens was used to conduct IDA using 44 pairs of spectrally-matched short and long-duration ground motions. This analysis aimed at incorporating ground-motion variability for better generalized observations and developing collapse fragility curves using different IMs to compare the effect of ground-motion duration.

The last stage of this study extended the calibrated model to full SCBFs archetype buildings to study the effect of ground-motion duration on full structures. Two buildings, a three-story and nine-story structure that resembled the original SAC buildings, but modified to have SCBFs as lateral support system instead of moment resisting frames, were used. Two planer frames were adopted from the two buildings and used for the analysis. The same 44 spectrally-matched pairs previously used in the post-test analysis were used to conduct nonlinear time history analysis and study the effect of duration. All the ground motions were scaled to two hazard levels for a deterministic time history analysis: 10% exceedance in 50 years and 2% exceedance in 50 years. All analysis results were interpreted in a comparative way to isolate the ground-motion duration effects.

8.2 OBSERVATIONS AND CONCLUSIONS

Several conclusions can be drawn from the various analytical and experimental parts of this study:

- In general, the seismic response of SCBFs is more sensitive to material behavior and low-cycle fatigue related input and less sensitive to brace meshing or element-modeling parameters. Moreover, SCBFs models are less sensitive to the input parameters under cyclic loading when compared to the ground motions. Thus, many of our models under simplified loading scenarios are best-suited for comparative studies, but also emphasize the importance of using realistic ground motions to assess seismic response.
- The sensitivity analysis performed in Chapter 3 shows that the choice of the modeling parameters can significantly affect the interpreted displacement capacities. This is crucial because some models such as *Steel02* in OpenSees are commonly used by the research and engineering community, but without proper calibration or validation in many cases.
- When modeling variability is averaged out, the assessment results show a reduction in the drift capacity of SCBFs when subjected to long-duration ground motions. There is about 7% reduction in the single-braced frame drift capacity for every 10-sec increase in the duration of the earthquake. These

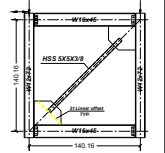
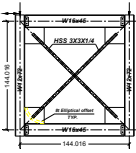
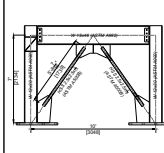
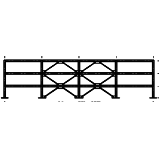
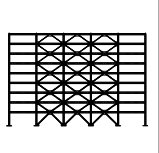
values agree with the comparable values determined from the calibrated model of the tested specimens in the post-test analysis.

- For the short and long spectrally-matched tests, the final damage state defined by the two brace rupture was observed at 200% scale of the original long-duration ground motion (after 7 runs) versus 225% scale (after 20 runs) in case of the short-duration one. The larger short-duration ground-motion intensity produced larger displacement and strain demands produced the same effect as the long-duration one.
- The seismic capacity of SCBFs is not governed by acceleration or force demands but rather displacement or strain cycles. This argument is supported by the experimental evidence that almost a similar force capacity, mainly the force needed for the two braces to undergo inelastic buckling, was observed for all tested three specimens, i.e., they were insensitive to the earthquake duration. In fact, the stiffness degradation, i.e., period elongation, due to brace buckling can reduce the force demands, but brace rupture may still occur at lower forces due to fatigue, which can be an extremely serious factor considering the SCBFs structural integrity in the face of aftershocks or stability and collapse concerns in multi-story SCBFs.
- In terms of the SCBFs' structural response, the tested frames lost about 25% of the lateral stiffness after both braces buckled, and 75% loss of stiffness after the braces ruptured. The adopted AISC design approach for SCBF beams for the unbalanced brace forces was validated as no evidence of yielding or plastic deformation was reported during any of the tests.
- The shake table tests confirm the results from recent numerical studies that earthquake duration effects can lead to premature seismic failures or lower capacities, which provides more confidence for future initiatives to consider duration effects as part of the seismic design provisions. The tests also highlighted the importance of the fatigue role in dictating SCBFs seismic capacities and the need for well-verified numerical models for low-cycle fatigue. The experimental data provided in this study can be used in future verification studies.
- Using the calibrated model from the post-test analysis, it was shown that the fatigue parameters available from the literature can lead to different analysis results, which highlights how the fatigue parameters can affect the inferred seismic response of SCBFs under different earthquake loading scenarios. Most of the models predicted brace rupture at lower drift values. Note: even though there was large variability in the results, all the variation was on the conservative side where force or displacement capacities were underestimated.
- The fatigue parameters values provided by Salawdeh and Goggins [2013] can be considered the most relatively accurate in predicting the observed experimental behavior with an average variation of 6.8% and 7.3% in force and drift capacity, respectively. On the other hand, values reported by Chen

and Mahin [2010] seem to give the largest variation from the experimental results, with an average variation of 15% and 39.83% in force and drift capacity, respectively.

- From the archetype buildings analysis at the 10%/50-years hazard level, the results showed very limited deformation and little concentration of inelastic deformation over building height. In the three-story building, the ground-motion duration did not have any specific adverse effects. For the nine-story case, the long-duration suite of ground motions caused an average higher percentage of drift concentrated at the first floor, which was about a 25% increase in the drift demand compared to the short-duration ground motions.
- At 2%/50-years hazard level, both archetype SCBFs experienced relatively more damage under the long-duration ground motions. The damage included severe brace buckling that exceeded three times the brace width and complete brace ruptures in many cases. In some cases, a soft-story mechanism was reported where all the braces within a certain floor were ruptured. In the case of the nine-story SCBF, about 50% higher drift demands and larger number of soft-story mechanisms were reported in the case of long-duration earthquakes.
- The presented results from the archetype SCBFs analysis—especially that which pertains to the story mechanisms or possible brace rupture—are yet another means of highlighting the importance of considering ground-motion duration in future designs or performance-based assessment.
- Overall, it was shown and demonstrated throughout this study that severe structural damage or even full collapse might have a larger probability of occurrence because of larger damage accumulation in SCBF braces associated with longer duration effects.
- In summary, long-duration earthquakes are shown to have two main effects as reported from the various analytical and experimental parts of this study; they summarized in Table 8.1. First, longer duration ground motions can lead to an increase in drift demands for multi-story SCBFs relative to shorter duration motions with similar force demands. The second effect is a reduction of up to 47% in displacement capacities of SCBFs at failure or collapse when compared to spectrally-matched short-duration ground motions. This overall conclusion is based on several frames and brace configurations that varied from single-story/single-bay to multi-story/multi-bay SCBFs. The provided table also shows the different global and local slenderness range of values for all braces considered in this study, which is shown to have a large impact on the low-cycle fatigue life of the braces. Such values follow current codes and detailing practices for SCBFs, yet render the braces and overall frame behavior sensitive to duration effects.

Table 8.1 Summary of the variation in the seismic demand in SCBFs as obtained from the various analytical and experimental parts of this study.

Frame Type					
Study type	Numerical	Numerical	Experimental /Numerical	Numerical	Numerical
Scale	Full	Full	1/2	Full	Full
Variation in drift % at collapse	47	42	45	30	37
Variation in acceleration % at collapse	12	8	10	5	7
Global slenderness (kL/r)	67	78	72	82 → 112	70 → 112
Local slenderness (b/t)	11.3	10.0	11.4	7.6 → 10.0	7.6 → 14.0



8.3 FUTURE WORK

Based on the research reported herein, several aspects pertaining to this work deserve further study:

- There is an urgent need to assess existing steel and braced buildings—especially older buildings with limited ductility—located in the Pacific Northwest of the United States where longer duration earthquakes are expected from Cascadia Subduction zone ruptures. Performance-based assessment using comprehensive frameworks, e.g., FEMA P-58 [2018], can be an appropriate methodology to determine whether existing buildings with braced frames should be retrofitted.
- New research is needed to develop accurate fragility curves under suites of long-duration earthquakes and incorporate into assessment frameworks.
- There is a need for more experimental testing of large-scale and full-scale braces but under realistic short and long-duration earthquake loading for calibrating better empirical models to address fatigue. Evaluation of the behavior of SCBFs using hybrid simulation can be ideal where only the braces can be tested experimentally and other system components that are expected to remain elastic (columns, beams, and connections) can be modeled computationally. Such testing will provide a feasible means to reduce testing expenses (time and material) while providing new datasets of strain and fatigue life of full-scale braces under realistic earthquake loading. Moreover, hybrid testing can also help investigate how the brace design parameters, such

as global and local slenderness, will affect its response to short and long-duration earthquakes.

- As shown in Table 8.1, all of the SCBFs were designed according to the current design code that specifies limits for both the global and local slenderness ratios for the braces design, defined as kL/r and b/t , respectively. These limits are set based on short-duration or crustal ground-motion records. One way of incorporating duration effects in future design provisions would be to define restrictive limits for these slenderness ratios, change SCBFs detailing to alter the global and local brace buckling behavior to reduce the damaging content of low-cycle fatigue, and reduce or eliminate SCBFs sensitivity to long-duration earthquakes. This will require new research to experiment with various design details and local and global slenderness ratios to define what those limits should be..
- Output and results from the University of Washington M9 project can be further extended to address the scientific and engineering challenges in reducing the risk of experiencing a M9 earthquake along the Cascadia subduction zone fault. For instance, it would be beneficial to test SCBFs under the synthetic long-duration ground motions developed by the M9 project.
- More investigation on the effect of ground-motion duration on structural response is required based on specific characterization of the seismic hazard in regions where long-duration motions are expected. The ultimate goal here is to implement design parameters and provide design guidance to account for duration effects. Potential ways would include incorporating simple factors to adjust the design force to consider the duration effect based on spatial distributions and hazard maps for longer duration scenarios.

REFERENCES

- Aguero A., Izvernari C., Tremblay R. (2006). Modelling of the seismic response of concentrically braced steel frames using the OpenSees analysis environment, *Inter. J. Adv. Steel Constr.*, 2(3): 242–274.
- AISC (2001). *AISC Manual of Steel Construction: Load and Resistance Factor Design*, American Institute of Steel Construction, Chicago, IL.
- AISC (2002). *Seismic Provisions for Structural Steel Buildings*, American Institute of Steel Construction, Chicago, IL.
- ASCE (2013). *Minimum Design Loads for Buildings and Other Structures, Standard ASCE/SEI 7-10*, American Society of Civil Engineer, Reston, VA.
- Aslani F., Goel S.C. (1989). Experimental and analytical study of the inelastic behavior of double angle bracing members under severe cyclic loading, *Research Report UMCE 89-5*, Department of Civil Engineering, University of Michigan, Ann Arbor, MI.
- Astaneh-Asl A. (1983). *Cyclic Behavior of Double Angle Bracing Members with End Gusset Plates*, Ph.D. Thesis, Department of Civil Engineering, Department of Civil Engineering, University of Michigan, Ann Arbor, MI.
- Barbosa A.R., Ribeiro F.L., Neves L.A. (2016). Influence of earthquake ground-motion duration on damage estimation: application to steel moment resisting frames, *Earthq. Eng. Struct. Dyn.*, 46(1): 27–49.
- Black R.; Wenger W., Popov E. (1980) Inelastic buckling of steel struts under cyclic load reversals, *EERC/UCB Report 80/40*, Berkeley: Earthquake Engineering Research Center, University of California, Berkeley, CA.
- Bommer J.J., Martinez-Pereira A. (2000). Strong motion parameters: definition, usefulness and predictability, *Proceedings*, 12th World Conference on Earthquake Engineering, Auckland, New Zealand.
- Brown V.L.S. (1989). *Stability of Gusseted Connections in Steel Structures*, Ph.D. Thesis, Department of Civil Engineering, University of Delaware, Newark, DE.
- Chandramohan R. (2016). *Duration of Earthquake Ground Motion: Influence on Structural Collapse Risk and Integration in Design and Assessment Practice*, Ph.D. thesis, Department of Civil and Environmental Engineering, Stanford University, Stanford, CA.
- Chandramohan R., Baker J.W., Deierlein G.G. (2016a). Impact of hazard-consistent ground motion duration in structural collapse risk assessment, *Earthq. Eng. Struct. Dyn.*, 45(8): 1357–1379.
- Chandramohan R., Baker J.W., Deierlein G.G. (2016b). Quantifying the influence of ground motion duration on structural collapse capacity using spectrally equivalent records, *Earthq. Spectra*, 32(2): 927–950.
- Chandramohan R., Lin, T., Backer, J. W., and Deierlein, G. G. (2013). “Influence of ground motion spectral shape and duration on seismic collapse risk.” 10th International Conference on Urban Earthquake Engineering, Tokyo Institute of Technology, Tokyo Japan.
- Chen C., Mahin S.A. (2012). Performance-based seismic demand assessment of concentrically braced steel frame buildings, *PEER Report No. 2012/103*, Pacific Earthquake Engineering Research Center, University of California, Berkeley, CA.
- Chen L., Tirca L. (2013). Simulating the seismic response of concentrically braced frames using physical theory brace models, *Open J. Civil Eng.*, 2013, 3: 69–81, DOI: 10.4236/ojce.2013.32A008.
- Cheng J.J.R., Yam M.C.H., Hu S.Z. (1994). Elastic buckling strength of gusset plate connections, ASCE, *J. Struct. Eng.*, 120(2): 538–559
- Clark K.A. (2009). *Experimental Performance of Multi-Story X-Braced SCBF Systems*, Ph.D. Thesis, Department of Civil and Environmental Engineering, University of Washington, Seattle, WA.
- Coffin Jr. L.F. (1953). A study of the effects of cyclic thermal stresses on a ductile metal, ASME, *Trans.*, 76: 931–950.
- FEMA (1997). *FEMA 273: NEHRP Guidelines for the Seismic Rehabilitation of Buildings*, Federal Emergency Management Agency, Washington, DC.
- FEMA (2000). *FEMA 355C: State of the Art Report on Systems Performance of Steel Moment Frames Subject to Earthquake Ground Motion Shaking*, H. Krawinkler, ed., Federal Emergency Management Agency, Washington, DC.
- FEMA (2008) *FEMA P-695, Quantification of Building Seismic Performance Factors*, ATC-63 Project Report. Federal Emergency Management Agency, Washington, D.C.

- FEMA (2018). *FEMA P-58, Seismic Performance Assessment of Buildings*, Vol. 1, Federal Emergency Management Agency, Washington, D.C.
- Foschaar J.C., Baker J.W., Deierlein G.G. (2012). Preliminary assessment of ground motion duration effects on structural collapse, *Proceedings*, 15th World Conference on Earthquake Engineering, Lisbon, Portugal.
- Foutch D.A., Goel S.C. Roeder C.W. (1987). Seismic testing of full-scale steel building—Part I, ASCE, *J. Struct. Eng.*, 113(11): 2111–2129.
- Goel, S.C., El-Tayem A.A. (1986). Cyclic behavior of angle x-bracing with welded connections, ASCE, *J. Struct. Eng.*, 112(11): 2528–2539.
- Grondin G.Y., Nast T.E., Cheng J.J.R. (2001) Strength and stability of corner gusset plates under cyclic loading, *Proceedings*, Annual Technical Session and Meeting, Structural Stability Research Council, Ft. Lauderdale, FL.
- Gross J.L., Cheok G (1988), Experimental study of gusseted connections for laterally braced steel buildings, *NISTIR 88-3849*, National Institute of Standards and Technology, Gaithersburg, MD.
- Gunnarsson I.R. (2004). *Numerical Performance Evaluation of Braced Frame Systems*, Masters Thesis, Department of Civil and Environmental Engineering, University of Washington, Seattle, WA.
- Hancock J., Boomer J.J. (2007). Using spectral matched records to explore the influence of strong-motion duration on inelastic structural response, *Soil Dyn. Earthq. Eng.*, 27(4): 291–299.
- Hardash S.G., Bjorhovde R. (1985). New design criteria for gusset plate in tension, *AISC, Eng. J.*, 22(2): 77–94
- Hassan E.M., Mahmoud H. (2017). Modeling resolution effects on the seismic response of a hospital steel building, *J. Construct. Steel Res.*, 139: 254–271.
- Herman D. (2006). *Further Improvements on and Understanding of SCBF Systems*, Ph.D. Thesis, Department of Civil and Environmental Engineering, University of Washington, Seattle, WA.
- Hsiao P.C. (2012). *Seismic Performance Evaluation of Concentrically Braced Frames*, Ph.D. Thesis, Department of Civil and Environmental Engineering, University of Washington, Seattle, WA.
- Hsiao P.C., Lehman D.E., Roeder C.W. (2012). Improved analytical model for special concentrically braced frames, *J. Construct. Steel Res.*, 73: 80–94.
- Hu S.Z., Cheng J.J.R, (1987). Compressive behavior of gusset plate connections, *Structural Engineering Report No. 153*, Department of Civil and Environmental Engineering, University of Alberta, Edmonton, Canada.
- Ikeda K., Mahin S.A. (1986). Cyclic response of steel braces, ASCE, *J. Struct. Eng.*, 112(2): 342–361.
- IBC (2006). *Structural/Seismic Design Manual*, International Building Code, Vol. 3, Whittier, CA.
- Johnson S.M. (2005). *Improved Seismic Performance of Special Concentrically Braced Frames*, Ph.D. Thesis, Department of Civil and Environmental Engineering, University of Washington, Seattle WA.
- Kahn L.F., Hanson R.D. (1976). Inelastic cycles of axially loaded steel members,” ASCE, *J. Struct. Div.*, 102(ST5): 947–959.
- Kanvinde A.M., (2004). Micromechanical simulation of earthquake induced fracture in steel structures, *Technical Report 145*, John A. Blume Earthquake Engineering Center, Stanford University, Stanford, CA.
- Karamanci E., Lignos D.G. (2014). Computational approach for collapse assessment of concentrically braced frames in seismic regions, ASCE, *J. Struct. Eng.*, 140(8): A4014019.
- Kotulka B.A. (2007). *Analysis for a Design Guide On Gusset Plates used in Special Concentrically Braced Frames*, Ph.D. Thesis, Department of Civil and Environmental Engineering, University of Washington, Seattle, WA.
- Kunnath S.K., El-Bahy A., Taylor A., Stone W. (1997). Cumulative seismic damage of reinforced concrete bridge piers, *NISTIR 97-6075*, National Institute of Standards and Technology, Gaithersburg, MD.
- Lai J., Mahin, S. (2012). Experimental and analytical studies on the seismic behavior of conventional and hybrid braced frames, *PEER Report No. 2013/20*, Pacific Earthquake Engineering Research Center, University of California, Berkeley, CA.
- Laplace P.N., Sanders, D., Saiidi, M. S., & Douglas, B. (1999). Shake table testing of flexure dominated reinforced concrete bridge columns, Doctoral dissertation, University of Nevada, Reno.
- Lee T.-H., Mosalam K.M. (2005). Seismic demand sensitivity of reinforced concrete shear-wall building using FOSM method, *Earthq. Eng. Struct. Dyn.*, 34(14): 1719–1736.
- Lee S., Goel S.C. (1987) Seismic behavior of hollow and concrete filled square tubular bracing members, *Research Report UMCE 87-11*, Department of Civil Engineering, University of Michigan, Ann Arbor, MI.

- Li T., Marafi N.A., Sen A.D., Berman J.W., Eberhard M.O., Lehman D.E., Roeder C.W. (2019). Seismic performance of special concentrically braced frames in deep basins during subduction-zone earthquakes, *Eng. Struct.*, 188: 87–103.
- Li, Y., Song R., Van De Lindt J. (2014). Collapse fragility of steel structures subjected to earthquake mainshock-aftershock sequence, *ASCE, J. Struct. Eng.*, 140(12), DOI: 10.1061/(ASCE)ST.1943-541X.0001019
- Lignos D., Chung Y. Nagae T., Nakashima M. (2011). Numerical and experimental evaluation of seismic capacity of high-rise steel buildings subjected to long duration earthquakes, *Comp. Struct.*, 89(11–12): 959–967.
- Lignos D., Karamanci E. (2013). Predictive equations for modelling cyclic buckling and fracture of steel braces, *Proceedings*, 10th International Conference on Urban Earthquake Engineering, Tokyo, Japan.
- Liu J., Astaneh-Asl A. (2004). Moment-rotation parameters for composite shear tab connections, *ASCE, J. Struct. Eng.*, 130(9): 1371–1380.
- Lu X., Fu G., Shi W., Lu W. (2008). Shake table model testing and its application, *Struct. Design Tall Special Bldg.*, 17(1): 181–201.
- Lumpkin E.J. (2009). *Enhanced Seismic Performance of Multi-Story Special Concentrically Brace Frames using a Balanced Design Procedure*, Ph.D. thesis, Department of Civil and Environmental Engineering, University of Washington, Seattle, WA.
- Manson S.S. (1965). Fatigue: a complex subject—some simple approximations, *Exper. Mech.*, 5(7): 193–226.
- Marafi N.A., Eberhard M.O., Berman J.W., Wirth E.A., Frankel A.D. (2019). Impacts of Simulated M9 Cascadia subduction zone motions on idealized systems, *Earthq. Spectra*, DOI: 10.1193/052418EQS123M
- Marsh M.L., Gianotti C.M. (1995). Inelastic structural response to Cascadia subduction zone earthquakes, *Earthq. Spectra*, 11(1): 63–89.
- McKenna F., Fenves G.L., Scott M.H. (2006). OpenSees: Open System for Earthquake Engineering Simulation, Pacific Earthquake Engineering Research Center, University of California, Berkeley, CA, retrieved from <http://opensees.berkeley.edu>.
- Menegotto M. Pinto P.E. (1973). Method of analysis for cyclically loaded RC plane frames including changes in geometry and non-elastic behavior of elements under combined normal force and bending, *Proceedings, IABSE Symposium on Resistance and Ultimate Deformability of Structures*, pp. 15–22, Lisbon, Portugal.
- Mohammed M.S. (2016). *Effect of Earthquake Duration on Reinforced Concrete Bridge Columns*, Ph.D. Thesis, Department of Civil and Environmental Engineering, University of Nevada, Reno, NV.
- Ngeljaratan L., Moustafa M.A. (2017). Digital image correlation for dynamic shake table test measurements, *Proceedings*, 7th International Conference on Advances in Experimental Structural Engineering, Pavia, Italy.
- Ngeljaratan L., Moustafa M.A. (2018). Novel digital image correlation instrumentation for large-scale shake table tests, *Proceedings*, 11th National Conference on Earthquake Engineering, Los Angeles, CA.
- Ou Y.-C., Song J., Wang P.-H., Adidharma L., Chang K.-C., Lee G.C. (2014). Ground motion duration effects on hysteretic behavior of reinforced concrete bridge columns, *ASCE, J. Struct. Eng.*, 140(3), DOI: 10.1061/(ASCE)ST.1943-541X.0000856.
- Padgett J.E., DesRoches R. (2007). Bridge functionality relationships for improved seismic risk assessment of transportation networks, *Earthq. Spectra*, 23(1): 115–130.
- Palmer K.D., Roeder C.W., Lehman D.E., Okazaki T., Shield C.K., Powell J. (2012). Concentric X-braced frames with HSS bracing, *Inter. J. Steel Struct.*, 12(3): 443–459.
- PEER (2011). PEER Strong Motion Database, Pacific Earthquake Engineering Research, University of California, <http://peer.berkeley.edu/smcat/>.
- Pereira J.C.R., De Jesus A.M.P., Fernandes A.A., Xavier J., Martins B. (2014). Comparisons of monotonic, low-cycle and ultra-low-cycle fatigue behaviours of x52, x60 and x65 piping steel grades, *Proceedings*, ASME 2014 Pressure Vessels and Piping Conference, pp. V06AT06A015–V06AT06A015, Anaheim, CA.
- Popov E.P., Takanashi K., Roeder C.W. (1976). Structural steel bracing systems: Behavior under cyclic loading, *EERC Report. No. 76-17*, Earthquake Engineering Research Center, University of California, Berkeley, CA.
- Porter K.A., Beck J.L., Shaikhutdinov R.V. (2002). Sensitivity of building loss estimates to major uncertain variables, *Earthq. Spectra*, 18(4): 719–743.
- Powell J. (2009) *Evaluation of Special Concentrically Braced Frames for Improved Seismic Performance and Constructability*, Masters Thesis, Department of Civil Eng a thesis submitted in partial fulfillment of the MSCE, University of Washington, Seattle; December.

- Rabinovitch J.S., Cheng J.J.R. (1993). Cyclic behavior of steel gusset plate connections, *Structural Engineering Report No. 191*, Department of Civil and Environmental Engineering, University of Alberta, Edmonton, Canada.
- Raghunandan M., Liel A.B. (2013). Effect of ground motion duration on earthquake-induced structural collapse. *Structural Safety*, 41, 119-133.
- Raghunandan M., Liel A.B., Luco N. (2015). Collapse risk of buildings in the Pacific Northwest region due to subduction earthquakes, *Earthq. Spectra*, 31(4): 2087–2115.
- Ranf R.T. (2005). Damage accumulation in lightly confined reinforced concrete bridge columns, *PEER Report No. 2005/08*, Pacific Earthquake Engineering Research Center, University of California, Berkeley, CA.
- Roeder C.W., Lumpkin E.J., Lehman D.E. (2012). Seismic performance assessment of concentrically braced steel frames, *Earthq. Spectra*, 28(2): 709–727.
- SAC Steel Project (1997). Protocol for fabrication, inspection, testing and documentation of beam-column connection tests and other experiments, Eds. P. Clark, K. Frank, H. Krawinkler, and R. Shaw, *Report No. SAC/BD-97/02*, SAC Joint Venture, Sacramento, CA.
- Salawdeh S., Goggins J. (2013). Numerical simulation for steel brace members incorporating a fatigue model, *Eng. Struct.*, 46: 332–349.
- Santagati S., Bolognini D., Nascimbene R. (2012). Strain life analysis at low-cycle fatigue on concentrically braced steel structures with RHS shape braces. *J. Earthq. Eng.*, 16(sup1): 107–137.
- SeismoSoft (2010). *SeismoMatch*, Version 2.0.
- Sheng N., Yam M.C.H., Lu V.P. (2002). Analytical investigation and the design of the compressive strength of steel gusset plate connections, *J. Construct. Steel Res.*, 58: 1473–1493.
- Song R., Li Y., van de Lindt J.W. (2014). Impact of earthquake ground motion characteristics on collapse risk of post-mainshock buildings considering aftershocks, *Engineering Structures*, 81, 349-361.
- Stapleton S.E. (2004). *Performance of Poorly Confined Reinforced Concrete Columns in Long-Duration Earthquakes*, Ph.D. Thesis, Department of Civil and Environmental Engineering, Washington State University, Pullman, WA
- Thompson T.J. (2004). *The Effects of Long-Duration Earthquakes on Concrete Bridges with Poorly Confined Columns*, Masters Thesis, Department of Civil and Environmental Engineering, University of Washington, Seattle, WA.
- Thornton W.A. (1984). Bracing connections for heavy construction, *AISC, Eng. J.*, 21(3): 139–148.
- Tirca L., Chen L. (2014). Numerical simulation of inelastic cyclic response of HSS braces upon fracture, *Adv. Steel Construct.*, 10(4): 442–462.
- Tirca L., Chen L., Tremblay R. (2015). Assessing collapse safety of CBF buildings subjected to crustal and subduction earthquakes, *J. Construct. Steel Res.*, 115: 47–61.
- Uriz P. (2005). *Towards Earthquake Resistant Design of Concentrically Braced Steel Buildings*, Ph.D. Thesis, Department of Civil and Environmental Engineering, University of California, Berkeley, CA.
- Uriz P., Mahin S.A. (2004). Seismic performance assessment of concentrically braced steel frames, *Proceedings*, 13th World Conference on Earthquake Engineering, Vancouver, B.C., Canada.
- Uriz P., Mahin S.A. (2008). Toward earthquake resistant design of concentrically braced steel frame structures, *PEER Report No. 2008/08*, Pacific Earthquake Engineering Research Center, University of California, Berkeley, CA.
- U.S.G.S. (2017) Earthquake Facts and Statistics, U.S. Geological Survey, accessed March 22, 2018, <https://earthquake.usgs.gov/earthquakes/browse/stats.php>.
- Vamvatsikos D., Cornell C.A. (2002). Incremental dynamic analysis, *Earthq. Eng. Struct. Dyn.*, 31(3): 491–514.
- Wakabayashi M., Nonaka T., Nakamura T., Morino S., Yoshida N. (1973). Experimental studies on the behavior of steel bars under repeated axial loading—part 1, rectangular cross-section, *Bulletin*, Disaster Prevention Research Institute, Kyoto University, (16B): 113–125.
- Walbridge S.S., Grondin G.Y., Cheng J.J.R. (1998). An analysis of the cyclic behavior of steel gusset plate connections, *Structural Engineering Report No. 225*, Department of Civil and Environmental Engineering, University of Alberta, Edmonton, Canada.
- Wen H., Mahmoud H. (2015). New model for ductile fracture of metal alloys. I: Monotonic loading, *ASCE, J. Eng. Mech.*, 142(2), DOI: 10.1061/(ASCE)EM.1943-7889.0001009.
- Whitmore R.E. (1952). *Experimental Investigation of Stresses in Gusset Plates*, Masters Thesis, Department of Civil Engineering, University of Tennessee, Knoxville, TN.

- Workman G.H. (1969). *The Inelastic Behavior of Multistory Braced Frame Structures Subjected to Earthquake Excitation*, Ph.D. Thesis, Department of Civil Engineering, University of Michigan, Ann Arbor, MI.
- Xu P., Goel S.C. (1990). Behavior of double channel bracing members under large cyclic deformations, *Research Report UMCE 90-1*, Department of Civil Engineering, University of Michigan, Ann Arbor, MI.

PEER REPORTS

PEER reports are available as a free PDF download from <https://peer.berkeley.edu/peer-reports>. In addition, printed hard copies of PEER reports can be ordered directly from our printer by following the instructions at <https://peer.berkeley.edu/peer-reports>. For other related questions about the PEER Report Series, contact the Pacific Earthquake Engineering Research Center, 325 Davis Hall, Mail Code 1792, Berkeley, CA 94720. Tel.: (510) 642-3437; and Email: peer_center@berkeley.edu.

- PEER 2019/08** *Influence of Vertical Ground Motion on Bridges Isolated with Spherical Sliding Bearings.* Rushil Mojidra and Keri L. Ryan. December 2019.
- PEER 2019/07** *PEER Hub ImageNet (ϕ -Net): A Large-Scale Multi-Attribute Benchmark Dataset of Structural Images.* Yuqing Gao, and Khalid. M. Mosalam. November 2019.
- PEER 2019/06** *Fluid-Structure Interaction and Python-Scripting Capabilities in OpenSees.* Minjie Zhu and Michael H. Scott. August 2019.
- PEER 2019/05** *Expected Earthquake Performance of Buildings Designed to the California Building Code (California Alfred E. Alquist Seismic Safety Publication 19-01).* Grace S. Kang, Sifat Muin, Jorge Archbold, Bitanoosh Woods, and Khalid Mosalam. July 2019.
- PEER 2019/04** *Aftershock Seismic Vulnerability and Time-Dependent Risk Assessment of Bridges.* Sujith Mangalathu, Mehrdad Shokrabadi, and Henry V. Burton. May 2019.
- PEER 2019/03** *Ground-Motion Directivity Modeling for Seismic Hazard Applications.* Jennifer L. Donahue, Jonathan P. Stewart, Nicolas Gregor, and Yousef Bozorgnia. Review Panel: Jonathan D. Bray, Stephen A. Mahin, I. M. Idriss, Robert W. Graves, and Tom Shantz. May 2019.
- PEER 2019/02** *Direct-Finite-Element Method for Nonlinear Earthquake Analysis of Concrete Dams Including Dam–Water–Foundation Rock Interaction.* Arnkjell Løkke and Anil K. Chopra. March 2019.
- PEER 2019/01** *Flow-Failure Case History of the Las Palmas, Chile, Tailings Dam.* R. E. S. Moss, T. R. Gebhart, D. J. Frost, and C. Ledezma. January 2019.
- PEER 2018/08** *Central and Eastern North America Ground-Motion Characterization: NGA-East Final Report.* Christine Goulet, Yousef Bozorgnia, Norman Abrahamson, Nicolas Kuehn, Linda Al Atik, Robert Youngs, Robert Graves, and Gail Atkinson. December 2018.
- PEER 2018/07** *An Empirical Model for Fourier Amplitude Spectra using the NGA-West2 Database.* Jeff Bayless, and Norman A. Abrahamson. December 2018.
- PEER 2018/06** *Estimation of Shear Demands on Rock-Socketed Drilled Shafts subjected to Lateral Loading.* Pedro Arduino, Long Chen, and Christopher R. McGann. December 2018.
- PEER 2018/05** *Selection of Random Vibration Procedures for the NGA-East Project.* Albert Kottke, Norman A. Abrahamson, David M. Boore, Yousef Bozorgnia, Christine Goulet, Justin Hollenback, Tadahiro Kishida, Armen Der Kiureghian, Olga-Joan Ktenidou, Nicolas Kuehn, Ellen M. Rathje, Walter J. Silva, Eric Thompson, and Xiaoyue Wang. December 2018.
- PEER 2018/04** *Capturing Directivity Effects in the Mean and Aleatory Variability of the NGA-West 2 Ground Motion Prediction Equations.* Jennie A. Watson-Lamprey. November 2018.
- PEER 2018/03** *Probabilistic Seismic Hazard Analysis Code Verification.* Christie Hale, Norman Abrahamson, and Yousef Bozorgnia. July 2018.
- PEER 2018/02** *Update of the BChydro Subduction Ground-Motion Model using the NGA-Subduction Dataset.* Norman Abrahamson, Nicolas Kuehn, Zeynep Gulerce, Nicholas Gregor, Yousef Bozorgnia, Grace Parker, Jonathan Stewart, Brian Chiou, I. M. Idriss, Kenneth Campbell, and Robert Youngs. June 2018.
- PEER 2018/01** *PEER Annual Report 2017–2018.* Khalid Mosalam, Amarnath Kasalanati, and Selim Günay. June 2018.
- PEER 2017/12** *Experimental Investigation of the Behavior of Vintage and Retrofit Concentrically Braced Steel Frames under Cyclic Loading.* Barbara G. Simpson, Stephen A. Mahin, and Jiun-Wei Lai, December 2017.
- PEER 2017/11** *Preliminary Studies on the Dynamic Response of a Seismically Isolated Prototype Gen-IV Sodium-Cooled Fast Reactor (PGSFR).* Benshun Shao, Andreas H. Schellenberg, Matthew J. Schoettler, and Stephen A. Mahin. December 2017.
- PEER 2017/10** *Development of Time Histories for IEEE693 Testing and Analysis (including Seismically Isolated Equipment).* Shakhzod M. Takhirov, Eric Fujisaki, Leon Kempner, Michael Riley, and Brian Low. December 2017.

- PEER 2017/09** *“R” Package for Computation of Earthquake Ground-Motion Response Spectra.* Pengfei Wang, Jonathan P. Stewart, Yousef Bozorgnia, David M. Boore, and Tadahiro Kishida. December 2017.
- PEER 2017/08** *Influence of Kinematic SSI on Foundation Input Motions for Bridges on Deep Foundations.* Benjamin J. Turner, Scott J. Brandenburg, and Jonathan P. Stewart. November 2017.
- PEER 2017/07** *A Nonlinear Kinetic Model for Multi-Stage Friction Pendulum Systems.* Paul L. Drazin and Sanjay Govindjee. September 2017.
- PEER 2017/06** *Guidelines for Performance-Based Seismic Design of Tall Buildings, Version 2.02.* TBI Working Group led by co-chairs Ron Hamburger and Jack Moehle: Jack Baker, Jonathan Bray, C.B. Crouse, Greg Deierlein, John Hooper, Marshall Lew, Joe Maffei, Stephen Mahin, James Malley, Farzad Naeim, Jonathan Stewart, and John Wallace. May 2017.
- PEER 2017/05** *Recommendations for Ergodic Nonlinear Site Amplification in Central and Eastern North America.* Youssef M.A. Hashash, Joseph A. Harmon, Okan Ilhan, Grace A. Parker, and Jonathan P. Stewart. March 2017.
- PEER 2017/04** *Expert Panel Recommendations for Ergodic Site Amplification in Central and Eastern North America.* Jonathan P. Stewart, Grace A. Parker, Joseph P. Harmon, Gail M. Atkinson, David M. Boore, Robert B. Darragh, Walter J. Silva, and Youssef M.A. Hashash. March 2017.
- PEER 2017/03** *NGA-East Ground-Motion Models for the U.S. Geological Survey National Seismic Hazard Maps.* Christine A. Goulet, Yousef Bozorgnia, Nicolas Kuehn, Linda Al Atik, Robert R. Youngs, Robert W. Graves, and Gail M. Atkinson. March 2017.
- PEER 2017/02** *U.S.–New Zealand–Japan Workshop: Liquefaction-Induced Ground Movements Effects, University of California, Berkeley, California, 2–4 November 2016.* Jonathan D. Bray, Ross W. Boulanger, Misko Cubrinovski, Kohji Tokimatsu, Steven L. Kramer, Thomas O'Rourke, Ellen Rathje, Russell A. Green, Peter K. Robinson, and Christine Z. Beyzaei. March 2017.
- PEER 2017/01** *2016 PEER Annual Report.* Khalid M. Mosalam, Amarnath Kasalanati, and Grace Kang. March 2017.
- PEER 2016/10** *Performance-Based Robust Nonlinear Seismic Analysis with Application to Reinforced Concrete Bridge Systems.* Xiao Ling and Khalid M. Mosalam. December 2016.
- PEER 2017/09** *Detailing Requirements for Column Plastic Hinges subjected to Combined Flexural, Axial, and Torsional Seismic Loading.* Gabriel Hurtado and Jack P. Moehle. December 2016.
- PEER 2016/08** *Resilience of Critical Structures, Infrastructure, and Communities.* Gian Paolo Cimellaro, Ali Zamani-Noori, Omar Kamouh, Vesna Terzic, and Stephen A. Mahin. December 2016.
- PEER 2016/07** *Hybrid Simulation Theory for a Classical Nonlinear Dynamical System.* Paul L. Drazin and Sanjay Govindjee. September 2016.
- PEER 2016/06** *California Earthquake Early Warning System Benefit Study.* Laurie A. Johnson, Sharyl Rabinovici, Grace S. Kang, and Stephen A. Mahin. July 2006.
- PEER 2016/05** *Ground-Motion Prediction Equations for Arias Intensity Consistent with the NGA-West2 Ground-Motion Models.* Charlotte Abrahamson, Hao-Jun Michael Shi, and Brian Yang. July 2016.
- PEER 2016/04** *The M_w 6.0 South Napa Earthquake of August 24, 2014: A Wake-Up Call for Renewed Investment in Seismic Resilience Across California.* Prepared for the California Seismic Safety Commission, Laurie A. Johnson and Stephen A. Mahin. May 2016.
- PEER 2016/03** *Simulation Confidence in Tsunami-Driven Overland Flow.* Patrick Lynett. May 2016.
- PEER 2016/02** *Semi-Automated Procedure for Windowing time Series and Computing Fourier Amplitude Spectra for the NGA-West2 Database.* Tadahiro Kishida, Olga-Joan Ktenidou, Robert B. Darragh, and Walter J. Silva. May 2016.
- PEER 2016/01** *A Methodology for the Estimation of Kappa (κ) from Large Datasets: Example Application to Rock Sites in the NGA-East Database and Implications on Design Motions.* Olga-Joan Ktenidou, Norman A. Abrahamson, Robert B. Darragh, and Walter J. Silva. April 2016.
- PEER 2015/13** *Self-Centering Precast Concrete Dual-Steel-Shell Columns for Accelerated Bridge Construction: Seismic Performance, Analysis, and Design.* Gabriele Guerrini, José I. Restrepo, Athanassios Vervelidis, and Milena Massari. December 2015.
- PEER 2015/12** *Shear-Flexure Interaction Modeling for Reinforced Concrete Structural Walls and Columns under Reversed Cyclic Loading.* Kristijan Kolozvari, Kutay Orakcal, and John Wallace. December 2015.
- PEER 2015/11** *Selection and Scaling of Ground Motions for Nonlinear Response History Analysis of Buildings in Performance-Based Earthquake Engineering.* N. Simon Kwong and Anil K. Chopra. December 2015.

- PEER 2015/10** *Structural Behavior of Column-Bent Cap Beam-Box Girder Systems in Reinforced Concrete Bridges Subjected to Gravity and Seismic Loads. Part II: Hybrid Simulation and Post-Test Analysis.* Mohamed A. Moustafa and Khalid M. Mosalam. November 2015.
- PEER 2015/09** *Structural Behavior of Column-Bent Cap Beam-Box Girder Systems in Reinforced Concrete Bridges Subjected to Gravity and Seismic Loads. Part I: Pre-Test Analysis and Quasi-Static Experiments.* Mohamed A. Moustafa and Khalid M. Mosalam. September 2015.
- PEER 2015/08** *NGA-East: Adjustments to Median Ground-Motion Models for Center and Eastern North America.* August 2015.
- PEER 2015/07** *NGA-East: Ground-Motion Standard-Deviation Models for Central and Eastern North America.* Linda Al Atik. June 2015.
- PEER 2015/06** *Adjusting Ground-Motion Intensity Measures to a Reference Site for which $V_{S30} = 3000$ m/sec.* David M. Boore. May 2015.
- PEER 2015/05** *Hybrid Simulation of Seismic Isolation Systems Applied to an APR-1400 Nuclear Power Plant.* Andreas H. Schellenberg, Alireza Sarebanha, Matthew J. Schoettler, Gilberto Mosqueda, Gianmario Benzoni, and Stephen A. Mahin. April 2015.
- PEER 2015/04** *NGA-East: Median Ground-Motion Models for the Central and Eastern North America Region.* April 2015.
- PEER 2015/03** *Single Series Solution for the Rectangular Fiber-Reinforced Elastomeric Isolator Compression Modulus.* James M. Kelly and Niel C. Van Engelen. March 2015.
- PEER 2015/02** *A Full-Scale, Single-Column Bridge Bent Tested by Shake-Table Excitation.* Matthew J. Schoettler, José I. Restrepo, Gabriele Guerrini, David E. Duck, and Francesco Carrea. March 2015.
- PEER 2015/01** *Concrete Column Blind Prediction Contest 2010: Outcomes and Observations.* Vesna Terzic, Matthew J. Schoettler, José I. Restrepo, and Stephen A Mahin. March 2015.
- PEER 2014/20** *Stochastic Modeling and Simulation of Near-Fault Ground Motions for Performance-Based Earthquake Engineering.* Mayssa Dabaghi and Armen Der Kiureghian. December 2014.
- PEER 2014/19** *Seismic Response of a Hybrid Fiber-Reinforced Concrete Bridge Column Detailed for Accelerated Bridge Construction.* Wilson Nguyen, William Trono, Marios Panagiotou, and Claudia P. Ostertag. December 2014.
- PEER 2014/18** *Three-Dimensional Beam-Truss Model for Reinforced Concrete Walls and Slabs Subjected to Cyclic Static or Dynamic Loading.* Yuan Lu, Marios Panagiotou, and Ioannis Koutromanos. December 2014.
- PEER 2014/17** *PEER NGA-East Database.* Christine A. Goulet, Tadahiro Kishida, Timothy D. Ancheta, Chris H. Cramer, Robert B. Darragh, Walter J. Silva, Youssef M.A. Hashash, Joseph Harmon, Jonathan P. Stewart, Katie E. Wooddell, and Robert R. Youngs. October 2014.
- PEER 2014/16** *Guidelines for Performing Hazard-Consistent One-Dimensional Ground Response Analysis for Ground Motion Prediction.* Jonathan P. Stewart, Kioumars Afshari, and Youssef M.A. Hashash. October 2014.
- PEER 2014/15** *NGA-East Regionalization Report: Comparison of Four Crustal Regions within Central and Eastern North America using Waveform Modeling and 5%-Damped Pseudo-Spectral Acceleration Response.* Jennifer Dreiling, Marius P. Isken, Walter D. Mooney, Martin C. Chapman, and Richard W. Godbee. October 2014.
- PEER 2014/14** *Scaling Relations between Seismic Moment and Rupture Area of Earthquakes in Stable Continental Regions.* Paul Somerville. August 2014.
- PEER 2014/13** *PEER Preliminary Notes and Observations on the August 24, 2014, South Napa Earthquake.* Grace S. Kang and Stephen A. Mahin, Editors. September 2014.
- PEER 2014/12** *Reference-Rock Site Conditions for Central and Eastern North America: Part II – Attenuation (Kappa) Definition.* Kenneth W. Campbell, Youssef M.A. Hashash, Byungmin Kim, Albert R. Kottke, Ellen M. Rathje, Walter J. Silva, and Jonathan P. Stewart. August 2014.
- PEER 2014/11** *Reference-Rock Site Conditions for Central and Eastern North America: Part I - Velocity Definition.* Youssef M.A. Hashash, Albert R. Kottke, Jonathan P. Stewart, Kenneth W. Campbell, Byungmin Kim, Ellen M. Rathje, Walter J. Silva, Sissy Nikolaou, and Cheryl Moss. August 2014.
- PEER 2014/10** *Evaluation of Collapse and Non-Collapse of Parallel Bridges Affected by Liquefaction and Lateral Spreading.* Benjamin Turner, Scott J. Brandenburg, and Jonathan P. Stewart. August 2014.
- PEER 2014/09** *PEER Arizona Strong-Motion Database and GMPEs Evaluation.* Tadahiro Kishida, Robert E. Kayen, Olga-Joan Ktenidou, Walter J. Silva, Robert B. Darragh, and Jennie Watson-Lamprey. June 2014.
- PEER 2014/08** *Unbonded Pretensioned Bridge Columns with Rocking Detail.* Jeffrey A. Schaefer, Bryan Kennedy, Marc O. Eberhard, and John F. Stanton. June 2014.

- PEER 2014/07** *Northridge 20 Symposium Summary Report: Impacts, Outcomes, and Next Steps*. May 2014.
- PEER 2014/06** *Report of the Tenth Planning Meeting of NEES/E-Defense Collaborative Research on Earthquake Engineering*. December 2013.
- PEER 2014/05** *Seismic Velocity Site Characterization of Thirty-One Chilean Seismometer Stations by Spectral Analysis of Surface Wave Dispersion*. Robert Kayen, Brad D. Carkin, Skye Corbet, Camilo Pinilla, Allan Ng, Edward Gorbis, and Christine Truong. April 2014.
- PEER 2014/04** *Effect of Vertical Acceleration on Shear Strength of Reinforced Concrete Columns*. Hyerin Lee and Khalid M. Mosalam. April 2014.
- PEER 2014/03** *Retest of Thirty-Year-Old Neoprene Isolation Bearings*. James M. Kelly and Niel C. Van Engelen. March 2014.
- PEER 2014/02** *Theoretical Development of Hybrid Simulation Applied to Plate Structures*. Ahmed A. Bakhaty, Khalid M. Mosalam, and Sanjay Govindjee. January 2014.
- PEER 2014/01** *Performance-Based Seismic Assessment of Skewed Bridges*. Peyman Kaviani, Farzin Zareian, and Ertugrul Taciroglu. January 2014.
- PEER 2013/26** *Urban Earthquake Engineering*. Proceedings of the U.S.-Iran Seismic Workshop. December 2013.
- PEER 2013/25** *Earthquake Engineering for Resilient Communities: 2013 PEER Internship Program Research Report Collection*. Heidi Tremayne (Editor), Stephen A. Mahin (Editor), Jorge Archbold Monterossa, Matt Brosman, Shelly Dean, Katherine deLaveaga, Curtis Fong, Donovan Holder, Rakeeb Khan, Elizabeth Jachens, David Lam, Daniela Martinez Lopez, Mara Minner, Geffen Oren, Julia Pavicic, Melissa Quinonez, Lorena Rodriguez, Sean Salazar, Kelli Slaven, Vivian Steyert, Jenny Taing, and Salvador Tena. December 2013.
- PEER 2013/24** *NGA-West2 Ground Motion Prediction Equations for Vertical Ground Motions*. September 2013.
- PEER 2013/23** *Coordinated Planning and Preparedness for Fire Following Major Earthquakes*. Charles Scawthorn. November 2013.
- PEER 2013/22** *GEM-PEER Task 3 Project: Selection of a Global Set of Ground Motion Prediction Equations*. Jonathan P. Stewart, John Douglas, Mohammad B. Javanbarg, Carola Di Alessandro, Yousef Bozorgnia, Norman A. Abrahamson, David M. Boore, Kenneth W. Campbell, Elise Delavaud, Mustafa Erdik, and Peter J. Stafford. December 2013.
- PEER 2013/21** *Seismic Design and Performance of Bridges with Columns on Rocking Foundations*. Grigorios Antonellis and Marios Panagiotou. September 2013.
- PEER 2013/20** *Experimental and Analytical Studies on the Seismic Behavior of Conventional and Hybrid Braced Frames*. Jiun-Wei Lai and Stephen A. Mahin. September 2013.
- PEER 2013/19** *Toward Resilient Communities: A Performance-Based Engineering Framework for Design and Evaluation of the Built Environment*. Michael William Mieler, Bozidar Stojadinovic, Robert J. Budnitz, Stephen A. Mahin, and Mary C. Comerio. September 2013.
- PEER 2013/18** *Identification of Site Parameters that Improve Predictions of Site Amplification*. Ellen M. Rathje and Sara Navidi. July 2013.
- PEER 2013/17** *Response Spectrum Analysis of Concrete Gravity Dams Including Dam-Water-Foundation Interaction*. Arnkjell Løkke and Anil K. Chopra. July 2013.
- PEER 2013/16** *Effect of Hoop Reinforcement Spacing on the Cyclic Response of Large Reinforced Concrete Special Moment Frame Beams*. Marios Panagiotou, Tea Visnjic, Grigorios Antonellis, Panagiotis Galanis, and Jack P. Moehle. June 2013.
- PEER 2013/15** *A Probabilistic Framework to Include the Effects of Near-Fault Directivity in Seismic Hazard Assessment*. Shrey Kumar Shahi, Jack W. Baker. October 2013.
- PEER 2013/14** *Hanging-Wall Scaling using Finite-Fault Simulations*. Jennifer L. Donahue and Norman A. Abrahamson. September 2013.
- PEER 2013/13** *Semi-Empirical Nonlinear Site Amplification and its Application in NEHRP Site Factors*. Jonathan P. Stewart and Emel Seyhan. November 2013.
- PEER 2013/12** *Nonlinear Horizontal Site Response for the NGA-West2 Project*. Ronnie Kamai, Norman A. Abramson, Walter J. Silva. May 2013.
- PEER 2013/11** *Epistemic Uncertainty for NGA-West2 Models*. Linda Al Atik and Robert R. Youngs. May 2013.
- PEER 2013/10** *NGA-West 2 Models for Ground-Motion Directionality*. Shrey K. Shahi and Jack W. Baker. May 2013.

- PEER 2013/09** *Final Report of the NGA-West2 Directivity Working Group.* Paul Spudich, Jeffrey R. Bayless, Jack W. Baker, Brian S.J. Chiou, Badie Rowshandel, Shrey Shahi, and Paul Somerville. May 2013.
- PEER 2013/08** *NGA-West2 Model for Estimating Average Horizontal Values of Pseudo-Absolute Spectral Accelerations Generated by Crustal Earthquakes.* I. M. Idriss. May 2013.
- PEER 2013/07** *Update of the Chiou and Youngs NGA Ground Motion Model for Average Horizontal Component of Peak Ground Motion and Response Spectra.* Brian Chiou and Robert Youngs. May 2013.
- PEER 2013/06** *NGA-West2 Campbell-Bozorgnia Ground Motion Model for the Horizontal Components of PGA, PGV, and 5%-Damped Elastic Pseudo-Acceleration Response Spectra for Periods Ranging from 0.01 to 10 sec.* Kenneth W. Campbell and Yousef Bozorgnia. May 2013.
- PEER 2013/05** *NGA-West 2 Equations for Predicting Response Spectral Accelerations for Shallow Crustal Earthquakes.* David M. Boore, Jonathan P. Stewart, Emel Seyhan, and Gail M. Atkinson. May 2013.
- PEER 2013/04** *Update of the AS08 Ground-Motion Prediction Equations Based on the NGA-West2 Data Set.* Norman Abrahamson, Walter Silva, and Ronnie Kamai. May 2013.
- PEER 2013/03** *PEER NGA-West2 Database.* Timothy D. Ancheta, Robert B. Darragh, Jonathan P. Stewart, Emel Seyhan, Walter J. Silva, Brian S.J. Chiou, Katie E. Wooddell, Robert W. Graves, Albert R. Kottke, David M. Boore, Tadahiro Kishida, and Jennifer L. Donahue. May 2013.
- PEER 2013/02** *Hybrid Simulation of the Seismic Response of Squat Reinforced Concrete Shear Walls.* Catherine A. Whyte and Bozidar Stojadinovic. May 2013.
- PEER 2013/01** *Housing Recovery in Chile: A Qualitative Mid-program Review.* Mary C. Comerio. February 2013.
- PEER 2012/08** *Guidelines for Estimation of Shear Wave Velocity.* Bernard R. Wair, Jason T. DeJong, and Thomas Shantz. December 2012.
- PEER 2012/07** *Earthquake Engineering for Resilient Communities: 2012 PEER Internship Program Research Report Collection.* Heidi Tremayne (Editor), Stephen A. Mahin (Editor), Collin Anderson, Dustin Cook, Michael Erceg, Carlos Esparza, Jose Jimenez, Dorian Krausz, Andrew Lo, Stephanie Lopez, Nicole McCurdy, Paul Shipman, Alexander Strum, Eduardo Vega. December 2012.
- PEER 2012/06** *Fragilities for Precarious Rocks at Yucca Mountain.* Matthew D. Purvance, Rasool Anooshehpour, and James N. Brune. December 2012.
- PEER 2012/05** *Development of Simplified Analysis Procedure for Piles in Laterally Spreading Layered Soils.* Christopher R. McGann, Pedro Arduino, and Peter Mackenzie-Helwein. December 2012.
- PEER 2012/04** *Unbonded Pre-Tensioned Columns for Bridges in Seismic Regions.* Phillip M. Davis, Todd M. Janes, Marc O. Eberhard, and John F. Stanton. December 2012.
- PEER 2012/03** *Experimental and Analytical Studies on Reinforced Concrete Buildings with Seismically Vulnerable Beam-Column Joints.* Sangjoon Park and Khalid M. Mosalam. October 2012.
- PEER 2012/02** *Seismic Performance of Reinforced Concrete Bridges Allowed to Uplift during Multi-Directional Excitation.* Andres Oscar Espinoza and Stephen A. Mahin. July 2012.
- PEER 2012/01** *Spectral Damping Scaling Factors for Shallow Crustal Earthquakes in Active Tectonic Regions.* Sanaz Rezaeian, Yousef Bozorgnia, I. M. Idriss, Kenneth Campbell, Norman Abrahamson, and Walter Silva. July 2012.
- PEER 2011/10** *Earthquake Engineering for Resilient Communities: 2011 PEER Internship Program Research Report Collection.* Heidi Faison and Stephen A. Mahin, Editors. December 2011.
- PEER 2011/09** *Calibration of Semi-Stochastic Procedure for Simulating High-Frequency Ground Motions.* Jonathan P. Stewart, Emel Seyhan, and Robert W. Graves. December 2011.
- PEER 2011/08** *Water Supply in regard to Fire Following Earthquake.* Charles Scawthorn. November 2011.
- PEER 2011/07** *Seismic Risk Management in Urban Areas.* Proceedings of a U.S.-Iran-Turkey Seismic Workshop. September 2011.
- PEER 2011/06** *The Use of Base Isolation Systems to Achieve Complex Seismic Performance Objectives.* Troy A. Morgan and Stephen A. Mahin. July 2011.
- PEER 2011/05** *Case Studies of the Seismic Performance of Tall Buildings Designed by Alternative Means.* Task 12 Report for the Tall Buildings Initiative. Jack Moehle, Yousef Bozorgnia, Nirmal Jayaram, Pierson Jones, Mohsen Rahnama, Nilesh Shome, Zeynep Tuna, John Wallace, Tony Yang, and Farzin Zareian. July 2011.
- PEER 2011/04** *Recommended Design Practice for Pile Foundations in Laterally Spreading Ground.* Scott A. Ashford, Ross W. Boulanger, and Scott J. Brandenberg. June 2011.

- PEER 2011/03** *New Ground Motion Selection Procedures and Selected Motions for the PEER Transportation Research Program.* Jack W. Baker, Ting Lin, Shrey K. Shahi, and Nirmal Jayaram. March 2011.
- PEER 2011/02** *A Bayesian Network Methodology for Infrastructure Seismic Risk Assessment and Decision Support.* Michelle T. Bensi, Armen Der Kiureghian, and Daniel Straub. March 2011.
- PEER 2011/01** *Demand Fragility Surfaces for Bridges in Liquefied and Laterally Spreading Ground.* Scott J. Brandenberg, Jian Zhang, Pirooz Kashighandi, Yili Huo, and Minxing Zhao. March 2011.
- PEER 2010/05** *Guidelines for Performance-Based Seismic Design of Tall Buildings.* Developed by the Tall Buildings Initiative. November 2010.
- PEER 2010/04** *Application Guide for the Design of Flexible and Rigid Bus Connections between Substation Equipment Subjected to Earthquakes.* Jean-Bernard Dastous and Armen Der Kiureghian. September 2010.
- PEER 2010/03** *Shear Wave Velocity as a Statistical Function of Standard Penetration Test Resistance and Vertical Effective Stress at Caltrans Bridge Sites.* Scott J. Brandenberg, Naresh Bellana, and Thomas Shantz. June 2010.
- PEER 2010/02** *Stochastic Modeling and Simulation of Ground Motions for Performance-Based Earthquake Engineering.* Sanaz Rezaeian and Armen Der Kiureghian. June 2010.
- PEER 2010/01** *Structural Response and Cost Characterization of Bridge Construction Using Seismic Performance Enhancement Strategies.* Ady Aviram, Božidar Stojadinović, Gustavo J. Parra-Montesinos, and Kevin R. Mackie. March 2010.
- PEER 2009/03** *The Integration of Experimental and Simulation Data in the Study of Reinforced Concrete Bridge Systems Including Soil-Foundation-Structure Interaction.* Matthew Dryden and Gregory L. Fenves. November 2009.
- PEER 2009/02** *Improving Earthquake Mitigation through Innovations and Applications in Seismic Science, Engineering, Communication, and Response.* Proceedings of a U.S.-Iran Seismic Workshop. October 2009.
- PEER 2009/01** *Evaluation of Ground Motion Selection and Modification Methods: Predicting Median Interstory Drift Response of Buildings.* Curt B. Haselton, Editor. June 2009.
- PEER 2008/10** *Technical Manual for Strata.* Albert R. Kottke and Ellen M. Rathje. February 2009.
- PEER 2008/09** *NGA Model for Average Horizontal Component of Peak Ground Motion and Response Spectra.* Brian S.-J. Chiou and Robert R. Youngs. November 2008.
- PEER 2008/08** *Toward Earthquake-Resistant Design of Concentrically Braced Steel Structures.* Patxi Uriz and Stephen A. Mahin. November 2008.
- PEER 2008/07** *Using OpenSees for Performance-Based Evaluation of Bridges on Liquefiable Soils.* Stephen L. Kramer, Pedro Arduino, and HyungSuk Shin. November 2008.
- PEER 2008/06** *Shaking Table Tests and Numerical Investigation of Self-Centering Reinforced Concrete Bridge Columns.* Hyung IL Jeong, Junichi Sakai, and Stephen A. Mahin. September 2008.
- PEER 2008/05** *Performance-Based Earthquake Engineering Design Evaluation Procedure for Bridge Foundations Undergoing Liquefaction-Induced Lateral Ground Displacement.* Christian A. Ledezma and Jonathan D. Bray. August 2008.
- PEER 2008/04** *Benchmarking of Nonlinear Geotechnical Ground Response Analysis Procedures.* Jonathan P. Stewart, Annie On-Lei Kwok, Youssef M. A. Hashash, Neven Matasovic, Robert Pyke, Zhiliang Wang, and Zhaohui Yang. August 2008.
- PEER 2008/03** *Guidelines for Nonlinear Analysis of Bridge Structures in California.* Ady Aviram, Kevin R. Mackie, and Božidar Stojadinović. August 2008.
- PEER 2008/02** *Treatment of Uncertainties in Seismic-Risk Analysis of Transportation Systems.* Evangelos Stergiou and Anne S. Kiremidjian. July 2008.
- PEER 2008/01** *Seismic Performance Objectives for Tall Buildings.* William T. Holmes, Charles Kircher, William Petak, and Nabih Youssef. August 2008.
- PEER 2007/12** *An Assessment to Benchmark the Seismic Performance of a Code-Conforming Reinforced Concrete Moment-Frame Building.* Curt Haselton, Christine A. Goulet, Judith Mitrani-Reiser, James L. Beck, Gregory G. Deierlein, Keith A. Porter, Jonathan P. Stewart, and Ertugrul Taciroglu. August 2008.
- PEER 2007/11** *Bar Buckling in Reinforced Concrete Bridge Columns.* Wayne A. Brown, Dawn E. Lehman, and John F. Stanton. February 2008.
- PEER 2007/10** *Computational Modeling of Progressive Collapse in Reinforced Concrete Frame Structures.* Mohamed M. Talaat and Khalid M. Mosalam. May 2008.

- PEER 2007/09** *Integrated Probabilistic Performance-Based Evaluation of Benchmark Reinforced Concrete Bridges.* Kevin R. Mackie, John-Michael Wong, and Božidar Stojadinović. January 2008.
- PEER 2007/08** *Assessing Seismic Collapse Safety of Modern Reinforced Concrete Moment-Frame Buildings.* Curt B. Haselton and Gregory G. Deierlein. February 2008.
- PEER 2007/07** *Performance Modeling Strategies for Modern Reinforced Concrete Bridge Columns.* Michael P. Berry and Marc O. Eberhard. April 2008.
- PEER 2007/06** *Development of Improved Procedures for Seismic Design of Buried and Partially Buried Structures.* Linda Al Atik and Nicholas Sitar. June 2007.
- PEER 2007/05** *Uncertainty and Correlation in Seismic Risk Assessment of Transportation Systems.* Renee G. Lee and Anne S. Kiremidjian. July 2007.
- PEER 2007/04** *Numerical Models for Analysis and Performance-Based Design of Shallow Foundations Subjected to Seismic Loading.* Sivapalan Gajan, Tara C. Hutchinson, Bruce L. Kutter, Prishati Raychowdhury, José A. Ugalde, and Jonathan P. Stewart. May 2008.
- PEER 2007/03** *Beam-Column Element Model Calibrated for Predicting Flexural Response Leading to Global Collapse of RC Frame Buildings.* Curt B. Haselton, Abbie B. Liel, Sarah Taylor Lange, and Gregory G. Deierlein. May 2008.
- PEER 2007/02** *Campbell-Bozorgnia NGA Ground Motion Relations for the Geometric Mean Horizontal Component of Peak and Spectral Ground Motion Parameters.* Kenneth W. Campbell and Yousef Bozorgnia. May 2007.
- PEER 2007/01** *Boore-Atkinson NGA Ground Motion Relations for the Geometric Mean Horizontal Component of Peak and Spectral Ground Motion Parameters.* David M. Boore and Gail M. Atkinson. May 2007.
- PEER 2006/12** *Societal Implications of Performance-Based Earthquake Engineering.* Peter J. May. May 2007.
- PEER 2006/11** *Probabilistic Seismic Demand Analysis Using Advanced Ground Motion Intensity Measures, Attenuation Relationships, and Near-Fault Effects.* Polsak Tothong and C. Allin Cornell. March 2007.
- PEER 2006/10** *Application of the PEER PBEE Methodology to the I-880 Viaduct.* Sashi Kunnath. February 2007.
- PEER 2006/09** *Quantifying Economic Losses from Travel Forgone Following a Large Metropolitan Earthquake.* James Moore, Sungbin Cho, Yue Yue Fan, and Stuart Werner. November 2006.
- PEER 2006/08** *Vector-Valued Ground Motion Intensity Measures for Probabilistic Seismic Demand Analysis.* Jack W. Baker and C. Allin Cornell. October 2006.
- PEER 2006/07** *Analytical Modeling of Reinforced Concrete Walls for Predicting Flexural and Coupled-Shear-Flexural Responses.* Kutay Orakcal, Leonardo M. Massone, and John W. Wallace. October 2006.
- PEER 2006/06** *Nonlinear Analysis of a Soil-Drilled Pier System under Static and Dynamic Axial Loading.* Gang Wang and Nicholas Sitar. November 2006.
- PEER 2006/05** *Advanced Seismic Assessment Guidelines.* Paolo Bazzurro, C. Allin Cornell, Charles Menun, Maziar Motahari, and Nicolas Luco. September 2006.
- PEER 2006/04** *Probabilistic Seismic Evaluation of Reinforced Concrete Structural Components and Systems.* Tae Hyung Lee and Khalid M. Mosalam. August 2006.
- PEER 2006/03** *Performance of Lifelines Subjected to Lateral Spreading.* Scott A. Ashford and Teerawat Juirnarongrit. July 2006.
- PEER 2006/02** *Pacific Earthquake Engineering Research Center Highway Demonstration Project.* Anne Kiremidjian, James Moore, Yue Yue Fan, Nesrin Basoz, Ozgur Yazali, and Meredith Williams. April 2006.
- PEER 2006/01** *Bracing Berkeley. A Guide to Seismic Safety on the UC Berkeley Campus.* Mary C. Comerio, Stephen Tobriner, and Ariane Fehrenkamp. January 2006.
- PEER 2005/17** *Earthquake Simulation Tests on Reducing Residual Displacements of Reinforced Concrete Bridges.* Junichi Sakai, Stephen A Mahin, and Andres Espinoza. December 2005.
- PEER 2005/16** *Seismic Response and Reliability of Electrical Substation Equipment and Systems.* Junho Song, Armen Der Kiureghian, and Jerome L. Sackman. April 2006.
- PEER 2005/15** *CPT-Based Probabilistic Assessment of Seismic Soil Liquefaction Initiation.* R. E. S. Moss, R. B. Seed, R. E. Kayen, J. P. Stewart, and A. Der Kiureghian. April 2006.
- PEER 2005/14** *Workshop on Modeling of Nonlinear Cyclic Load-Deformation Behavior of Shallow Foundations.* Bruce L. Kutter, Geoffrey Martin, Tara Hutchinson, Chad Harden, Sivapalan Gajan, and Justin Phalen. March 2006.

- PEER 2005/13** *Stochastic Characterization and Decision Bases under Time-Dependent Aftershock Risk in Performance-Based Earthquake Engineering.* Gee Liek Yeo and C. Allin Cornell. July 2005.
- PEER 2005/12** *PEER Testbed Study on a Laboratory Building: Exercising Seismic Performance Assessment.* Mary C. Comerio, Editor. November 2005.
- PEER 2005/11** *Van Nuys Hotel Building Testbed Report: Exercising Seismic Performance Assessment.* Helmut Krawinkler, Editor. October 2005.
- PEER 2005/10** *First NEES/E-Defense Workshop on Collapse Simulation of Reinforced Concrete Building Structures.* September 2005.
- PEER 2005/09** *Test Applications of Advanced Seismic Assessment Guidelines.* Joe Maffei, Karl Telleen, Danya Mohr, William Holmes, and Yuki Nakayama. August 2006.
- PEER 2005/08** *Damage Accumulation in Lightly Confined Reinforced Concrete Bridge Columns.* R. Tyler Ranf, Jared M. Nelson, Zach Price, Marc O. Eberhard, and John F. Stanton. April 2006.
- PEER 2005/07** *Experimental and Analytical Studies on the Seismic Response of Freestanding and Anchored Laboratory Equipment.* Dimitrios Konstantinidis and Nicos Makris. January 2005.
- PEER 2005/06** *Global Collapse of Frame Structures under Seismic Excitations.* Luis F. Ibarra and Helmut Krawinkler. September 2005.
- PEER 2005/05** *Performance Characterization of Bench- and Shelf-Mounted Equipment.* Samit Ray Chaudhuri and Tara C. Hutchinson. May 2006.
- PEER 2005/04** *Numerical Modeling of the Nonlinear Cyclic Response of Shallow Foundations.* Chad Harden, Tara Hutchinson, Geoffrey R. Martin, and Bruce L. Kutter. August 2005.
- PEER 2005/03** *A Taxonomy of Building Components for Performance-Based Earthquake Engineering.* Keith A. Porter. September 2005.
- PEER 2005/02** *Fragility Basis for California Highway Overpass Bridge Seismic Decision Making.* Kevin R. Mackie and Božidar Stojadinović. June 2005.
- PEER 2005/01** *Empirical Characterization of Site Conditions on Strong Ground Motion.* Jonathan P. Stewart, Yoojoong Choi, and Robert W. Graves. June 2005.
- PEER 2004/09** *Electrical Substation Equipment Interaction: Experimental Rigid Conductor Studies.* Christopher Stearns and André Filiatrault. February 2005.
- PEER 2004/08** *Seismic Qualification and Fragility Testing of Line Break 550-kV Disconnect Switches.* Shakhzod M. Takhirov, Gregory L. Fenves, and Eric Fujisaki. January 2005.
- PEER 2004/07** *Ground Motions for Earthquake Simulator Qualification of Electrical Substation Equipment.* Shakhzod M. Takhirov, Gregory L. Fenves, Eric Fujisaki, and Don Clyde. January 2005.
- PEER 2004/06** *Performance-Based Regulation and Regulatory Regimes.* Peter J. May and Chris Koski. September 2004.
- PEER 2004/05** *Performance-Based Seismic Design Concepts and Implementation: Proceedings of an International Workshop.* Peter Fajfar and Helmut Krawinkler, Editors. September 2004.
- PEER 2004/04** *Seismic Performance of an Instrumented Tilt-up Wall Building.* James C. Anderson and Vitelmo V. Bertero. July 2004.
- PEER 2004/03** *Evaluation and Application of Concrete Tilt-up Assessment Methodologies.* Timothy Graf and James O. Malley. October 2004.
- PEER 2004/02** *Analytical Investigations of New Methods for Reducing Residual Displacements of Reinforced Concrete Bridge Columns.* Junichi Sakai and Stephen A. Mahin. August 2004.
- PEER 2004/01** *Seismic Performance of Masonry Buildings and Design Implications.* Kerri Anne Taeko Tokoro, James C. Anderson, and Vitelmo V. Bertero. February 2004.
- PEER 2003/18** *Performance Models for Flexural Damage in Reinforced Concrete Columns.* Michael Berry and Marc Eberhard. August 2003.
- PEER 2003/17** *Predicting Earthquake Damage in Older Reinforced Concrete Beam-Column Joints.* Catherine Pagni and Laura Lowes. October 2004.
- PEER 2003/16** *Seismic Demands for Performance-Based Design of Bridges.* Kevin Mackie and Božidar Stojadinović. August 2003.

- PEER 2003/15** *Seismic Demands for Nondeteriorating Frame Structures and Their Dependence on Ground Motions.* Ricardo Antonio Medina and Helmut Krawinkler. May 2004.
- PEER 2003/14** *Finite Element Reliability and Sensitivity Methods for Performance-Based Earthquake Engineering.* Terje Haukaas and Armen Der Kiureghian. April 2004.
- PEER 2003/13** *Effects of Connection Hysteretic Degradation on the Seismic Behavior of Steel Moment-Resisting Frames.* Janise E. Rodgers and Stephen A. Mahin. March 2004.
- PEER 2003/12** *Implementation Manual for the Seismic Protection of Laboratory Contents: Format and Case Studies.* William T. Holmes and Mary C. Comerio. October 2003.
- PEER 2003/11** *Fifth U.S.-Japan Workshop on Performance-Based Earthquake Engineering Methodology for Reinforced Concrete Building Structures.* February 2004.
- PEER 2003/10** *A Beam-Column Joint Model for Simulating the Earthquake Response of Reinforced Concrete Frames.* Laura N. Lowes, Nilanjan Mitra, and Arash Altoontash. February 2004.
- PEER 2003/09** *Sequencing Repairs after an Earthquake: An Economic Approach.* Marco Casari and Simon J. Wilkie. April 2004.
- PEER 2003/08** *A Technical Framework for Probability-Based Demand and Capacity Factor Design (DCFD) Seismic Formats.* Fatemeh Jalayer and C. Allin Cornell. November 2003.
- PEER 2003/07** *Uncertainty Specification and Propagation for Loss Estimation Using FOSM Methods.* Jack W. Baker and C. Allin Cornell. September 2003.
- PEER 2003/06** *Performance of Circular Reinforced Concrete Bridge Columns under Bidirectional Earthquake Loading.* Mahmoud M. Hachem, Stephen A. Mahin, and Jack P. Moehle. February 2003.
- PEER 2003/05** *Response Assessment for Building-Specific Loss Estimation.* Eduardo Miranda and Shahram Taghavi. September 2003.
- PEER 2003/04** *Experimental Assessment of Columns with Short Lap Splices Subjected to Cyclic Loads.* Murat Melek, John W. Wallace, and Joel Conte. April 2003.
- PEER 2003/03** *Probabilistic Response Assessment for Building-Specific Loss Estimation.* Eduardo Miranda and Hesameddin Aslani. September 2003.
- PEER 2003/02** *Software Framework for Collaborative Development of Nonlinear Dynamic Analysis Program.* Jun Peng and Kincho H. Law. September 2003.
- PEER 2003/01** *Shake Table Tests and Analytical Studies on the Gravity Load Collapse of Reinforced Concrete Frames.* Kenneth John Elwood and Jack P. Moehle. November 2003.
- PEER 2002/24** *Performance of Beam to Column Bridge Joints Subjected to a Large Velocity Pulse.* Natalie Gibson, André Filiatrault, and Scott A. Ashford. April 2002.
- PEER 2002/23** *Effects of Large Velocity Pulses on Reinforced Concrete Bridge Columns.* Greg L. Orozco and Scott A. Ashford. April 2002.
- PEER 2002/22** *Characterization of Large Velocity Pulses for Laboratory Testing.* Kenneth E. Cox and Scott A. Ashford. April 2002.
- PEER 2002/21** *Fourth U.S.-Japan Workshop on Performance-Based Earthquake Engineering Methodology for Reinforced Concrete Building Structures.* December 2002.
- PEER 2002/20** *Barriers to Adoption and Implementation of PBEE Innovations.* Peter J. May. August 2002.
- PEER 2002/19** *Economic-Engineered Integrated Models for Earthquakes: Socioeconomic Impacts.* Peter Gordon, James E. Moore II, and Harry W. Richardson. July 2002.
- PEER 2002/18** *Assessment of Reinforced Concrete Building Exterior Joints with Substandard Details.* Chris P. Pantelides, Jon Hansen, Justin Nadauld, and Lawrence D. Reaveley. May 2002.
- PEER 2002/17** *Structural Characterization and Seismic Response Analysis of a Highway Overcrossing Equipped with Elastomeric Bearings and Fluid Dampers: A Case Study.* Nicos Makris and Jian Zhang. November 2002.
- PEER 2002/16** *Estimation of Uncertainty in Geotechnical Properties for Performance-Based Earthquake Engineering.* Allen L. Jones, Steven L. Kramer, and Pedro Arduino. December 2002.
- PEER 2002/15** *Seismic Behavior of Bridge Columns Subjected to Various Loading Patterns.* Asadollah Esmaeily-Gh. and Yan Xiao. December 2002.

- PEER 2002/14** *Inelastic Seismic Response of Extended Pile Shaft Supported Bridge Structures.* T.C. Hutchinson, R.W. Boulanger, Y.H. Chai, and I.M. Idriss. December 2002.
- PEER 2002/13** *Probabilistic Models and Fragility Estimates for Bridge Components and Systems.* Paolo Gardoni, Armen Der Kiureghian, and Khalid M. Mosalam. June 2002.
- PEER 2002/12** *Effects of Fault Dip and Slip Rake on Near-Source Ground Motions: Why Chi-Chi Was a Relatively Mild M7.6 Earthquake.* Brad T. Aagaard, John F. Hall, and Thomas H. Heaton. December 2002.
- PEER 2002/11** *Analytical and Experimental Study of Fiber-Reinforced Strip Isolators.* James M. Kelly and Shakhzod M. Takhirov. September 2002.
- PEER 2002/10** *Centrifuge Modeling of Settlement and Lateral Spreading with Comparisons to Numerical Analyses.* Sivapalan Gajan and Bruce L. Kutter. January 2003.
- PEER 2002/09** *Documentation and Analysis of Field Case Histories of Seismic Compression during the 1994 Northridge, California, Earthquake.* Jonathan P. Stewart, Patrick M. Smith, Daniel H. Whang, and Jonathan D. Bray. October 2002.
- PEER 2002/08** *Component Testing, Stability Analysis and Characterization of Buckling-Restrained Unbonded Braces™.* Cameron Black, Nicos Makris, and Ian Aiken. September 2002.
- PEER 2002/07** *Seismic Performance of Pile-Wharf Connections.* Charles W. Roeder, Robert Graff, Jennifer Soderstrom, and Jun Han Yoo. December 2001.
- PEER 2002/06** *The Use of Benefit-Cost Analysis for Evaluation of Performance-Based Earthquake Engineering Decisions.* Richard O. Zerbe and Anthony Falit-Baiamonte. September 2001.
- PEER 2002/05** *Guidelines, Specifications, and Seismic Performance Characterization of Nonstructural Building Components and Equipment.* André Filiatrault, Constantin Christopoulos, and Christopher Stearns. September 2001.
- PEER 2002/04** *Consortium of Organizations for Strong-Motion Observation Systems and the Pacific Earthquake Engineering Research Center Lifelines Program: Invited Workshop on Archiving and Web Dissemination of Geotechnical Data, 4–5 October 2001.* September 2002.
- PEER 2002/03** *Investigation of Sensitivity of Building Loss Estimates to Major Uncertain Variables for the Van Nuys Testbed.* Keith A. Porter, James L. Beck, and Rustem V. Shaikhutdinov. August 2002.
- PEER 2002/02** *The Third U.S.-Japan Workshop on Performance-Based Earthquake Engineering Methodology for Reinforced Concrete Building Structures.* July 2002.
- PEER 2002/01** *Nonstructural Loss Estimation: The UC Berkeley Case Study.* Mary C. Comerio and John C. Stallmeyer. December 2001.
- PEER 2001/16** *Statistics of SDF-System Estimate of Roof Displacement for Pushover Analysis of Buildings.* Anil K. Chopra, Rakesh K. Goel, and Chatpan Chintanapakdee. December 2001.
- PEER 2001/15** *Damage to Bridges during the 2001 Nisqually Earthquake.* R. Tyler Ranf, Marc O. Eberhard, and Michael P. Berry. November 2001.
- PEER 2001/14** *Rocking Response of Equipment Anchored to a Base Foundation.* Nicos Makris and Cameron J. Black. September 2001.
- PEER 2001/13** *Modeling Soil Liquefaction Hazards for Performance-Based Earthquake Engineering.* Steven L. Kramer and Ahmed-W. Elgamal. February 2001.
- PEER 2001/12** *Development of Geotechnical Capabilities in OpenSees.* Boris Jeremić. September 2001.
- PEER 2001/11** *Analytical and Experimental Study of Fiber-Reinforced Elastomeric Isolators.* James M. Kelly and Shakhzod M. Takhirov. September 2001.
- PEER 2001/10** *Amplification Factors for Spectral Acceleration in Active Regions.* Jonathan P. Stewart, Andrew H. Liu, Yoojoong Choi, and Mehmet B. Baturay. December 2001.
- PEER 2001/09** *Ground Motion Evaluation Procedures for Performance-Based Design.* Jonathan P. Stewart, Shyh-Jeng Chiou, Jonathan D. Bray, Robert W. Graves, Paul G. Somerville, and Norman A. Abrahamson. September 2001.
- PEER 2001/08** *Experimental and Computational Evaluation of Reinforced Concrete Bridge Beam-Column Connections for Seismic Performance.* Clay J. Naito, Jack P. Moehle, and Khalid M. Mosalam. November 2001.
- PEER 2001/07** *The Rocking Spectrum and the Shortcomings of Design Guidelines.* Nicos Makris and Dimitrios Konstantinidis. August 2001.

- PEER 2001/06** *Development of an Electrical Substation Equipment Performance Database for Evaluation of Equipment Fragilities.* Thalia Agnanos. April 1999.
- PEER 2001/05** *Stiffness Analysis of Fiber-Reinforced Elastomeric Isolators.* Hsiang-Chuan Tsai and James M. Kelly. May 2001.
- PEER 2001/04** *Organizational and Societal Considerations for Performance-Based Earthquake Engineering.* Peter J. May. April 2001.
- PEER 2001/03** *A Modal Pushover Analysis Procedure to Estimate Seismic Demands for Buildings: Theory and Preliminary Evaluation.* Anil K. Chopra and Rakesh K. Goel. January 2001.
- PEER 2001/02** *Seismic Response Analysis of Highway Overcrossings Including Soil-Structure Interaction.* Jian Zhang and Nicos Makris. March 2001.
- PEER 2001/01** *Experimental Study of Large Seismic Steel Beam-to-Column Connections.* Egor P. Popov and Shakhzod M. Takhirov. November 2000.
- PEER 2000/10** *The Second U.S.-Japan Workshop on Performance-Based Earthquake Engineering Methodology for Reinforced Concrete Building Structures.* March 2000.
- PEER 2000/09** *Structural Engineering Reconnaissance of the August 17, 1999 Earthquake: Kocaeli (Izmit), Turkey.* Halil Sezen, Kenneth J. Elwood, Andrew S. Whittaker, Khalid Mosalam, John J. Wallace, and John F. Stanton. December 2000.
- PEER 2000/08** *Behavior of Reinforced Concrete Bridge Columns Having Varying Aspect Ratios and Varying Lengths of Confinement.* Anthony J. Calderone, Dawn E. Lehman, and Jack P. Moehle. January 2001.
- PEER 2000/07** *Cover-Plate and Flange-Plate Reinforced Steel Moment-Resisting Connections.* Taejin Kim, Andrew S. Whittaker, Amir S. Gilani, Vitelmo V. Bertero, and Shakhzod M. Takhirov. September 2000.
- PEER 2000/06** *Seismic Evaluation and Analysis of 230-kV Disconnect Switches.* Amir S. J. Gilani, Andrew S. Whittaker, Gregory L. Fenves, Chun-Hao Chen, Henry Ho, and Eric Fujisaki. July 2000.
- PEER 2000/05** *Performance-Based Evaluation of Exterior Reinforced Concrete Building Joints for Seismic Excitation.* Chandra Clyde, Chris P. Pantelides, and Lawrence D. Reaveley. July 2000.
- PEER 2000/04** *An Evaluation of Seismic Energy Demand: An Attenuation Approach.* Chung-Che Chou and Chia-Ming Uang. July 1999.
- PEER 2000/03** *Framing Earthquake Retrofitting Decisions: The Case of Hillside Homes in Los Angeles.* Detlof von Winterfeldt, Nels Roselund, and Alicia Kitsuse. March 2000.
- PEER 2000/02** *U.S.-Japan Workshop on the Effects of Near-Field Earthquake Shaking.* Andrew Whittaker, Editor. July 2000.
- PEER 2000/01** *Further Studies on Seismic Interaction in Interconnected Electrical Substation Equipment.* Armen Der Kiureghian, Kee-Jeung Hong, and Jerome L. Sackman. November 1999.
- PEER 1999/14** *Seismic Evaluation and Retrofit of 230-kV Porcelain Transformer Bushings.* Amir S. Gilani, Andrew S. Whittaker, Gregory L. Fenves, and Eric Fujisaki. December 1999.
- PEER 1999/13** *Building Vulnerability Studies: Modeling and Evaluation of Tilt-up and Steel Reinforced Concrete Buildings.* John W. Wallace, Jonathan P. Stewart, and Andrew S. Whittaker, Editors. December 1999.
- PEER 1999/12** *Rehabilitation of Nonductile RC Frame Building Using Encasement Plates and Energy-Dissipating Devices.* Mehrdad Sasani, Vitelmo V. Bertero, James C. Anderson. December 1999.
- PEER 1999/11** *Performance Evaluation Database for Concrete Bridge Components and Systems under Simulated Seismic Loads.* Yael D. Hose and Frieder Seible. November 1999.
- PEER 1999/10** *U.S.-Japan Workshop on Performance-Based Earthquake Engineering Methodology for Reinforced Concrete Building Structures.* December 1999.
- PEER 1999/09** *Performance Improvement of Long Period Building Structures Subjected to Severe Pulse-Type Ground Motions.* James C. Anderson, Vitelmo V. Bertero, and Raul Bertero. October 1999.
- PEER 1999/08** *Envelopes for Seismic Response Vectors.* Charles Menun and Armen Der Kiureghian. July 1999.
- PEER 1999/07** *Documentation of Strengths and Weaknesses of Current Computer Analysis Methods for Seismic Performance of Reinforced Concrete Members.* William F. Cofer. November 1999.
- PEER 1999/06** *Rocking Response and Overturning of Anchored Equipment under Seismic Excitations.* Nicos Makris and Jian Zhang. November 1999.

- PEER 1999/05** *Seismic Evaluation of 550 kV Porcelain Transformer Bushings.* Amir S. Gilani, Andrew S. Whittaker, Gregory L. Fenves, and Eric Fujisaki. October 1999.
- PEER 1999/04** *Adoption and Enforcement of Earthquake Risk-Reduction Measures.* Peter J. May, Raymond J. Burby, T. Jens Feeley, and Robert Wood. August 1999.
- PEER 1999/03** *Task 3 Characterization of Site Response General Site Categories.* Adrian Rodriguez-Marek, Jonathan D. Bray and Norman Abrahamson. February 1999.
- PEER 1999/02** *Capacity-Demand-Diagram Methods for Estimating Seismic Deformation of Inelastic Structures: SDF Systems.* Anil K. Chopra and Rakesh Goel. April 1999.
- PEER 1999/01** *Interaction in Interconnected Electrical Substation Equipment Subjected to Earthquake Ground Motions.* Armen Der Kiureghian, Jerome L. Sackman, and Kee-Jeung Hong. February 1999.
- PEER 1998/08** *Behavior and Failure Analysis of a Multiple-Frame Highway Bridge in the 1994 Northridge Earthquake.* Gregory L. Fenves and Michael Ellery. December 1998.
- PEER 1998/07** *Empirical Evaluation of Inertial Soil-Structure Interaction Effects.* Jonathan P. Stewart, Raymond B. Seed, and Gregory L. Fenves. November 1998.
- PEER 1998/06** *Effect of Damping Mechanisms on the Response of Seismic Isolated Structures.* Nicos Makris and Shih-Po Chang. November 1998.
- PEER 1998/05** *Rocking Response and Overturning of Equipment under Horizontal Pulse-Type Motions.* Nicos Makris and Yiannis Roussos. October 1998.
- PEER 1998/04** *Pacific Earthquake Engineering Research Invitational Workshop Proceedings, May 14–15, 1998: Defining the Links between Planning, Policy Analysis, Economics and Earthquake Engineering.* Mary Comerio and Peter Gordon. September 1998.
- PEER 1998/03** *Repair/Upgrade Procedures for Welded Beam to Column Connections.* James C. Anderson and Xiaojing Duan. May 1998.
- PEER 1998/02** *Seismic Evaluation of 196 kV Porcelain Transformer Bushings.* Amir S. Gilani, Juan W. Chavez, Gregory L. Fenves, and Andrew S. Whittaker. May 1998.
- PEER 1998/01** *Seismic Performance of Well-Confined Concrete Bridge Columns.* Dawn E. Lehman and Jack P. Moehle. December 2000.

PEER REPORTS: ONE HUNDRED SERIES

- PEER 2012/103** *Performance-Based Seismic Demand Assessment of Concentrically Braced Steel Frame Buildings.* Chui-Hsin Chen and Stephen A. Mahin. December 2012.
- PEER 2012/102** *Procedure to Restart an Interrupted Hybrid Simulation: Addendum to PEER Report 2010/103.* Vesna Terzic and Božidar Stojadinovic. October 2012.
- PEER 2012/101** *Mechanics of Fiber Reinforced Bearings.* James M. Kelly and Andrea Calabrese. February 2012.
- PEER 2011/107** *Nonlinear Site Response and Seismic Compression at Vertical Array Strongly Shaken by 2007 Niigata-ken Chuetsu-oki Earthquake.* Eric Yee, Jonathan P. Stewart, and Kohji Tokimatsu. December 2011.
- PEER 2011/106** *Self Compacting Hybrid Fiber Reinforced Concrete Composites for Bridge Columns.* Pardeep Kumar, Gabriel Jen, William Trono, Marios Panagiotou, and Claudia Ostertag. September 2011.
- PEER 2011/105** *Stochastic Dynamic Analysis of Bridges Subjected to Spatially Varying Ground Motions.* Katerina Konakli and Armen Der Kiureghian. August 2011.
- PEER 2011/104** *Design and Instrumentation of the 2010 E-Defense Four-Story Reinforced Concrete and Post-Tensioned Concrete Buildings.* Takuya Nagae, Kenichi Tahara, Taizo Matsumori, Hitoshi Shiohara, Toshimi Kabeyasawa, Susumu Kono, Minehiro Nishiyama (Japanese Research Team) and John Wallace, Wassim Ghannoum, Jack Moehle, Richard Sause, Wesley Keller, Zeynep Tuna (U.S. Research Team). June 2011.
- PEER 2011/103** *In-Situ Monitoring of the Force Output of Fluid Dampers: Experimental Investigation.* Dimitrios Konstantinidis, James M. Kelly, and Nicos Makris. April 2011.
- PEER 2011/102** *Ground-Motion Prediction Equations 1964–2010.* John Douglas. April 2011.
- PEER 2011/101** *Report of the Eighth Planning Meeting of NEES/E-Defense Collaborative Research on Earthquake Engineering.* Convened by the Hyogo Earthquake Engineering Research Center (NIED), NEES Consortium, Inc. February 2011.
- PEER 2010/111** *Modeling and Acceptance Criteria for Seismic Design and Analysis of Tall Buildings.* Task 7 Report for the Tall Buildings Initiative - Published jointly by the Applied Technology Council. October 2010.
- PEER 2010/110** *Seismic Performance Assessment and Probabilistic Repair Cost Analysis of Precast Concrete Cladding Systems for Multistory Buildings.* Jeffrey P. Hunt and Božidar Stojadinovic. November 2010.
- PEER 2010/109** *Report of the Seventh Joint Planning Meeting of NEES/E-Defense Collaboration on Earthquake Engineering. Held at the E-Defense, Miki, and Shin-Kobe, Japan, September 18–19, 2009.* August 2010.
- PEER 2010/108** *Probabilistic Tsunami Hazard in California.* Hong Kie Thio, Paul Somerville, and Jascha Polet, preparers. October 2010.
- PEER 2010/107** *Performance and Reliability of Exposed Column Base Plate Connections for Steel Moment-Resisting Frames.* Ady Aviram, Božidar Stojadinovic, and Armen Der Kiureghian. August 2010.
- PEER 2010/106** *Verification of Probabilistic Seismic Hazard Analysis Computer Programs.* Patricia Thomas, Ivan Wong, and Norman Abrahamson. May 2010.
- PEER 2010/105** *Structural Engineering Reconnaissance of the April 6, 2009, Abruzzo, Italy, Earthquake, and Lessons Learned.* M. Selim Günay and Khalid M. Mosalam. April 2010.
- PEER 2010/104** *Simulating the Inelastic Seismic Behavior of Steel Braced Frames, Including the Effects of Low-Cycle Fatigue.* Yuli Huang and Stephen A. Mahin. April 2010.
- PEER 2010/103** *Post-Earthquake Traffic Capacity of Modern Bridges in California.* Vesna Terzic and Božidar Stojadinović. March 2010.
- PEER 2010/102** *Analysis of Cumulative Absolute Velocity (CAV) and JMA Instrumental Seismic Intensity (I_{JMA}) Using the PEER–NGA Strong Motion Database.* Kenneth W. Campbell and Yousef Bozorgnia. February 2010.
- PEER 2010/101** *Rocking Response of Bridges on Shallow Foundations.* Jose A. Ugalde, Bruce L. Kutter, and Boris Jeremic. April 2010.
- PEER 2009/109** *Simulation and Performance-Based Earthquake Engineering Assessment of Self-Centering Post-Tensioned Concrete Bridge Systems.* Won K. Lee and Sarah L. Billington. December 2009.

- PEER 2009/108** *PEER Lifelines Geotechnical Virtual Data Center.* J. Carl Stepp, Daniel J. Ponti, Loren L. Turner, Jennifer N. Swift, Sean Devlin, Yang Zhu, Jean Benoit, and John Bobbitt. September 2009.
- PEER 2009/107** *Experimental and Computational Evaluation of Current and Innovative In-Span Hinge Details in Reinforced Concrete Box-Girder Bridges: Part 2: Post-Test Analysis and Design Recommendations.* Matias A. Hube and Khalid M. Mosalam. December 2009.
- PEER 2009/106** *Shear Strength Models of Exterior Beam-Column Joints without Transverse Reinforcement.* Sangjoon Park and Khalid M. Mosalam. November 2009.
- PEER 2009/105** *Reduced Uncertainty of Ground Motion Prediction Equations through Bayesian Variance Analysis.* Robb Eric S. Moss. November 2009.
- PEER 2009/104** *Advanced Implementation of Hybrid Simulation.* Andreas H. Schellenberg, Stephen A. Mahin, Gregory L. Fenves. November 2009.
- PEER 2009/103** *Performance Evaluation of Innovative Steel Braced Frames.* T. Y. Yang, Jack P. Moehle, and Božidar Stojadinovic. August 2009.
- PEER 2009/102** *Reinvestigation of Liquefaction and Nonliquefaction Case Histories from the 1976 Tangshan Earthquake.* Robb Eric Moss, Robert E. Kayen, Liyuan Tong, Songyu Liu, Guojun Cai, and Jiaer Wu. August 2009.
- PEER 2009/101** *Report of the First Joint Planning Meeting for the Second Phase of NEES/E-Defense Collaborative Research on Earthquake Engineering.* Stephen A. Mahin et al. July 2009.
- PEER 2008/104** *Experimental and Analytical Study of the Seismic Performance of Retaining Structures.* Linda Al Atik and Nicholas Sitar. January 2009.
- PEER 2008/103** *Experimental and Computational Evaluation of Current and Innovative In-Span Hinge Details in Reinforced Concrete Box-Girder Bridges. Part 1: Experimental Findings and Pre-Test Analysis.* Matias A. Hube and Khalid M. Mosalam. January 2009.
- PEER 2008/102** *Modeling of Unreinforced Masonry Infill Walls Considering In-Plane and Out-of-Plane Interaction.* Stephen Kadysiewski and Khalid M. Mosalam. January 2009.
- PEER 2008/101** *Seismic Performance Objectives for Tall Buildings.* William T. Holmes, Charles Kircher, William Petak, and Nabih Youssef. August 2008.
- PEER 2007/101** *Generalized Hybrid Simulation Framework for Structural Systems Subjected to Seismic Loading.* Tarek Elkhoraibi and Khalid M. Mosalam. July 2007.
- PEER 2007/100** *Seismic Evaluation of Reinforced Concrete Buildings Including Effects of Masonry Infill Walls.* Alidad Hashemi and Khalid M. Mosalam. July 2007.

The Pacific Earthquake Engineering Research Center (PEER) is a multi-institutional research and education center with headquarters at the University of California, Berkeley. Investigators from over 20 universities, several consulting companies, and researchers at various state and federal government agencies contribute to research programs focused on performance-based earthquake engineering.

These research programs aim to identify and reduce the risks from major earthquakes to life safety and to the economy by including research in a wide variety of disciplines including structural and geotechnical engineering, geology/seismology, lifelines, transportation, architecture, economics, risk management, and public policy.

PEER is supported by federal, state, local, and regional agencies, together with industry partners.



PEER Core Institutions

University of California, Berkeley (Lead Institution)
California Institute of Technology
Oregon State University
Stanford University
University of California, Davis
University of California, Irvine
University of California, Los Angeles
University of California, San Diego
University of Nevada, Reno
University of Southern California
University of Washington

PEER reports can be ordered at <https://peer.berkeley.edu/peer-reports> or by contacting

Pacific Earthquake Engineering Research Center
University of California, Berkeley
325 Davis Hall, Mail Code 1792
Berkeley, CA 94720-1792
Tel: 510-642-3437
Email: peer_center@berkeley.edu

ISSN 2770-8314
<https://doi.org/10.55461/ZONT9308>